



HAL
open science

Development and improvement of the diagnostic imaging tools for the characterization of tumor masses of the musculoskeletal system

Pedro Augusto Gondim Teixeira

► **To cite this version:**

Pedro Augusto Gondim Teixeira. Development and improvement of the diagnostic imaging tools for the characterization of tumor masses of the musculoskeletal system. Human health and pathology. Université de Lorraine, 2013. English. NNT : 2013LORR0178 . tel-01750355

HAL Id: tel-01750355

<https://hal.univ-lorraine.fr/tel-01750355>

Submitted on 29 Mar 2018

HAL is a multi-disciplinary open access archive for the deposit and dissemination of scientific research documents, whether they are published or not. The documents may come from teaching and research institutions in France or abroad, or from public or private research centers.

L'archive ouverte pluridisciplinaire **HAL**, est destinée au dépôt et à la diffusion de documents scientifiques de niveau recherche, publiés ou non, émanant des établissements d'enseignement et de recherche français ou étrangers, des laboratoires publics ou privés.



AVERTISSEMENT

Ce document est le fruit d'un long travail approuvé par le jury de soutenance et mis à disposition de l'ensemble de la communauté universitaire élargie.

Il est soumis à la propriété intellectuelle de l'auteur. Ceci implique une obligation de citation et de référencement lors de l'utilisation de ce document.

D'autre part, toute contrefaçon, plagiat, reproduction illicite encourt une poursuite pénale.

Contact : ddoc-theses-contact@univ-lorraine.fr

LIENS

Code de la Propriété Intellectuelle. articles L 122. 4

Code de la Propriété Intellectuelle. articles L 335.2- L 335.10

http://www.cfcopies.com/V2/leg/leg_droi.php

<http://www.culture.gouv.fr/culture/infos-pratiques/droits/protection.htm>



**UNIVERSITÉ
DE LORRAINE**

Ecole Doctorale BioSE (Biologie-Santé-Environnement)

Thèse

Présentée et soutenue publiquement pour l'obtention du titre de

DOCTEUR DE L'UNIVERSITE DE LORRAINE

Mention : « Sciences de la Vie et de la Santé »

par Pedro Augusto GONDIM TEIXEIRA

**Développement et amélioration des outils d'imagerie
médicale pour la caractérisation des masses tumorales
du système ostéo-articulaire**

Soutenue le 27 novembre 2013

Membres du jury :

Rapporteurs :	Professeur Anne COTTEN	Université Lille 2, France
	Professeur Jean-Luc DRAPE	Université Paris V, France
Examineurs :	Professeur Bruno VANDE BERG	Université Catholique de Louvain, Bruxelles, Belgique
	Professeur François SIRVEAUX	Université de Lorraine, Nancy, France
	Docteur Gabriela HOSSU	Université de Lorraine, Nancy, France
Directeur de thèse :	Professeur Alain BLUM	Université de Lorraine, Nancy, France

Laboratoire IADI : Imagerie Adaptative Diagnostique et Interventionnelle (INSERM U947), Tour Drouet -
4^{ème} étage, Rue Morvan 54511, Vandoeuvre-les-Nancy CEDEX.

TABLE DE MATIERES

TABLE DE MATIERES	1
REMERCIEMENTS	3
ABREVIATIONS	6
INTRODUCTION	7
CHAPITRE 1 – L’IMAGERIE PAR RESONANCE MAGNETIQUE	16
- Article 1 : <i>Dynamic MR imaging of Osteoid Osteomas : Correlation of semi-quantitative and quantitative perfusion parameters with patient symptoms and treatment outcome</i>	18
- Article 2 : <i>Differentiation between benign and malignant non-fatty soft tissue masses using diffusion weighted MR: Correlation between ADC values and lesion signal on T2 weighted sequences</i>	28
- Article 3 : <i>1H MR spectroscopy of cadaveric thigh muscles before and after calcium carbonate injection: Understanding the influence of calcium crystals on the quantification of the choline peak</i>	37
- Discussion et conclusions.....	47
CHAPITRE 2 – LA TOMODENSITOMETRIE	48
- Article 1 : <i>Dose reduction in musculoskeletal CT: Tips and Tricks</i>	50
- Article 2 : <i>Imaging follow-up of patients with osteoid osteomas after percutaneous ablative laser therapy: Is there a place for CT perfusion?</i>	61
- Article 3 : <i>Wide area detector CT perfusion: Can it differentiate osteoid osteomas from other lytic bone lesions?</i>	70
- Article 4 : <i>Bone marrow edema pattern identification in patients with lytic bone lesions using digital subtraction angiography-like bone subtraction on large area detector CT</i>	77
- Article 5 : <i>Total hip prosthesis CT with single energy projection based metallic artifact reduction technique: Impact on the evaluation of specific peri-prosthetic soft tissue structures</i>	87

- Discussion et conclusions.....	96
CHAPITRE 3 – L’ÉCHOGRAPHIE.....	98
- Article 1: <i>Tumours and pseudotumours of the soft tissue in adults: Perspectives and current role of sonography.....</i>	100
- Article 2: <i>Contrast-enhanced ultrasonography of peripheral soft-tissue tumors: Feasibility study and preliminary results.....</i>	117
- Discussion et conclusions.....	127
CONCLUSION.....	128
REFERENCES BIBLIOGRAPHIQUES.....	130
ANNEXES.....	133
- Annexe 1 : Classification des tumeurs des parties molles de l’OMS simplifié.....	133
- Annexe 2 : Classification des tumeurs osseuses de l’OMS simplifié.....	134
RESUME.....	135
ABSTRACT.....	135

REMERCIEMENTS

Cette thèse est le résultat des efforts de toute une équipe dont j'ai eu le bonheur et la chance de faire partie. Je me réjouis donc de remercier les personnes qui directement ou indirectement ont contribué à la réalisation de ce travail.

Je tiens à remercier tout d'abord le professeur Jacques Felblinger, directeur du laboratoire d'imagerie adaptative diagnostique et interventionnelle (IADI) pour l'opportunité de travailler dans cette institution. Son appui m'a ouvert les portes et m'a donné les moyens techniques et relationnels pour réaliser cette thèse.

Je remercie mon directeur de thèse, le professeur Alain Blum pour avoir eu confiance en moi et m'avoir donné le temps et la liberté de suivre les voies que me semblaient les plus pertinentes. Avec un regard critique et innovateur le professeur Blum fut un élément indispensable pour l'aboutissement de ces travaux.

Ma chère Co-directrice le Dr. Gabriela Hossu était de mon côté lors des multiples challenges scientifiques que cette thèse a pu produire. Elle m'a montré la voie de la persévérance et a fait le pont entre les mondes scientifique et médical, parfois très différents. Cette thèse nous a mis en contact et en plus d'une collègue j'ai gagné une amie. Merci pour ton aide précieuse.

Madame le professeur Anne Cotten par ses publications a été pour moi une source d'inspiration professionnelle bien avant mon arrivée en France. Je me sens très honoré par sa présence dans le jury de cette thèse et je lui suis profondément reconnaissant pour ses remarques et conseils pendant le suivi et l'évaluation de ces travaux.

Je remercie chaleureusement le professeur Jean-Luc Drapé de l'attention et de l'intérêt portés sur mon travail. Ses remarques pertinentes et constructives me permettront d'améliorer et enrichir cette thèse et d'autres travaux à venir.

Le professeur Bruno Vande Berg, président du jury de thèse, représente une des équipes phare dans l'imagerie ostéo-articulaire mondiale avec un regard différencié et unique sur les pathologies ostéo-articulaires. Je remercie le professeur Vande Berg pour la sincérité de ses remarques et ses questions pointues que me poussent vers l'avant.

Le professeur François Sirveaux chirurgien orthopédique fait un lien fondamental entre les radiologues et les patients, permettant que travaux scientifiques réalisés dans le cadre de cette thèse contribuent et restent fixes sur le but ultime : l'amélioration des soins dispensés aux patients avec une pathologie ostéo-articulaire. Je remercie le professeur Sirveaux pour l'aide apportée à la réalisation de cette thèse depuis le début.

Le Dr. François Kauffmann a été un élément clef pour la réalisation des travaux portant sur la spectroscopie proton. Quand le futur paraissait sombre et les résultats incompréhensibles le Dr. Kauffmann nous a donné les connaissances nécessaires et nous a montré la bonne voie. Je vous remercie énormément pour votre aide.

Je remercie le professeur Roland Kreis de l'Université de Berne en Suisse pour son aide précieuse dans l'interprétation des données spectroscopiques.

Le Dr. Bailiang Chen a travaillé dur dans le post traitement des données de diffusion et a apporté une aide fondamentale à la réalisation des travaux portant sur cette technique. Au Dr. Chen je laisse le message suivant : Thank you so much, I couldn't have done this without you!

Travailler avec le Dr. Anou Sewonu a été un grand plaisir. Le support technique et l'aide informatique offert par le Dr. Sewonu m'a « sauvé la vie » à plusieurs reprises pendant cette thèse. Je te remercie pour ta disponibilité et ta volonté d'aider.

Je remercie le Dr. Marine Beaumont pour l'aide apporté au calcul et interprétation des paramètres perfusionnels quantitatifs. Cette collaboration a beaucoup enrichi les travaux qui portaient sur cette technique et va sans doute ouvrir les portes pour de projets futurs.

Mon amie Frédérique Gay a travaillé dur sur la diffusion en IRM, sans ses efforts les deadlines n'auraient jamais pu être assurées. Merci beaucoup Fred !

La collaboration avec Jean-Baptiste Meyer a permis de démontrer le potentiel des nouvelles techniques de réduction des artéfacts métalliques. Un travail avec des résultats positifs si flagrants qui fait de cette technique un outil indispensable à l'évaluation des prothèses dans notre service. Merci Jean-Baptiste !

Je remercie le Dr. Francis Pierucci et Mme Valérie Zimmermann pour leur accueil et leurs conseils sur l'exploration des tumeurs en échographie.

Je n'oublierai pas de remercier le Dr. Alban Gervaise, qui m'a beaucoup appris sur la radioprotection en scanographie, pour sa collaboration.

Un grand merci aux Docteurs Emilien Micard et Freddy Odille pour leur aide dans le domaine hostile (au moins pour moi) du recalage des images.

Mon ami et collègue le Dr. Matthias Louis a été responsable d'une grande partie des confirmations histologiques et des traitements percutanés des patients inclus dans ce protocole. Je remercie mon ami Matthias pour son aide et pour son travail considérablement augmenté pendant la réalisation de ces travaux.

Je remercie les inséparables docteurs Sabine Aptel et Ariane Raymond pour leur patience et compréhension envers moi, pendant un période particulièrement difficile de leurs carrières où mon absence a augmenté leur charge de travail.

Je remercie mes collègues manipulateurs pour l'intérêt et le dévouement à réaliser de la meilleure façon possible des protocoles de recherche lourds et compliqués chez une population de patients parfois difficile. L'aboutissement de cette thèse reflète votre effort.

Aux internes, force motrice de mes vacances pendant cette thèse, je tiens à présenter mes plus sincères excuses. Le temps dédié à la recherche ne m'a pas permis de participer comme je devrais à votre formation. J'ai une dette envers vous.

Il est très difficile et injuste de remercier avec des simples mots la personne qui est à l'origine de tout... C'est grâce à ma chère épouse Sophie que je suis ici (en France), que j'ai eu l'opportunité de travailler dans un centre d'excellence, que j'ai pu mener ces travaux. Sans son support inconditionnel dans tous les fronts de ma vie, rien de cela n'aurait été possible... je ne serais même pas sur ce continent et ma vie ne serait qu'une version plus triste de celle que je mène aujourd'hui.

A ma petite fille Charlotte je remercie tout simplement d'exister et de faire de moi un papa très heureux !

Même avec un effort soutenu, dans cette vie, je ne serai pas à la hauteur de rétribuer tout le dévouement de mes parents, André et Eunice, à mon éducation et à ma formation. Amo vocês do fundo do coração!

Finalement, je voulais dédier cette thèse à mon Grand Père le professeur Rodolfo Teixeira, médecin, chercheur, mon maître, collègue et ami. C'est en essayant de suivre tes pas que je suis arrivé jusqu'ici. Merci infiniment.

ABREVIATIONS ET SYMBOLES

ADC	Coefficient de Diffusion Apparent (Apparent diffusion coefficient)
ANSM	Agence Nationale de Sécurité du Médicament et des produits de santé
CAV	Centre Alexis Vautrin
CCEG	Centre Chirurgical Emile Gallé
CEC	Centre d'investigation Clinique Epidémiologie Clinique
CHU	Centre Hospitalier Universitaire
CPP	Comité de Protection des Personnes
DSA	Angiographie de Soustraction Numérique (Digital subtraction Angiography)
EVEC	Espace Extra Vasculaire Extra Cellulaire
IADI	Imagerie Adaptative Diagnostique et Interventionnelle
INSERM	Institut National de la Santé et de la Recherche Médicale
IRM	Imagerie par Résonance Magnétique
OMS	Organisation Mondiale de Santé
TDM	Tomodensitométrie
TOMP	Tumeurs Osseuses Malignes Primitives
TRICKS	Time Resolved Imaging of Contrast Kinetics
T1	Temps de relaxation longitudinale
T2	Temps de relaxation transversale
UH	Unités Hounsfield

INTRODUCTION

Les tumeurs ou néoplasies ostéo-articulaires sont une source fréquente de consultation en médecine générale et chirurgie orthopédique, mais leur fréquence exacte n'est pas connue (1,2). Ces lésions, sont caractérisées par une prolifération inadaptée des cellules, sans relation avec la croissance des tissus normaux avoisinants. La présentation clinique est extrêmement variée : les lésions peu agressives sont peu symptomatiques et ont une importance parfois purement esthétique. Les lésions agressives sont souvent douloureuses pouvant envahir des structures adjacentes et à distance (métastase). Ce type de tumeur peut avoir des conséquences fonctionnelles et psychiques importantes pour le patient pouvant même impliquer leur pronostic vital (3–5). Pour ces lésions, l'exérèse chirurgicale complète et précoce reste aujourd'hui le seul traitement curatif (6,7).

Dans le groupe des néoplasies ostéo-articulaires, on distingue les tumeurs d'origine osseuse et les tumeurs des parties molles. Les tumeurs des parties molles représentent moins de 1% des cancers (8). Le nombre de nouveaux cas est de l'ordre de 10 000 par an aux Etats-Unis et de 1800 par an en France (9). Les masses des parties molles se développent principalement dans les muscles des membres, mais elles peuvent apparaître en n'importe quelle localisation anatomique. Ces lésions affectent principalement les patients âgés. 56.8% d'entre-elles sont découvertes après 55 ans mais 9% concernent les patients de moins de 20 ans (10). L'incidence des tumeurs bénignes est plus difficile à définir. Celles-ci sont environ 100 fois plus fréquentes que les tumeurs malignes, mais des nombreuses tumeurs bénignes cutanées et sous-cutanées de petite taille ne nécessitent aucun bilan d'imagerie et par conséquent ne sont pas explorées en imagerie (8,11).

Les tumeurs osseuses sont des pathologies rares et de ce fait mal connues. Aux Etats-Unis, l'incidence des tumeurs osseuses malignes primitives (TOMP) est de 10 cas par an pour un million d'habitants (8). Parmi ces tumeurs, l'ostéosarcome est le plus fréquent (30% à 35% de TOMP) ; il représente 0,2% de tous les cancers et son incidence est de 100 à 150 cas par an en France. Viennent ensuite les chondrosarcomes (25% des TOMP) et les sarcomes d'Ewing (20% des TOMP) dont l'incidence est de 50 à 80 cas par an en France (12,13). Les tumeurs osseuses secondaires sont, quant à elles, plus fréquentes que les TOMP ; elles touchent environ 60% des patients atteints de cancer (en sachant que le cancer est la deuxième cause de mortalité en France).

Le système ostéo-articulaire est composé d'une vaste gamme de tissus d'origine mésenchymateuse. Les tumeurs ostéo-articulaires ont, par conséquent une diversité histologique exubérante. Depuis 2002 l'Organisation Mondiale de la Santé (OMS), dans la nouvelle classification des tumeurs osseuses et des parties molles reconnaît, 194 entités histologiques distinctes de

néoplasies ostéo-articulaires (54 osseuses et 140 des parties molles) (annexes 1 et 2)(8). Cette hétérogénéité histologique explique en partie la performance médiocre des méthodes de diagnostic non-invasives à caractériser ces lésions et à évaluer l'agressivité des lésions d'un même type histologique. La distinction bénin-malin est importante pour déterminer l'agressivité d'une masse ostéo-articulaire. Néanmoins le type histologique seul ne permet pas de prédire l'évolution d'une tumeur. La détermination du pronostic, essentielle pour prendre une décision thérapeutique, dépend de très nombreux facteurs dont certains sont définis par l'imagerie.

Les méthodes d'imagerie actuelles permettent dans la grande majorité des cas de confirmer la présence d'une lésion tumorale identifiée cliniquement, pouvant également visualiser des lésions non-suspectées quand le tableau clinique est moins exubérant (Fig. 1). Avec l'augmentation de la disponibilité et de la performance des méthodes d'imagerie en coupe, notamment l'imagerie par résonance magnétique (IRM) le diagnostic des tumeurs ostéo-articulaires se fait de plus en plus précocement (Fig. 2).

Le traitement d'une tumeur ostéo-articulaire peut varier d'une exérèse simple ou d'un suivi clinique pour les tumeurs non-agressives à une exérèse en bloc avec des marges saines, associée à une radio et/ou chimiothérapie pour les tumeurs agressives. Le diagnostic précoce permet une réduction de la morbidité, de la prise en charge chirurgicale avec l'utilisation de techniques moins invasives (e.g. chirurgie de sauvetage du membre) (Fig. 3) (14). L'amélioration de la performance diagnostique en association aux thérapies adjuvantes (e.g. chimio et radiothérapie) a eu un impact positif sur la survie des patients porteurs d'une néoplasie ostéo-articulaire agressive (3,15).



Fig. 1 : Patient de 15 ans présentant des gonalgies inflammatoires. Bilan étiologique. A) Coupe sagittale IRM pondérée T2 avec saturation de la graisse montrant une petite lésion tumorale hétérogène dans la partie proximale du gastrocnémien latéral (flèche). B) Multiples calcifications visibles au sein de cette lésion en scanner (flèche). Ces anomalies sont évocatrices d'une myosite ossifiante.

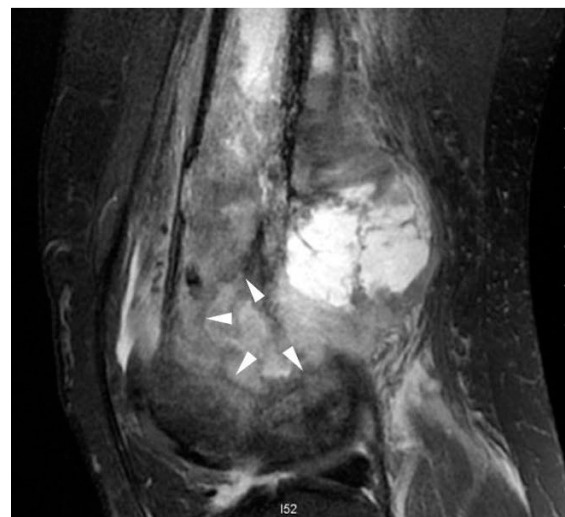


Fig. 2: Coupe sagittale IRM pondérée T2 avec saturation de la graisse d'une patiente de 64 ans, présentant un ostéosarcome du fémur. Notez l'extension des anomalies de signal intra médullaires au delà des bords de la lyse osseuse (flèches).



Fig. 3 : Radiographie post opératoire du fémur distal d'un patient opéré d'un ostéosarcome avec une chirurgie de sauvetage du membre inférieur. Notez les prothèses de reconstruction métalliques et la reconstitution avec une allogreffe de fibula (flèche).

Différentes méthodes d'imagerie peuvent être utilisées isolément ou en association pour l'évaluation des tumeurs ostéo-articulaires. Les radiographies standards, l'échographie, la tomодensitométrie (TDM), l'IRM et l'imagerie par radionucléides peuvent faire partie du bilan de caractérisation des tumeurs ostéo-articulaires. Aucune de ces méthodes ne fournit seule toutes les informations nécessaires pour définir la prise en charge de l'ensemble des tumeurs ostéo-articulaires. Dans le but d'avoir une évaluation tumorale la plus précise possible, plusieurs méthodes d'imagerie sont utilisées en association. La littérature manque encore de données précises sur le rôle et les indications de chaque méthode. Néanmoins l'importance de l'échographie, de la TDM et de l'IRM pour l'investigation des tumeurs ostéo-articulaires est consensuelle. L'IRM est actuellement la méthode la plus performante. Avec un contraste tissulaire nettement supérieur aux autres techniques, elle permet une analyse précise des tissus mous et osseux, profonds et superficiels. La TDM, importante pour l'analyse de l'os et des lésions calcifiées, est utilisée pour la recherche de métastases thoraco-abdominales. De plus, les reconstructions scanographiques multi planaires et en 3-D facilitent la planification de l'acte chirurgical et de la voie d'abord des biopsies. Finalement, l'échographie, méthode anodine, largement disponible et peu coûteuse permet une analyse précise des lésions des parties molles superficielles et de leur rapport avec les structures adjacentes.

Malgré l'impact positif de l'imagerie médicale sur le pronostic des patients porteurs d'une néoplasie ostéo-articulaire les méthodes disponibles sont encore peu performantes pour déterminer l'agressivité lésionnelle (1). L'analyse classique des images basée sur des critères morphologiques est insuffisante pour caractériser un nombre significatif de tumeurs ostéo-articulaires (16). Ce manque de performance a des conséquences importantes. Une biopsie osseuse ou des parties molles est encore nécessaire chez un grand nombre de patients porteurs d'une tumeur

non-agressive. Les techniques de biopsie percutanée (guidée ou non par imagerie) ou chirurgicale sont minimalement invasives, cependant elles peuvent avoir des complications importantes (infection, saignement, douleur résiduelle) et sont responsables d'une augmentation du coût de la prise en charge (17). En outre, un retard diagnostique d'une lésion prise à tort pour bénigne ou avec une biopsie percutanée non concluante peut influencer négativement le pronostic du patient.

	Total 597	Services spécialisés	Centres non spécialisés
Erreur de diagnostic	18 %	12,3 %	27,4 %
Complications per-op	10 %	4,1 %	29 %
Pb. dans le traitement	19,3 %	4,1 %	36,3 %
Modif. du pronostic	10 %	3,5 %	17,4 %

Tableau 1 : Tableau montrant les résultats et complications, après biopsie pour tumeur osseuse, en fonction du centre, aux Etats Unis d'après Mankin et al.

La croissance soutenue d'une lésion tumorale peut alourdir et réduire l'efficacité du traitement chirurgical. Un traitement chirurgical inadapté non associé à une thérapie adjuvante, augmente le risque de récurrence, ainsi que le nombre et la difficulté des procédures chirurgicales de sauvetage. Finalement, la complexité de la prise en charge augmente quand il s'agit d'une tumeur maligne. Si le traitement des tumeurs bénignes peut s'envisager dans un service non spécialisé, il est en revanche déraisonnable d'entreprendre le traitement d'une tumeur maligne primitive osseuse dans un service non spécialisé par des médecins non habitués à cette pathologie. La prise en charge des patients porteurs d'une tumeur ostéo-articulaire maligne dans des services non spécialisés aboutissait à une multiplication par 3 des erreurs diagnostiques et par 10 des entraves au traitement (Tableau I) (17). Dans ce contexte, les enjeux du développement et de l'amélioration d'outils d'imagerie pour la caractérisation des tumeurs ostéo-articulaires sont capitaux.

Une demande croissante pour une amélioration de la caractérisation tumorale non-invasive a conduit à des avancées majeures sur les techniques d'imagerie médicale. D'importants développements techniques achevés par les constructeurs, ont favorisé l'application en pratique clinique de méthodes d'imagerie fonctionnelle de plus en plus performantes. Par conséquent, l'imagerie fonctionnelle est devenue une partie intégrante du bilan de caractérisation tumorale dans les centres de référence oncologiques (18). Les techniques fonctionnelles les plus utilisées actuellement permettent :

- L'analyse approfondie du rehaussement tumoral (perfusion) ;
- L'évaluation indirecte de la structure cellulaire (Imagerie par diffusion, élastographie et perfusion quantitative) ;
- L'estimation de la concentration de plusieurs marqueurs biochimiques des cellules tumorales (spectroscopie proton en IRM).

Critères d'inclusion
Patient adressé pour l'investigation d'une tumeur des os ou des parties molles périphériques supposée primitive
Plus de 18 ans
Pas d'altération de l'état de conscience
Signature du consentement éclairé
Critères d'exclusion
Notion d'allergie au Sonovue, aux produits de contraste iodé ou aux chélates de gadolinium
Femme enceinte ou susceptible de l'être
Femmes en cours d'allaitement
Syndrome coronarien aigu ou cardiopathie ischémique instable
Insuffisance rénale
Contre-indication à l'IRM

Tableau 2 : Critères d'inclusion et d'exclusion de l'étude de caractérisation des tumeurs ostéo-articulaires.

Des études fondamentales ont montré une bonne corrélation entre plusieurs de ces paramètres fonctionnels et l'histologie tumorale (18–20). Cependant, l'absence de critères diagnostiques validés et d'uniformisation des protocoles d'acquisition, rend l'application clinique de ces nouveaux outils difficile.

La plupart des techniques d'imagerie fonctionnelle disponibles ont initialement été développées pour la neuroradiologie, la sénologie ou l'imagerie de la prostate. Ces techniques ont commencé, plus récemment, à être adaptées à l'imagerie ostéo-articulaire. Cette adaptation est particulièrement difficile car certains des composants histologiques du système ostéo-articulaire rendent l'évaluation

fonctionnelle difficile. C'est le cas de l'os non-lytique avec la TDM de perfusion, les calcifications et la graisse pour la diffusion et la spectroscopie proton en IRM (19). Les paramètres d'acquisition doivent être adaptés au système ostéo-articulaire et parfois à un composant tissulaire spécifique (e.g. l'os, la graisse etc.). La perméabilité capillaire est corrélée à l'agressivité tumorale (21). Les parois des capillaires du corps humain et donc du système ostéo-articulaire sont dépourvues d'une barrière hémato-encéphalique, permettant ainsi le passage des produits de contraste utilisés en pratique courante (e.g. à base d'iode et de gadolinium) (22). De ce fait des modèles mathématiques complexes et par conséquent moins fiables sont nécessaires pour estimer la perméabilité capillaire en imagerie ostéo-articulaire (23). Les difficultés pour l'utilisation des méthodes d'imagerie fonctionnelle ne sont pas seulement dans le domaine de l'acquisition des données, mais également dans leur post traitement. Des logiciels capables de traiter les données acquises sont souvent indisponibles et le support d'une structure de recherche est encore nécessaire. C'est le cas pour l'obtention des paramètres de perfusion quantitatifs ou pour l'analyse des spectres acquis en IRM.

Afin d'étudier différentes techniques d'imagerie fonctionnelle (IRM, TDM et échographie) dans la prise en charge des tumeurs osteo-articulaires, une étude de type recherche biomédicale mono centrique à recrutement prospectif a été lancée en 2009. Les objectifs de cette étude sont de :

- 1) Comparer l'ensemble des outils d'imagerie dans la caractérisation des tumeurs ostéo-articulaires
- 2) Déterminer si l'association des outils les plus pertinents améliore la caractérisation tissulaire.
- 3) Déterminer s'il existe une corrélation entre certains paramètres et le grade histologique
- 4) Proposer à terme une démarche diagnostique cohérente et un itinéraire d'imagerie performant pour les tumeurs ostéo-articulaires
- 5) Proposer des outils de suivi permettant d'apprécier l'évolutivité tumorale avant la modification des données morpho volumétriques.

Cette étude a eu l'accord du Comité de protection des personnes (CPP) et est inscrite à l'Agence Nationale de Sécurité du Médicament et des produits de santé (ANSM) sous le numéro 2009-a0068-49/09.09.07. Le projet compte avec la collaboration de l'Institut de Cancérologie de Lorraine – Alexis Vautrin (ICL), le Centre Chirurgical Emile Gallé (CCEG) et le Centre d'Investigation Clinique Epidémiologie Clinique (CIC-EC). Les patients inclus ont été adressés au Service d'imagerie Guilloz au Centre Hospitalier Universitaire (CHU) de Nancy pour l'investigation d'une masse osseuse ou des parties molles. Les critères d'inclusion et d'exclusion sont présentés dans le tableau 2. Après l'obtention du consentement éclairé, les patients inclus bénéficient d'une évaluation par de multiples méthodes d'imagerie avec des techniques de perfusion, diffusion et spectroscopie proton selon le protocole suivant :

- IRM : Séquences classiques (acquisitions pondérées en T1 et T2 avec saturation de la graisse, avant et après l'injection du gadolinium), Séquences de perfusion ("time-resolved" 3-D [TRICKS]), Séquences pondérées en diffusion (acquisitions avec multiples b) et spectroscopie proton monovoxel (Fig. 4). Des IRM de 1.5 et 3.0 Tesla sont utilisées.

- TDM de perfusion volumique à basse dose réalisée sur un scanner à 320 détecteurs.

- Echographie avec injection de produit de contraste (Hexafluorure de soufre – sonovue®).

A ce jour, 447 patients ont été inclus sur un total de 808 attendus au terme du projet en 2018. Les patients inclus sont suivis cliniquement et par imagerie pendant et après leur traitement. Une corrélation histologique est disponible pour un nombre significatif de patients inclus, soit 265 (59.2%) à ce jour. Cette base de données permet non seulement d'étudier la performance des critères diagnostics pour l'évaluation de l'agressivité tumorale, mais aussi de réaliser une comparaison entre les différentes techniques d'imagerie fonctionnelle étudiées. La possibilité d'avoir une corrélation des résultats avec l'évolution clinique des patients est un des points forts de l'étude. Une autre particularité de cette base de données est de permettre une confrontation de la performance des différentes méthodes de perfusion étudiées (IRM, TDM et

échographie). Ces informations pourraient aider à définir plus précisément les indications de ces méthodes et optimiser la prise en charge des patients porteurs d'une tumeur ostéo-articulaire.

Le support du Laboratoire d'Imagerie Adaptative Diagnostique et Interventionnelle (IADI) INSERM U947 a permis l'analyse avancée d'une partie des données acquises dans cette étude notamment : le post traitement quantitatif des données perfusionnelles en IRM et TDM ; l'analyse des spectres obtenus en IRM avec la spectroscopie proton et l'analyse des données de diffusion. Une étude plus fondamentale sur la spectroscopie proton quantitative sur objet test a également été menée au sein du laboratoire.

Ce manuscrit est divisé en trois sections composées par l'ensemble des articles publiés ou en cours d'évaluation pour publication sur la thématique de la caractérisation des tumeurs ostéo-articulaires. Chaque section portera sur l'expérience acquise avec une des méthodes d'imagerie étudiées (IRM, TDM et échographie).

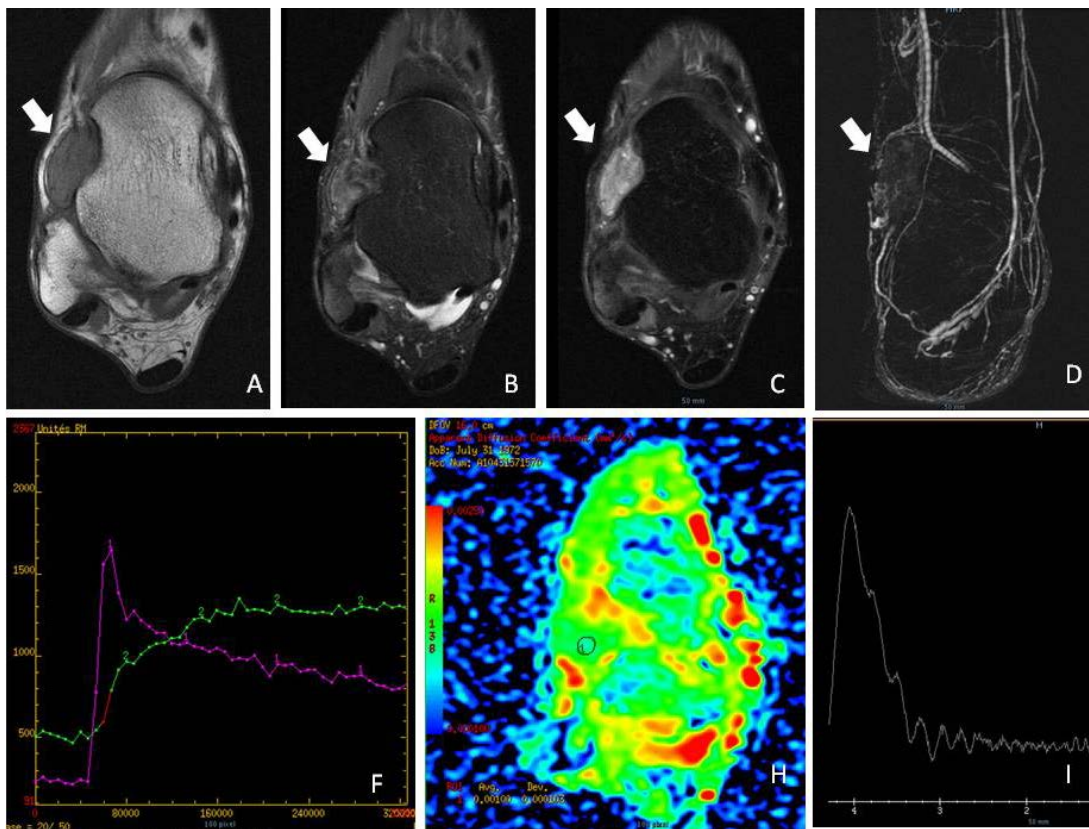


Fig. 4 : Protocole IRM de l'étude avec des séquences pondérées T1 (A), T2 fat sat (B), T1 fat sat post contraste (C), 3-D MIP à partir des séquences TRICKS (D). Une masse tissulaire rehaussée en regard de l'articulation talo-crurale est identifiée. E) Graphique intensité-temps démontrant le rehaussement de la masse (courbe verte) et de l'artère tibiale antérieure (courbe violette). F) Cartographie ADC de la zone d'étude calculée à partir des séquences de diffusion. G) Spectroscopie de protons de la masse.

Le premier chapitre, portant sur l'IRM, sera composée de trois articles :

- Corrélation entre les paramètres de perfusion semi-quantitatifs et quantitatifs en IRM et la réponse thérapeutique des patients porteurs d'un ostéome ostéoïde traités par ablation laser percutanée. Cet article a été publié dans le journal "European Radiology" ;
- L'imagerie de diffusion des tumeurs de parties molles non graisseuses : corrélation entre les valeurs de coefficient de diffusion apparente (ADC) et l'histologie. Cet article est en cours d'évaluation pour publication dans le journal "Radiology" ;
- Influence du calcium sur les mesures du pic de choline en spectroscopie proton en IRM des muscles de la cuisse. Cet article a été soumis à "European Radiology".

Le deuxième chapitre, portant sur la TDM, sera composé de quatre articles :

- Réduction de la dose en scanographie : conseils et astuces. Ecrit à partir d'un poster primé au congrès de la Radiological Society of North America (RSNA) en 2012. Cet article est en cours révision pour soumission à "European Radiology" ;
- L'intérêt du scanner de perfusion à basse dose sur l'évaluation de la réponse thérapeutique des patients porteurs d'un ostéome ostéoïde traités par ablation laser percutanée. Cet article, réalisé suite au travail mené avec l'IRM de perfusion des ostéomes ostéoïdes, est en cours d'évaluation pour publication dans le journal "British Journal of Radiology" ;
- Scanner de perfusion à large système de détecteurs : peut-t-il différencier les ostéomes-ostéoïdes d'autres lésions osseuses lytiques ? Cet article est en cours d'évaluation pour publication dans le journal "Diagnostic and Interventional Imaging" ;
- Performance de la soustraction osseuse par masque en scanner à large système de détection dans l'identification des anomalies œdémateuses de la moelle osseuse en regard de lésions osseuses lytiques en utilisant l'IRM comme gold standard. Cet article est accepté pour publication dans le journal "Investigative Radiology" ;
- TDM mono-énergétique des prothèses totales de hanche avec des algorithmes de réduction des artéfacts métalliques basés sur les projections des données brutes : impact sur l'analyse des structures péri-prothétiques. Cet article est en cours d'évaluation pour publication dans le journal "European Radiology".

Le troisième et dernier chapitre, portant sur l'échographie, sera composé de deux articles :

- Tumeurs et pseudo-tumeurs des parties molles de l'adulte. Apport actuel et perspectives de l'échographie. Cet article a été publié dans le journal "Diagnostic and Interventional Imaging" ;

- Echographie contrasté dans l'évaluation des masses périphériques des parties molles : étude de faisabilité et résultats préliminaires. Cet article a été publié dans le journal " Diagnostic and Interventional Imaging ".

CHAPITRE 1 – L'IMAGERIE PAR RESONANCE MAGNETIQUE

L'IRM, équipement actuellement ordinaire dans la plupart des services de radiologie ostéo-articulaire, représente l'aboutissement de l'effort scientifique de plusieurs équipes de recherche entre 1952 et 1978. Deux prix Nobels ont été consacrés au développement de l'IRM : sur les expériences avec la manipulation des noyaux à spin non nul et sur l'acquisition des images du corps humain à partir des signaux de radiofréquence provenant de la relaxation des spins (24,25). Depuis sa conception l'IRM n'a pas cessé d'évoluer. La vitesse d'acquisition a été nettement améliorée et l'utilisation du signal provenant de la relaxation des protons pour des applications autres que la formation de l'image ont été développées.

Pour étudier la perfusion des tissus, quelle que soit la méthode d'imagerie utilisée, plusieurs acquisitions sur la même région anatomique se succèdent dans le temps après l'injection endoveineuse du produit de contraste avec un délai inter acquisition pré défini. Les principaux avantages de l'IRM de perfusion par rapport aux autres méthodes sont sa haute sensibilité pour détecter le produit de contraste injecté (chélates de gadolinium) et le fait que la méthode n'utilise pas de radiation ionisante. Plusieurs paramètres peuvent être extraits à partir des données perfusionnelles : paramètres visuels (e.g. quantité et aspect des vaisseaux) ; la morphologie de la courbe de rehaussement ; paramètres semi-quantitatifs (e.g. temps du pic de rehaussement, pente de la courbe, temps de transit moyen) (Fig. 5) ; paramètres quantitatifs (e.g. volume plasmatique, constantes de transfert entre le plasma et le tissu extra-vasculaire extra-cellulaire [EVEC]). Les paramètres perfusionnels reflètent l'agressivité tumorale qui est fortement liée à la prolifération vasculaire (angiogénèse). La perfusion peut également aider à distinguer une récurrence tumorale et des remaniements fibro cicatriciels post chirurgicaux (26,27).

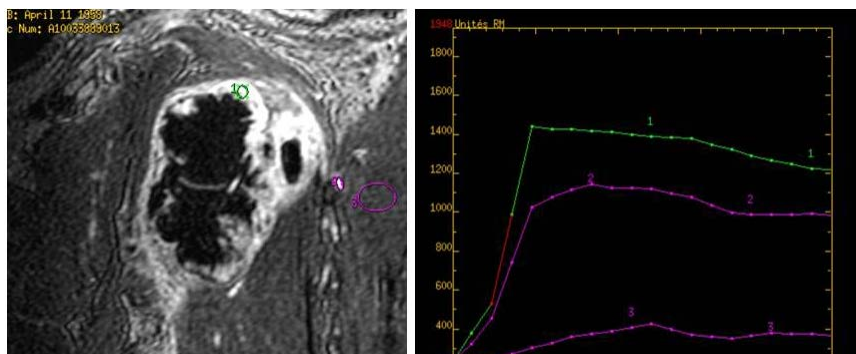


Fig. 5 : Patient de 50 ans porteur d'un sarcome différencié de l'humérus gauche. Evaluation perfusionnelle semi-quantitative. A) Image avec la séquence TRICKS post injection démontrant le rehaussement hétérogène de la lésion et le placement des ROIs. B) Courbe de rehaussement intensité vs temps permettant l'analyse du rehaussement artériel (1), tumoral (2) et du muscle sain (3). Notez le rehaussement précoce et intense de la tumeur par rapport à l'artère.

A température corporelle, les molécules d'eau diffusent de façon aléatoire. L'amplitude de ce déplacement est en rapport avec la structure cellulaire des tissus (28). La séquence de diffusion en IRM est sensible aux mouvements browniens des molécules d'eau dans l'espace EVEC. La diffusion des molécules d'eau dans un tissu peut être quantifiée par le calcul de l'ADC, qui exprime le rapport entre la perte de signal et l'amplitude du déplacement moléculaire en millimètres carrés par seconde. Généralement, la densité cellulaire des tumeurs malignes est plus importante que celle des tumeurs bénignes contribuant à la réduction de l'espace EVEC et restreignant ainsi la diffusion des molécules d'eau (Fig. 6). Néanmoins, d'autres facteurs, comme la structure collagénique et la viscosité du tissu peuvent influencer sur la diffusion des molécules d'eau ce qui rend plus difficile la corrélation des données perfusionnelles et la cellularité tumorale. L'identification de critères pour sensibiliser les séquences de perfusion aux variations de la cellularité tissulaire est donc d'intérêt.



Fig. 6 : Schéma démontrant la relation inversement proportionnelle entre la densité cellulaire et l'espace EVEC. Les bulles d'eau représentent des cellules, la surface verte libre l'espace EVEC. L'image A) illustre une tumeur bénigne et l'image B) une maligne. Notez la nette réduction de taille de l'espace EVEC entre A et B (Source internet : A. Philibert, www.entrelesjas.fr).

La spectro-IRM du proton a pour but la caractérisation biochimique et la détection de métabolites présents dans les tissus de façon non-invasive. La spectro-IRM repose sur le principe du décalage chimique. Chaque élément chimique a une fréquence de précession spécifique et l'intensité du signal provenant de ces éléments est proportionnelle à sa concentration. En pathologie ostéo-articulaire, seule la choline est recherchée. Elle participe au métabolisme phospholipidique des membranes cellulaires et son pic reflète la cellularité et le turn-over cellulaire (29–31). Les études ont démontré que l'estimation de la concentration en mmol/l de la choline augmente la performance de la spectro-IRM pour la différenciation bénin-malin des masses ostéo-articulaires. Néanmoins, la quantification de la choline est perturbée par la présence de calcifications intra lésionnelles (19). L'impact des particules de calcium sur les mesures du pic de choline n'est pas connu.

Dynamic MR imaging of osteoid osteomas: correlation of semiquantitative and quantitative perfusion parameters with patient symptoms and treatment outcome

Pedro A. Gondim Teixeira · Anne Chanson ·
Marine Beaumont · Sophie Lecocq · Matthias Louis ·
Béatrice Marie · François Sirveaux · Alain Blum

Received: 15 November 2012 / Revised: 14 March 2013 / Accepted: 15 March 2013 / Published online: 22 May 2013
© European Society of Radiology 2013

Abstract

Objective To evaluate the relationship between multiple MR perfusion parameters and symptoms of patients with osteoid osteomas after percutaneous laser therapy.

Methods MR perfusion studies of 20 patients diagnosed with an osteoid osteoma, treated with CT-guided percutaneous laser therapy, were retrospectively evaluated. Multiple perfusion parameters correlated with the treatment outcome and the presence of osteoid osteoma-related symptoms.

Results There were 16 successful treatments, 6 recurrences and a significant difference in the perfusion parameters of these groups ($P < 0.0001$). Patients with successful treatment demonstrated delayed progressive enhancement or no enhancement (mean time to peak = 182 s, mean delay to the arterial peak = 119.3 s). Patients with treatment failure demonstrated an early and steep enhancement (mean time to peak = 78 s and mean delay to the arterial peak = 24 s). Plasmatic volume and transfer constant values significantly changed after successful treatment ($P < 0.008$). MR perfusion

has a sensitivity and a specificity higher than 90 % in the detection of recurrent osteoid osteomas.

Conclusion The identification of an early and steep enhancement with short time to peak and a short delay between the arterial and nidus peaks on MR perfusion in the postoperative setting is highly indicative of an osteoid osteoma recurrence.

Key points

- Magnetic resonance perfusion is becoming widely used for several tumours.
- MR perfusion measurements correlate well with osteoid osteoma-related symptoms.
- MR perfusion has high diagnostic performance for osteoid osteoma recurrence.
- MR perfusion can improve the diagnostic confidence of osteoid osteoma recurrence.

Keywords Osteoid osteoma · Perfusion magnetic resonance imaging · Patient follow-up · Tumour recurrence · Percutaneous laser therapy

P. A. G. Teixeira · A. Chanson · S. Lecocq · M. Louis · A. Blum
Service D'imagerie Guilloz, CHU, Nancy 54000, France

P. A. G. Teixeira · M. Beaumont · A. Blum
Université de Lorraine, IADI, UMR S 947, Nancy, France

B. Marie
Service d'anatomo-pathologie, CHU, Nancy 54000, France

F. Sirveaux
Service de Chirurgie Traumatologique et Orthopédique,
Centre Chirurgical Emile Gallé, Nancy, France

P. A. G. Teixeira (✉)
Pedro Augusto Gondim Teixeira, 42 Rond Point Kleber,
54140 Jarville-la-Malgrange, France
e-mail: ped_gt@hotmail.com

Introduction

Osteoid osteoma is a benign neoplasm of the bone composed of hypervascular immature osteoid that can cause significant disability [1]. Currently, minimally invasive percutaneous radio or thermal ablation is the treatment of choice for this tumour [2–4]. Radiofrequency and laser therapy are the most commonly used methods and present similar effectiveness [5]. Although rare, osteoid osteoma recurrences after ablative therapy can occur. The primary success rates after percutaneous ablation reported in the literature varied from 73 % to 98 % [5–10].

Osteoid osteoma recurrences can be as symptomatic and debilitating as the primary lesion. In the postoperative setting,

pain unrelated to residual or recurrent tumour can occur in up to 40 % of patients even in the absence of treatment complications [9]. Nidus calcification or disappearance has been reported to be associated with successful percutaneous treatment [10, 11]. Despite this association conventional CT findings clearly do not correlate with the surgical outcome. Signal changes after percutaneous ablation of osteoid osteomas have been described in the literature [4, 12]. However no conventional MR findings have so far been associated with residual or recurrent osteoid osteomas. Finally, Vanderschueren et al. suggested that there could be a variation of the type of enhancement in the nidus related to the surgical outcome [7]. The lack of objective clinical and imaging criteria for the diagnosis of residual or recurrent osteoid osteoma may delay the treatment in patients with a recurrence and be at the origin of unnecessary secondary treatment.

With advances in the commercially available software for post-processing of dynamic MR studies, multiple semiquantitative perfusion parameters are at the disposal of the radiologist. In this study we sought to evaluate the relationship between multiple semiquantitative and quantitative MR perfusion parameters and patient symptoms after percutaneous laser therapy: curve morphology, time to peak, delay between arterial and nidus peaks, blood volume, maximum slope of increase, plasmatic volume, extracellular extravascular volume, and capillary transfer constants (K^{trans} and K_{ep}). The findings correlated with treatment success and with the presence of osteoid osteoma-related symptoms.

Materials and methods

Patients

From March 2009 to October 2012, 44 confirmed patients with osteoid osteomas underwent MR imaging in our institution after percutaneous ablative therapy. Among these patients 20 had dynamic studies with time-resolved contrast kinetics sequences available after treatment. All but one of the patients included were primarily treated in our institution. This patient had been treated with surgical curettage in another institution and was evaluated for a recurrence of the osteoid osteoma. One or multiple pre- and posttreatment MR studies were available for the study population, which had been performed at the request of their personal physicians. These studies were also considered in the evaluation. In our institution a single postoperative control study with gadolinium injection is usually performed to identify possible complications of percutaneous ablation. In cases with regression of patient symptoms some practitioners request additional MR evaluations before a second interventional procedure is performed. In four successfully treated patients

more than one postoperative study was performed. Among these patients one had local mechanical pain at the treatment site; one had no histological confirmation of the osteoid osteoma. The other two patients had a late control 1 year after treatment because of the location of these lesions (proximal femur and thoracic spine) to identify late but potentially serious complications in young patients, such as iatrogenic osteonecrosis and degenerative discopathy. A postoperative control 3 months after treatment is the recommendation in our institution. Variations in this delay were related scheduling and patient availability issues. All patients were evaluated with conventional CT. MR perfusion has been part of our standard imaging protocol for the diagnosis and follow-up of patients with a suspected osteoid osteoma since 2009 after the publication of various articles underscoring the added value of this technique in this setting [7, 13–15]. A dynamic MR perfusion sequence adds only 4 min to the duration of the conventional protocol, which, in this context, already requires intravenous contrast material.

All patients were examined and interviewed by a radiologist before treatment. In our institution CT-guided percutaneous laser therapy is the standard treatment for osteoid osteomas. Laser thermal ablation was performed using a continuous-wave semiconductor portable diode laser with a power of 2 W (total energy of 600–1,000 J) in all patients. Bone biopsy was performed per-operatively in all the patients with 11- to 13-G needles. Histological evaluation of the bone fragments yielded histological confirmation of osteoid osteoma in 11 patients.

In the remaining ten patients the histological diagnosis of osteoid osteoma was not reached. The diagnostic confirmation in these cases was based on the imaging characteristics, clinical findings and absence of an alternative diagnosis at histological analysis. The imaging signs considered as inclusion criteria were: hypodense lesion on CT (nidus) smaller than 2 cm, sclerotic bone reaction adjacent to the lesion and inflammatory reaction adjacent to the lesion (bone marrow oedema and/or periosteal hyperintensity on T2-weighted fat-saturated images). The clinical findings used as inclusion criteria and presented by all patients were: chronic non-mechanical pain for more than 6 months, pain worse at night and pain relieved by non-steroidal anti-inflammatory drugs (NSAIDs). The bone biopsies in all of these patients yielded normal or sclerotic cortical tissue. Patients with a known malignancy diagnosed elsewhere and with metastatic disease were excluded.

The symptoms considered to be related to an active osteoid osteoma nidus (e.g. pretreatment or in cases of residual or recurrent tumour) were the presence of an inflammatory type pain, nocturnal pain and the use of NSAIDs for pain control. The presence of any of these signs postoperatively characterised treatment failure. The patients with signs of recurrence underwent re-imaging

and some of them had secondary ablation therapy using the same method. All the patients without a recurrent osteoid osteoma had at least one follow-up study (standard procedure for detecting early postoperative complications).

A retrospective study based on the anonymous analysis of patient images with standard imaging methods does not require ethics committee approval in our institution.

Imaging protocol

Magnetic resonance imaging was performed at 1.5T (Signa HDxt, GE Healthcare, Milwaukee, WI, USA) using dedicated coils. An eight-channel knee coil was used for the evaluation of the elbow and forearm. A 12-channel-torso coil was used for the evaluation of the hip. A six-channel phase-array surface spine coil was used for the spine studies. MR perfusion studies were based on time-resolved 3D MR sequences with subtraction mask (TRICKS®) using the following acquisition parameters: TE min, flip angle 30, NEX 0.75, matrix, 320×224, FOV 21 cm, bandwidth 41 and thickness 2 mm. Fifteen millilitres of a gadolinium-based contrast material (MULTIHANCE® 20 ml, Bracco Diagnostics) was injected into a peripheral vein at an 0.5-ml/s injection rate with the aid of an injection pump (Spectris Solaris EP, Medrad INC, Indianola, PA, USA). A 40-s subtraction acquisition was obtained. Contrast material injection started 30 s after the beginning of the subtraction sequence for superior limb studies and 25 s after the beginning of the subtraction sequence for lower limb studies. Hence, the delay between contrast material injection and the beginning of the post-subtraction acquisition was 10 s for the superior limb and 15 s for the lower limb. Twenty phases lasting 10–14 s (variation depending on the field of view) were acquired after subtraction with no interval between them. Total duration of MR perfusion was about 240 s. In all studies conventional sequences were acquired, including at least one T1-weighted sequence and T2 fat-saturated sequences in two different orthogonal planes. CT studies were performed using a 320-detector system (Aquilion ONE, Toshiba Medical Systems, Otawara, Japan).

Image analysis and post processing

Conventional MR and CT images were evaluated on a PACS workstation (Impax V5, AGFA HealthCare, Ivry-sur-Seine, France). MR perfusion studies were post-processed with an AW console version 4.4 GE Healthcare using the Functool and readyVIEW applications. Time-to-intensity curves were constructed for all studies. Curve morphology analysis was based on the classification proposed by van Rijswijk et al. [16]. Five types were described. Type I designates a flat curve, type II progressive enhancement with no enhancement peak, type III an early

enhancement peak followed by a plateau, type IV an early enhancement peak followed by a washout and type V an early enhancement peak followed by progressive enhancement. Semiquantitative perfusion parameters (time to peak, delay between the arterial and nidus peaks) were calculated. Enhancement integral (blood volume) and maximum slope of increase colour maps were built and the average values were obtained from the nidus region.

Since the arterial input function was available for all data sets, a two-compartment pharmacokinetic model derived from the Brix model (Tofts model) was used for calculation of the quantitative perfusion parameters [17–19]:

$$C_t(t) = v_p C_p(t) + K^{trans} \int_0^t C_p(\tau) e^{-k_{ep}(t-\tau)} d\tau \quad (1)$$

The application of this pharmacokinetic model yielded three quantitative perfusion parameters: the nidus plasmatic volume (V_p %); the volume transfer constant from the plasma to the extravascular extracellular space (EES) (K^{trans}); the rate constant of the backflux from the EES to the plasma (k_{ep}). A fourth parameter, the EES volume (V_e %), was derived from the following relation:

$$V_e \% = K^{trans} / k_{ep}$$

The relation between the gadolinium concentration and the signal intensity was considered to be linear. Using Matlab (v. 7.2, the Mathworks, Natwick, MA, USA) the baseline of the intensity-time data from the arterial input ($C_p(t)$) and the nidus ($C_t(t)$) was set to zero. The difference in the time delay between the arterial input data and the lesion data was corrected. Then the intensity-time data were fitted using a Levenberg-Marquardt algorithm to a two-compartment pharmacokinetic model (1).

Non-subtracted TRICKS images were used for post-processing. The slice that depicted the largest portion of the nidus was selected for the whole evaluation. In the preoperative studies the ROIs were placed to occupy the whole nidus area. In the postoperative studies the ROIs were placed in the area of maximum enhancement at the treatment zone. Post-processing was performed by a trained physicist (M.B.) blinded to the treatment outcome. Two fellowship-trained radiologists with 20 and 5 years of clinical experience validated the ROI positioning in all cases.

The evaluated semiquantitative and quantitative perfusion parameters correlated with the surgical outcome in the postoperative studies. The earliest control study available for every patient was used for this purpose. Then the semiquantitative perfusion parameters from all the dynamic MR studies performed in the patients evaluated were analysed. Two groups of patients were formed: symptomatic and asymptomatic. The perfusion parameters from these two groups were compared. The quantitative perfusion parameters derived

from the Brix model, the curve morphology, the time to peak and the delay between arterial and nidus peaks from the different patients were compared directly. The semiquantitative parameters, blood volume and maximum slope of increase, obtained are not directly comparable because of the variation in the signal intensity with different coils and anatomical regions. The variation of the blood volume and the maximum slope of increase between pre- and postoperative studies was calculated for each patient. Then the variation in these parameters was compared in the patient population. In the three patients with a secondary treatment, the latest perfusion study performed before the procedure was used as a basis for comparison. The paired Student's *t* test was used for the evaluation of the statistical significance of the quantitative data. A *P* value less than 0.05 was used as the threshold for statistical significance.

Bone marrow oedema pattern (BMEP) was defined as hypersignal intensity of the bone marrow compared to that of the normal bone marrow on T2-weighted fat-saturated images. The presence and the size of BMEP adjacent to the osteoid osteoma nidi were compared between pre- and postoperative study pairs and correlated to the therapy outcome. The largest radius of the BMEP zone using the osteoid osteoma nidus as central referential was used for quantification.

Results

The mean age in the study population was 25.9 years. The male-to-female ratio was 4:1. The size of the osteoid osteoma nidi studied varied from 0.3 to 2.0 cm on CT. There were 20 primary and 3 secondary treatments with percutaneous laser therapy in the study population. In two of the patients included only postoperative MR perfusion studies were available. A total of 20 pre- and posttreatment MR perfusion study pairs were available in the study population (primary and secondary treatments added). A total of six osteoid osteoma recurrences were found in the study population. One patient had a primary recurrence after surgical curettage performed in another institution. Four patients had a primary recurrence after laser therapy. The primary success rate of percutaneous laser therapy was 70 %. Three patients were re-treated. Secondary success rate of percutaneous laser therapy was 100 %. The characteristics of the osteoid osteomas studied, the treatment outcome and the number of MR perfusion studies available for each patient are presented in Table 1.

An enhancement peak was observed in all 17 osteoid osteomas with no treatment evaluated. Either a washout or a plateau followed the enhancement peak in these patients. A type IV curve was found in 16 (94.1 %) and a type III curve was found in 1 (5.9 %) of these patients. The time to peak varied from 54 to 105 s (mean 79.4 ± 16.2), and the

delay between the arterial and nidus peaks varied from 0 to 45 s (mean 11.8 ± 14.7). After the analysis of these results type III and IV curves were considered indicative of an active nidus.

After percutaneous laser therapy (primary and secondary) 16 patients demonstrated a complete symptom regression of the osteoid osteoma-related symptoms (treatment success). The length of the follow-up in these patients varied from 6 to 42 months (mean: 22.6) and the delay from the treatment intervention to the first control study varied from 1 day to 4 months (mean 2.1). In these patients there was a clear change in the perfusion parameters with respect to the pretreatment study. In all of these patients there was a late progressive enhancement or no detectable enhancement in the nidus area. A type II curve was identified in 14 (87.5 %) of these patients. In two patients (12.5 %) there was no enhancement on MR perfusion (type I curve). Among the patients who had detectable enhancement the time to peak varied from 140 to 205 s (mean 182.2 ± 22.5), the delay between the arterial and nidus peaks varied from 65 to 152 s (mean 119.3 ± 26.3). After the analysis of these results type I and II curves were considered indicative of an inactive nidus. The differences in the time to peak and in the delay between the arterial and nidus peaks of the pretreatment and the successful posttreatment studies were statistically significant ($P < 0.0001$) (Fig. 1).

In the six patients with percutaneous laser therapy failure, the delay from the treatment intervention to the first control study varied from 1.5 to 14 months (mean 5 months). Among these patients five demonstrated an early enhancement peak (1 type III curve and 3 type IV curves). One patient demonstrated no detectable enhancement 1.5 months after treatment (type I curve). This patient underwent a second control study 6 months after treatment in which an early enhancement peak was detected (type IV curve) despite the absence of osteoid osteoma-related symptoms. It was only 9 months after treatment that osteoid osteoma symptoms became clinically apparent. The time to peak varied from 68 to 106 s $78 (\pm 15.9)$, and the delay between arterial and nidus peaks varied from 0 to 46 s $21.4 (\pm 16.3)$. The differences in the time to peak and the delay between the arterial and nidus peaks of the patients with successful and failed treatment were statistically significant ($P > 0.0001$). The differences in the curve morphology, time to peak and delay between the arterial and nidus peaks among pretreatment studies and the post-treatment recurrences were not statistically significant (*P* values varied from 0.23 to 0.88; Fig. 2). Table 2 shows a comparison of the perfusion parameters of the nidi of osteoid osteomas with no therapy, those treated successfully and those with treatment failure.

There was a decrease in the blood volume and in the maximum slope of increase with respect to the preoperative study in 14 patients (87.5 %) with a treatment success. In the patients with treatment failure there was a drop in the

Table 1 The characteristics of the osteoid osteomas studied, treatment outcome and number of MR perfusion studies performed in the study population

	Location	Size (cm)	Recurrence	Secondary treatment	Number of studies	Preoperative study
Patient 1	Knee	1	No	No	2	Yes
Patient 2	Forearm	1.1	No	No	2	Yes
Patient 3	Femur	0.8	No	No	2	Yes
Patient 4	Tibia	1.9	Yes	No	3	Yes
Patient 5	Scapula	0.9	Yes	No	3	Yes
Patient 6	Radius	1	No	No	3	Yes
Patient 7	Femur	0.8	No	No	2	Yes
Patient 8	Tibia	0.4	No	No	2	Yes
Patient 9	Femur	0.6	No	No	2	Yes
Patient 10	Spine	0.9	No	No	4	Yes
Patient 11	Femur	0.3	No	No	3	Yes
Patient 12	Knee	0.3	No	No	2	Yes
Patient 13	Elbow	0.9	No	No	2	Yes
Patient 14	Thigh	1.5	Yes	Yes	4	Yes
Patient 15	Tibia	1	No	No	2	Yes
Patient 16	Spine	0.9	No	No	3	Yes
Patient 17	Tibia	0.7	No	No	2	Yes
Patient 18	Spine	0.9	Yes	Yes	4	No
Patient 19	Ulna	1.3	Yes	No	3	No
Patient 20	Spine	2	Yes	No	1	No

maximum slope of increase no higher than 8.9 % and the mean blood volume actually increased by 17.8 % (Table 2).

The quantitative perfusion parameters found were comparable to what is described in the literature for other types of tumour [20]. The mean values and standard deviation of the quantitative perfusion parameters for the pretreatment, posttreatment with success and after failed treatment are demonstrated in Table 3. The parameters related to EES to plasma backflux (k_{ep}) could not be adequately calculated for patients with curve morphology types I and II (16 patients) since the washout phase was not available in the acquired data. In one patient after a successful treatment the k^{trans} value was aberrant and was not included in the calculations. When compared to the pretreatment studies, there was a statistically significant drop in $V_p\%$ values in all patients with a successful treatment ($P < 0.0001$). The K_{trans} values between pretreatment and successful treatment studies were statistically different ($P = 0.0086$). The K_{trans} values after successful treatment were reduced in 57.8 % and increased in 42.2 % of the patients. The mean values of all the quantitative perfusion parameters studied were similar between pretreatment and recurrences (Table 3). The differences in $V_p\%$, $V_e\%$, k^{trans} and k_{ep} between these two groups were not statistically significant ($P = 0.5057, 0.8417, 0.8262, 0.4092$ respectively).

A total of 51 MR perfusion studies were available (preoperative studies and postoperative follow-ups). MR

perfusion was performed in 28 patients with and in 23 without osteoid osteoma-related symptoms. Among the symptomatic patients 96.4 % had an enhancement curve morphology of type III, IV or V while only 8.6 % of the asymptomatic patients demonstrated these curve types. The time to peak and the delay between the arterial and nidus peaks were significantly longer in patients without osteoid osteoma-related symptoms (< 0.0001). The time to peak and the delay between the arterial and nidus peak in the symptomatic and asymptomatic patients were respectively 78.0 (± 20.1) versus 174.8 (± 43.8) s and 14.9 (± 17.5) versus 109.3 (± 47.1) s. In two patients with a treatment failure the perfusion changes suggestive of an active nidus preceded the appearance of symptoms.

There were a total of 34 postoperative MR perfusion controls (primary and secondary treatments added) available in the study population. In the posttreatment setting if curves with morphology of types III and IV are considered signs of an active nidus (treatment failure), the sensitivity and specificity of either of these criteria for the detection of a recurrent osteoid osteoma were 92.3 % and 95.2 %. If a time to peak shorter than 120 s (or no detectable enhancement) and a delay between the arterial and nidus peak shorter than 50 s (or no detectable enhancement) were considered diagnostic criteria for recurrent osteoid osteoma, MR perfusion would have the same sensitivity and specificity (92.3 % and 95.2 %).

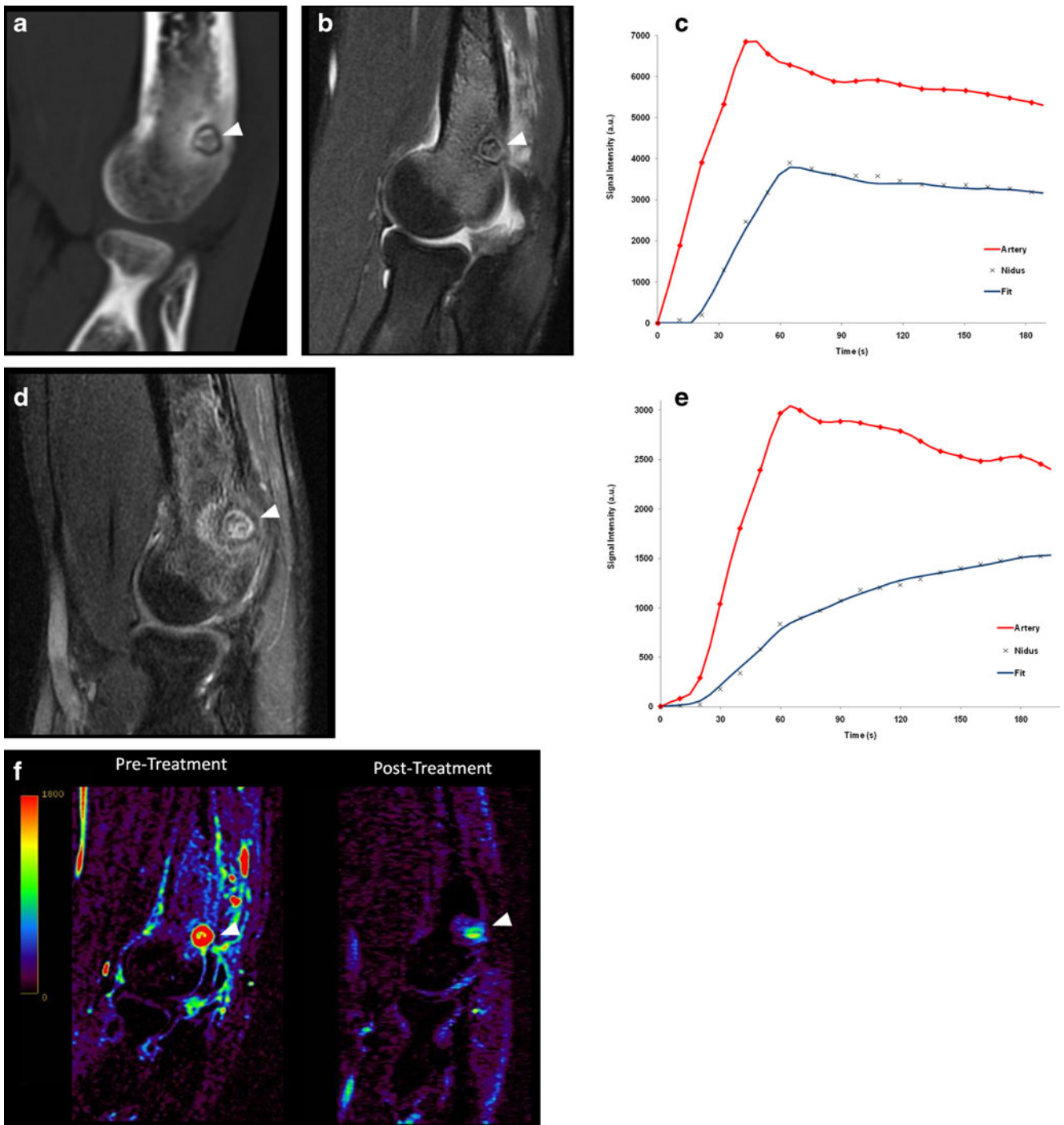


Fig. 1 A 17-year-old male patient with a biopsy-proven osteoid osteoma of the humeral pallet successfully treated with percutaneous laser therapy. The patient has been followed for 38 months and is asymptomatic. **a** Sagittal CT image demonstrating a sub-cortical 0.9-cm nidus with central calcification (*arrowhead*) surrounded by a halo of bone sclerosis. **b** Sagittal T2-weighted fat-saturated MR image of the same anatomical region demonstrating the nidus (*arrowhead*) and the adjacent bone marrow oedema pattern area. **c** Time to intensity curve depicting the intensity values and the fitted curve of the nidus enhancement (*blue curve*) and the enhancement curve nearby radial recurrent artery (*red curve*). Note the early and steep enhancement of the nidus

followed by a washout (curve type IV). The delay between the arterial and nidus peaks is null. **d** Post-treatment sagittal T2-weighted fat-saturated MR image of the same patient at the nidus area (*arrowheads*) demonstrating the residual postoperative bone marrow oedema pattern. **e** Time-to-intensity curve depicting the enhancement curves of the nidus (*red curve*) and the nearby radial recurrent artery (*blue curve*) after surgery. There is a clear change in the nidus enhancement pattern, which is now progressive and delayed (curve type II). **f** Blood volume coloured map before and after treatment with the same colour scale demonstrating a drop in the nidus blood volume after treatment (*arrowheads*)

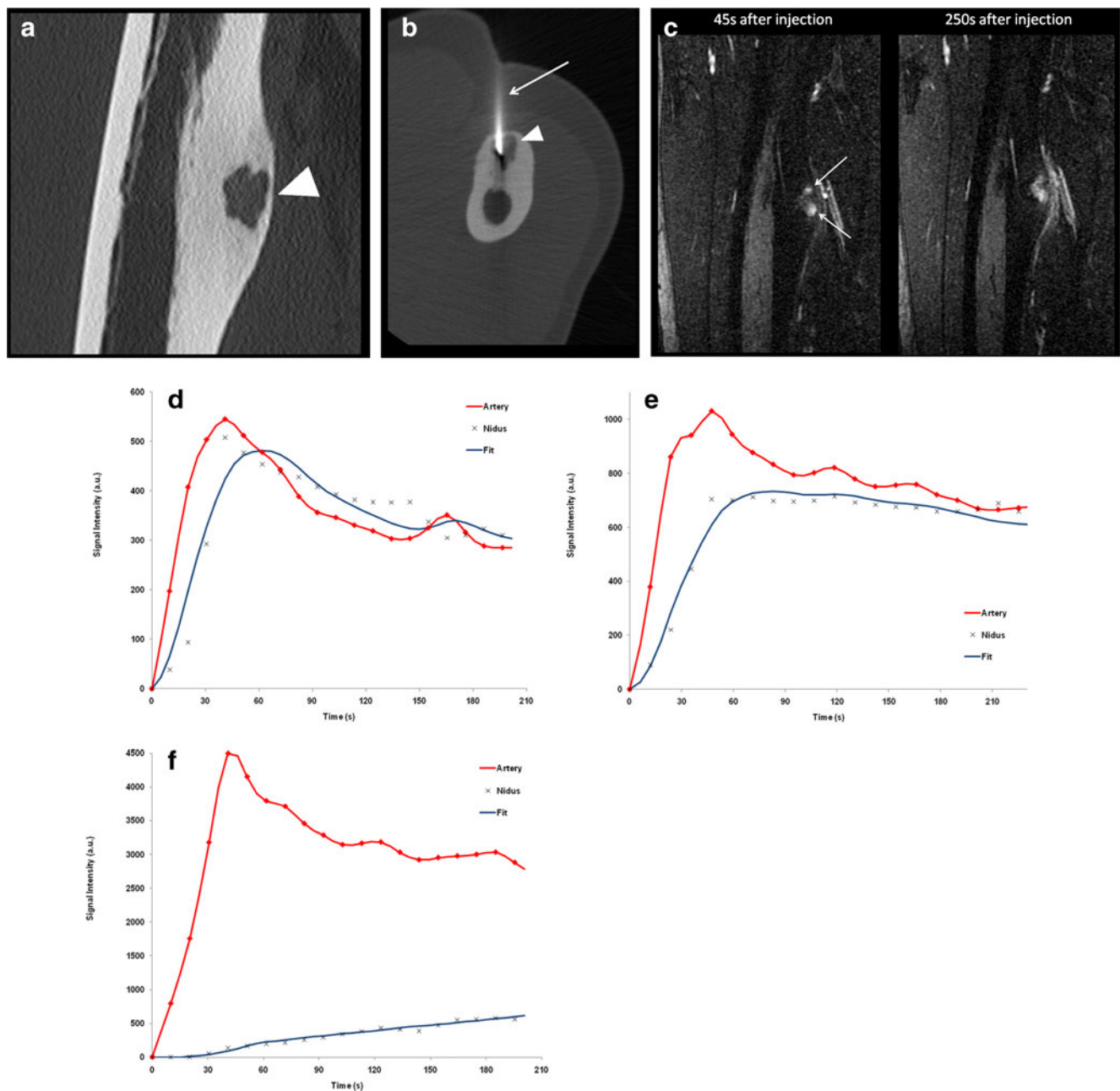


Fig. 2 A 23-year-old male patient with a biopsy-proven osteoid osteoma of the femoral diaphysis with osteoid osteoma recurrence after percutaneous laser therapy. **a** Sagittal CT image demonstrating a 1.5-cm sub-periosteal nidus (*arrowhead*) with a marked periosteal reaction. **b** Needle placement of the primary treatment depicting an adequate needle position (*arrow*) inside the nidus (*arrowhead*). **c** Non-subtracted time-resolved 3D MR image on the sagittal plane 45 and 250 s after injection of the first postoperative control study 1.5 months after treatment demonstrating two foci of early enhancement (*arrows*) indicative of residual osteoid osteoma tissue. Note the diffuse enhancement of the nidus area on the later phase that obscures the visualisation of the residual tumour. **d**, **e** and **f** Time-to-intensity curves before

treatment, after primary treatment and after secondary treatment of the same patient respectively. The intensity values and the fitted curve of the nidus enhancement (*blue curve*) and the enhancement curve of the nearby deep femoral artery (*red curve*) are shown. Before treatment, the early and steep enhancement typical of the osteoid osteoma followed by a washout (curve type IV) is seen. After failed treatment there is persistent early enhancement at the nidus and the patient had osteoid osteoma-related symptoms at the time of this study. The enhancement curve after secondary treatment shows a definite change in the nidus curve morphology, which shows a progressive and delayed enhancement. This patient was followed for 30 months after the secondary treatment and is asymptomatic

BMEP was identified in 18 out of the 20 pretreatment studies (90 %) and in all patients after treatment regardless of the outcome and presence of symptoms. In the patient

population the largest radius of BMEP varied from 0 to 5.5 cm (mean 1.72 cm). With respect to the variation size of the BMEP zones after treatment in patients with

Table 2 Comparison of the perfusion parameters of the osteoid osteoma nidi with no therapy, those treated successfully and those with treatment failure

	Pretreatment	Success	Failure
Curve morphology	17 (III:1 IV:16)	16 (I:2 II:14)	6 (I:1 III:1 IV:4)
TTP (mean)	79.4 (±16.2)	182.2 (±22.5)	78 (±15.9)
Delay to art peak (mean)	11.8 (14.7)	119.3 (±26.3)	21.4 (±16.3)
Maximum slope variation	x	40.5 % drop	8.9 % drop
Blood volume variation	x	47.9 % drop	17.8 % increase

TTP = Time to peak

recurrence: two remained stable, two decreased and one increased in size (one patient with recurrence did not have a preoperative study available). In patients with a successful treatment the size of the BMEP remained stable in three patients, decreased in eight and increased in four. The increase in the radius of BMEP after treatment has a sensitivity of 20 % and a specificity of 73 % for the detection of osteoid osteoma recurrence.

Discussion

The typical enhancement pattern of untreated osteoid osteomas has been described in the literature [14, 15]. A time to peak of less than 90 s followed by a washout or an enhancement plateau is seen in patients with an osteoid osteoma [15]. The same enhancement pattern was found on the pretreatment studies available for the patients evaluated. This enhancement pattern corresponds to the type III and IV curve morphologies described by van Rijswijk et al. [16]. In most of the articles about the perfusion of osteoid osteomas the main focus was the preoperative characterisation and diagnosis of these lesions in atypical cases and not the evaluation of the nidus activity postoperatively [14, 15, 21].

Early enhancement at the nidus region after percutaneous ablation therapy has been associated with osteoid osteoma recurrences. This finding might be related to the presence of residual or recurrent osteoid osteoma as early enhancement

is not seen on coagulative necrosis after percutaneous ablation therapy [7]. So far, however, there has not been a comparison of the same perfusion parameters of the osteoid osteoma nidi before treatment, after successful treatment and after failed treatment. The diagnostic performance of MR perfusion for the detection of osteoid osteoma recurrences is therefore difficult to ascertain.

The results presented demonstrate that there is a statistically significant difference in the various semiquantitative MR perfusion parameters evaluated between patients with successful treatment and those with an osteoid osteoma recurrence. The curve morphology and the time to peak, delay between the arterial and nidus peaks found in patients with a recurrent osteoid osteoma were similar to those found in the preoperative studies (*P* values varied from 0.23 to 0.88). The similar perfusion pattern in pretreatment osteoma nidi and after failed laser therapy suggests the presence of residual tumour or new tumoral growth. On the other hand, there was a significant difference in all semiquantitative MR perfusion parameters between preoperative and successful postoperative studies (*P*<0.0001).

The quantitative perfusion parameters evaluated also demonstrated a significant variation after successful treatment. There was a drop in the $V_p\%$ in all patients treated with success, which reflects the changes of the capillary network in the nidus. This finding is probably related to the limited capillary volume in coagulative necrosis zones after laser therapy. k^{trans} represents the transfer coefficient of the contrast media from the intravascular compartment to EES and is related to the vascular permeability. The flow input function and the tumour cellular structure also have an influence on k^{trans} values [19, 22]. Despite the significant differences of the k^{trans} values before and after successful treatment, the tendency of variation in k^{trans} values was less clear. In about 60 % of the patients, there was a k^{trans} drop after successful treatment; in the other patients the k^{trans} values increased. This finding is probably related to flow variations at the nidus after treatment [19]. All the quantitative perfusion parameters in patients with an osteoid osteoma recurrence were similar to those found in pretreatment studies. The presence of residual or recurrent osteoid osteoma tissue in patients with a treatment failure, which have, eligibly, the same perfusion pattern of pretreatment osteoid osteomas, probably explains these results.

Table 3 Mean values and standard deviation of the quantitative perfusion parameters studied before treatment and according to the treatment outcome

	Pretreatment	Success	Failure
$V_p\%$	32.36 (±23.0)	7.9 % (±10.4)	30.88 % (±23.9)
$V_e\%$	40.95 (±19.4)	x	20.09 % (±20.0)
k^{trans} (min-1)	0.74 (±0.6)	0.181 (±0.16)	0.86 (±1.1)
k_{ep} (min-1)	2.22 (±1.59)	x	2.37 (±2.81)

V_p = Plasmatic volume

V_e = Extravascular extracellular space volume

k^{trans} = Transfer constant from plasma to extravascular extracellular space

k_{ep} = Rate constant of the backflux

After percutaneous laser therapy, a curve morphology type III or IV, a time to peak of less than 120 s and a delay between the arterial and nidus peaks of less than 50 are very suggestive of a recurrent or residual osteoid osteoma. The association of these three criteria on MR perfusion for the detection of osteoid osteoma recurrence yielded sensitivity and specificity values of 92.3 % and 95.2 % respectively. MR perfusion can identify perfusion changes very early after treatment. In one patient with a successful treatment a clear change in the nidus perfusion parameters compared with the preoperative study had already been identified on the first postoperative day. MR perfusion was able to detect tumour recurrence as early as 1.5 months after treatment. Finally, two out of the six patients with recurrent tumour MR perfusion demonstrated changes indicative of tumour recurrence before osteoid osteoma-related clinical symptoms were present.

Contrast enhancement and BMEP at the treatment site on conventional MR sequences are frequent findings after percutaneous laser therapy. These findings are not directly related to the treatment outcome, and an enhancing zone around the needle tract has been described after successful radiofrequency therapy [12]. BMEP was found in all patients after treatment and was a poor indicator of the treatment outcome. An increase in the radius of the BMEP zone after treatment had a sensitivity and a specificity of 20 % and 73 % for the detection of recurrences. There was, however, a significant difference in the perfusion parameters between patients with and those without osteoid osteoma-related symptoms. Osteoid osteomas have a high metabolism and are well known for their production of inflammatory mediators, which are responsible for the patient's pain [23]. The results presented suggest that an early and steep enhancement on MR perfusion (curve types III, IV or V), a short time to peak and a short delay between the arterial and nidus peaks are indicative of a metabolically active nidus. On the other hand, a perfusion study demonstrating a slow progressive enhancement (curve type II) or no enhancement at all is suggestive of an inactive nidus.

The blood volume and the maximum slope of increase are related to the micro-vascular density and the velocity of contrast enhancement in a tumour respectively [24]. The nidi of osteoid osteomas are highly vascularised [1]. The comparison of these parameters before and after therapy may be an indication of the presence of residual osteoid osteoma tissue. This theory is supported by our results. First there was a mean drop of 40 % in both of these parameters after successful treatment compared with preoperative studies. Second, in the patients with a tumour recurrence there was a less than 10 % drop in the blood volume and an increase in the maximum slope of increase compared with pretreatment levels.

This study has some limitations. The number of patients with a recurrence was limited. Despite this limited number of patients, the differences in the perfusion pattern between

patients with successful and failed treatment were statistically significant. The different anatomical locations of the osteoid osteoma nidi (altering the arterial input function), the use of different coils and variable machine calibrations used in the different studies might have influenced quantitative perfusion parameters, hindering inter-patient comparisons. The length of the acquisition protocol did not include the washout phase in lesions with delayed enhancement (curve type II). In these patients the k_{ep} and $V_e\%$ could not be calculated. Histological confirmation was not possible for all the patients. As minimally invasive percutaneous ablation has been adopted as the treatment of choice for osteoid osteomas, the rate of histological confirmation of these lesions has dropped considerably [4, 7, 25]. Clinical and imaging signs of osteoid osteomas have been extensively described [1, 2, 7, 12, 26]. That, added to the absence of alternative diagnosis in the bone biopsies performed preoperatively, provides sufficient evidence to support the diagnosis of osteoid osteoma in patients without histological confirmation.

In summary, the identification of an enhancement curve type III or IV in the nidus with short time to peak and a short delay between the arterial and nidus peaks on MR perfusion in the postoperative setting is highly indicative of an osteoid osteoma recurrence. According to these criteria, MR perfusion has sensitivity and specificity greater than 90 % of the detection of recurrent lesions. There is also a close correlation between the perfusion parameters studied and the osteoid osteoma-related symptoms. The quantitative parameters studied, particularly $V_p\%$ and K_{trans} , correlated well with the treatment outcome. These findings help to clarify the diagnostic criteria for osteoid osteoma recurrences, which can be useful in clinically challenging cases.

Acknowledgements This work was supported by the French Society of Radiology (SFR—Société Française de Radiologie) through a research grant. We also thank Chakib Bereksi-Reguig for the assistance in data post processing.

References

1. Kransdorf MJ, Stull MA, Gilkey FW, Moser RP Jr (1991) Osteoid osteoma. *Radiographics* 11:671–696
2. Lee EH, Shafi M, Hui JHP (2006) Osteoid osteoma: a current review. *J Pediatr Orthop* 26:695–700
3. Cioni R, Armillotta N, Bargellini I, Zampa V, Cappelli C, Vagli P, Boni G, Marchetti S, Consoli V et al (2004) CT-guided radiofrequency ablation of osteoid osteoma: long-term results. *Eur Radiol* 14:1203–1208
4. Cantwell CP, Obyrne J, Eustace S (2004) Current trends in treatment of osteoid osteoma with an emphasis on radiofrequency ablation. *Eur Radiol* 14:607–617
5. Gebauer B, Tunn P-U, Gaffke G, Melcher I, Felix R, Stroszczyński C (2006) Osteoid osteoma: experience with laser- and radiofrequency-induced ablation. *Cardiovasc Intervent Radiol* 29:210–215

6. Becce F, Theumann N, Rochette A, Larousserie F, Campagna R, Cherix S, Guillou L, Mouhsine E, Anract P et al (2010) Osteoid osteoma and osteoid osteoma-mimicking lesions: biopsy findings, distinctive MDCT features and treatment by radiofrequency ablation. *Eur Radiol* 20:2439–2446
7. Vanderschueren GM, Taminiou AHM, Obermann WR, Van den Berg-Huysmans AA, Bloem JL, Van Erkel AR (2007) The healing pattern of osteoid osteomas on computed tomography and magnetic resonance imaging after thermocoagulation. *Skeletal Radiol* 36:813–821
8. Roqueplan F, Porcher R, Hamzé B, Bousson V, Zouari L, Younan T, Parlier-Cuau C, Laredo J-D (2010) Long-term results of percutaneous resection and interstitial laser ablation of osteoid osteomas. *Eur Radiol* 20:209–217
9. Omlor G, Merle C, Lehner B, Ewerbeck V, Rehnitz C, Weber M-A, Ludwig K (2012) CT-guided percutaneous radiofrequency ablation in osteoid osteoma: re-assessments of results with optimized technique and possible pain patterns in mid-term follow-up. *Rofö* 184:333–339
10. Lindner NJ, Ozaki T, Roedel R, Gosheger G, Winkelmann W, Wörtler K (2001) Percutaneous radiofrequency ablation in osteoid osteoma. *J Bone Joint Surg Br* 83:391–396
11. Martel J, Bueno A, Ortiz E (2005) Percutaneous radiofrequency treatment of osteoid osteoma using cool-tip electrodes. *Eur J Radiol* 56:403–408
12. Lee MH, Ahn JM, Chung HW, Lim HK, Suh JG, Kwag HJ, Hong HP, Kim BM (2007) Osteoid osteoma treated with percutaneous radiofrequency ablation: MR imaging follow-up. *Eur J Radiol* 64:309–314
13. Levine E, Neff JR (1983) Dynamic computed tomography scanning of benign bone lesions: preliminary results. *Skeletal Radiol* 9:238–245
14. Zampa V, Bargellini I, Ortori S, Faggioni L, Cioni R, Bartolozzi C (2009) Osteoid osteoma in atypical locations: the added value of dynamic gadolinium-enhanced MR imaging. *Eur J Radiol* 71:527–535
15. Von Kalle T, Langendörfer M, Fernandez FF, Winkler P (2009) Combined dynamic contrast-enhancement and serial 3D-subtraction analysis in magnetic resonance imaging of osteoid osteomas. *Eur Radiol* 19:2508–2517
16. Van Rijswijk CSP, Geirnaerd MJA, Hogendoorn PCW, Taminiou AHM, Van Coevorden F, Zwinderman AH, Pope TL, Bloem JL (2004) Soft-tissue tumors: value of static and dynamic gadopentetate dimeglumine-enhanced MR imaging in prediction of malignancy. *Radiology* 233:493–502
17. Brix G, Semmler W, Port R, Schad LR, Layer G, Lorenz WJ (1991) Pharmacokinetic parameters in CNS Gd-DTPA enhanced MR imaging. *J Comput Assist Tomogr* 15:621–628
18. Tofts PS (1997) Modeling tracer kinetics in dynamic Gd-DTPA MR imaging. *J Magn Reson Imaging* 7:91–101
19. Tofts PS, Brix G, Buckley DL, Evelhoch JL, Henderson E, Knopp MV, Larsson HB, Lee TY, Mayr NA et al (1999) Estimating kinetic parameters from dynamic contrast-enhanced T(1)-weighted MRI of a diffusible tracer: standardized quantities and symbols. *J Magn Reson Imaging* 10:223–232
20. Juan C-J, Chen C-Y, Jen Y-M, Liu H-S, Liu Y-J, Hsueh C-J, Wang C-Y, Chou Y-C, Chai Y-T et al (2009) Perfusion characteristics of late radiation injury of parotid glands: quantitative evaluation with dynamic contrast-enhanced MRI. *Eur Radiol* 19:94–102
21. Liu PT, Chivers FS, Roberts CC, Schultz CJ, Beauchamp CP (2003) Imaging of osteoid osteoma with dynamic gadolinium-enhanced MR imaging. *Radiology* 227:691–700
22. Chu J-P, Mak HK-F, Yau KK-W, Zhang L, Tsang J, Chan Q, Ka-Kit Leung G (2012) Pilot study on evaluation of any correlation between MR perfusion (Ktrans) and diffusion (apparent diffusion coefficient) parameters in brain tumors at 3 Tesla. *Canc Imag* 12:1–6
23. Mungo DV, Zhang X, O'Keefe RJ, Rosier RN, Puzas JE, Schwarz EM (2002) COX-1 and COX-2 expression in osteoid osteomas. *J Orthop Res* 20:159–162
24. Courcoutsakis N, Spanoudaki A, Maris TG, Astrinakis E, Spanoudakis E, Tsatalas C, Prassopoulos P (2012) Perfusion parameters analysis of the vertebral bone marrow in patients with Ph¹⁻ chronic myeloproliferative neoplasms (Ph(neg) MPN): a dynamic contrast-enhanced MRI (DCE-MRI) study. *J Magn Reson Imaging* 35:696–702
25. Akhlaghpour S, Aziz Ahari A, Ahmadi SA, Arjmand Shabestari A, Gohari Moghaddam K, Alinaghizadeh MR (2010) Histological evaluation of drill fragments obtained during osteoid osteoma radiofrequency ablation. *Skeletal Radiol* 39:451–455
26. Chai JW, Hong SH, Choi J-Y, Koh YH, Lee JW, Choi J-A, Kang HS (2010) Radiologic diagnosis of osteoid osteoma: from simple to challenging findings. *Radiographics* 30:737–749

Differentiation between Benign and Malignant Non-Fatty Soft Tissue Masses using Diffusion weighted Magnetic Resonance: Correlation between ADC Values and Lesion Signal on T2 Weighted Sequences.

Frederique Gay, Pedro A. Gondim Teixeira, Chen Baillang, Marie Zins, Jacques Felblinger, Alain Blum

Submitted to Radiology on August 29th 2013.

Abstract

Purpose: To determine the accuracy of diffusion-weighted imaging DWI MR, alone and combined with T2-weighted sequences, in differentiating benign from malignant non-fatty soft tissue masses of the extremities and trunk.

Materials and Methods: This prospective study was approved by institutional review board, and informed consent was obtained. 100 patients with histologically confirmed non-fatty soft tissue masses underwent MR imaging that included DW, T2 weighted FSE, and gadolinium enhanced MR sequences. The signal intensity on T2 weighted fat-saturated sequences was used to classify lesions in two groups: hyper intense and iso or hypo intense with respect to muscle.

Results: There was a significant difference in the ADC values of benign and malignant lesions ($p < 0.0001$; mean ADC value $1.58 \pm 0.59 \text{ mm}^2/\text{s}$ for benign and $1.14 \pm 0.33 \text{ mm}^2/\text{s}$ for malignant lesions). Both single b600 and multi b DWI protocols presented similar results. The threshold of $1.39 \text{ mm}^2/\text{s}$ yielded a sensitivity, specificity, PPV and NPV of 84%, 61%, 47% and 87% respectively. There was an increase in specificity (78%) when only T2 hyperintense tumors were considered. There was no statistically significant change in ADC values between iso/hypo intense tumors (mean ADC value $1.04 \pm 0.51 \text{ mm}^2/\text{s}$) and malignant tumors.

Conclusion: The T2 signal of non-fatty soft tissue masses should be considered in the interpretation of ADC values. The DWI presents a good performance for the benign-malignant differentiation in T2 hyperintense lesions.

Introduction

Magnetic Resonance (MR) imaging is the method of choice for the evaluation and staging of soft tissue tumors. MR based morphologic analysis is performed routinely for the evaluation of soft tissue masses and is supported by the high tissue contrast, multiplanar capabilities and high spatial resolution offered by current imaging protocols (1). Despite the use of a systematic approach a large number of soft tissue tumors cannot be characterized with conventional imaging methods and are deemed indeterminate (2-5). For these lesions the world health organization recommends a histologic confirmation increasing health care costs and patient morbidity (6). Functional and metabolic imaging techniques, such as diffusion weighted imaging (DWI) are now used to improve diagnostic accuracy of MR imaging in characterizing soft tissue tumors and may improve the differentiation between benign and malignant masses (7-10).

DWI has been used for various musculoskeletal applications including tumor evaluation (11, 12). The apparent diffusion coefficient (ADC) values have been reported to be significantly higher in benign musculoskeletal tumors than in malignant ones (1, 13-15). Recent studies have demonstrated that the analysis of ADC values can be used for the differentiation between benign and malignant masses in some histologic sub-groups of soft tissue tumors (16, 17). Some investigators, however, have reported overlapping apparent diffusion coefficient (ADC) values in benign and malignant soft tissue tumors (18). This can be partially explained by the fact that ADC values can be affected by extracellular matrix structure and composition, which may act as confounding factors (19, 20). Soft tissue tumors have a great histologic diversity and advanced tumors may have several compartments of viable and necrotic tissue (6, 21). Additionally, DWI outside the brain is hampered by technical difficulties of which gross motion and magnetic field inhomogeneity (off-isocentre acquisition, air-soft tissue interfaces) are the most relevant (22).

The signal intensity on T2 weighted MR images can also reflect the internal structure of soft tissue tumors (5). The correlation of ADC values with the lesion's signal on T2 weighted sequences may be useful in the benign-malignant differentiation and might help establish general diagnostic criteria for DWI of soft tissue masses (23). The purpose of our study is to assess the performance of quantitative DWI to differentiate benign from malignant soft tissue masses of various histologic sub-types in adults. Two different DWI protocols were evaluated (dual b and multi b) and the ADC

F. Gay – Corresponding author, P. Teixeira, S. Lecocq, A. Blum
Service d'Imagerie Guilloz, Hôpital Central, CHU-Nancy, 29 Av. Mar Lattre de Tassigny, 54000 Nancy, France.
e-mail : frederique.gay1@gmail.com

Baillang C, P. Teixeira, J Felblinger
Université de Lorraine, IADI, UMR S 947, Tour Drouet Rue du Morvan
54511 Vandoeuvre-lès-Nancy France.

M. Zins
Hôpitaux Universitaires Paris Ile-de-France Ouest, Ste Péline AP-HP
49 Rue Mirabeau 75016, Paris, France.

values were correlated to the lesion's signal intensity on T2 weighted images.

Material and methods

Patients

From November 2011 to March 2013 we prospectively included 400 patients clinically suspected to have a bone or soft tissue neoplasm in a research protocol. This project was approved by our institutional ethics committee and informed consent was obtained from all patients before inclusion. Confirmed or suspected pregnancy was considered an exclusion criterion. Patients with MRI contraindications (e.g., cardiac pacemaker) or with renal insufficiency (e.g., glomerular filtration rate < 30 mL/min) were also excluded. All patients were over 18 years-old and underwent contrast enhanced MRI with DWI for tumor characterization and were examined by a physician before MRI.

Among the patients evaluated in the research protocol cited above there were 173 bone tumors and 227 soft tissue tumors which were considered for inclusion in the present study. Among these 67 patients with lipomatous tumors were excluded. Additionally 60 patients were excluded: in 4 patients the histological analysis was inconclusive. 8 patients were excluded due to significant motion artifacts on DWI images. Finally, 48 had no anatomopathologic correlation available (no clinical indication, refusals, patient lost in the follow-up). A probable imaging diagnosis was possible in 35 of these patients (23 vascular malformations or hematomas, 7 peripheral nerve sheath tumors, two probable gout tophi, one soft tissue sarcoidosis, one glomus tumor and one myositis ossificans). In the remaining 13 imaging was inconclusive (Fig. 1).

Hence the final study population was composed of 100 patients (46 women and 54 men age: 19–86 years) with histologically confirmed non-fatty soft tissue masses of the extremities or trunk.

MRI examination

Magnetic resonance imaging was performed at 1.5-T (Signa HDxt, GE Healthcare, Milwaukee, WI, USA) using dedicated coils. In all studies conventional sequences were acquired, including at least one T1 weighted sequence and T2 fat-saturated fast spin echo (FSE) sequences in two different orthogonal planes. T1 weighted fat-saturated sequences after gadolinium injection were available for all patients. The acquisition parameters were adapted to the anatomic region evaluated. On T2 weighted sequences TE values were kept between 30 and 60 ms independent of the anatomic location.

DWIs were obtained before contrast medium administration. A single shot pulsed gradient spin echo (PGSE) diffusion weighted sequence with echo-planar imaging read-out was performed at all three imaging axis directions. In order to reduce the image distortion but reserve enough signal to noise ratio (SNR), only partial Fourier acquisition was used (parallel imaging option was

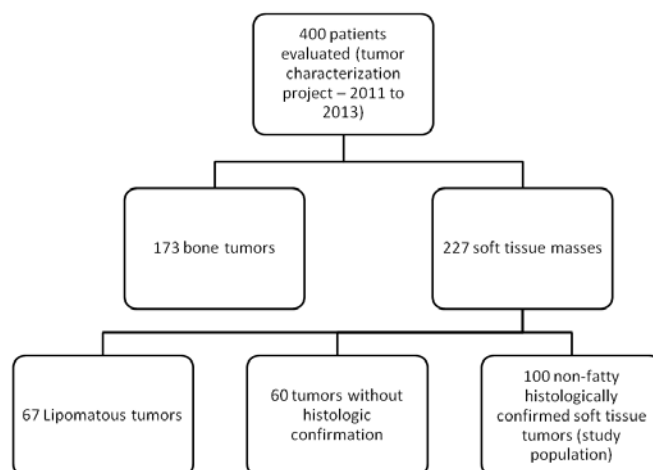


Fig. 1 – Diagram demonstrating the selection of the study population

switched off). The RF excitation of this sequence is spatially spectrally selective, thus only protons in water are excited. The acquisition parameters used were: TE minimal, TR 5000 msec NEX 6, bandwidth 250 Hz, slice thickness 6mm, gap 0, matrix size 128x80. The FOV and the slice thickness were adapted to the patient anatomy. The acquisition time was 1 minute 40 seconds. A single b-value setting was first used with $b = 600 \text{ s/mm}^2$ following one non-diffusion weighted measurement ($b=0$). This DWI protocol was standard for all the patients included and will be designated as dual b protocol.

ADC values from multiple b value diffusion weighted acquisition were obtained for all patients with two different acquisition protocols. From November 2011 to March 2012 a DWI sequence with b values of 0 and 1000 s/mm^2 was performed in addition to the standard protocol to allow multi b value ADC calculation. 83 patients were evaluated with this technique. This sequence was acquired with the same acquisition parameters used for the standard DWI protocol as was performed immediately after the $b=600 \text{ s/mm}^2$ acquisition. The acquisition time was 1 minute 49 seconds.

From March 2012 to March 2013 the standard protocol was complemented by a full multi b value acquisition sequence. The b values of 0, 600 and 1000 s/mm^2 were acquired continuously in the same sequence. The acquisition parameters were set as close as possible to the dual b protocol: TE minimal, TR 5000, bandwidth 250 Hz, slice thickness 6mm, gap 0, matrix 128x80. This sequence offered a NEX modulation as a feature and 1, 6 and 8 NEX were used for b 0, 600 and 1000 s/mm^2 respectively. The acquisition time of the complete DWI protocol (dual and multi b protocols added) varied from 3 minutes 29 seconds to 4 minutes 20 seconds depending on the protocol used size of the tumor and anatomic region.

Image analysis and data post processing

A radiologist with 6 years of experience in musculoskeletal MRI reviewed the images and verified the ROI position in all cases. The reader was blinded to tumor histology. Images were analyzed and the ROI's were placed on an AW console

workstation version 4.4 GE Healthcare using the Functool application. First the conventional MRI images were reviewed and compared to ADC color maps from the dual b DWI acquisition. Elliptical ROI's were placed at the minimal ADC areas of the tumor. Areas of tumor necrosis and calcification were avoided. Minimal ADC areas were used for the evaluation because multiple studies in the literature support the notion that minimal ADC is better correlated to tumor cellularity (24).

For data acquired before March 2012, an in-house software (Matlab R2010, the Mathworks, Natwick, MA, USA) was developed and used to calculate the multi b ADC values as follows: the diffusion signal at each voxel was first normalized by the non-diffusion weighted signal for either diffusion acquisition. Then a standard linear regression with least squares was applied to the logarithm of the normalized values to fit the Gaussian displacement model (25). Data acquired after March 2012 were post processed using Functool application at the AW console workstation version 4.4 GE Healthcare. ROI were placed in the same anatomic region used for the dual b protocol using conventional T2 weighted signal images in addition to diffusion weighted images as a basis for comparison. A preliminary study was performed in our institution confirmed that the ADC values calculated from these two protocols were comparable.

The signal intensity on T2 weighted fat-saturated sequences of the tumors evaluated using normal muscle as a standard for comparison was considered. These lesions were subjectively classified in two groups: hyper intense and iso or hypo intense with respect to the muscle. For heterogenous lesions the predominant signal intensity of the solid tumor component was taken in consideration for this analysis. The ADC values obtained with the different acquisition protocols and the signal intensity of the lesions on T2 weighted sequences were compared with histopathological findings.

Statistical analysis

Statistical analysis was performed using STATA software. The unpaired Student's t-test was used to determine the significance of the differences in ADC values. A p-value of < 0.05 was used as the threshold for statistical significance. Receiver Operating Characteristic Curves (ROC) were used in order to determine a ADC value threshold for the differentiation between benign and malignant masses (26). Based on this analysis sensitivity, specificity, positive predictive value (PPV), negative predictive value (NPV) and accuracy of the DWI protocols used for benign-malignant differentiation were calculated.

Table 1 - Histological diagnosis of benign and malignant tumors

Benign tumors		
Epidermal tumors et adnexielle tumors		
	Kerotoacanthoma	1
	Epidermal cyst	3
	Eccrine adenoma	1
Fibroblastic or myofibroblastic tumors		
	Nodular fasciitis	1
	Hystiocyoma	1
	Leiomyoma	4
	Myxoma	6
	Desmoplastic fibroblastoma	1
	Fibromatosis	2
	Pleomorphic Hyalinizing Angiectatic Tumor (PHAT)	1
	Desmoid tumor	7
	Giant cell tumor	15
	Glomic tumor	1
Vascular tumors		
	Hemangioma	7
	Vascular malformation	1
	Hématoma	2
Nerve tumors		
	Schwannoma	10
	Ganglioneuroma	1

Synovial or pseudo-synovial tumors		
	Pigmented villonodular synovitis PVNS	1
	Synovial chondromatosis	1
	Synovial cyst	1
Non Classified		
	Granuloma epithelioid	1
	Myositis	1
	total	70

Malignant tumors		
Sarcoma		
	Synovial sarcoma	4
	Sarcoma spindle cell	7
	Pleomorphic sarcoma	1
	Sarcoma NOS (not otherwise specified)	6
	Pleomorphic rhabdomyosarcoma	1
	Fibrosarcoma	1
	Dermatofibrosarcoma	2
	Pleomorphic liposarcoma	1
	MPNST Malignant Peripheral Nerve Sheet Tumor	3
	Melanoma	2
	Adenocarcinoma	1
	Neuroendocrine carcinoma	1
	total	30

Results

Seventy benign and 30 malignant tumors were identified by histopathological analysis. A summary of the histologic types of the tumors evaluated is presented in table 1. Tumor diameter ranged from 14 to 190mm (mean 93mm) for the malignant tumors, and from 7 to 175 mm (mean 42mm) for the benign tumors. The anatomic distribution of these tumors was as follows: lower limbs: 50 (36 benign, 14 malignant); upper limbs: 35 (25 benign, 10 malignant); abdominal wall: 3 (2 benign, 1 malignant); chest wall: 5 (3 benign, 2 malignant); head and neck: 2 (1 benign, 1 malignant) and pelvis: 5 (3 benign, 2 malignant).

There was a significant difference in the ADC values of benign and malignant lesions with both dual and multi b protocols ($p < 0.0001$). The mean ADC value for benign and malignant lesions were $1.58 \pm 0.59 \text{ mm}^2/\text{s}$ and $1.14 \pm 0.33 \text{ mm}^2/\text{s}$ with a dual b protocol and 1.53 ± 0.55 and $1.07 \pm 0.27 \text{ mm}^2/\text{s}$ with the multi b protocol (Fig. 2). The ADC value range of the histologic subtypes of this population is presented on table 2. As expected the ADC values from the multi b acquisition were slightly smaller than those from the dual b, thus ROC curve analysis was performed to establish a protocol specific threshold. The thresholds of $1.39 \text{ mm}^2/\text{s}$ and $1.33 \text{ mm}^2/\text{s}$ were retained for dual b and multi b protocols respectively. This analysis yielded sensitivity, specificity, PPV, NPV and accuracy of 84%, 61%, 47%, 87% and 67% for dual and 80%, 63%, 50%, 87% and 68% for multi b protocols (Fig. 3).

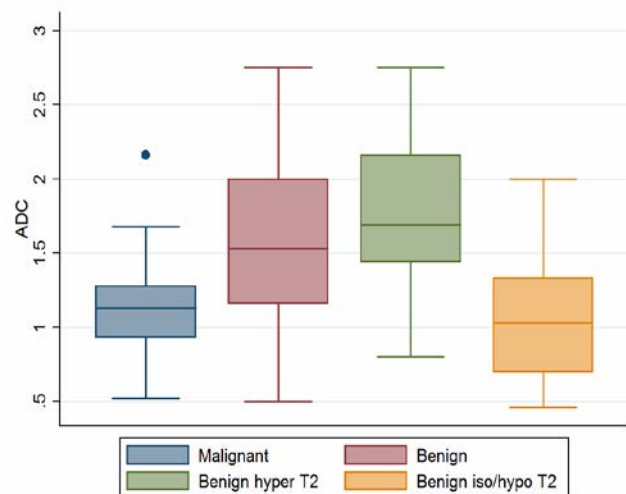


Fig. 2 – Box plot Graphic correlating the apparent diffusion coefficient (ADC) on dual b protocol with the histologic type and the T2 signal intensity. Malignant tumors had significantly lower ADC than benign lesions for benign hyper T2 group and benign group lesion ($p < 0.05$). There was a larger difference in ADC values between malignant and benign T2 hyperintense lesions. The ADC values between benign iso/hypointense tumors and malignant tumors were similar.

Table 2- Mean ADC values ($\times 10^{-3} \text{ mm}^2/\text{s}$) of the soft tissue tumors histologic sub-types in the studied population.

Benign tumors	Nb	b600	b600 1000
Leiomyoma	4	1.63 +/-0.4	1.64 +/- 0.41
Myxoma	6	2.52 +/- 0.35	2.25 +/- 0.46
Desmoid tumor	7	0.98 +/- 0.58	0.92 +/-0.36
Giant cell tumor	15	1.37 +/- 0.47	1.21 +/- 0.46
Hemangioma	7	1.70 +/-0.31	1.79 +/-0.45
Schwannoma	10	1.48 +/- 0.22	1.42 +/- 0.24
total	70	1.58 +/- 0.59	1.53 +/-0.55
Malignant tumors	Nb	b600	b600 1000
Sarcoma	23	1.15 +/- 0.37	1.12 +/- 0.31
total	30	1.14 +/- 0.33	1.07 +/- 0.27

When the T2 signal of the lesions evaluated was taken in account 19% of the lesions were found to be iso/hypo intense to the muscle on T2 weighted images (Fig. 4). All of these lesions were benign. The histology of these tumors is presented on table 3. None of the malignant tumors evaluated were iso/hypo intense. The ADC values of iso/hypo intense lesions were significantly smaller than those of benign hyper intense lesions in both DWI protocols ($p < 0.0001$ and 0.0003 for dual and multi b protocols

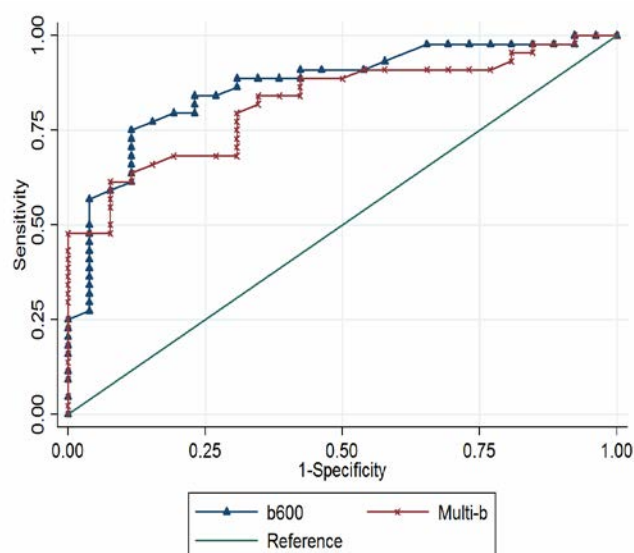


Fig. 3-Receiver operating characteristics curves (ROC) show performance of DWI using dual b (b600) and multi b protocols for the differentiation between benign and malignant T2 hyperintense lesions. Note that both dual and multi b DWI protocols presented similar results. The area under curve (AUC) was similar with these two protocols (AUC, 0.857; standard error SE = 0.042; 95% versus AUC, 0.822; standard error SE = 0.049; 95% for dual and multi b protocols respectively).

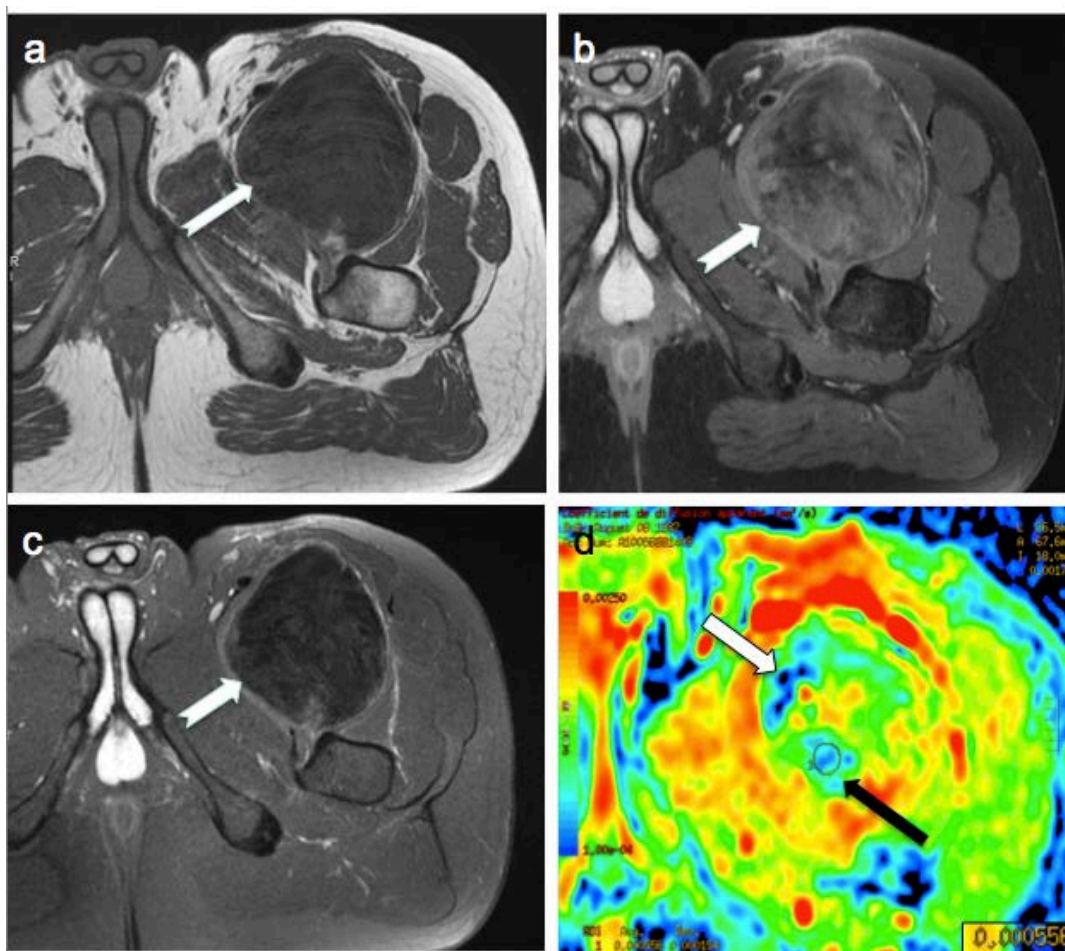


Fig. 4 – 30 year-old man with a desmoid tumor of the proximal left thigh. Axial T1 weighted (A), T2 weighted fat-saturated (B) and T1 weighted fat-saturated (C) MR images are shown. A large mass with regular contours (white arrows in A, B and C), predominantly hypointense on T2 weighted sequences, is seen in inter-muscular position. The lesion does not enhance after gadolinium injection. The ADC color map of this lesion at the corresponding anatomic region is shown in D. At the area of minimal ADC is identified and measured $0.5 \times 10^{-3} \text{ mm}^2/\text{s}$ (black arrow). Note that there are flow voids inside this lesion (deep femoral artery) that should not be considered in the ADC analysis (white arrow)

respectively). The mean ADC values using the standard dual b protocol were $1.78 \pm 0.52 \text{ mm}^2/\text{s}$ for hyperintense lesions and $1.04 \pm 0.51 \text{ mm}^2/\text{s}$ for iso/hypointense lesions. Moreover there was no statistically significant change in ADC values between iso/hypo intense tumors and malignant tumors in any of the protocols evaluated ($p = 0.38$ and 0.85 for dual and multi b protocols).

ROC curve analysis demonstrated that if the iso/hypo intense lesions were not considered there was a non-negligible increase in the sensitivity of DWI for benign-malignant differentiation of soft tissue masses in both DWI protocols studied (Fig. 5 and 6). The ROC curves obtained from the ADC value analysis of three different sub-groups were compared: of all lesions confounded; T2 hyperintense lesions only and T2 iso/hypointense lesions only (Fig. 7). The sensitivity, specificity, PPV, NPV and accuracy of ADC values for the benign-malignant differentiation of T2 hyperintense lesions only (51 benign lesions and on 30 malignant) using the a threshold value of $1.39 \text{ mm}^2/\text{s}$ were: 80%, 78%, 68%, 86% and 79% for the dual b protocol and using a threshold value of 1.33 were 80%, 68%, 60%, 85% and 72% for the multi b protocol. A comparison of the performance of DWI in these three groups is presented on Figure 3.

When only T2 hyperintense lesions were considered there were 10 false positive cases using the standard dual b DWI protocol (benign lesions with an $\text{ADC} < 1.395 \times 10^{-3} \text{ mm}^2/\text{s}$). The histology of these cases was as follows: giant cell tumor of the tendon sheath (GCT TS) (3 cases), schwannoma (3 cases), epidermoid cyst (2 cases), desmoids tumor (1 case) and leiomyoma (1 case). There were 6 false negative cases in the studied population: non-specific sarcoma (2 cases), fibrosarcoma (1 case), malignant peripheral nerve sheath tumor (1 case), spindle cell sarcoma (1 case) and melanoma (1 case).

Discussion

To our knowledge this is the largest study evaluating the value of diffusion weighted magnetic resonance to differentiate benign from malignant non-fatty soft tissue masses. We found that benign and malignant soft tissue masses of various histologic sub-types can be differentiated based on minimal ADC values with good sensitivity and intermediate specificity (84%, 61% respectively). ADC values did not help in differentiating iso and hypo T2

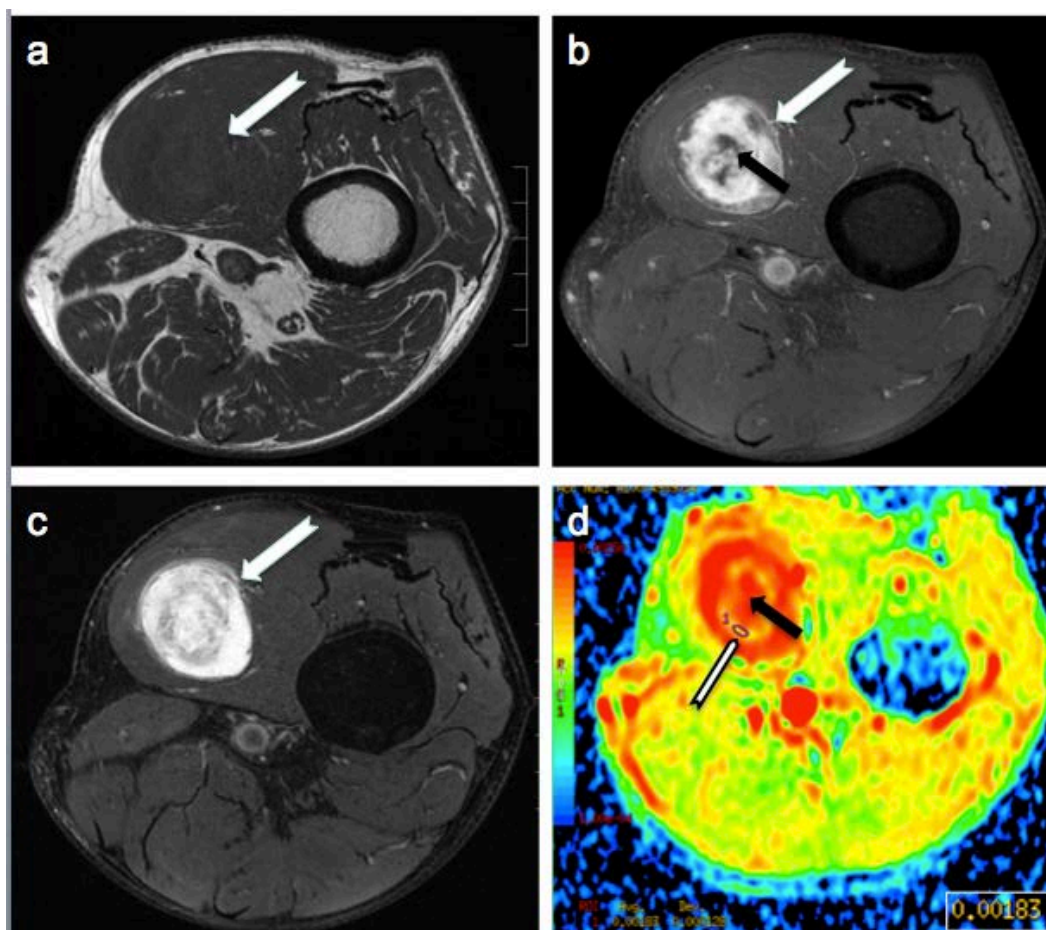


Fig. 5 - Schwannoma of the upper limb in a 78 year-old man. Axial T1 weighted (A), T2 weighted fat-saturated (B) and T1 weighted fat-saturated (C) MR images are shown. A well defined intra-muscular mass is seen at the vastus medialis (white arrows in A, B and C). This lesion has a heterogeneous predominantly hyperintense T2 signal, with cystic degeneration areas identified after gadolinium injection (black arrow in C). The ADC color map of this lesion at the corresponding anatomic region is shown in D. The minimal ADC zone is identified (white arrow) and estimated at $1.83 \times 10^{-3} \text{ mm}^2/\text{s}$. Note that the areas of cystic degeneration present high ADC values (black arrow).

lesions. Thus, the tumor signal intensity on T2 weighted fat-saturated sequences should always be taken into account. Whereas ADC values of benign and malignant lesions are significantly different is still debated in the literature (10). Some authors failed to identify significant differences in ADC between these two groups of lesions (14, 18, 20). However, the study by van Rijswijk and al. included only 22 patients (14) in the study by Einarsdottir and al. the ADC value were calculated from large ROI (18). More recently various studies have demonstrated that DWI of benign lesions yielded significantly higher ADC values than malignant tumors (14, 15, 27). In a large cohort, Nagata and al, found a significant difference for the non myxoid tumors, and obtained almost the same threshold, but did not demonstrate its accuracy. In an important series, Neubauer et al (28) analyzed the ADC values of 44 pediatric patients with soft tissue tumor and tumor-like conditions, and reported a sensitivity and specificity over 90% for benign-malignant differentiation but the prevalence of the different histology sub-types of soft tissue tumors is different between pediatric and adult patients (29). Hypointense T2 benign lesions and malignant lesions could not be differentiated confidently based on ADC values alone ($p = 0.38$). However, hypointense T2 soft tissue tumors are relatively rare (19% of our patient population)

and were all benign in our study. This is in accordance with the results published by Chen and by Wu (5, 19). Although ADC values are correlated with the cellularity of soft-tissue tumors, other factors might influence the diffusion of the water molecules at the extra-cellular space. Tissues that appear hypointense on T2 weighted sequences include fibrosis, hemosiderin and calcification and are found in lesion such as desmoids tumor, fibroma, GCT TS, hemorrhagic masses, pigmented villonodular synovitis (PVNS) or hemorrhagic masses (5). This explains the relatively low ADC values (30, 31). The interpretation of the ADC of such lesions should be undertaken with caution. On a practical basis, hypointense tumors on T2 weighted sequences may be considered as probably benign, but the diagnosis should be confirmed by their characteristics in classical sequences.

When only T2 hyperintense tumors were considered there was a considerable increase in specificity with a similar sensitivity (78% and 80% respectively). The MR image characterization of non-cystic T2 hyperintense lesions is difficult based on conventional sequences because many tumors of various histologic types present this signal pattern (5). In the absence of other distinguishing features on conventional sequences, DWI could be of particularly useful for the evaluation of T2 hyperintense tumors.

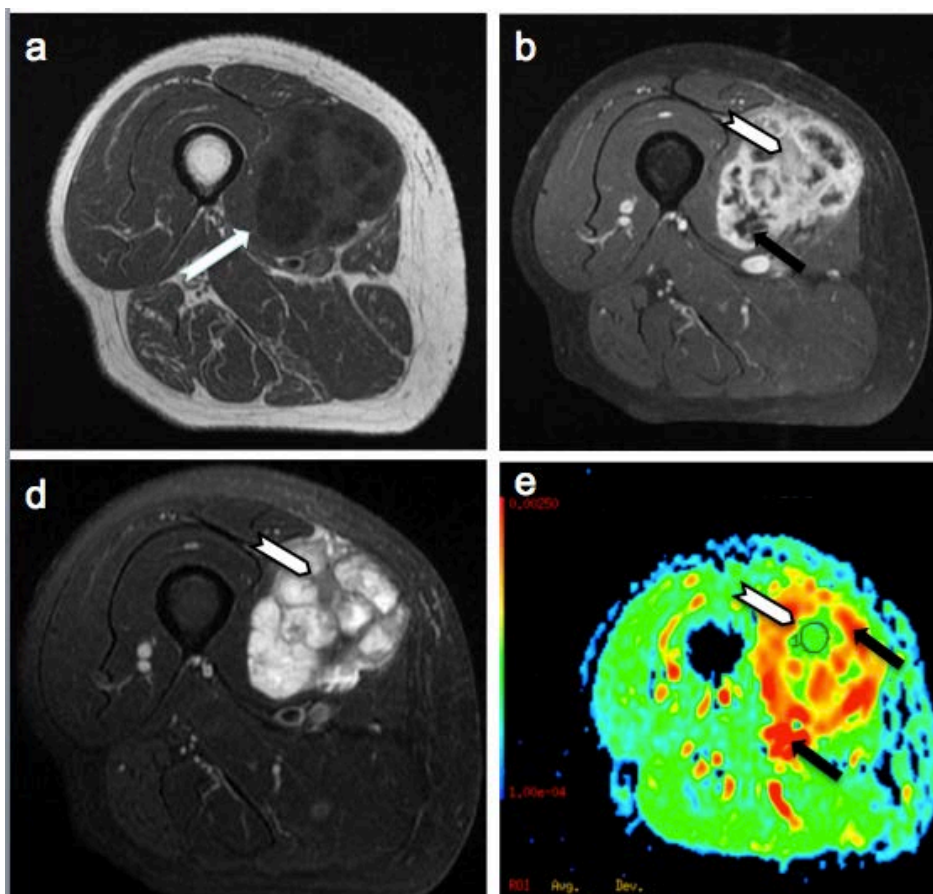


Fig. 6 - Undifferentiated grade 3 sarcoma of the medial compartment of the thigh in a 80 year-old woman. A) Axial T1 weighted MR image showing a large intra-muscular heterogeneous lesion is seen at the vastus medialis (white arrow). B) Axial T1 weighted fat-saturated post gadolinium injection demonstrating multiple necrotic areas (black arrows) and an enhancing tissular component (white arrow). C) Axial T2 weighted fat-saturated image depicting the heterogeneous signal intensity of this lesion with a solid component that is hyperintense with respect to the adjacent muscles (white arrow). D) ADC color map of this lesion at the corresponding anatomic region showing that the tissular component of this lesion has a lower ADC value ($1.07 \times 10^{-3} \text{ mm}^2/\text{s}$) indicative of a malignant lesion (white arrow), whereas the necrotic areas present high ADC values (black arrows).

Four out of 7 desmoids tumors were iso or hypointense on T2 weighted sequences. The mean ADC values of these tumors were $0.98 \pm 0.57 \text{ mm}^2/\text{s}$ and did not allow differentiation with malignant tumors. Desmoid tumors are usually heterogeneous and may present variable T2 signal intensity (32). Oka et al reported statistically significant ADC values between desmoids tumors and malignant soft tissue tumors (16). These authors however, did not directly correlate the T2 signal intensity of the desmoids tumors with the ADC values.

There were 10 false positive among hyperintense T2 lesions, of which 3 schwannomas. Histologically schwannomas show a variable distribution of Antoni A and B regions. Antoni A regions are composed of organized spindle cells arranged in short bundles or interlacing fascicles, whereas Antoni B regions are hypocellular and contain loosely arranged myxoid tissue (33.) Antoni A predominant schwannomas might have a lower ADC, which could explain these findings. PVNS was also a cause of false positives. These lesions are usually T2 hypointense and despite their benign nature, some may present features of aggressive lesions with high cellularity and mitotic activity which probably accounts for the low ADC values (34). Finally two epidermoid cysts were also identified in this

group. The compact lamellae of keratin debris usually found in these lesions probably limit water diffusibility (35). There was no evident explanation for the remaining false positive and for the false negative cases encountered. Both dual and multi b DWI protocols presented quite similar results for the differentiation between benign and malignant tumors. There was actually a small decrease in specificity (68% versus 78 % regarding to T2 hyperintense lesions) with multi b acquisition which was probably related to the low SNR in the b 1000 s/mm^2 acquisitions. Chen et al studied the impact b value variation on ADC measurements (36). Similar results have been demonstrated on breast imaging (36, 37). These authors demonstrated that Multi b DWI protocols lead only to a minor increase in the precision of ADC values at the expense of an increase in motion artifacts. These findings favor the use of a simplified dual b DWI protocol with a b600 s/mm^2 value for soft tissue tumor characterization with no compromise to the diagnostic performance.

Our study has several limitations: Two different methods were used for multi b ADC calculation. Multi b value sequences were not available in our department before March 2012. Changing the acquisition protocol was preferable because the new sequence minimizes motion artifacts, facilitates post processing and it compensates for

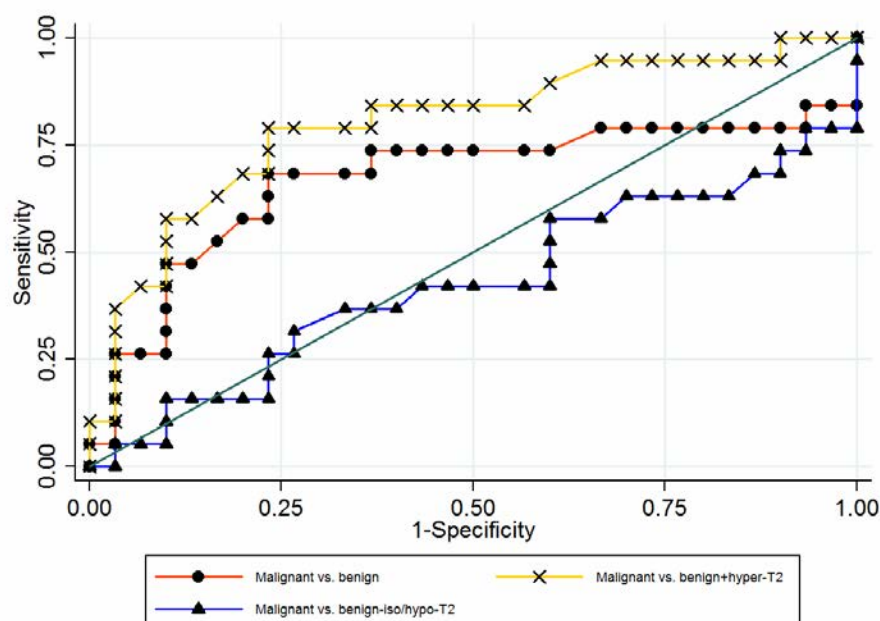


Fig. 7 - ROC curve based on ADC values acquired with the dual b DWI protocol. Three curves are presented for benign versus malignant differentiation of lesions studied: without considering the lesion's T2 signal (red curve), for hyper T2 signal lesions only (yellow curve) and for Iso/hypo T2 lesions only (blue curve). In the yellow curve the area under curve (AUC) was higher (AUC, 0.857; standard error SE = 0.042; 95%) than for the red curve (AUC, 0.771; standard error SE = 0.055; 95%). Furthermore, Area under curve (AUC) for iso/hypointense T2 benign lesions (blue curve) (AUC, 0.571; standard error SE = 0.089; 95%) not significantly different from the chance diagonal (AUC, 0.5), meaning that this technique have no ability to discriminate benign from malignant lesions.

signal loss on higher b values by increasing the NEX, and also allows exactly the same TE value for the two b-value settings. There were a limited number of hypointense T2 lesions included to define the ADC value threshold and the differentiation between benign and malignant T2 hypointense tumors was not possible. Further studies dedicated for this specific sub group of soft tissue tumors are necessary. The use of DWI is difficult in the extremities due to prominent image distortion with EPI acquisitions. These distortions hindered ROI positioning in some cases. Finally the ROI position of the dual b standard protocol and of multi b value acquisition sequence employed after March 2012 was not strictly the same due to technical limitations of the post processing software, which did not allow ROI position propagation between two different sequences.

In conclusion, we found a statistically significant difference in ADC values between benign and malignant soft tissue tumors in adults in a population with a wide range of tumor histologic sub-types. However, signal intensity on T2 weighted images should always be considered in the interpretation of ADC values. Iso or hypointense T2 benign tumors could not be confidently differentiated from malignant tumors based on ADC values. DWI and ADC values should not be used for this group of tumors, because they present misleadingly low ADC values. On the other hand ADC value analysis can be used for the benign-malignant differentiation of hyperintense T2 lesions with high sensitivity and specificity. In this context DWI can be a valuable tool for tumor characterization.

Acknowledgements

This work was supported by the French society of radiology (Société Française de Radiologie – SFR) through a research grant.

Bibliography

- Costa FM, Canella C, Gasparetto E. Advanced magnetic resonance imaging techniques in the evaluation of musculoskeletal tumors. *Radiol Clin North Am*;49(6):1325-58, vii-viii.
- Costa FM, Ferreira EC, Vianna EM. Diffusion-weighted magnetic resonance imaging for the evaluation of musculoskeletal tumors. *Magn Reson Imaging Clin N Am*;19(1):159-80.
- Charles-Edwards EM, deSouza NM. Diffusion-weighted magnetic resonance imaging and its application to cancer. *Cancer Imaging*. 2006;6:135-43.
- Gielen JL, De Schepper AM, Vanhoenacker F, et al. Accuracy of MRI in characterization of soft tissue tumors and tumor-like lesions. A prospective study in 548 patients. *Eur Radiol*. 2004;14(12):2320-30.
- Wu JS, Hochman MG. Soft-tissue tumors and tumorlike lesions: a systematic imaging approach. *Radiology*. 2009;253(2):297-316.
- Fletcher CD. The evolving classification of soft tissue tumours: an update based on the new WHO classification. *Histopathology*. 2006;48(1):3-12.
- Fayad LM, Jacobs MA, Wang X, Carrino JA, Bluemke DA. Musculoskeletal tumors: how to use anatomic, functional, and metabolic MR techniques. *Radiology*;265(2):340-56.
- Koh DM, Collins DJ. Diffusion-weighted MRI in the body: applications and challenges in oncology. *AJR Am J Roentgenol*. 2007;188(6):1622-35.

9. Koh DM, Takahara T, Imai Y, Collins DJ. Practical aspects of assessing tumors using clinical diffusion-weighted imaging in the body. *Magn Reson Med Sci.* 2007;6(4):211-24.
10. Vermoolen MA, Kwee TC, Nieuvelstein RA. Apparent diffusion coefficient measurements in the differentiation between benign and malignant lesions: a systematic review. *Insights into imaging.* 2012;3(4):395-409.
11. Bley TA, Wieben O, Uhl M. Diffusion-weighted MR imaging in musculoskeletal radiology: applications in trauma, tumors, and inflammation. *Magn Reson Imaging Clin N Am.* 2009;17(2):263-75.
12. Colagrande S, Carbone SF, Carusi LM, Cova M, Villari N. Magnetic resonance diffusion-weighted imaging: extraneurological applications. *Radiol Med.* 2006;111(3):392-419.
13. Herneth AM, Guccione S, Bednarski M. Apparent diffusion coefficient: a quantitative parameter for in vivo tumor characterization. *Eur J Radiol.* 2003;45(3):208-13.
14. van Rijswijk CS, Kunz P, Hogendoorn PC, Taminiau AH, Doornbos J, Bloem JL. Diffusion-weighted MRI in the characterization of soft-tissue tumors. *J Magn Reson Imaging.* 2002;15(3):302-7.
15. Nagata S, Nishimura H, Uchida M, et al. Diffusion-weighted imaging of soft tissue tumors: usefulness of the apparent diffusion coefficient for differential diagnosis. *Radiat Med.* 2008;26(5):287-95.
16. Oka K, Yakushiji T, Sato H, et al. Usefulness of diffusion-weighted imaging for differentiating between desmoid tumors and malignant soft tissue tumors. *J Magn Reson Imaging.* 2011;33(1):189-93.
17. Oka K, Yakushiji T, Sato H, et al. Ability of diffusion-weighted imaging for the differential diagnosis between chronic expanding hematomas and malignant soft tissue tumors. *J Magn Reson Imaging.* 2008;28(5):1195-200.
18. Einarsdottir H, Karlsson M, Wejde J, Bauer HC. Diffusion-weighted MRI of soft tissue tumours. *Eur Radiol.* 2004;14(6):959-63.
19. Chen CK, Wu HT, Chiou HJ, et al. Differentiating benign and malignant soft tissue masses by magnetic resonance imaging: role of tissue component analysis. *Journal of the Chinese Medical Association : JCMSA.* 2009;72(4):194-201.
20. Maeda M, Matsumine A, Kato H, et al. Soft-tissue tumors evaluated by line-scan diffusion-weighted imaging: influence of myxoid matrix on the apparent diffusion coefficient. *J Magn Reson Imaging.* 2007;25(6):1199-204.
21. Lang P, Wendland MF, Saeed M, et al. Osteogenic sarcoma: noninvasive in vivo assessment of tumor necrosis with diffusion-weighted MR imaging. *Radiology.* 1998;206(1):227-35.
22. Scherrer B, Gholipour A, Warfield SK. Super-resolution reconstruction to increase the spatial resolution of diffusion weighted images from orthogonal anisotropic acquisitions. *Medical image analysis.* 2012;16(7):1465-76.
23. Wu LM, Xu JR, Ye YQ, Lu Q, Hu JN. The clinical value of diffusion-weighted imaging in combination with T2-weighted imaging in diagnosing prostate carcinoma: a systematic review and meta-analysis. *AJR Am J Roentgenol;*199(1):103-10.
24. Hirano M, Satake H, Ishigaki S, Ikeda M, Kawai H, Naganawa S. Diffusion-weighted imaging of breast masses: comparison of diagnostic performance using various apparent diffusion coefficient parameters. *AJR Am J Roentgenol;*198(3):717-22.
25. E.M. Haacke RWB, M. R. Thompson, and R. Venkatesan. *Magnetic Resonance Imaging: Physical Principles and Sequence Design.* , 1999.
26. Obuchowski NA. Receiver operating characteristic curves and their use in radiology. *Radiology.* 2003;229(1):3-8.
27. Geith T, Schmidt G, Biffar A, et al. Comparison of qualitative and quantitative evaluation of diffusion-weighted MRI and chemical-shift imaging in the differentiation of benign and malignant vertebral body fractures. *AJR Am J Roentgenol;*199(5):1083-92.
28. Neubauer H, Evangelista L, Hassold N, et al. Diffusion-weighted MRI for detection and differentiation of musculoskeletal tumorous and tumor-like lesions in pediatric patients. *World journal of pediatrics : WJP.* 2012;8(4):342-9.
29. Fletcher CD. Distinctive soft tissue tumors of the head and neck. *Modern pathology : an official journal of the United States and Canadian Academy of Pathology, Inc.* 2002;15(3):324-30.
30. Sundaram M, McGuire MH, Schajowicz F. Soft-tissue masses: histologic basis for decreased signal (short T2) on T2-weighted MR images. *AJR Am J Roentgenol.* 1987;148(6):1247-50.
31. Le Bihan D. Apparent Diffusion Coefficient and Beyond: What Diffusion MR Imaging Can Tell Us about Tissue Structure. *Radiology.* 2013;268(2):318-22.
32. Lee JC, Thomas JM, Phillips S, Fisher C, Moskovic E. Aggressive fibromatosis: MRI features with pathologic correlation. *AJR Am J Roentgenol.* 2006;186(1):247-54.
33. Murphey MD, Smith WS, Smith SE, Kransdorf MJ, Temple HT. From the archives of the AFIP. Imaging of musculoskeletal neurogenic tumors: radiologic-pathologic correlation. *Radiographics : a review publication of the Radiological Society of North America, Inc.* 1999;19(5):1253-80.
34. Murphey MD, Rhee JH, Lewis RB, Fanburg-Smith JC, Flemming DJ, Walker EA. Pigmented villonodular synovitis: radiologic-pathologic correlation. *Radiographics : a review publication of the Radiological Society of North America, Inc.* 2008;28(5):1493-518.
35. Lee HS, Joo KB, Song HT, et al. Relationship between sonographic and pathologic findings in epidermal inclusion cysts. *Journal of clinical ultrasound : JCU.* 2001;29(7):374-83.
36. Chen X, He XJ, Jin R, et al. Conspicuity of breast lesions at different b values on diffusion-weighted imaging. *BMC cancer.* 2012;12:334.
37. Bogner W, Gruber S, Pinker K, et al. Diffusion-weighted MR for differentiation of breast lesions at 3.0 T: how does selection of diffusion protocols affect diagnosis? *Radiology.* 2009;253(2):341-51.

Influence of Calcium on Choline Measurements by ¹H MR Spectroscopy of the Thigh Muscles.

Pedro A. Gondim Teixeira, Gabriela Hossu, François Kauffmann, Anous Sewonu, Jean-Marc Constans, Alain Blum, Jacques Felblinger

Submitted to *European Radiology* on September 13th 2013.

Abstract

Objective: to study the effects of calcium on the choline peak measurements with ¹H MR spectroscopy.

Material and methods: Human striated muscle contains known concentrations of choline. The thigh muscles of two cadaveric specimens were prospectively evaluated on a 3T MR unit before and after the injection of a mixture of calcium carbonate (up to 0.4322g) and non-ionic water. The choline peaks of 147 spectra from 10 different anatomic locations were quantitatively evaluated using the internal water peak as a reference with two different analysis methods. The influence of the calcium concentration and its disposition with respect to the main magnetic field were considered. B₀ phase maps were used to evaluate field inhomogeneities.

Results: Both methods used for spectral analysis yielded similar results. The presence of calcium lead to a 43% underestimation of the choline peak and the choline concentration, which were statistically significant (p = 0.0002 and 0.0036). The mean choline concentration before and after CaCO₃ injection were: 3.53 ± 1.72 mmol/L and 1.58 ± 0.63 mmol/L. The influence of calcium carbonate on the choline peak estimations were proportional to the tissue calcium concentration. There was a significant position dependent difference in the estimation of the choline peak amplitude (p < 0.0154). Calcium injection lead to an increase in field inhomogeneities of the same magnitude seen adjacent to vascular calcifications.

Conclusion: the quantitative analysis of calcified tumor spectra should be interpreted with caution. The quantitative evaluation of choline (peak amplitude and concentration) was significantly underestimated in the presence of Calcium, which might cause misinterpretations of MR spectra.

Key words: ¹H MR spectroscopy, quantitative, calcium, choline, B₀ mapping

Introduction

The role of Proton (¹H) MR spectroscopy in the diagnosis, follow-up and prognostic assessment of tumor masses of various organs and systems has been widely demonstrated in the literature¹⁻⁴. The concentration of tumor choline compounds (choline, phosphocholine and glycerolphosphocholine), expressed here as choline, are related with the rate of cellular proliferation and reflect tumor aggressiveness⁵. Various studies have demonstrated that the presence of a choline peak at 3.2 ppm can assist in the non-invasive characterization of tumors⁶. Quantitative estimation of the choline concentration using internal non-suppressed water peak is of particular interest because it increases the diagnostic performance of MR spectroscopy and allows direct inter and intra patient comparisons⁷.

Some authors have suggested that the presence of intra tumoral calcifications or ossifications might have a negative influence on the quality of MR spectroscopy data^{8,9}. Intra tumoral calcifications can be found in or adjacent to neoplasms of multiple organs and systems (e.g. breast, brain, prostate, musculoskeletal). The presence of calcium leads to magnetic field inhomogeneities which can be responsible for water and metabolite peak widening, base line anomalies and noise increase^{10,11}. These perturbations may hinder spectral analysis and have an impact on the estimation of metabolite concentration and on the reproducibility of the technique. There is limited information in the literature on the influence of calcium crystals on ¹H MR spectroscopy choline measurements and quantification.

In this study, we sought to evaluate the influence of calcium on the subjective and quantitative evaluation choline peak with ¹H MR spectroscopy. Since a direct evaluation of the calcium influence on MR spectroscopic choline measurements in tumors is particularly difficult "in vivo", a thigh muscle phantom was used. This information may help understand the limitations of this technique on tumors containing calcifications or ossifications which might have an impact on the interpretation and analysis of the spectra from these lesions.

P. Teixeira – corresponding author, A. Blum
Service d'Imagerie Guilloz, Hôpital Central, CHU-Nancy, 29 Av. Mar Lattre de Tassigny, 54000 Nancy, France.
e-mail: ped_gt@hotmail.com

P. Teixeira, G. Hossu, A. Sewonu, J Felblinger
Université de Lorraine, IADI, UMR S 947, Tour Drouet Rue du Morvan 54511 Vandoeuvre-lès-Nancy France.

F. Kauffmann - Université de Caen, LMNO, UMR 6139, Bd du maréchal Juin, 14032 Caen Cedex.

Jm. Constans - Service de radiologie, CHU d' Amiens, Hôpital Nord, Place Victor Pauchet, 80054 Amiens Cedex, France.

Material and Methods

Phantom conception

Normal skeletal muscle contains choline in a relatively high concentration¹². ¹H MR spectroscopy can detect a choline peak in normal human skeletal muscle¹². Choline is a relatively stable metabolite. Studies have demonstrated that choline compounds can be identified with conventional acquisition protocols post mortem⁹.

We obtained two fresh frozen lower limbs (foot to hip) from an 80 year-old female and from an 86 year-old male cadavers from the anatomy laboratory of our institution. These specimens were deep frozen and were conserved in a -30°C freezer. While frozen the specimen thighs were sectioned in 7 cm slabs in the axial plane. 3 thigh slabs were obtained from one specimen and one from the other. The thigh slabs were left to thaw at room temperature 24 hours before imaging. Once thawed the slabs were put in a plastic container and were immersed in non-ionic water. The temperature during acquisition was controlled continuously by two optical MR compatible (Neoptix™-Reflex™). One was placed inside the femoral bone marrow at the center of the slab and the other was placed in contact with the outer surface of the slab (Fig. 1). A color strip was used for specimen pH estimation after thawing. In our institution studies using fully anonymized cadaveric specimens donated to science do not require ethics committee approval.

Based on the study of proximal human femori obtained after total hip replacement surgery, the mean calcium concentration at the proximal femur was reported to vary from 39.46 to 160.04 mg/g¹³. The concentration of 80 mg/g of calcium at the region of interest (ROI) was thus used to simulate a partially calcified or ossified lesion. Calcium phosphate and carbonate compounds participate in tissue mineralization process in both vertebrates and invertebrates^{14,15}. Calcium carbonate (CaCO₃) is widely available (commonly used in the pharmaceuticals as anti-acid and as a nutritional supplement) and have similar biochemical and electromagnetic properties as calcium phosphate compounds which are the most abundant calcium compounds in bone^{16,17}.

¹H MR spectroscopy was performed at the same anatomic region before and after the injection of CaCO₃ and pure non-ionic water (control data). Spectra were acquired from a tube with 10 cm in length and 3 cm in diameter containing a solution of choline chloride (Sigma-Aldrich, CAS number 67-48-1) and non-ionic water with a concentration of 5 mmol/L. The coil loading was similar in all experiments (a cadaveric slab was positioned inside the coil adjacent to the choline tube) and the voxel size was 30 x 15 x 12 mm.

Imaging protocol

All acquisitions were performed in a GE Healthcare 3.0T MR scanner, Signa HDxt with an eight-channel rigid knee coil. Anatomic images were acquired from all cadaveric slabs

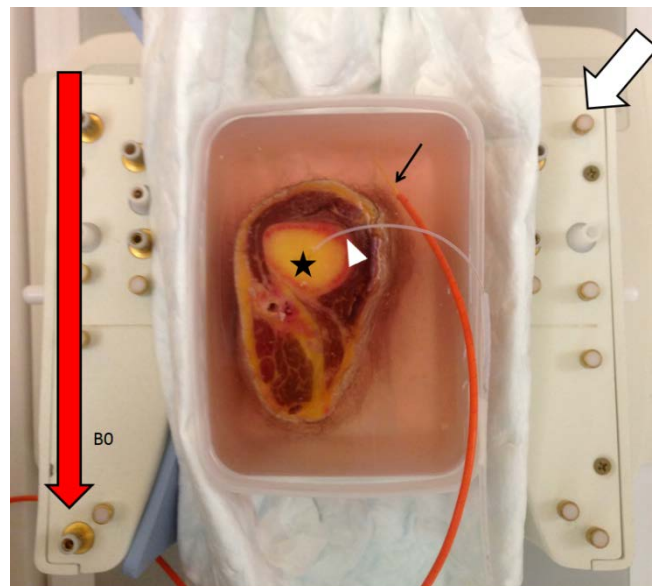


Fig. 1 - Photograph depicting the used phantom. A 7 cm slab of a cadaveric thigh specimen (star) is positioned inside a recipient filled with non-ionic water. The phantom is positioned inside an 8 channel knee coil (white arrow). Two temperature probes are seen. One is positioned inside the femoral medullary cavity (white arrowhead) and the other at the outer surface of the specimen (black arrow). The long red arrow demonstrates the direction of the main magnetic field (B_0) vector with respect to the phantom. Injections were performed with the specimen in this position with a needle path parallel to the long axis of the muscle fibers.

before and after the injections. Axial, sagittal and coronal T1-weighted FSE images; axial T2-weighted fat-saturated FSE images and axial T2* weighted fat-saturated gradient echo images were acquired. B_0 mapping was performed in two specimen slabs using a double echo gradient echo sequence (TR = 258.6 ms, TE1/TE2 = 4.6/6.9 ms, Matrix/FOV = 128x128/200mm, flip angle = 60°, Slice thickness/Slice gap = 4.1 mm/1.5 mm). This scanning protocol yields field inhomogeneities images, which are reconstructed in frequency scale (Hz).

Single voxel ¹H MR spectroscopy (PRESS sequence) was performed with chemical shift selective water suppression (CHESS) technique using the following settings: Scan number 64, TR 3000 ms, TE 144 ms. Acquisition time was 4 minutes 24 seconds. Two voxel sizes were used 30x15x12 mm and 30x12x12. Temperature settings were changed to accommodate to phantom temperature variation during acquisition. On 4 different muscle regions and on the external reference choline tube MR spectroscopy was performed with 4 different echo times (TE = 35, 100, 144 and 288 ms) to allow T2 estimation of water and choline. T2 was estimated by using a conventional exponential fitting. One of the specimen slabs was imaged twice before CaCO₃ injection with a 4-week interval to assess the stability of choline measurements after a freezing-thawing cycle.

The standard position for the evaluation of all specimen slabs was with the long axis of the muscle fibers perpendicular to

the main magnetic field (horizontal) (Fig 1). For three muscle regions MR spectroscopy was performed with the slab in a different position with respect to the main magnetic field (B_0) before and after CaCO_3 injection). In this alternative slab position the long axis of the muscle fibers was parallel to B_0 . After the MR spectroscopy evaluation, CT was performed in all specimen slabs with a GE Healthcare lightspeed scanner (kVp 80, mAs 100, slice thickness 0.6 mm, FOV 12 cm).

Calcium carbonate injection

Using a precision scale (Mettler Toledo international inc. model Ax204) 0.432 g of CaCO_3 powder were obtained and mixed with 10 ml of non-ionic water. Considering the voxel size used the maximum approximate calcium carbonate concentration attained at the ROI was 80mg/g. The injections were performed with an 18G needle directly on the quadriceps and hamstring muscle group. Air injection was meticulously avoided. The needle path was parallel to the long axis of the sectioned muscle fibers to limit damage to the tissue architecture (Fig. 1).

A musculoskeletal radiologist (P.T.) analyzed the conventional MR images acquired and selected all the intra-muscular voxel locations. Injections were performed by the same physician at the selected pre-selected areas by correlating the tendino-muscular anatomy seen on anatomic MR images with the macroscopic analysis of the specimen slabs. The ROI position was confirmed to be centered at the injection area on the conventional sequences acquired after injection. Two injection protocols were used.

- Single injection protocol:

10 ml of the CaCO_3 suspension or pure non-ionic water were slowly injected through a single entry point.

- Multiple injection protocol:

1 ml injections of a 10 ml CaCO_3 suspension or pure non-ionic water were performed successfully at the same anatomic area. Without taking the phantom out of the coil or changing the coil position with respect to the table (zeroed coil) a spectrum was acquired using the same voxel position and the same shimming options after each 1 ml injection. This procedure was repeated until all 10 ml were delivered in the selected ROI.

Data post processing

Visual analysis and post processing of the spectra were performed by three examiners in consensus: one fellowship trained musculoskeletal radiologist with 6 years of clinical experience (P.T.) and two physicists specialized on 1H MR spectroscopy (G.H and F.K) with 7 and 15 years of experience respectively. Spectra were judged over the aspect of the base line, peak width and the distinction of choline and creatine peaks. Spectral quality assessment was based on the width of the water peak (LNWH) and the level of water suppression achieved.

Choline compounds (Cho) were identified at 3.2 ppm (214 Hz at 18°C) and the water peak was identified as 4.87 ppm (0 Hz at 18°C). For every MR spectroscopy acquisition three spectra were generated: a noise spectrum (1 excitation), a spectrum with an unsuppressed water peak (2 excitations) and a spectrum after water suppression (61 excitations).

Spectroscopy data was analyzed with a semi-automated process using the advanced method for accurate, robust, efficient spectral fitting (AMARES) in the Java (Sun Microsystems) based MR user's interface (jMRUI) package (version 5.0). Spectra were processed with zero-order hard phase correction individually. The peak integral values of the non-suppressed water signal and choline signal were quantified. Peak selection was performed manually. Up to 7 peaks were selected in addition to those previously mentioned to facilitate spectral modeling and ameliorate peak fitting. No prior knowledge of peak relation was used. Residual water or lipid peaks hindering adequate fitting of the metabolites of interest were removed with the peak removal tool (HLSVD propack¹⁸). Adequate fitting in all spectra was verified by a physicist (G.H.) and a radiologist (P.T.).

The amplitude measurements were verified with a fully-automated spectroscopy analysis method (SCI-MRS-LAB) which uses an extension of the linear combination model¹⁹ and Scilab, a free and Open Source software (distributed under CeCILL license - GPL compatible) developed by Scilab Enterprises. An eddy current correction was performed for all spectra²⁰. The spectral model was a linear combination type that can be expressed as the sum of three terms: the prior knowledge signal for Cho and creatine (Cr) signal, a linear combination model for all other resonances and a baseline. Maximal numbers of models of resonance signals outside the interval of 2.9 to 3.3 ppm is limited to 15. Initial conditions were estimated with a Hankel-Lanczos decomposition. Unknown parameters of the total spectra (water, lipids, Cho, Cr and baseline), were estimated using a weighted-least-square model with windows in both time and frequency domain. Maximal number of degrees of freedom for prior knowledge signal model was 10 for the line base model and 10 for each resonances. Other prior knowledge data were added as constraints.

Choline concentrations, in units of mmol/L, were estimated using the non-suppressed water peak as an internal reference compound. The choline (Cho) concentrations were calculated using the following equation:

$$Cho = \frac{S_{Cho}}{S_{H2O}} \times \frac{n_{H2O}}{n_{Cho} MW_{H2O}} \times \frac{fT_1(H_2O)}{fT_1(Cho)} \times \frac{fT_2(H_2O)}{fT_2(Cho)} \times CF_{H2O}$$

where S_{Cho} is the area of choline peak at 3.2 ppm, S_{H2O} is the area of the non-suppressed water signal, $n_{H2O} = 2$, $n_{Cho} = 9$ (from 3 CH3 groups), $MW = 18.0153 \times 10^{-6}$ kg/mmol, $fT_1 = 1 - \exp(-TR/T1)$, $fT_2 = \exp(-TE/T2)$. With the use of a TR of 3000 ms the influence of T1 on the concentration calculation was considered negligible: $fT1 = 1 - \exp(-TR/T1) = 1$. The

CFH_2O is 0.77 (i.e., 77% water content of muscle) and is believed to be relatively constant between different muscle groups both in normal and in diseased states¹². Peak amplitudes were corrected with respect to the signal gain selected for each acquisition. Since there was a change in the water content at the voxel after injection, the non-suppressed water peak of the same voxel location acquired before injection was used for choline concentration calculations which were calibrated to the external reference. B_0 map analysis was performed using Matlab (v. 7.2, the Mathworks, Natwick, MA, USA). Post-processing included masking of image areas expected to be influenced by susceptibility (image background, bone region). As the acquired data only featured very few phase wrap, it was unnecessary to perform unwrapping operations which are usually needed in the computation of field maps. By dividing the acquired ΔB_0 images by the nominal field value (127.77 MHz), the field maps were converted into parts-per-million (ppm). The disturbance in B_0 at a voxel area similar to the voxels used on spectroscopy (30 mm×12 mm or 19 pixels×8 pixels) was compared in areas of normal muscle, injected calcium, injected pure water and vascular calcifications (deep superficial femoral artery).

Statistical analysis was performed by using R Development Core Team software version R (ver. 3.0.1 2013). The measurements obtained with both post processing methods were compared simultaneously with linear models. For each peak amplitude measurement a linear multivariate model that explains SCI-MRS-LAB estimation by JMRUI estimation and by instrumental variables was estimated. The main hypothesis is that if the two methods were perfect, both estimations would be equal and no significant effects of instrumental variables would be detected. The following instrumental variables were considered: the specimen slabs used, muscle sub-group, proximity to the femoral diaphysis, position of the slab with respect to B_0 and the intra-voxel concentration of non-ionic water and $CaCO_3$.

The influence of various instrumental variables on the quantification of metabolite (water and choline compound) peaks was tested by using a log linear model. The following instrumental variables were considered: the specimen slabs used, muscle sub-group, proximity to the femoral diaphysis, position of the slab with respect to B_0 , TE and the intra-voxel concentration of non-ionic water and $CaCO_3$. The student's T test was used for the comparison of mean choline concentrations. A p value less than 0.05 was used as the threshold for statistic significance.

Statistical analysis

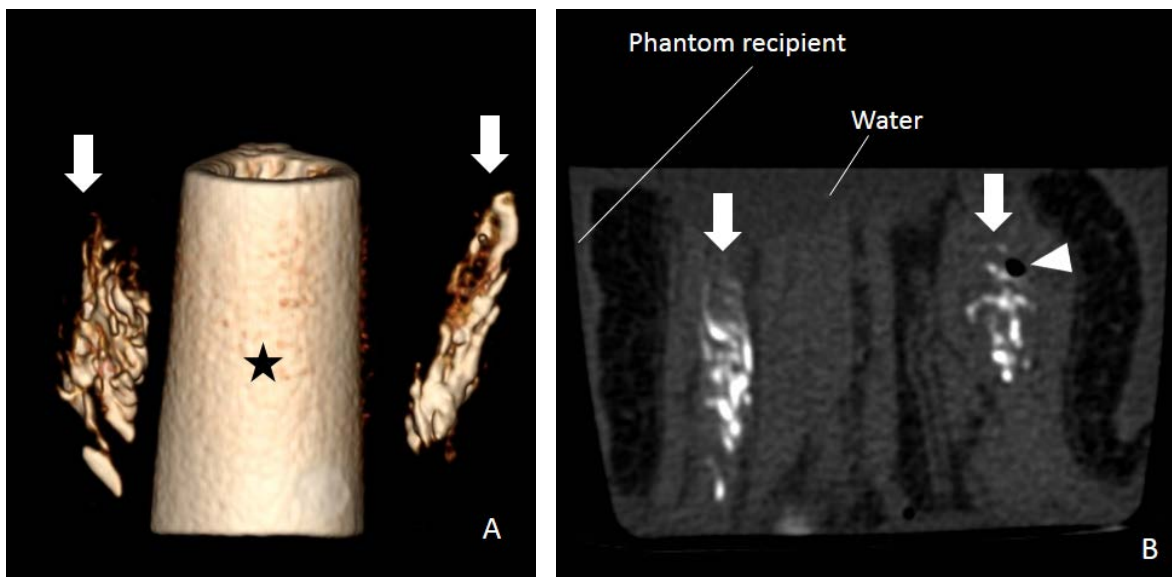


Fig. 2 - CT images of thigh specimen of an 80 year-old male. A) Volume rendering 3-D reformat showing the morphologic aspect of the injected calcium carbonate, in two different injection points (white arrows). Note that the distribution of the calcium particles is preferentially oriented parallel to the long axis of the muscle fibers. The sectioned femur is seen at the center of the image (star). B) Coronal oblique CT reformat using an intermediate window setting of the same specimen demonstrating the distribution of the injected calcium at the quadriceps muscle. Note a small air bubble contaminating the injection site on the left (arrowhead).

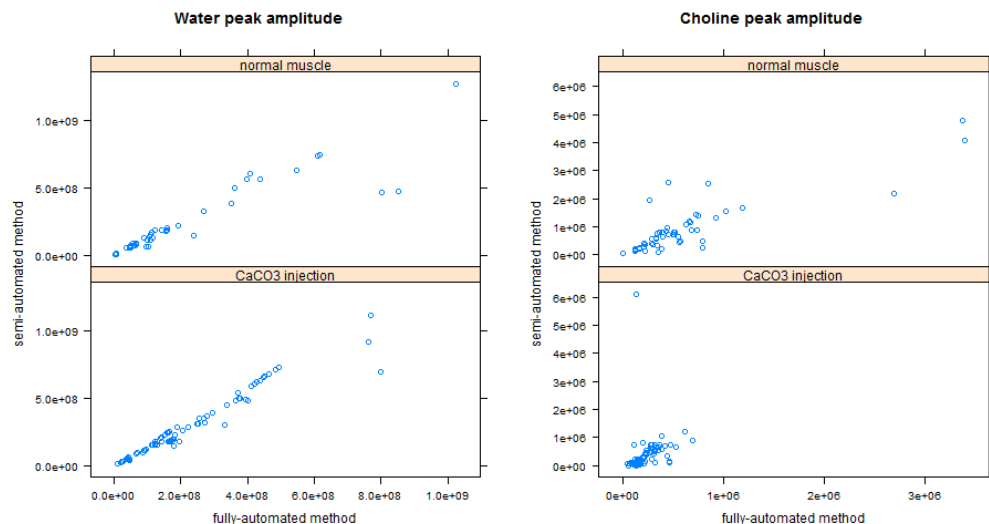


Fig. 3 - Graphic demonstrating the correlation of the measured amplitudes the water and choline peaks in normal muscle and in muscle after injection of CaCO_3 of all the spectra studied using the semi- and fully-automated post-processing methods. Note the good correlation of the results of both methods especially for the water peak. The R^2 values were 0.95 for the water peak and 0.75 for the choline peak.

Results

A total of 147 spectra from 10 different voxel locations were analyzed. 7 voxels were positioned at the quadriceps muscle (4 at the vastus lateralis and 3 at the vastus medialis) and 3 voxels were positioned at the hamstring muscles one at the biceps femoris muscle and two at the semimembranous muscle). The quality of these spectra based on the LNWH and the water suppression level was considered good for all anatomic locations. LNWH varied from 13 to 28 Hz (mean 19.3 Hz) and the water suppression level varied from 79 to 96% (mean 92.7%). The pH in the specimen was acidic (roughly 6). Temperature varied from 17-18 °C at the center of the slab and remained constant (18 °C) at its external surface. CT images confirmed the presence of calcium with an

even distribution in the ROI zones. The analysis of CT images has demonstrated that after injection the calcium deposition tended to follow the orientation of the muscle fibers (path of least resistance) (Fig. 2).

There was a good agreement in the amplitude measurements obtained with both methods of spectral analysis, with the exception of six spectra (standardized residuals). The percentage of variance (R^2) between the two processes was 95% for the water peak and 75% for the choline peak (Fig. 3). In 2 muscle locations 4 spectra were acquired before any injection at different times. In these spectra the mean variation coefficient for water and choline peak estimation was 23.1% and of 18.8% with semi-automated and 9.7% and 8.2% with the fully-automated spectral analysis.

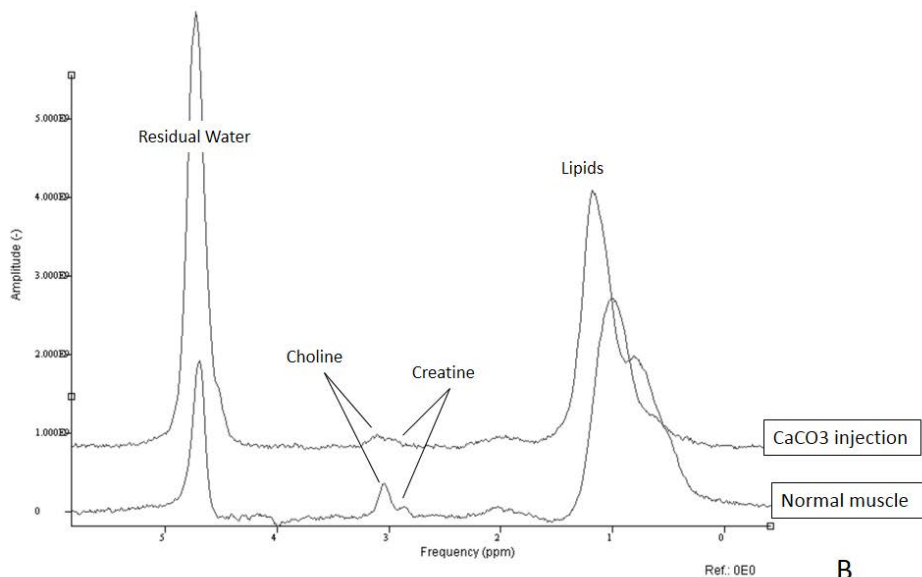
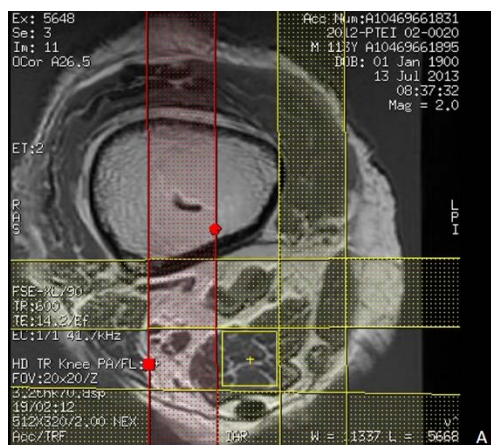


Fig. 4 – Axial T1 weighted MR image of the distal thigh of an 86 year-old male cadaveric specimen showing the positioning of the spectroscopy voxel at the semimembranous muscle (yellow square). Saturation bands were placed adjacent to the voxel boundaries (dotted bands in red and yellow). B) ^1H MR water-suppressed spectra acquired with a TE of 144 ms from the voxel shown in A) before (normal muscle) and after calcium injection (CaCO_3 injection). The water, choline compound, creatine and lipids peaks are identified. There is a noticeable reduction in the amplitude of the choline peak after calcium injection. Note also the artificial increase in the residual water peak

19 Spectra from 9 anatomic regions before any injection were available. Water and choline peaks were identified in all normal muscle voxel locations. The mean amplitudes of water and choline peaks in these muscle regions were $1.21\text{E}+08 \pm 4.92\text{E}+08$, $9.33\text{E}+05 \pm 3.50\text{E}+05$ arb. unit. In the two muscle locations that were evaluated with a 4-week interval the choline peak was similar (variation less than 3%): $1.13\text{E}+06$ arb. unit and $1.16\text{E}+06$ arb. unit for voxel 1 and $1.15\text{E}+06$ and $1.12\text{E}+06$ arb. unit for voxel 2. The water and choline T2 estimation on normal muscle based on 3 voxel locations were 54.8 and 129 milliseconds. The mean normal muscle choline concentration was 4.20 ± 1.95 mmol/L.

10 ml of pure non-ionic water was injected in 3 different muscle regions in order to provide a basis for the analysis of the CaCO_3 influence. The mean choline peak amplitude in these regions before and after pure water injection was $1.13\text{E}+06 \pm 4.74\text{E}+05$ arb. unit and $1.01\text{E}+06 \pm 8.23\text{E}+05$ arb. unit with the semi-automated analysis. The variation coefficient of the choline peak amplitudes after pure water injection was 10%. These differences were not statistically significant ($p = 0.9610$). The mean choline concentration in these voxels before and after pure water injection was 3.95 ± 1.84 mmol/L and 3.58 ± 3.01 mmol/L. In light of these results the choline concentration in a given muscle region was considered to be constant before and after injection.

43 spectra from a total of 8 voxel locations pre and post CaCO_3 injection were available. The mean choline amplitude before and after CaCO_3 injection was $9.72\text{E}+05 \pm 3.14\text{E}+05$ arb. unit and $5.52\text{E}+05 \pm 2.03\text{E}+05$ arb. unit. The mean reduction in the choline peak amplitude after CaCO_3 injection was 43.1% (Fig. 4). These differences were statistically significant ($p = 0.0002$). The mean choline concentration in these voxels before and after CaCO_3 injection was significantly different: 3.53 ± 1.72 mmol/L and 1.58 ± 0.63 mmol/L ($p = 0.0036$). The degree of

underestimation of the choline peak amplitude after injection was related to the tissue concentration of CaCO_3 . In the three voxels of the multiple injection protocol there was a progressive decrease in the choline amplitude estimation inversely proportional to the tissue CaCO_3 concentration (Fig. 5).

Six pairs of spectra of the same anatomic region with different slab positions were available (2 before injection, 1 after injection of water only and 1 after injection of CaCO_3). The visual spectral quality was better when muscle fiber orientation was parallel to B_0 (alternative position). In these spectra the water, choline and creatine peaks were narrower and differentiation between the choline and creatine peaks was easier (Fig. 6). There was a significant position-dependent difference in the estimation of the choline peak amplitude ($p < 0.0154$). This position-dependent variation in the choline estimation was higher when CaCO_3 was injected. The mean variation coefficient of the choline peak amplitude was 17.7% before calcium injection and 53.2% after, however these differences were not statistically significant ($p > 0.33$). On the other hand with the fully-automated method the position related differences in the choline peak amplitude were only significant when CaCO_3 was injected ($p = 0.0067$ and 0.1855 with and without CaCO_3 injection respectively).

The standard errors, confidence intervals and the p values for the comparisons of the choline amplitude with respect to the injections (water and CaCO_3) and the phantom orientation with both analysis methods are presented in table 1.

Phase mapping demonstrated that similar to vascular calcifications ($\frac{\Delta B_0}{B_0} = 0.07 \pm 0.58$ ppm), CaCO_3 injection ($\frac{\Delta B_0}{B_0} = 0.57 \pm 0.17$ ppm) lead to an increase in field inhomogeneities. Field inhomogeneities in these areas were more pronounced than in the normal muscle ($\frac{\Delta B_0}{B_0} = 0.16 \pm 0.05$ ppm) and water-only injection ($\frac{\Delta B_0}{B_0} = 0.11 \pm 0.04$ ppm) (Fig. 7). The nominal values of field inhomogeneities adjacent to areas containing calcium were around 0.5ppm.

Discussion

When compared to pure water only the injection of a CaCO_3 suspension lead to a significant underestimation of the amplitude of choline peaks of the thigh muscles ($p < 0.0002$). In the presence of CaCO_3 the choline peak areas were roughly 40% smaller than in the measurements before injection. Additionally the influence of CaCO_3 on the choline peak underestimation was proportional to its concentration inside the voxel. These results suggest that the evaluation of choline compounds on ^1H MR spectroscopy of tumors might be influenced by the presence and the amount of intra-lesional calcification. Such an underestimation might lead to errors not only in the characterization of calcified tumors but also in

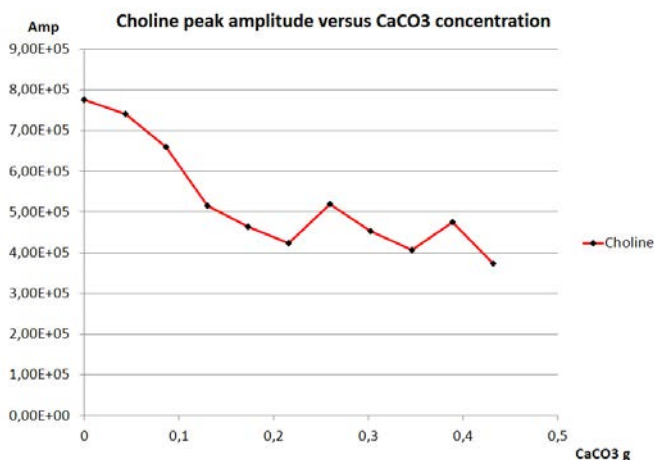


Fig. 5 – Graphic correlating the amplitude (arbitrary units) of the choline compounds peak and the tissue concentration of CaCO_3 in the biceps femoris muscle of a 80 year-old cadaveric specimen. The underestimation of the choline peak progressively decreases as the concentration of CaCO_3 increases.

the post treatment follow-up, since calcification may appear after radio, chemo

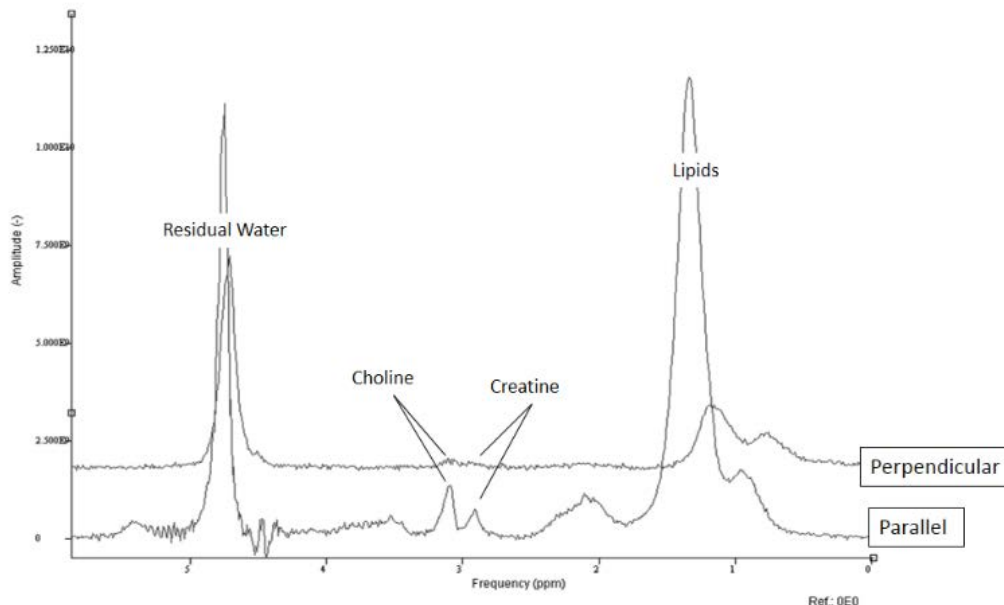


Fig. 6 – 1H MR water-suppressed spectra (TE of 144 ms) of the semi-membranous muscle of a 80 year-old female specimen after CaCO₃ injection acquired with the long axis of the muscle fibers perpendicular and parallel to B₀. A noticeable position dependent change in the spectral profile. When the calcium particles were preferentially dispersed perpendicular to B₀ there is a drop in the estimation of the choline peak amplitude. Profile changes are equally perceptible in the other frequencies of the spectra.

The semi-automated method used (AMARES) does not use any prior knowledge of peak relations and the operator manually chose the peak to be quantified. On the other hand with the fully-automated method peaks were selected automatically based on a 1H MR spectroscopic data base of multiple metabolites. The fact that the amplitude measurements acquired with these two different methods were comparable helps support and validate the presented results. Additionally, this dual verification makes the possibility of estimation bias due to systematic fitting variations unlikely. There is no consensus in the literature on

which one is the best method for spectral analysis and both have been used with success for the evaluation of tumors in clinical practice²³⁻²⁶. Furthermore, Hardman et al. have demonstrated profile changes in prostate spectra in the presence of calcifications¹¹. Similar spectral anomalies were seen after CaCO₃ injection on muscle. Since the real concentration of choline was not altered by the injections, these profile changes probably explain the underestimation of the choline peaks in the presence of calcium.

Table 1 - Standard errors, confidence intervals and the p values for the comparisons of the choline amplitude with respect to various instrumental variables analyzed.

	Jmru					Sci- MRS-Lab				
	estimate	Std error	CI 2.5%	CI 97.5%	p	estimate	Std error	CI 2.5%	CI 97.5%	p
water only injection	0,0676	0,5901	-66,72	244,01	0,9089	-0,3183	0,2833	-58,48	27,43	0,2633
CaCO₃ injection	-1,0153	0,2715	-78,83	-37,99	0,0003	-0,7983	0,1304	-65,23	-41,74	< 0.0001
position (no injection)	-0,7208	0,794	-89,9	134,08	0,3657	0,5075	0,3812	-21,88	253,22	0,1855
Position (CaCO₃)	0,3525	0,3637	-30,74	192,22	0,3342	0,4811	0,1746	14,51	128,57	0,0067

Std = Standard

CI = Confidence interval

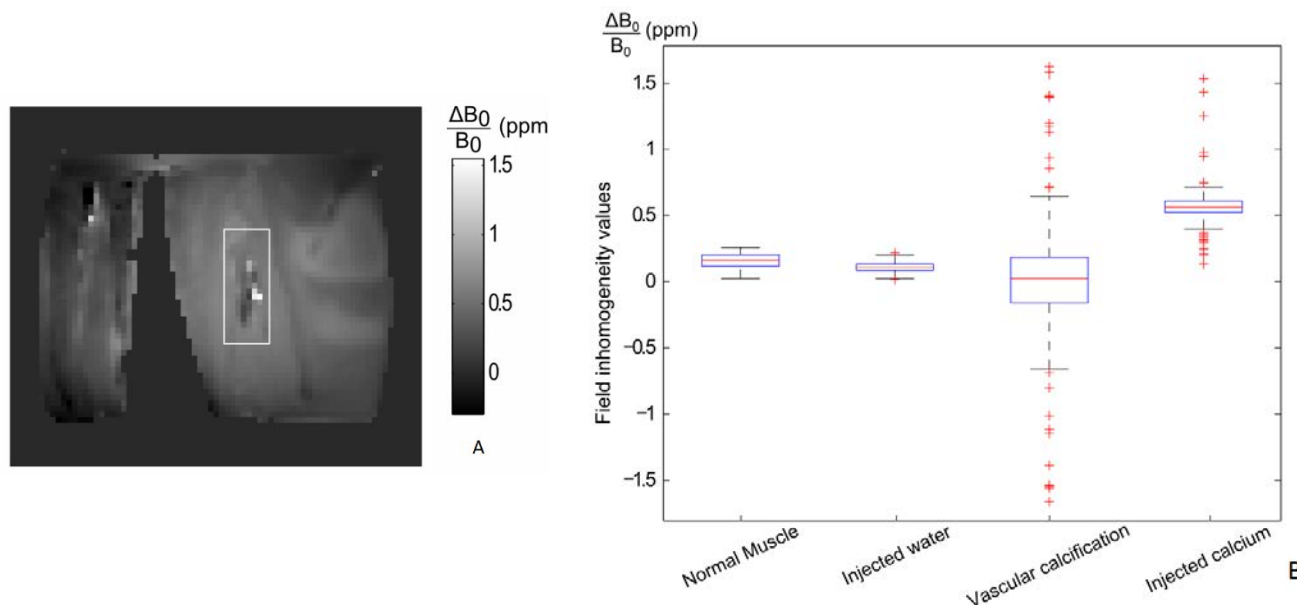


Fig. 7 – A) B_0 map demonstration of the field inhomogeneities adjacent to injected CaCO_3 (white square). B) Boxplot representation of the magnetic field inhomogeneities in areas of normal muscle, water-only injection, vascular calcifications and CaCO_3 injection based on B_0 mapping data. Note that the variation in pixel frequencies is larger in areas of vascular calcification and calcium injection. It is worthy of notice that a few phase wraps remained around the areas of vascular calcification and CaCO_3 injection. These anomalies account for some of the outliers present in the graph.

The relation between the tissue architecture and the main magnetic field direction influenced the profile of the ^1H MR spectra acquired. There was a significant change in the choline peak amplitude related with the phantom position with respect to B_0 ($p < 0.0001$). Changes in tissue structure are responsible for spectral profile differences, which might have an influence on the estimation of the choline peak amplitude. This effect is related to an orientation dependent bipolar splitting phenomena which leads to changes in the profile of the muscular metabolite peaks²⁷. Such effects will probably exist in tumors with an organized cellular structure or that infiltrate tissues with a preferential orientation with respect to the magnetic field.

Tumor and peri-tumor calcifications are frequent finding and may present varied morphology. The morphology of these calcifications is usually related to tissue architecture and assumes different aspects on the different organs and systems^{28–31}. The distribution of CaCO_3 in the phantom had a preferential geometrical distribution that followed the orientation of the muscle fibers (path of least resistance). The effects of calcium on the choline peak estimations were also influenced by its distribution. In the presence of calcium, the variation in the choline peak amplitude estimations with different phantom position was higher when compared to muscle with no injection or water-only injections. However, this effect was only significant with the fully automated spectral analysis. We hypothesize that the higher order curve fitting employed in the fully automated analysis allowed to identify the calcium related profile anomalies of the spectra better than the semi-automated method.

As suggested by various authors the presence of calcium generated measurable magnetic field inhomogeneities^{8,9}. CaCO_3 injections lead to a disturbance in field homogeneity that was similar to that caused by vascular calcifications. In addition to changes in the spectral profile calcium related magnetic susceptibility may lead to a reduction on the T2 relaxation times around calcium crystals through a T2* effect³². Water and choline T2 relaxation times are important factors in the estimation of choline concentration based on the internal water peak. Further studies are necessary to characterize the influence of calcium-related field inhomogeneities on the choline concentration estimations. Due to an orientation dependent underestimation of the choline peak, the presence of calcium had a significant impact on concentration estimation. There was a mean 55% drop in the choline concentration estimations of the same anatomic region after calcium injection. In addition to this effect, the presence of calcium will likely have an influence on the T2 relaxation of water and choline, which in turn could alter choline concentration estimates in calcified tissues. These results indicate that choline concentration estimates in calcified lesions should be interpreted with caution since gross errors may be originated by the presence of calcium compounds. Additionally, since the effects of calcium are not only dependent on its concentration, the determination of a correction factor for choline peak amplitude is difficult.

This work has several limitations. First and most importantly, calcium carbonate was introduced into the phantom in a non-physiologic manner. The injection of pure water and water-calcium suspension lead to instrumental spectral perturbations, which interfered with curve fitting for

metabolite peak estimations. However, the variations in the amplitude measurements were statistically significant and both types of spectral analysis produced similar results on the calcium influence of choline peak amplitude estimations, which strengthen the validity of our findings. CaCO_3 is not the predominant form of calcium present on mineralized human tissue. Various calcium compounds of higher complexity are present in calcified tissue. Calcium carbonate shares with various other calcium compounds similar biochemical and electromagnetic properties which may reflect the influence of more complex crystals on ^1H MR spectroscopic measurements^{16,17}. On the lack of a better option, non-ionic water was used as a carrier for CaCO_3 particles. This external water input lead to an increase in tissue water concentration, which precluded the use of water peak measurements after injection on the analysis. Additionally the increase in free interstitial water interfered with T2 measurement of water and choline after calcium injection.

In conclusion, although further studies are necessary to evaluate the influence of calcium particles on in vivo MR spectroscopy, quantitative analysis of calcified tumor spectra should be interpreted with caution. The quantitative evaluation of choline (peak amplitude and concentration) was significantly disturbed by the presence of CaCO_3 , which lead to an underestimation of the choline peak amplitude of the thigh muscles. Such anomalies might lead to diagnostic errors based on misinterpretations of MR spectra. The influence of calcium is likely related magnetic susceptibility effects, which leads to profile changes in the spectra disturbing spectral fitting. These anomalies are not only related to the concentration of calcium but also to the geometric orientation of the calcium particles with respect to the main magnetic field, which precluded the determination of a correction factor.

Acknowledgments

This work was supported by the French Society of Radiology (SFR- Société Française de Radiologie) through a research grant. The authors wish to thank FEDER and Region Lorraine for their support on this research.

Bibliography

1. Sabatier J, Gilard V, Malet-Martino M, et al. Characterization of choline compounds with in vitro ^1H magnetic resonance spectroscopy for the discrimination of primary brain tumors. *Invest. Radiol.* 1999;34(3):230–235.
2. Baltzer PAT, Dietzel M. Breast lesions: diagnosis by using proton MR spectroscopy at 1.5 and 3.0 T--systematic review and meta-analysis. *Radiology.* 2013;267(3):735–746.
3. Boonsirikamchai P, Choi S, Frank SJ, et al. MR imaging of prostate cancer in radiation oncology: what radiologists need to know. *Radiogr. Rev. Publ. Radiol. Soc. North Am. Inc.* 2013;33(3):741–761.

4. Fayad LM, Barker PB, Jacobs MA, et al. Characterization of musculoskeletal lesions on 3-T proton MR spectroscopy. *AJR Am. J. Roentgenol.* 2007;188(6):1513–1520.
5. Wehrl HF, Schwab J, Hasenbach K, et al. Multimodal elucidation of choline metabolism in a murine glioma model using magnetic resonance spectroscopy and ^{11}C -choline positron emission tomography. *Cancer Res.* 2013;73(5):1470–1480.
6. Russo F, Mazzetti S, Grignani G, et al. In vivo characterisation of soft tissue tumours by 1.5-T proton MR spectroscopy. *Eur. Radiol.* 2012;22(5):1131–1139.
7. Fayad LM, Wang X, Salibi N, et al. A feasibility study of quantitative molecular characterization of musculoskeletal lesions by proton MR spectroscopy at 3 T. *AJR Am. J. Roentgenol.* 2010;195(1):W69–75.
8. Wang C-K, Li C-W, Hsieh T-J, et al. In vivo ^1H MRS for musculoskeletal lesion characterization: which factors affect diagnostic accuracy? *NMR Biomed.* 2012;25(2):359–368.
9. Fayad LM, Bluemke DA, McCarthy EF, et al. Musculoskeletal tumors: use of proton MR spectroscopic imaging for characterization. *J. Magn. Reson. Imaging JMRI.* 2006;23(1):23–28.
10. Chen Y, Cai S, Cai C, et al. High-resolution NMR spectroscopy in inhomogeneous fields via Hadamard-encoded intermolecular double-quantum coherences. *NMR Biomed.* 2012;25(9):1088–1094.
11. Hardman RL, El-Merhi F, Jung AJ, et al. Fast T2*-weighted MRI of the prostate at 3 Tesla. *J. Magn. Reson. Imaging JMRI.* 2011;33(4):902–907.
12. Fayad LM, Salibi N, Wang X, et al. Quantification of muscle choline concentrations by proton MR spectroscopy at 3 T: technical feasibility. *AJR Am. J. Roentgenol.* 2010;194(1):W73–79.
13. Brodziaak-Dopierała B, Kowol J, Kwapuliński J, et al. Lead and calcium content in the human hip joint. *Biol. Trace Elem. Res.* 2011;144(1-3):6–16.
14. Combes C, Rey C. Amorphous calcium phosphates: synthesis, properties and uses in biomaterials. *Acta Biomater.* 2010;6(9):3362–3378.
15. Rey C, Combes C, Drouet C, et al. Bone mineral: update on chemical composition and structure. *Osteoporos. Int. J. Establ. Result Coop. Eur. Found. Osteoporos. Natl. Osteoporos. Found. USA.* 2009;20(6):1013–1021.
16. Hopkins JA, Wehrli FW. Magnetic susceptibility measurement of insoluble solids by NMR: magnetic susceptibility of bone. *Magn. Reson. Med. Off. J. Soc. Magn. Reson. Med. Soc. Magn. Reson. Med.* 1997;37(4):494–500.
17. Kumar M, Gupta R. Diamagnetic bulk susceptibility data of $\text{C}_{14}\text{H}_{11}\text{BrN}_2\text{O}_3\text{S}$. In: Gupta RR, ed. *Diamagnetic Susceptibility of Organic Compounds, Oils, Paraffins and Polyethylenes*. Vol 27B. Berlin, Heidelberg: Springer Berlin Heidelberg; 2008:3237–3238. Available at: http://www.springermaterials.com/docs/info/978-3-540-45860-9_1879.ris. Accessed August 15, 2013.
18. Larsen RM. Lanczos bidiagonalization with partial reorthogonalization. 1998.

19. Provencher SW. Estimation of metabolite concentrations from localized in vivo proton NMR spectra. *Magn. Reson. Med. Off. J. Soc. Magn. Reson. Med. Soc. Magn. Reson. Med.* 1993;30(6):672–679.
20. Klose U. In vivo proton spectroscopy in presence of eddy currents. *Magn. Reson. Med. Off. J. Soc. Magn. Reson. Med. Soc. Magn. Reson. Med.* 1990;14(1):26–30.
21. Plzak J, Kalitova P, Urbanova M, et al. Subcutaneous calcification in the pectoralis major flap: a late complication of radiotherapy. *Br. J. Radiol.* 2011;84(1007):e221–223.
22. Kennedy GA, Restall J, Morris K, et al. Post-therapy calcification can result in false-positive fluorodeoxyglucose positron emission tomography scans in patients with non-Hodgkin's lymphoma. *Leuk. Lymphoma.* 2010;51(2):348–349.
23. Baik H-M, Su M-Y, Yu H, et al. Quantification of choline-containing compounds in malignant breast tumors by ¹H MR spectroscopy using water as an internal reference at 1.5 T. *Magma New York N.* 2006;19(2):96–104.
24. Lee CW, Lee J-H, Kim DH, et al. Proton magnetic resonance spectroscopy of musculoskeletal lesions at 3 T with metabolite quantification. *Clin. Imaging.* 2010;34(1):47–52.
25. Helms G. The principles of quantification applied to in vivo proton MR spectroscopy. *Eur. J. Radiol.* 2008;67(2):218–229.
26. J M Constans et al. Effects of reactive oxygen species on metabolism monitored by longitudinal ¹H single voxel MRS follow-up in patients with mitochondrial disease or cerebral tumors. In: *J. Phys.* Vol 261 012011.; 2011.
27. Vermathen P, Boesch C, Kreis R. Mapping fiber orientation in human muscle by proton MR spectroscopic imaging. *Magn. Reson. Med. Off. J. Soc. Magn. Reson. Med. Soc. Magn. Reson. Med.* 2003;49(3):424–432.
28. Suh JH, Gardner JM, Kee KH, et al. Calcifications in prostate and ejaculatory system: a study on 298 consecutive whole mount sections of prostate from radical prostatectomy or cystoprostatectomy specimens. *Ann. Diagn. Pathol.* 2008;12(3):165–170.
29. Tse GM, Tan P-H, Pang ALM, et al. Calcification in breast lesions: pathologists' perspective. *J. Clin. Pathol.* 2008;61(2):145–151.
30. Resnick D. *Diagnosis of bone and joint disorders.* Saunders; 2002.
31. Tanaka Y, Takeuchi K, Maeda T. [Calcification in gliomas: first report with special reference to roentgenological calcification (author's transl)]. *No Shinkei Geka.* 1975;3(3):219–225.
32. Brown MA, Semelka RC. *MRI: Basic Principles and Applications.* John Wiley & Sons; 2011.

Discussion et conclusions :

Les résultats présentés sur la perfusion, la diffusion et la spectroscopie du proton en IRM, contribuent à mieux comprendre les particularités et les performances de ces techniques appliquées à des scénarios cliniques courants de la radiologie ostéo-articulaire oncologique.

L'IRM de perfusion s'est avérée être une méthode performante pour le diagnostic précoce des récidives d'ostéome ostéoïde avec plus de 90% de sensibilité, spécificité. Les données sur la perfusion quantitative des masses ostéo-articulaires sont encore rares dans la littérature. Les paramètres perfusionnels quantitatifs des ostéomes ostéoïdes décrits sont importants pour établir une base de comparaison pour de futures études sur la perfusion des tumeurs ostéo-articulaires. Malgré ces résultats encourageants, nous sommes encore loin d'une uniformisation des données perfusionnelles quantitatives. Il n'existe pas de consensus sur le modèle mathématique pour le calcul des paramètres quantitatifs, ni sur le logiciel de post traitement à utiliser. Ces facteurs sont encore des barrières importantes pour la comparaison des données perfusionnelles quantitatives. Beaucoup de travail est encore nécessaire pour établir les paramètres de post traitement optimaux.

L'imagerie classique manque de spécificité pour caractériser les masses des parties molles non graisseuses. Il existe une grande similitude entre l'aspect morphologique des lésions bénignes et malignes dans ce sous-groupe des tumeurs ostéo-articulaires. La plupart des tumeurs des parties molles non graisseuses, quelle que soit leur agressivité, est hypo-intenses en pondération T1 et hyper-intenses en pondération T2. Les résultats présentés dans le domaine de la diffusion permettent d'avancer dans l'étude des tumeurs des parties molles et aident à définir les bases pour l'utilisation des valeurs ADC en pratique courante. Les résultats ont montré une bonne performance de la diffusion pour l'évaluation des lésions hyper-intenses sur les séquences pondérées T2. Par contre, l'IRM de diffusion n'as pas aidé dans la caractérisation des lésions hypo- ou iso-intenses en T2.

La spectro-IRM quantitative est encore difficile à appliquer en routine clinique. Les multiples expériences réalisées en environnement contrôlé montrent que cette technique est très sensible aux variations de l'homogénéité du champ magnétique et à la structure du tissu étudié. La présence de cristaux de calcium entraîne une réduction de l'amplitude du pic de la choline et de la créatine, proportionnelle à la concentration du calcium. Cependant, les variations de profil du spectre, liées au rapport entre la morphologie et la distribution du calcium dans les tissus et la direction du champ magnétique principal, ont empêché la détermination d'un facteur de correction applicable en clinique.

CHAPITRE 2 – LA TOMODENSITOMETRIE

Le scanner utilise les données provenant de l'atténuation d'un faisceau de rayon X qui traverse le corps sur de multiples projections pour reconstruire une image de la structure interne de la zone d'intérêt. Malgré la haute performance de l'IRM pour l'étude des pathologies ostéo-articulaires, la TDM est encore largement utilisée. Actuellement plusieurs nouveaux modèles de scanner sont commercialisés (e.g. Double source, à capteurs plan, à large système de détection). Les scanners à large système de détection sont particulièrement adaptés à l'imagerie ostéo-articulaire car ils permettent l'étude des articulations entières en mode séquentiel avec un seul tour de l'ampoule à rayons X (Fig. 7). Par conséquent, le post traitement des données est facilité, car tous les voxels d'un volume quelconque sont acquis pratiquement en même temps et il n'y a pas d'interpolation entre les coupes en mode séquentiel.

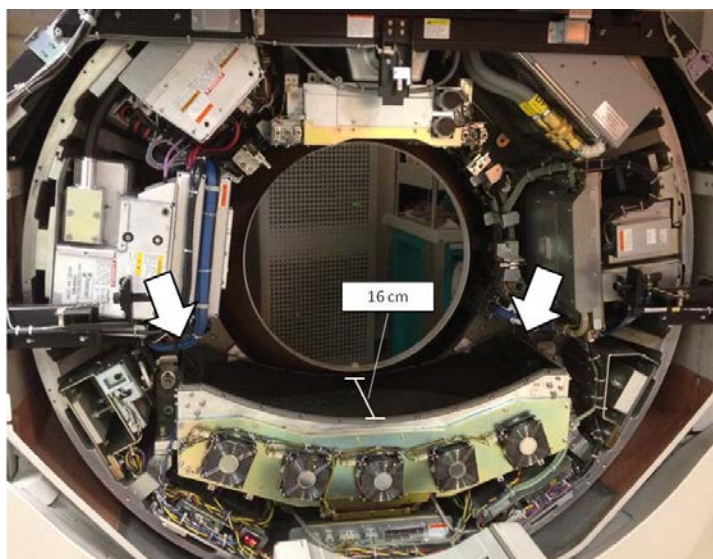


Fig. 7 : Scanner à large système de détection. Les détecteurs sont identifiés par les flèches blanches.

Les radiologues et manipulateurs ont un rôle important dans la réduction de la dose. Des protocoles d'acquisition plus complexes exigent des mesures de radioprotection spécifiques qui doivent être connues et appliquées.

L'IRM est le gold standard pour l'évaluation perfusionnelle du système ostéo-articulaire. La TDM de perfusion est moins sensible aux variations de concentration du produit de contraste, et reste une source d'irradiation. Néanmoins la TDM de perfusion présente certains avantages. La densité en unités de hounsfield (UH) est directement proportionnelle à la concentration du produit de contraste tissulaire, ce qui facilite l'analyse et la fiabilité du post-traitement des

L'irradiation liée à la TDM a augmenté significativement la dose délivrée aux patients lors de la prise en charge médicale (32). De ce fait, l'application de techniques d'imagerie avancées en scanner a été longtemps limitée. D'importantes avancées technologiques ont contribué à changer cette situation. C'est le cas de la reconstruction itérative, et des systèmes de détection plus larges et de haute sensibilité qui ont contribué à une réduction massive de l'irradiation délivrée tout en gardant une qualité d'image optimale. En plus de l'appareillage, les

données perfusionnelles (33). Le scanner offre, en plus, une haute résolution temporelle (jusqu'à 200 ms par volume), indépendante de la résolution spatiale et est moins susceptible aux artefacts que l'IRM. La littérature manque d'études permettant une comparaison de la performance de ces deux techniques dans l'évaluation des tumeurs ostéo-articulaires.

Les lésions osseuses non-lytiques ou densément calcifiées sont un obstacle important à l'application de la perfusion en TDM à l'imagerie ostéo-articulaire. Les techniques classiques de soustraction osseuse sont basées sur la densité et la disposition anatomique de l'os, empêchant l'analyse du rehaussement des lésions de densité calcique. La soustraction par masque en TDM, similaire à la soustraction osseuse utilisée en angiographie numérique (DSA), permet la visualisation du rehaussement des lésions osseuses non-lytiques ou calcifiées. La soustraction osseuse type DSA aide à la caractérisation tumorale dans la mesure où elle facilite la visualisation du rehaussement des lésions osseuses et permet l'identification de l'œdème osseux péri-lésionnel. La performance de la TDM avec la soustraction osseuse type DSA pour identifier l'œdème osseux péri-lésionnel n'est pas connue.

La TDM est également une méthode utilisée pour le suivi des patients traités chirurgicalement d'une tumeur ostéo-articulaire. Les implants métalliques, souvent utilisés dans les chirurgies de sauvetage des membres, sont à l'origine d'une dégradation significative de la qualité d'image en TDM. En plus de la dispersion du faisceau de rayons X, la présence de matériel métallique entraîne une importante atténuation de celui-ci (durcissement), ce qui crée des disparités entre le modèle mathématique utilisé pour reconstruire l'image et les données acquises par la machine (34,35). Les nouvelles techniques de réduction des artefacts métalliques, basées sur l'analyse des projections des données brutes (sinogramme) ont permis une amélioration significative de la qualité d'image scanographique en présence de matériels métalliques (36). Néanmoins l'impact de ces techniques sur l'évaluation des tissus péri-articulaires n'a pas encore été étudié.

Dose reduction in Musculoskeletal CT: Tips and Tricks

Alban Gervaise, Pedro A. Gondim Teixeira, Nicolas Villani, Sophie Lecocq, Matthias Louis, Alain Blum

Submitted to *Radiographics* on June 2013

ABSTRACT

Due to improvements in temporal and spatial resolution, and despite its radiating character, CT is still indicated for the assessment of many musculoskeletal disorders. New exploration techniques, such as dynamic CT of the joints and bone perfusion imaging, are now available in musculoskeletal imaging. However, they require the repetition of many acquisition phases which lead to an increase in dose. For these new applications and for spine and proximal joint imaging in the vicinity of radiosensitive organs, optimization and dose reduction are critical.

In this pictorial essay, we discuss several dose optimization and reduction options, relying on behavioral and technical factors. Among them, tube current and tube potential optimization are still critical and must be adapted to the type of exploration and the body habitus of each patient. Recent technical improvements can also help to reduce the doses like automatic tube current modulation, active collimation or new CT iterative reconstructions. Although these technical improvements allow for an important dose reduction, behavioral factors such as respecting the indications and limiting scan coverage remain essential. Finally, we will also indicate how to optimize and reduce the doses in specific techniques applied to musculoskeletal imaging, such as dynamic CT, bone and soft tissue perfusion CT.

Summary statement:

This pictorial essay reviews the different methods available for optimizing and/or reducing radiation dose in musculoskeletal CT, particularly under special conditions such as perfusion and dynamic CT.

RSNA Exhibit space numbers: LL-MKE4361, 2012 RSNA Annual Meeting

Awards: Certificate of Merit

A. Gervaise – Corresponding author
Medical Imaging Department, Legouest Military Instruction Hospital, 27 Avenue de Plantières, BP 90001, 57077 Metz Cedex 3, France
e-mail: alban.gervaise@hotmail.fr

P. Teixeira, S. Lecocq, M. Louis, A. Blum
Service d'Imagerie Guilloz, Hôpital Central, CHU-Nancy, 29 Av. Mar Lattre de Tassigny, 54000 Nancy, France.

N. Villani
Medical Radiophysics Unit, CRAN UMR 7039 CNRS, Centre Alexis Vautrin, Avenue de Bourgogne, 54511 Vandoeuvre-les-Nancy, France

Teaching points:

1. Respecting the clinical indications to a given CT study is essential.
2. The limitation of the scan coverage is a very simple way to reduce the dose.
3. A precise centering of the anatomical zone to be scanned at the isocenter of the CT gantry provides optimal image quality and delivered dose.
4. For vascular or perfusion examinations and CT-arthrography, it is better to use low kV.
5. The high natural contrast of bone structures allows low-dose acquisitions with considerable noise but with no affect on the interpretation.

INTRODUCTION

Since its introduction in the 1970s, computed tomography (CT) has played an important role in the diagnosis of musculoskeletal (MSK) disorders. It quickly became the method of choice for the diagnosis of traumatic, degenerative or developmental lesions. Although image quality is hindered by metallic artifacts, CT is still indicated in post-operative imaging (1-3). Today, CT is also widely used in interventional imaging (i.e., guided injection, biopsy, vertebroplasty, etc...) (4).

The diagnostic performance of CT is however limited by the low-contrast resolution, which leads to a poor analysis of soft tissues when compared with magnetic resonance imaging (MRI). The analysis of intra-articular lesions is also very difficult in the absence of intra-articular contrast. CT studies may also be an important source of ionizing radiation. This may help explain the prominent role of MRI in the evaluation of musculoskeletal disorders.

With multi-detector computed tomography (MDCT), wide-area detector systems and a significant reduction in radiation exposure, CT has regained some of its former importance in the evaluation of the musculoskeletal system. Spatial and temporal resolutions were considerably increased. Sub-millimetric isotropic acquisition allows multi-planar and volume rendering (VR) three-dimensional (3D) reformations, improving the diagnosis and pre operative planning of bone and soft tissues disorders (5). Improvements in temporal resolution limit motion artifacts especially in large-volume explorations, which are particularly suitable for the evaluation of polytraumatised patients with musculoskeletal injuries. Additionally, high temporal resolution allows dynamic imaging of joints. Techniques which had a limited clinical application, such as CT perfusion became increasingly available for musculoskeletal imaging. With CT perfusion, multiple and successive phases are acquired allowing an optimal analysis

of the contrast bolus passage providing a functional evaluation of bone and soft tissues tumors. Compared to MRI CT perfusion has the advantage of being technically easier to analyze and more reproducible (6). Other benefits of CT scanning include a lower cost, better availability, fewer contraindications, and the possibility to image post-operative or unstable patients (4,7).

After discussing the particularities of the musculoskeletal CT dose reduction, we will discuss in detail the various methods of dose reduction in the field of musculoskeletal imaging, with a special emphasis on both behavioral and technical factors.

WHY SHOULD THE DOSE BE REDUCED?

Dose reduction and optimization is important because CT is the largest source of medical radiation and some authors suggest that low-level radiation exposure due to CT-scans are associated with a potential risk for malignancy (8-9). Precautionary principle and the ALARA concept enforce that dose should be kept as low as possible, while maintaining an acceptable image quality.

WHEN TO APPLY DOSE REDUCTION TECHNIQUES?

All CT examinations should have an optimized dose depending on body regions scanned, clinical conditions and scanner characteristics. But dose reduction and optimization is crucial in some cases: for young patients (the potential risk of cancer is higher than for old patient); for exams performed near radiosensitive organs (i.e. lumbar spine, shoulder, hip CT); for perfusion and dynamic CT with acquisition of numerous phases; for pregnant women and for patients with chronic diseases requiring recurrent follow-ups.

WHAT ARE THE PARTICULARITIES OF THE DOSE REDUCTION IN MSK CT?



Fig. 1 - Wrist CT-scan for scaphoid fracture. The limitation of the scan coverage from 12 cm (a) to 6 cm (b) leads to a 50 % dose reduction.

Dose reduction in musculoskeletal CT has some particularities compared to chest or abdominopelvic CT. For example, substitution of the CT-scan by MRI or ultrasound is often possible. The CT-scan is also often limited to a single unenhanced phase. MSK CT is performed to evaluate different types of anatomical structures with different sizes (peripheral vs. proximal joints), at locations with different radio-sensitivity and tissue weighting coefficients. Many different types of CT based examinations ("standard"-CT, CT-arthrography, vascular examination, dynamic and perfusion CT) are available. Thus, the acquisition parameters are very different from one type of study to the other (for example, tube voltage setting ranges from 80 kV for a peripheral joint to 120 or 140 kV for the spine) and the doses are also very diverse and can vary by a factor of 1 to 1000! (for example, a low-dose wrist CT with an effective dose of 0.014 mSv VS. a standard-dose lumbar spine CT with an effective dose of 14 mSv). Tissue weighting coefficients (k) are also very different from one anatomic region to the other (for example, the lumbar spine has a k of 11.2 [quite similar to the abdomen] and the wrist has a k of only 0.22). In anatomic areas like spine, pelvic and shoulder girdles, the k factors are high and for these regions, dose reduction and optimization is paramount.

HOW TO REDUCE THE DOSE?

The rationale for CT dose reduction arises from the three bases of radioprotection: justification, optimization and substitution) (10). These bases have notably been grouped in the precautionary principle ALARA (As Low As Reasonably Achievable). The ALARA principle has been widely and repetitively discussed in the literature (7, 11-14). We are going to approach each of these bases successively demonstrating their behavioral implications, technological fundamentals and focusing on their application in musculoskeletal CT.

BEHAVIORAL FACTORS

Awareness and education. The level of education and awareness among radiologists and technologists are important elements in the process of dose reduction. For example, Wallace et al (15) showed that after educating a physician in dose reduction techniques, it was possible to reduce, by 29 %, the lumbar spine CT doses used within several institutions. This education also emphasizes the situations in which the reduction in the dose is especially important. The awareness of radiologists is also increasingly guaranteed by the software used in the gathering and analysis of the doses delivered. This kind of software allows for dosimetric monitoring per patient and detects the cumulate dose, which is sometimes high. The software also includes dosimetric warnings that help optimize the protocols and help monitor the overall reduction in the doses during optimization [16, 17]

Justification and substitution. [TP] Respecting the clinical indications to a given CT study is essential. Substitution is also important, particularly in musculoskeletal CT, because alternative imaging methods that do not deploy ionizing radiation, such as ultrasound or MRI are often available (4, 7, 18). For example, Oikarinen et al (19) showed that out of 30 lumbar spine CT scans performed on patients younger than 35 years in only seven (23 %) of them the indication could be justified. Among these studies, 20 could have been replaced by MRI, and three patients needed no imaging at all. Clarke et al (20) also showed that 90 % of lumbar spine CT scans could have been replaced by MRI.

Scan coverage. [TP] The limitation of the scan coverage is a very simple way to reduce the dose in some CT studies (21): "The smaller the exposed area, the smaller the dose". The CT-scan coverage must be limited to the zone of interest, previously identified in the scout views (Fig 1).

Number of phases. The CT-scan dose can also be mastered by reducing the number of acquisitions (i.e., phases). In musculoskeletal CT, most examinations consist of a single-phase unenhanced acquisition. But, one should be careful with multiple phases exams performed during some procedures and techniques: interventional CT, perfusion CT or dynamic CT. If it's not possible to reduce the number of phases, one should try to reduce the dose of these phases by a limitation of the scan coverage or by lowering the delivered dose (Fig 2).

Position and centering. [TP] A precise centering of the anatomical zone to be scanned at the isocenter of the CT gantry provides optimal image quality and delivered dose because more interpolations of the data are performed in the center of the gantry than in its periphery (22) (Fig 3). The width of the scanned volume should also be as narrow as possible to limit scattered radiation and beam-hardening artifacts. For examples, shoulder girdles should be placed on different levels when exploring the shoulder and for elbow CT, arm should not be placed in the axial plane to avoid beam-hardening artifact (Table 1). During acquisitions

on the lower limb, the contra-lateral limb should be flexed out of the scanning field when possible (Fig 4). Additionally peripheral joints should be scanner as far as possible from the trunk of the patient in order to decrease the dose received in radiosensitive organs (Fig 5). Some CT-scan allows a lateral shift of the table to center the peripheral joints. For some special condition, a good position of the joint (i.e. neutral rotation or extern rotation for shoulder CT-arthrography) also allows to avoid multiple acquisitions.

TECHNICAL FACTORS

Scan modes. While the spread of MDCT the helical mode lead to a replacement of the sequential mode, the development of area-detector CT-scanners lead to its come back. For example, 320-detector row CT scanners now allow the acquisition of a 16 cm volume, covering the entire length of most joints with a single tube rotation (i.e. shoulder, wrist and hand, hip, sacroiliac, knee, ankle and foot). With this volume acquisition mode it is possible to reduce considerably the acquisition time and the motion artifacts. It also allows a reduction of the dose by suppressing overranging which is characteristic of the helical mode (23). Thus, when evaluating small parts with a 16- or 64-detector row CT, sequential or step-and-shoot acquisition mode should be used (11, 24).

Tube potential. Reduction of the tube kilovoltage (kV) accounts for an important dose reduction but it is also responsible for increase in image noise (25). In practice, the increase in noise is not detrimental to the analysis of bone structure, thanks to its high natural contrast. It is therefore possible to image peripheral joints with 80 kV (Fig 6-7). For large proximal joints (i.e., shoulder, hip, sacroiliac, spine), the kV must be adapted to the body habitus of the patients: 120 kV for a standard patient, 100 kV for thin patients and 135-140 kV for patients with excess weight to maintain adequate image quality. Because the attenuation value of the iodine is better with low kV, **[TP] for vascular or perfusion examinations and CT-arthrography, it is better to use low kV** (maximal kV of 100-120) (Fig 8). For example, for CT-arthrography of peripheral joint, kV should be set at 80 kV and for proximal joint arthrography (i.e. hip and shoulder CT-arthrography) kV should be set at 100 kV.

Tube current and mAs. The reduction in mA causes a proportional decrease of the dose but also an increase in image noise (when the radiation dose decreases by $1/c$, the image noise increases by the square root of c). This can be deleterious to the interpretation of the examinations which require a good contrast-to-noise ratio, as in the case for discoradicular pathologies (26). But **[TP] the high natural contrast of bone structures allows low-dose acquisitions with considerable noise but with no affect on the interpretation** (Fig 6-7).

Pitch. With some current MDCT scanners using the concept of effective mAs (mAs/pitch), pitch modification has no influence on the dose because it is automatically adapted

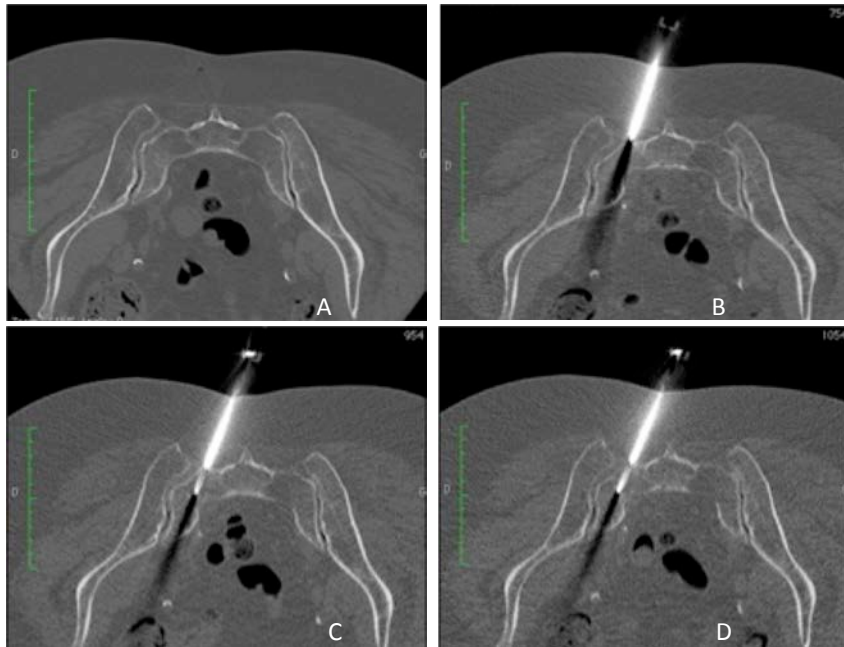


Fig. 2 -Sacral biopsy with progressive tube current decreasing for control acquisitions. The initial acquisition was acquired with standard parameters (a: 300 mA with CTDI = 29 mGy). The good CNR at the bone structures allows an important reduction of mA without impairing adequate needle guidance (b: 100 mA with CTDI = 14.7 mGy; c: 50 mA with CTDI = 7.4 mGy; d: 30 mA with CTDI = 4.5 mGy).

to the mA (27). As a general rule, the pitch factor should be adapted to the clinical conditions in order to avoid motion artifacts and to follow the contrast bolus during vascular studies. A high pitch, of about 1.5, is preferred to reduce the acquisition time and motion artifacts (for example for the exploration of a poly-traumatized patient). The pitch should, however, remain lower than 2 to keep an optimal quality for multiplanar reformations and to avoid helical artifacts (11). In contrast, a small pitch is preferred to reduce metal hardware-related artifacts (28) (Fig 9).

Slice thickness. In general, acquisitions are performed with thin slices (0.5–1 mm) required for bone structure analysis and reconstructed in thicker slices (2-5 mm) for soft tissues analysis. Sub-millimetric slices improve spatial resolution, reduce partial volume effects and allow the reconstruction in a quasi-isotropic volume (29). On the other hand, thin slice acquisition can lead to an increase in image noise (30). So, whereas the acquisition is made in sub-millimetric

slices, the soft tissues analysis is performed on thick slices with a better signal-to-noise ratio (Fig 6).

Iterative reconstruction. The use of iterative reconstruction algorithms allows a considerable noise reduction (30 to 50 %) in comparison with standard Filtered Back Projection reconstructions (31, 32). Thanks to this noise reduction, it is possible to reduce dose while keeping an equivalent image quality. Whereas iterative reconstruction is particularly interesting to reduce the dose of examinations maintaining a good SNR (for example, lumbar spine CT), it is less useful in cases directed primarily to bone analysis, for example in search of a fracture. The high natural contrast of bone structures allows for low-dose acquisitions sometimes noisy, but with no affect on the interpretation. However, one of the main advantages of iterative reconstruction is the reduction of artifacts associated with beam hardening with FBP (33) (Fig 10). Iterative reconstruction is also very interesting for bone and soft tissue analysis when metal

Table 1. Tips and tricks on patient's positioning

Joint	Positioning
Shoulder	shoulder girdles should be placed on different levels
Elbow	Elbow should be positioning above the head and in complete flexion or extension to avoid beam-hardening artifact
Wrist and hand	Joint should be scanned as far as possible from the trunk of the patient and placed at the isocenter of the gantry
Hip	Hip should be placed as much as possible at the isocenter of the gantry
Knee, ankle and foot	Joint should be scanned as far as possible from the trunk of the patient and the contralateral limb should be flexed out

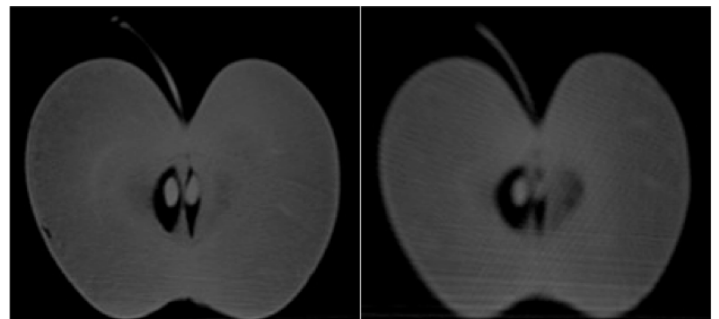


Fig. 3 - Example showing the image quality of an apple at the isocenter of the gantry (a) and at its periphery (b). Note the degradation of the image quality and the spatial resolution when the apple is not centered (b).

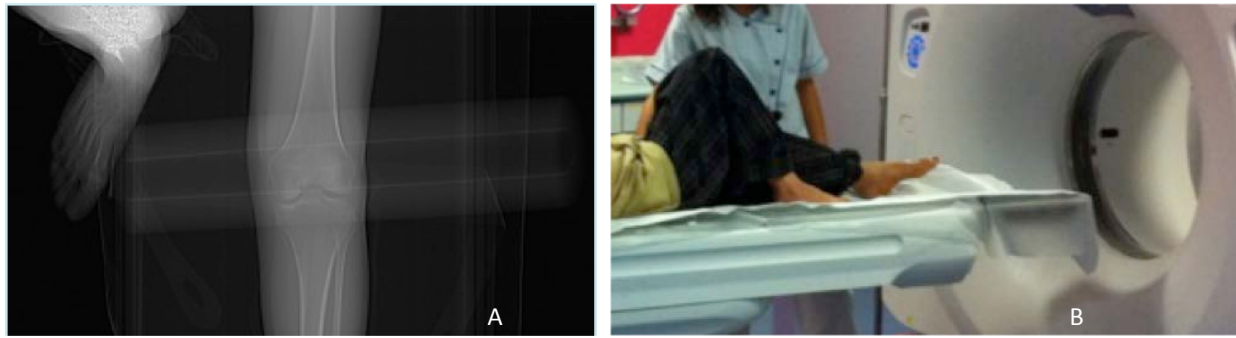


Fig. 4 - CT scan topogram before acquisition of a knee CT (a) and position of the patient during the acquisition (b). During acquisitions on the lower limb, the contralateral limb should be flexed out of the scanning field when possible to limit scattered radiation and beam-hardening artifacts.

hardware is present. Traditionally, a better visualization of metallic materials requires an increase of parameters such as the kVp, the mAs, as well as a low pitch and a thin collimation. All these parametric changes are a source of dose increase. Iterative reconstruction reduces the metal and streaks artifacts while keeping a low dose due to the optimization of the acquisition parameters.

Overranging shield. The overranging corresponds to an additional layer of tissue irradiated adjacent to the volume to be scanned because the reconstruction of the first and last slices requires data beyond the boundaries of this volume. The overranging is more significant with small acquisitions, high pitch values and for CT scanners with a large beam collimation. The overranging shields reduce the overranging by using an active collimation in the z-axis at the beginning and at the end of the helical CT scan (34). These shields are particularly interesting for the study of small length body parts with a 16- or 64-detector row CT, when overranging is an important factor affecting the radiation dose delivered to the patient (35). Most of new area-detector-CT scanners have an overranging shield. If overranging shields are not available, other methods can also reduce overranging: reduction of the pitch value (as overranging decreases when the pitch decreased), or acquisition with sequential mode (without helical acquisition, there is no overranging!) when possible with an area-detector-CT.

SPECIAL CONDITIONS

Metal artifact reduction.

When metal is exposed to a polychromatic X-ray it creates data inconsistencies between the model used by the reconstruction algorithm and the actual data. As a result beam hardening and photon starvation artifacts are generated (36). Traditionally, a better visualization of metallic materials requires the increase of parameters such as the kVp, the mAs, as well as a low pitch and a thin collimation. All these parametric changes are a source of dose increase. Metal artifact reduction methods are very interesting for soft tissues analysis when metal hardware is present because their application can avoid a dose increase due to the optimization of the acquisition parameters (Fig

11) (kV should be kept high but mAs can be reduced to a normal setting depending on the joint). One of the most promising techniques available for metal artifact reduction is raw data based reformatted projection metal detection and segmentation. In this technique CT data is Fourier transformed into a sinogram which is analyzed to detect and segment metal. The metal sinogram is excluded from the data set and the missing information is then calculated based on the symmetrical filling of the k space and replace before image reconstruction. Multiple studies have demonstrated the effectiveness of this technique in correcting metal artifacts (36-39). Most of MAR techniques need retrospective reconstruction but new prospective methods will be soon available. Some MAR techniques can also be performed on dual-energy acquisition images.



Fig. 5 - CT-scan topogram before acquisition of a hand CT. Peripheral joints should be scanner as far as possible from the trunk of the patient in order to decrease the dose received in radiosensitive organs and should be scanned at the isocenter of the CT gantry to provide optimal image quality.

Dynamic CT

The improvement of the temporal resolution of MDCT and the development of area-detector CT scanners allow dynamic studies of peripheral joints by the mean of multiple successive acquisitions of the same anatomical region during motion. A kinematic study is possible in helical mode with a 64-detector row CT scanner but this technique creates many motion and band artifacts as well as an important increase in radiation dose making it a lot less efficient than area-detector CT scanners (40). With



Fig. 6 - CT-scan of the right wrist of a 20-year-old man during the preoperative assessment of a parachute trauma with 0.5 mm axial slices in bone window centered on the distal extremity of the radius (a), coronal reformation in bone window in 1.5 mm slice (b), and 3D reformation in Volume Rendering (c). Note the good analysis of the bone structures thanks to coronal and 3D reformations in spite of the important reduction of the acquisition parameters (volume acquisition in 200 x 0.5 mm, 80 kV, 50 mAs, rotation time 0.5s) and scan dose (DLP = 39.3 mGy.cm and effective dose = 0.008 mSv).

area-detector CT scanners, it is possible to acquire a volume up to 16 cm in length with a single tube rotation. A tube rotation speed of 0.35 s combined with a partial reconstruction technique of the data warrants a temporal resolution as low as 0.22 s. Volume acquisition mode also presents some advantages: reduction of the dose compared to the helical mode and the temporal uniformity of the acquired volume (every single voxel acquired at the same time with no table movement and no gaps) [42].

The adaptation of the acquisition parameters, the limitation of the scan coverage, the number of phases as well as the application of iterative reconstruction algorithms, help maintain a low radiation dose. On a peripheral joint, performing a low-dose acquisition with an effective dose lower than 1 mSv without compromise to the interpretation of the motion is possible. For the dynamic exploration of the hip or the shoulder, it is particularly important to reduce radiation dose by optimizing the scan

parameters. If the kinematic study concerns only the bone segments, the high natural contrast of the bone allows a considerable reduction in mAs. It is also important to reduce and to center the zone of interest. For most kinematic studies in daily practice the motion speed can be controlled by the patient and an intermittent acquisition mode can be used. In this mode a delay is introduced between each acquisition (leading to a small and controlled decrease of the temporal resolution) reducing the number of phases. Generally less than 15 phases are needed for a standard dynamic CT examination. Intermittent acquisition allows a considerable reduction in radiation dose by reducing the exposure time. On the pelvis, the radiation dose can be maintained under 10 mSv, which corresponds to that of a standard multiphasic abdominopelvic CT (Fig 12).

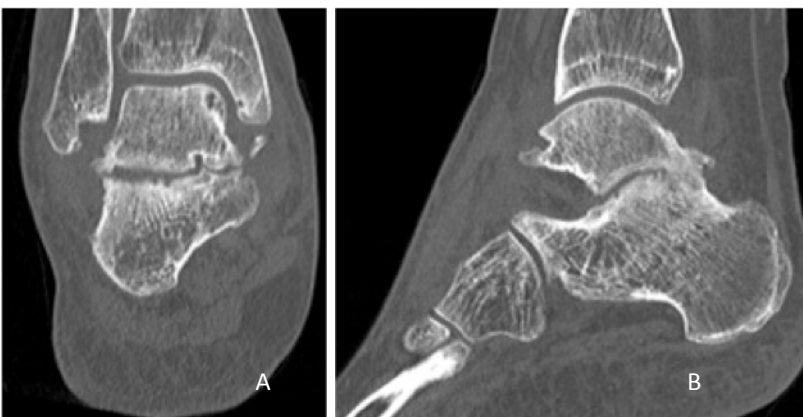


Fig. 7 - CT-scan of an ankle with 0.5 mm axial (a) and coronal slices (b) performed with 80 kV, 50 mAs. Note the good analysis of bone structures in spite of the important reduction of the acquisition parameters and scan dose (DLP = 39,3 mGy.cm).

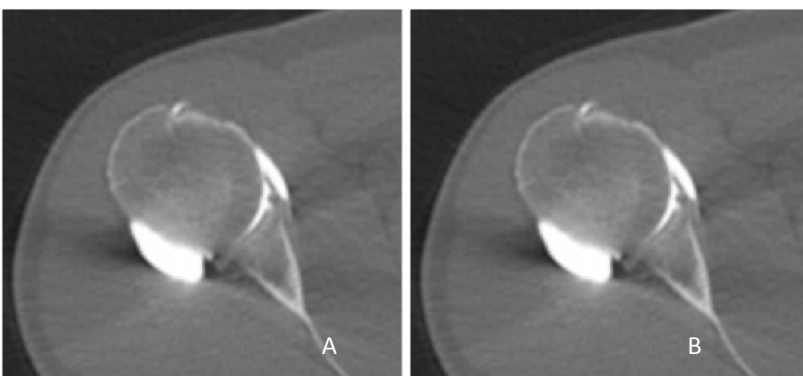


Fig. 8 - Example of a shoulder CT-arthrography with two acquisitions at 80 and 140 kV. Note the good image quality at 80 kV due to the increase of attenuation value of iodine with an increase in contrast to noise ratio.

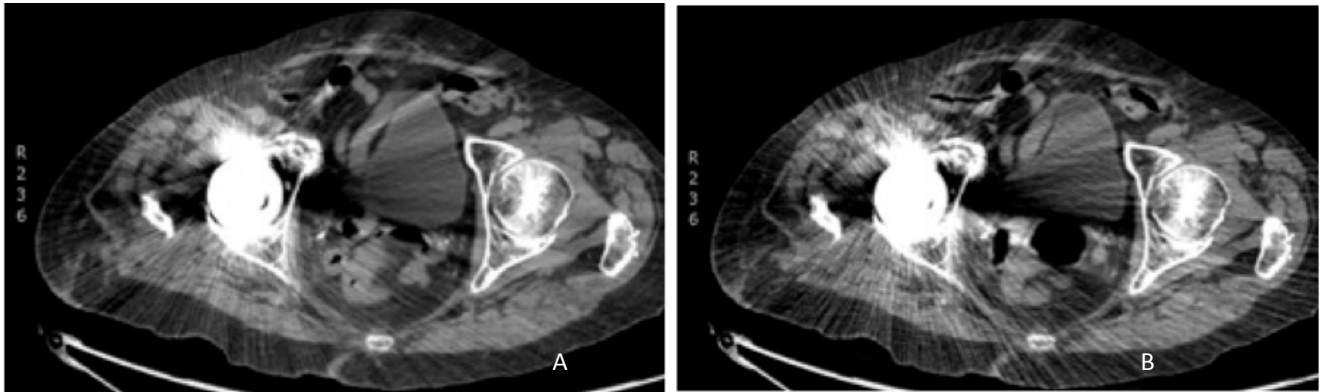


Fig. 9 - Hip CT-scan with two acquisitions (a) 140 kV, 240 mA and pitch = 0.531 ; (b) 120 kV, 100 mA, pitch = 0.969. Note the better soft tissue analysis near the metal hardware with the increase of kVp and mAs, with a low pitch and a thin collimation but also the increase of the dose.



Fig. 10 - Shoulder CT images reconstructed with standard filtered back projection (FBP) (a,b) and Adaptive Iterative Dose Reduction 3D (AIDR 3D) (c,d) in a 59-years-old-man. 0.5 mm axial slices (a,c) and 0.5 mm coronal reformations (b,d) in bone windowing. Note the noise reduction with AIDR 3D compared to FBP associated with a reduction of streak artifacts (volumic acquisition in 240 x 0.5 mm, 120 kV, 150 mAs, rotation time 0.75 s, DLP = 151 mGy.cm and effective dose = 1 mSv).

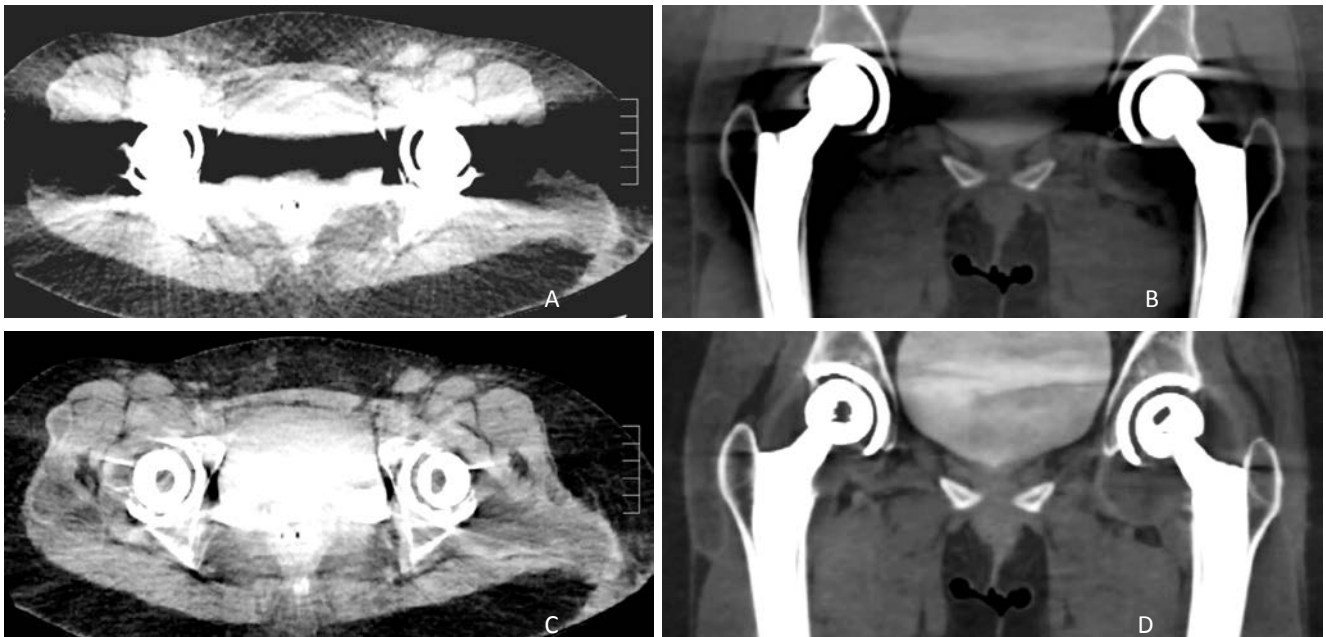


Fig. 11 - Hip CT-scan of a 27 years-old female patient with rheumatoid arthritis treated with Rituximab and bilateral total hip arthroplasty (volumic acquisition with 320×0.5 mm detector collimation, 120 kV, 100 mAs, DLP = 161 mGy.cm and effective dose = 1.2 mSv). Axial slice (a) and coronal reformation (b) with iterative reconstruction and axial slice (c) and coronal reformation (d) with a metal artifact reduction algorithm. Note the important reduction of metal artifacts and the better soft tissue analysis with metal artifact reduction algorithm compared to standard iterative reconstruction algorithm.

Perfusion CT

CT perfusion of bone and soft tissue tumors are possible in clinical practice due to improvement of the MDCT's temporal resolution and the development of area-detector CT scanners. CT perfusion studies provide data comparable to that of an MRI on tumor vascularity, with a better visualization of bone reactive changes and tumor neovascularization. The quantification of the enhancement is also easier on CT perfusion compared to MRI perfusion (42). Perfusion studies can be performed in helical mode with MDCT scanners with bidirectional scanning or in volume mode with area-detector CT scanners. Tumor perfusion in volume mode, without table movement, can reduce motion artifacts and improve the quality of the reconstructions and perfusion curves. This technique also

allows the use of the first acquisition as a bone subtraction mask, thus improving the detection and characterization of intra-osseous abnormalities. However, CT based perfusion studies lead to an important increase in radiation dose.

To control the radiation dose the coverage area is limited to the zone of interest (approximately 4 to 8 cm), kV and mAs are reduced and adapted to the body habitus of the patient and to the anatomical zone (kV can be decreased because attenuation values of iodine are higher with low kV) and the number of phases is limited to 15 (with an acquisition interval of five seconds for the first nine phases [arterial phase], and then of 10 seconds for the later phases [venous phases]). All these measures provide a perfusion study with a total DLP usually between 500 to 800 mGy.cm (Fig 13).



Fig. 12 - Dynamic CT scan of the subtalar joint of the right ankle of a 39-year-old woman presenting with a calcification of cervical ligament of the sinus tarsi. Examination performed with a 320-detector row CT with acquisition of 7 dynamic phases during eversion/inversion motion of the ankle (120 kV, 75 mAs, rotation time 0.5s, DLP = 811 mGy.cm, corresponding to an effective dose of 0.6 mSv). Sagittal reformation on the subtalar joint shows the ligament calcification (a). 3D Volume Rendering reformations focused on the subtalar joint during the eversion/inversion motion of the ankle (b,c) showing the range of motion of the right ankle. In despite of the ligament calcification, this dynamic study shows a normal articular range of motion.

Dual-energy CT

All manufacturers provide dual energy acquisition on their CT scanners. The techniques used among them are however, quite different. This might have an influence on the results and on the clinical applications of these techniques. Dual-energy CT has several potential applications in the evaluation of musculoskeletal disorders but further studies are still necessary to fully assess its performance (43).

One application concerns the detection and characterization of urate deposits in gout (44). An initial study by Nicolaou *et al.* (45) with a dual-source CT scanner showed that the acquisition of all peripheral joints (elbows, wrists, hands, knees, ankles and feet) provides a good sensitivity and specificity for the detection and the location of tophaceous gout with a total effective dose that varied between 2 to 3 mSv. With the 320-detector row CT, a dual-energy technique is obtained from the successive

acquisition of two volumes at different kVp acquired without table feed (the first acquisition with a high kilovoltage and a low milliamperage, and the opposite for the second). Thanks to post-treatment software, this method differentiates the deposits of gout from simple calcium deposits, while keeping a low total effective dose (Figure 14).

Another application of dual-energy CT is bone removal during reconstruction, allowing the identification of bone marrow edema. Pache *et al.* (46) showed that it is possible to see a post-traumatic bone marrow edema on knee dual-energy CT, with an increase of the radiation of approximately 28% compared with single-energy CT.

Finally, Subhas *et al.* (47) showed that compared to a single-energy acquisition dual-energy CT provides a better signal to noise ratio relationship on CT-arthrography of the shoulder with an equivalent dose.

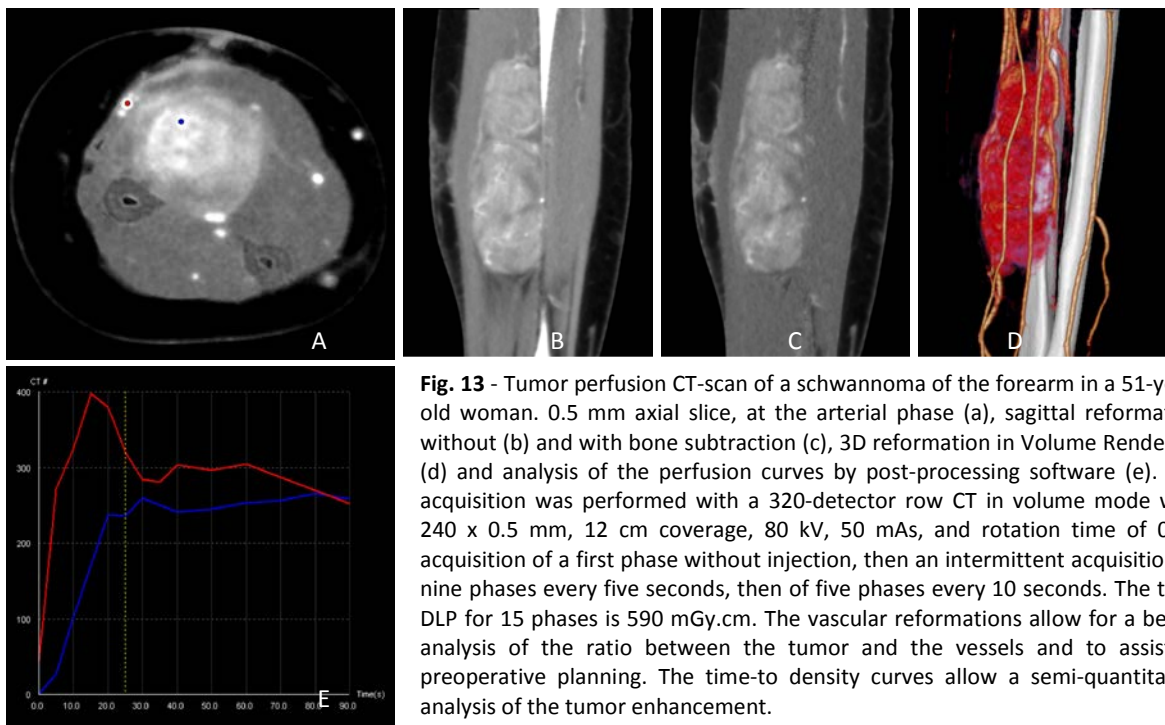


Fig. 13 - Tumor perfusion CT-scan of a schwannoma of the forearm in a 51-year-old woman. 0.5 mm axial slice, at the arterial phase (a), sagittal reformation without (b) and with bone subtraction (c), 3D reformation in Volume Rendering (d) and analysis of the perfusion curves by post-processing software (e). The acquisition was performed with a 320-detector row CT in volume mode with 240 x 0.5 mm, 12 cm coverage, 80 kV, 50 mAs, and rotation time of 0.5s, acquisition of a first phase without injection, then an intermittent acquisition of nine phases every five seconds, then of five phases every 10 seconds. The total DLP for 15 phases is 590 mGy.cm. The vascular reformations allow for a better analysis of the ratio between the tumor and the vessels and to assist in preoperative planning. The time-to density curves allow a semi-quantitative analysis of the tumor enhancement.

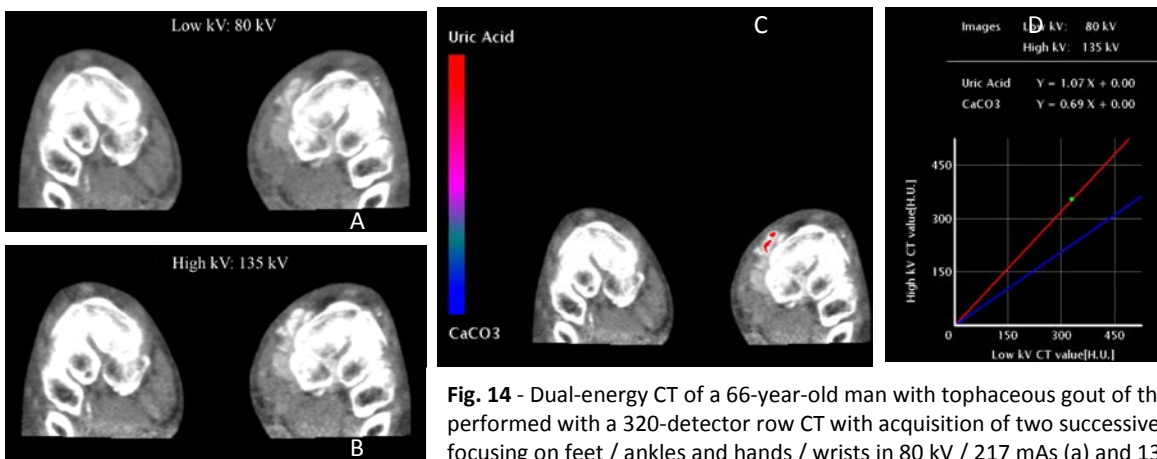


Fig. 14 - Dual-energy CT of a 66-year-old man with tophaceous gout of the feet. Examination performed with a 320-detector row CT with acquisition of two successive volumes of 16 cm focusing on feet / ankles and hands / wrists in 80 kV / 217 mAs (a) and 135 kV / 37 mAs (b) (collimation of 320 x 0.5 mm, rotation time of 0.75s). The total dose is 397 mGy.cm, corresponding to an effective dose of 0.09 mSv. Post-processing (c, d) allows for the characterization of the urate deposits by differentiating them from calcifications, thus confirming the diagnosis of tophaceous gout.

CONCLUSION:

Behavioral factors such as justification and substitution remain essential. The limitation of the scan coverage to the zone of interest and the centering of the scan are also simple ways to reduce the dose. Scan parameters such as tube voltage and tube current should be adapted to the type of acquisition and the body habitus of the patient. Recent technical innovations can also help to reduce the doses such as automatic tube current modulation, active collimation or new CT iterative reconstructions. During dynamic or perfusion CT, dose can be reduced by low kV acquisition, limitation of the scan coverage and limitation of the number of phases.

REFERENCES

- Blum A, Walter F, Ludig T, Zhu X, Roland J. Multislice CT: principles and new CT-scan applications. *J Radiol* 2000; 81:1597-1614
- Cotten A, Iochum S, Blum A. 3D imaging in musculoskeletal system. In: Baert AL, Caramella D, Bartolozzi C (eds) 3D image processing. Techniques and clinical applications. Springer, Berlin Heidelberg New York, 2002, pp 247–255.
- Fayad LM, Bluemke DA, Fishman EK. 2005. Musculoskeletal imaging with computed tomography and magnetic resonance imaging: when is computed tomography the study of choice? *Curr Probl Diagn Radiol* 2005; 34:220–237.
- West ATH, Marshall TJ, Bearcroft PW. CT of the musculoskeletal system: what is left is the days of MRI? *Eur Radiol* 2009;19:152-164.
- Iochum S, Ludig T, Walter F, Fuchs A, Henrot P, Blum A. Value of volume rendering in musculo-skeletal disorders. *J Radiol* 2001; 82:221–230.
- Goh V, Padhani AR. Imaging tumor angiogenesis: functional assessment using MDCT or MRI? *Abdom Imaging* 2006; 31:194-199.
- Semelka RC, Armao DM, Elias J, Huda W. Imaging strategies to reduce the risk of radiation in CT studies, including selective substitution with MRI. *JMRI* 2007; 25: 900-909.
- Smith-Bindman R, Lipson J, Marcus R et al. Radiation dose associated with common computed tomography examinations and the associated lifetime attributable risk of cancer. *Arch Intern Med* 2009; 169:2078-2086.
- Berrington de González A, Mahesh M, Kim KP et al. Projected cancer risks from computed tomography scans performed in the United States in 2007. *Arch Intern Med* 2009; 169:2071-2077.
- International Commission on Radiological Protection. Recommendations of the International Commission on Radiological Protection. ICRP Publication 26. 1977. Pergamon, Oxford.
- Kalra MK, Maher MM, Toth TL, Hamberg LM, Blake MA, Shepard JA, Saini S. Strategies for CT radiation dose optimization. *Radiology* 2004; 230:619-628.
- McCullough CH, Primak AN, Braun N, Kofler J, Yu L, Christner J. Strategies for reducing radiation dose in CT. *Radiol Clin North Am* 2009;47:27-40.
- Lee TY, Chhem RK. Impact of new technologies on dose reduction in CT. *Eur J Radiol* 2010; 76:28-35.
- Singh S, Kalra MK, Thrall JH, Mahesh M. CT radiation dose reduction by modifying primary factors. *J Am Coll Radiol* 2011; 8:369-372.
- Wallace AB, Goergen SK, Schick D, Soblusky T, Jolley D. Multidetector CT dose: clinical practice improvement strategies from a successful optimization program. *J Am Coll Radiol* 2010; 7:614-24.
- Tamm EP, Rong XJ, Cody DD, Ernst RD, Fitzgerald NE, Kundra V. Quality initiatives: CT radiation dose reduction: how to implement change without sacrificing diagnostic quality. *Radiographics* 2011;31:1823-32.
- Cook TS, Zimmerman SL, Steingall SR, Maidment AD, Kim W, Boonn WW. RADIANCE: An automated, enterprise-wide solution for archiving and reporting CT radiation dose estimates. *Radiographics*. 2011 Nov-Dec;31:1833-46.
- Borgen L, Ostense H, Strandén E, Olerud HM, Gudmundsen TE. Shift in imaging modalities of the spine through 25 years and its impact on patient ionizing radiation doses. *Eur J Radiol* 2006; 60 :115-119.
- Oikarinen H, Meriläinen S, Pääkkö E, Karttunen A, Nieminen MT, Tervonen O. Unjustified CT examinations in young patients. *Eur Radiol* 2009 ; 19: 1161-1165.
- Clarke JC, Cranley K, Kelly BE, Bell K, Smith PH. Provision of MRI can significantly reduce CT collective dose. *Br J Radiol* 2001; 74:926–931.
- Rehani MM, Bongartz G, Kalender W et al. Managing x-ray dose in computed tomography: ICRP special task force report. *Ann ICRP* 2000; 30:7-45.
- Kalra MK, Toth TL. Patient centering in MDCT: dose effects. In: Tack D, Genevois PA (eds) Radiation dose from adult and pediatric multidetector computed tomography. Springer, Berlin, 2007, pp 129-132.
- Gervaise A, Louis M, Batch T, Loeuille D, Noel A, Guillemain F, Blum A. Dose reduction at CT of the lumbar spine using a 320-detector row scanner: initial results. *J Radiol* 2010; 91:779-785.
- Schilham A, van der Molen AJ, Prokop M, Jong HW. Overranging at multi-section CT: an underestimated source of excess radiation exposure. *Radiographics* 2010; 30; 1057-1067.
- Mahesh M. Scan parameters and image quality in MDCT. In: Mahesh M (eds) MDCT physics: The basics—Technology, image quality and radiation dose. Lippincott Williams & Wilkins, Philadelphia, 2009, pp 47-78.
- Bohy P, de Maertelaer V, Roquigny A, Keyzer C, Tack D, Genevois PA. Multidetector CT in patients suspected of having lumbar disk herniation: comparison of standard-dose and simulated low-dose techniques. *Radiology* 2005; 244: 524-531.

27. Nagel HD. CT parameters that influence the radiation dose. In: Tack D, Genevois PA (eds) Radiation dose from adult and pediatric multidetector computed tomography. Springer, Berlin, 2007, pp 51-79.
28. Stradiotti P, Curti A, Castellazzi G, Zerbi A. Metal-related artifacts in instrumented spine. Techniques for reducing artifacts in CT and MRI: state of the art. *Eur Spine J* 2009; 18:S102-S108.
29. von Falck C, Galanski M, Shin H. Sliding-thin-slab averaging for improved depiction of low-contrast lesions with radiation dose savings at thin-section CT. *Radiographics* 2010; 30:317-326.
30. McNitt-Gray MF. AAPM/RSNA physics tutorial for residents: topics in CT. Radiation dose in CT. *Radiographics* 2002, 22:1541-1553.
31. Hara AK, Paden RG, Silva AC, Kujak JL, Lawder HJ, Pavlicek W. Iterative reconstruction technique for reducing body radiation dose at CT: feasibility study. *AJR Am J Roentgenol* 2009; 193: 764-771.
32. Gervaise A, Osemont B, Lecocq S, Micard E, Noel A, Felblinger J, Blum A. CT image quality improvement using adaptive iterative dose reduction with wide-volume acquisition on 320-detector CT. *Eur Radio* 2012;22(2):295-301.
33. Boas FE, Fleischmann D. Evaluation of two iterative techniques for reducing metal artifacts in computed tomography. *Radiology* 2011; 259:894-902.
34. Stierstorfer K, Kuhn U, Wolf H, Petersilka M, Suess C, Flohr T. Principle and performance of a dynamic collimation technique for spiral CT. (abstr) In: Radiological Society of North America scientific assembly and annual meeting program. Oak Brook, IL: Radiological Society of North America, 2007 SSA16-04.
35. Christner JA, Zavaletta VA, Eusemann CD, Walz-Flannigan AI, McCollough CH. Dose reduction in helical CT: dynamically adjustable z-axis X-ray beam collimation. *AJR Am J Roentgenol* 2010;194:W49-W55.
36. Yu L, Li H, Mueller J, Kofler JM, Liu X, Primak AN, et al. Metal artifact reduction from reformatted projections for hip prostheses in multislice helical computed tomography: techniques and initial clinical results. *Invest Radiol* 2009;44(11):691-6.
37. Li H, Noel C, Chen H, Harold Li H, Low D, Moore K, et al. Clinical evaluation of a commercial orthopedic metal artifact reduction tool for CT simulations in radiation therapy. *Med Phys* 2012;39(12):7507-17.
38. Meyer E, Raupach R, Lell M, Schmidt B, Kachelrieß M. Frequency split metal artifact reduction (FSMAR) in computed tomography. *Med Phys* 2012;39(4):1904-16.
39. Lee YH, Park KK, Song H-T, Kim S, Suh J-S. Metal artefact reduction in gemstone spectral imaging dual-energy CT with and without metal artefact reduction software. *Eur Radiol* 2012;22(6):1331-40.
40. Tay SC, Pimac AN, Fletcher JG, Schmidt B, Amrami KK, Berger RA, Mc Collough CH. Four-dimensional computed tomographic imaging in the wrist: proof of feasibility in a cadaveric model. *Skeletal Radiol* 2007; 36:1163-1169.
41. Wassilew GI, Janz V, Heller MO et al. Real time visualization of femoroacetabular impingement and subluxation using 320-slice computed tomography. *J Orthop Res* 2013;31:275-281.
42. Miles KA, Charnsangavej C, Lee F, Fishman E, Horton K, Lee TY. Application of CT in the investigation of angiogenesis in oncology. *Acad Radiol* 2001; 7:840-850.
43. Karcaaltincaba M, Aktas A. Dual-energy CT revisited with multidetector CT: review of principles and clinical applications. *Diagn Interv Radiol* 2001;17:181-194.
44. Choi HK, Al-Arfaj AM, Eftekhari A et al. Dual energy computed tomography in tophaceous gout. *Ann Rheum Dis* 2009;68:1609-1612.
45. Nicolaou S, Yong-Hing CJ, Galea-Soler S, Hou DJ, Louis L, Munk P. Dual-energy CT as a potential new diagnostic tool in the management of gout in the acute setting. *AJR Am J Roentgenol* 2010;194:1072-1078.
46. Pache G, Krauss B, Strohm P et al. Dual-energy CT virtual noncalcium technique: detecting posttraumatic bone marrow lesions- feasibility study. *Radiology* 2010;256:617-624.
47. Subhas N, Freire M, Primak AN et al. CT arthrography: in vitro evaluation of single and dual energy for optimization of technique. *Skeletal Radiol* 2010;39:1025-1031.

Imaging follow-up after percutaneous ablative laser therapy of patients with osteoid osteomas: Is there a place for low dose CT perfusion?

Pedro A. Gondim Teixeira, Marine Beaumont, Sophie Lecocq, Matthias Louis, Béatrice Marie, Alain Blum

Submitted to the British journal of Radiology on August 10th 2013

Abstract

Objective: Evaluate the performance of wide area detector CT perfusion in identifying osteoid osteoma recurrences ablative therapy and the radiation exposure levels it implies.

Methods: 13 patients with a final diagnosis of osteoid osteoma were evaluated before and after treatment. The study was prospective and approved by the ethics committee. CT studies were performed in a 320-detector row scanner using a low dose technique. Multiple semi-quantitative and quantitative perfusion parameters were correlated to the treatment outcome. The radiation dose delivered was assessed.

Results: There were 8 successful treatments, 5 recurrences and a significant difference in the perfusion parameters of these groups ($P < 0.045$). Patients with successful treatment demonstrated delayed progressive enhancement or no enhancement (mean time-to-peak = 101 s, mean delay to the arterial peak = 70.4 s). Patients with treatment failure demonstrated an early and steep enhancement (mean time-to-peak = 42 s and mean delay to the arterial peak = 13.8 s). Arterial flow, $V_p\%$ and K^{trans} values in the nidus significantly changed after successful treatment ($p < 0.007$). The mean effective dose per study was 2.828 +/- 3.550 mSv. The effective dose for the extremities varied from 0.09 to 0.3 mSv.

Conclusion: CT perfusion is highly sensitive and specific for the diagnosis of osteoid osteoma recurrences and presents a similar performance than MR perfusion. Radiation dose exposure warrants the clinical application of this method in the extremities only, in which case it represents a valid alternative to MR perfusion.

Advances in knowledge:

- 1- Low dose CT perfusion presents a similar performance than MR perfusion for the diagnosis of osteoid osteoma recurrences
- 2- The effective dose of CT perfusion in the extremities is very low and in which case it represents a valid alternative to MR perfusion.

Keywords: Perfusion imaging, Multidetector Computed Tomography, Osteoid Osteoma, follow-up, Low-dose.

Introduction

Osteoid osteoma is a benign neoplasm of the bone that can cause significant disability (1). Currently, minimally invasive percutaneous radio or thermal ablation is the treatment of choice for this tumor (2–4). The primary success rate of percutaneous ablative therapy varies from 70% to 98% in the literature (5–9). Osteoid osteoma recurrences can be as symptomatic and debilitating as the primary lesion. In the postoperative setting pain unrelated to residual or recurrent tumour can occur in up to 40% of patients even in the absence of treatment complications (8). In this context the clinical diagnosis of an osteoid osteoma recurrence can be difficult and patients may benefit from an early diagnostic confirmation.

Conventional CT remains the imaging method of choice for the diagnosis of osteoid osteomas. However, conventional CT findings are not sufficient to differentiate normal post operative findings and recurrence (7,10). Teixeira et al. have recently demonstrated that MR perfusion has a high sensitivity and specificity for the diagnosis of osteoid osteoma recurrences (7). In many European countries there is still a non negligible waiting time for an MR examination and CT becomes an option to expedite the diagnostic workup (11). The use of large area detector CT scanners with iterative reconstruction algorithms leads to a major dose reduction in comparison with conventional multi detector CT (12,13). The reduction in dose requirements facilitates the application of CT perfusion protocols in clinical practice, but there is limited information on when to use this technique and on its performance with respect to MR perfusion.

CT perfusion might be an option for the diagnosis of osteoid osteoma recurrences. In this study we sought to evaluate the performance of wide area detector CT perfusion in determining the activity of the nidi of osteoid osteomas after ablative therapy and the radiation exposure levels it implies. This work can help establish the role of this technique in the follow-up of patients with an osteoid osteoma.

Material and methods

Patients

13 patients with a final diagnosis of osteoid osteoma were evaluated at our institution from October 2010 to November 2012. This prospective study was approved by the local ethics

P. Teixeira – Corresponding author
Service d'Imagerie Guilloz, Hôpital Central, CHU-Nancy, 29 Av. Mar Lattre de Tassigny, 54000 Nancy, France.
e-mail: ped_gt@hotmail.com

committee and all patients were over 18 years old and signed an informed consent. The study population was composed of 11 males and 2 female with an age range of 19 to 52 years. In all patients CT perfusion, and conventional MR imaging were performed after treatment with percutaneous laser therapy. All but one of the patients included were primarily treated in our institution. This patient had been treated with surgical curettage in another institution and was evaluated for a recurrence of the osteoid osteoma. All patients were examined and interviewed by a radiologist before treatment. In our institution CT-guided percutaneous laser therapy is the standard treatment for osteoid osteomas. Laser thermal ablation was performed using a continuous-wave semiconductor portable diode laser with a power of 2 W (total energy of 600–1000 J) in all patients. Bone biopsy was performed per-operatively in all the patients with 11 to 13G needles. The delay between the percutaneous treatment and the control study varied from 2 to 6 months except in one patient. This patient had a control examination performed the day after the treatment because he was foreigner and could not return later for a control study.

Histologic evaluation of the bone fragments yielded histological confirmation of osteoid osteoma in 6 patients. In the remaining 7 patients the histologic diagnosis of osteoid osteoma was not reached. The diagnostic confirmation in these cases was based on the imaging characteristics, clinical findings and absence of an alternative diagnosis at histological analysis. The imaging signs considered as inclusion criteria were: hypodense lesion on CT (nidus) smaller than 2 cm; sclerotic bone reaction adjacent to the lesion; and inflammatory reaction adjacent to the lesion (bone marrow oedema and/or periosteal hyperintensity on T2-weighted fat-saturated images). The clinical findings used as inclusion criteria and presented by all patients were: chronic non-mechanical pain for more than 6 months; pain worse at night; pain relieved by non-steroidal anti-inflammatory drugs (NSAIDS). The bone biopsies in all of these patients yielded normal or sclerotic cortical tissue. Patients with a known malignancy diagnosed elsewhere and with metastatic disease were excluded.

The symptoms considered to be related to an osteoid osteoma recurrence (e.g. pre-treatment or in cases of residual or recurrent tumour) were the presence of an inflammatory type pain, nocturnal pain and the use of NSAIDS for pain control. The presence of any of these signs post-operatively characterised treatment failure.

All the patients without a recurrent osteoid osteoma had a follow-up study with CT perfusion. This study was performed to identify early post-operative complications. The patients without a recurrence were followed clinically for at least 6 months after the control study to confirm the absence of symptoms evocative of osteoid osteoma. The osteoid osteomas included were located at: Shoulder, forearm (2), elbow, lumbar spine (3 patients), hip (2 patients), around the knee (4 patients).

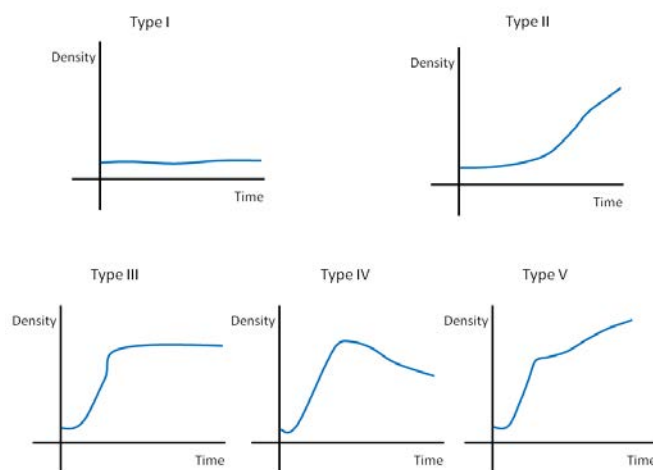


Fig. 1 - Schema representing the perfusion curve morphology types described by van Rijswijk CSP (13). Curve types III and IV are typical of an active osteoid osteoma nidus.

Imaging protocol

All studies were performed in a CT scanner with a large detector system with of 320-detector rows (Aquilion ONE, Toshiba Medical Systems, Otawara, Japan) using an iterative reconstruction algorithm. The patients with osteoid osteomas located in the extremities (shoulder, spine and hip excluded) were immobilized with an inflatable splint. Perfusion study was performed with an intermittent acquisition mode with no table feed. The protocol included 14-16 volumes (Tube rotation: 0.5 s, slice thickness: 0.5 mm, matrix of 512 x 512). The first 10 volumes were acquired with a 5 second delay between them (arterial phase). The last 4-6 volumes were acquired with a 10 second delay between them (venous phase). Tube output parameters were adapted to the anatomic region and are presented on table 2. A dual injection pump (Stellant D, Medrad INC, Indianola, PA, USA) was used for contrast injection. Iomeron® 400 (Bracco Imaging, Evry, France), with a concentration of 400 mg/ml was injected in all patients. Two milliliters per kilogram (up to a maximum of 150 ml) of the contrast media was injected in a single bolus through a peripheral venous access (18 G cannula) with an injection rate of 5 ml/s. Acquisition started 5 seconds after contrast injection. Total examination length was dependent on the number of volumes and varied from 85 to 105 seconds. The coverage in the z axis varied from 4 to 6 cm.

The volumic computed tomography dose index ($CTDI_{vol}$) and the global dose length product (DLP) was estimated based on a 32 cm phantom for the shoulder, hip and lumbar spine and 16 cm phantom for the knees, elbow, fore arm and foot. Effective dose estimations were done with a constant (k-factor) in $mGy \cdot cm \cdot mSv^{-1}$ of 0.0112 for the lumbar spine, 0.0073 for the hip, 0.0065 for the shoulders and 0.0004 for the knees, elbow and fore arm (14).

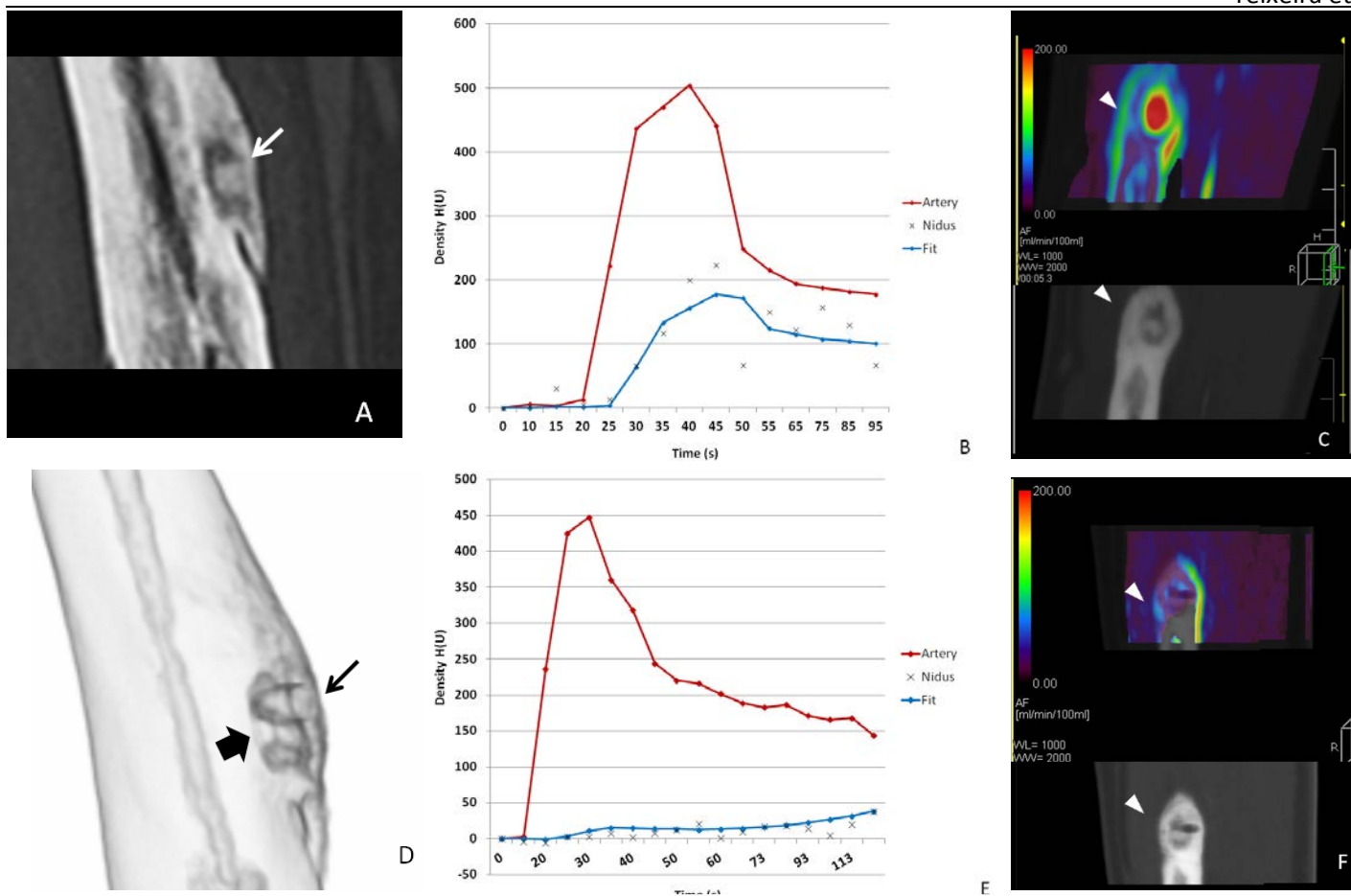


Fig. 2 – 22 year-old male with a typical osteoid osteoma of the mid diaphysis of the right radius before and after treatment. A) Coronal CT image showing a well defined nidus with a central calcification (white arrow) and a marked periosteal reaction. B) Pre-treatment time-to-density curve demonstrating a type IV enhancement curve of the nidus (Blue curve), with an early enhancement with respect to the ulnar artery (yellow curve). C) Arterial flow colored map in the sagittal plane demonstrating the high arterial flow in the nidus (white arrowheads) and the corresponding CT image. D) Volume rendered CT image depicting the nidus cavity (fat black arrow) and an adequate needle trajectory (thin black arrow) after percutaneous ablation therapy. E) Post-treatment CT perfusion time-to-density curve demonstrating the perfusion change in the nidus, which does not present any detectable enhancement (blue curve). F) Post operative arterial flow colored map in the sagittal plane demonstrating a marked drop in the nidus arterial flow (white arrowheads) with respect to the pre operative study and the corresponding CT image.

MR was performed with a 1.5T Signa HDxt (GE Healthcare, Milwaukee, WI, USA) scanner using dedicated coils. In all studies conventional sequences were acquired, including at least one T1 weighted sequence and T2 fat-saturated sequences in two different orthogonal planes.

Image analysis and post processing

All conventional CT and MR images were evaluated in a PACS station (Impax V5, AGFA HealthCare, Ivry-sur-Seine, France). Pre and post treatment CT perfusion images from all osteoid osteoma patients were post processed using two commercially available workstations: Display console v. 4.74 Toshiba Medical Systems (TDC application) and AW console version 4.4 GE Healthcare (Functool application). The slice that depicted the largest portion of the nidus was selected for the whole evaluation. In the pre-operative studies the ROIs were placed to occupy the whole nidus area. In the postoperative studies the ROIs were placed in the area of

maximum enhancement at the treatment zone. Post-processing was performed by a trained physicist (MB) blinded to the treatment outcome. Two fellowship-trained radiologists with 20 and 5 years of clinical experience validated the ROI positioning in all cases.

Time-to-density curves were constructed. Curve morphology analysis was based on the classification proposed by van Rijswijk et al (15). Five types were described. Type I designates a flat curve, type II progressive enhancement with no enhancement peak, type III an early enhancement peak followed by a plateau, type IV an early enhancement peak followed by a washout and type V an early enhancement peak followed by progressive enhancement. Semi-quantitative perfusion parameters (time-to-peak, delay between the arterial and nidus peaks) were calculated. Enhancement was considered significant if an increase of more than 15 Hounsfield units (HU) was detected. A single-input maximum slope algorithm was used to build an arterial flow colored map with a quantification of the arterial flow

(ml/sec/100ml) in the nidus. One millimeter-thick slices were used for the construction arterial flow maps.

Since the arterial input function was available for all data sets, a two-compartment pharmacokinetic model derived from the Brix model (Tofts model) was used for calculation of the quantitative perfusion parameters (16–18):

$$C_t(t) = v_p C_p(t) + K^{trans} \int_0^t C_p(\tau) e^{-k_{ep}(t-\tau)} d\tau \quad (1)$$

The application of this pharmacokinetic model yielded three quantitative perfusion parameters: The nidus plasmatic volume (V_p %); the volume transfer constant from the plasma to the extravascular extracellular space (EES) (K^{trans}); the rate constant of the backflux from the EES to the plasma (k_{ep}). A fourth parameter, the EES volume (V_e %) derived from the following relation:

$$V_e \% = K^{trans} / k_{ep}$$

Using Matlab (v. 7.2, the Mathworks, Natwick, MA, USA) the base line of the intensity-time data from the arterial input ($C_p(t)$) and the nidus ($C_t(t)$) was set to zero. The difference in the time delay between the arterial input data and the lesion data was corrected. Then the time-density data was fitted using a Levenberg-Marquardt algorithm to a two-compartment pharmacokinetic model (1).

Semi-quantitative and quantitative perfusion parameters evaluated correlated with the surgical outcome. Statistical

analysis was performed by using R Development Core Team software version R 2.13.1 (2011). Normal distribution assumption was tested by the Shapiro Wilk test. Since was not confirmed, the Wilcoxon rank test sum test was used for the evaluation of the statistic significance of the quantitative data. A p value less than 0.05 was used as the threshold for statistic significance.

Results

The age in the study population varied from 18 to 52 years (mean 29.6 years). There were 11 males and two females. Nidus size varied from 0.3 to 2.0 cm. Nidus calcification was seen in all patients, with three patients presenting a heavily calcified nidus.

In the patients for which a pre-treatment study was available the enhancement curves in were classified as type IV in 10 patients and type III in 2 patients (one patient had no pre-treatment study available) (Fig. 1). The time-to-peak in the nidus varied from 35 to 60 seconds (mean 47.4 +/- 8.67s). The delay between the arterial and the nidus peaks varied from 0 to 25 seconds (mean 11.3 +/- 8.55s). The arterial flow in the nidus area in (ml/sec/100ml) varied from 58 to 311 ml/sec/100ml (mean 173.3 +/- 77.3 ml/sec/100ml) in pre-treatment studies (Fig. 2). Nidus arterial flow was over 100 ml/sec/100ml in 10 patients. In the two patients with an arterial flow under 100 ml/sec/100ml, one had a densely calcified nidus and the other had a very small nidus measuring 0.1 x 0.8 mm.

Table 1- Comparison between the perfusion characteristics of the nidi of the osteoid osteomas studied before and after percutaneous ablation. Treatment failures are indicated in red.

Patients	1	2	3	4	5	6	7	8	9	10	11	12	13
Age	27	39	52	22	22	21	37	36	24	33	21	20	34
Size (cm)	1.1	0.7	1.7	0.8	1	0.8	0.3	0.4	0.7	1	1.3	2	0.5
Location	Elbow	Knee	Knee	Shoulder	Arm	Hip	Knee	Hip	Spine	Spine	Arm	Spine	Knee

Pre Treatment	Curve	III	IV	IV	IV	IV	IV	III	IV	IV	IV	IV	x	IV
	TTP (s)	60.00	60.00	50.00	50.00	45.00	40.00	58.00	38.00	35.00	50.00	40.00	x	43.00
	DAP (s)	25.00	20.00	5.00	15.00	5.00	5.00	25.00	11.00	5.00	15.00	0.00	x	5.00
	AF	311.0	58.0	86.00	147.00	248.00	143.00	162.00	110.00	255.00	113.00	215.00	x	233.00

Post Treatment	Curve	I	II	IV	III	I	II	II	II	I	IV	IV	IV	II
	TTP (s)	x	76.00	52.00	45.00	x	78.00	126.00	117.00	x	35.00	44.00	34.00	108.00
	DAP (s)	x	30.00	20.00	10.00	x	68.00	88.00	88.00	x	5.00	10.00	24.00	78.00
	AF	108.0	57.00	51.00	142.00	26.00	55.00	66.00	28.00	84.00	96.00	214.00	232.0	33.00
AF drop	65.20%	1.7%	40.6%	3.4%	89.5%	61.5%	59.2%	74.4%	67.0%	15.0%	0.40%	x	85.8%	

TTP = Time-to-peak

DAP = Delay to arterial peak

AF = Arterial Flow (ml/sec/100ml)

Eight of the patients studied presented a sustained regression of symptoms (treatment success). Among these patients a change in the time-to-density curve morphology with respect to the pre-operative study was present in cases (Fig. 2). Five of these patients presented a progressive enhancement (type II curve) and in three patients there was no detectable enhancement (type I curve). There was an increase in the time-to-peak and the delay between the arterial and the nidus peaks in all the patients with a measurable enhancement. In the control studies of these patients the time-to-peak varied from 76 to 126 seconds (mean 101.0 +/- 22.8s) and the delay between arterial and nidus peaks varied from 30 to 88 seconds (mean 70.4 +/- 24.0s). These differences with respect to pre-operative studies were not statistically significant ($p = 0.0625$ and 0.0579 respectively) due to the large number of patients with no detectable enhancement after treatment. The arterial flow in the eight patients successfully treated varied from 26 to 108 ml/sec/100ml (mean 47.8 +/- 16.4 ml/sec/100ml). With respect to the pre-treatment studies were statistically significant drop in nidus arterial flow ($p = 0.0078$). There was a mean drop in the nidus arterial flow of 63.0% after percutaneous treatment. All the patients controlled presented an individual drop of the arterial flow in the nidus except for one. This patient had an infra-millimetric pin head nidus and presented a low arterial flow measurement with respect to the others in the pre-treatment study.

Five patients presented a regression of inflammatory type pain (treatment failure). These patients presented a short symptom-free window (2-4 months) after the percutaneous treatment. Four presented a type IV and one a type III time-to-density curve. In the other patient the curve morphology changed from type IV to type III (both of which are characterized by a steep enhancement). Among these patients no significant changes in the time-to-peak, delay between the arterial and nidus peaks and arterial flow ($p = 0.625$, 0.712 , 0.125 respectively) between pre and post therapy studies (Fig. 3). The time-to-peak and delay between arterial and nidus peaks varied from 35 to 52s seconds (mean 42 +/- 7.5s) and from 5 to 24 seconds (mean 13.8 +/- 7.8s) respectively. In this group the arterial flow varied from 51 to 232 ml/sec/100ml (mean 147 +/- 76.7 ml/sec/100ml). The mean drop in the nidus arterial flow was 14.8%. The individual values of each of the perfusion parameters studied for these patients are presented on table 1. The differences in time-to-peak, delay between arterial and nidus peaks and arterial flow between patients with a successful and a failed treatment were also statistically significant ($p = 0.0079$, 0.0116 and 0.0450 respectively).

In the post-treatment setting if curves with morphology of types III and IV, are considered signs of an osteoid osteoma recurrence (treatment failure) the sensitivity and specificity of CT perfusion for the detection of a recurrent osteoid osteoma were 100%. If a time-to-peak shorter than 70 s (or no detectable enhancement) and a delay between the arterial and nidus peak shorter than 30 s (or no detectable enhancement) were considered diagnostic criteria for

recurrent osteoid osteoma CT perfusion would have the same sensitivity and specificity (100%).

Table 2 – Mean values and standard deviation of the quantitative perfusion parameters studied before treatment and according to the treatment outcome.

	pre	success	Failure
V_p (%)	24.1% +/- 18.3	4.52% +/- 3.26	23.1% +/- 15.6
V_e (%)	61.0% +/- 46.9	x	49.8% +/- 58.8
K^{trans} (min-1)	0.88 +/- 0.58	0.13 +/- 0.17	0.42 +/- 0.33
k_{ep} (min-1)	2.43 +/- 1.92	x	3.99 +/- 4.26

V_p = Plasmatic volume

V_e = Extravascular extracellular space volume

K^{trans} = Transfer constant from plasma to extravascular extracellular space

k_{ep} = rate constant of the backflux

The quantitative perfusion parameters found were comparable to what is described in the literature for other types of tumour (19). The mean values and standard deviation of the quantitative perfusion parameters for the pre treatment, post treatment with success and after failed treatment are demonstrated on Table 3. The parameters related to EES to plasma backflux (k_{ep}) could not be adequately calculated for patients with curve morphology types I and II since the washout phase was not available in the acquired data. In one patient after a successful treatment the K^{trans} value was aberrant and was not included in the calculations. In two patients with a recurrence the $V_e\%$ and k_{ep} were aberrant and were not included in the calculations. When compared to the pre-treatment studies, there was a statistically significant drop in $V_p\%$ values in all patients with a successful treatment ($p = 0.0147$). The K^{trans} values between pre-treatment and successful treatment studies was statistically different ($P = 0.0011$). There was a reduction in K^{trans} values in all patients after successful treatment. There was a decrease in the $V_p\%$ after successful treatment in 6 out of 8 (75%) patients. The mean values of all the quantitative perfusion parameters studied were similar between pre-treatment and recurrences (table 2).

The mean $CTDI_{vol}$ and DLP deployed with the protocol used were respectively 123.5 (+/- 50.8) mgy and 567.3 (+/- 185.1) mgy.cm. There was a larger variation in the effective dose values. Mean effective dose measured 2.828 (+/- 3.550) mSv. The mean effective dose was significantly higher on the shoulder, hip and lumbar spine studies in which it measured 2.92 to 10.89 mSv (mean 5.88 +/- 3.06 mSv) versus 0.14 to 0.3 mSv (mean 0.206 +/- 0.074 mSv) for the other studies (elbow, fore arm, knee and foot). The effective dose was 95.2% lower in the extremities. This was due to the variation of recommended conversion constant (K) between the different anatomic regions, which influence heavily the effective dose calculation (14). The tube output parameters, $CTDI_{vol}$, DLP and effective dose values for each examination are presented on Table 3.

Table 3 - Tube output parameters used and the corresponding delivered and effective dose.

	Loc	kV/mAS	CTDIvol (mgy)	DLP (mgy.cm)	Cov (cm)	dose (mSv)
Patient 1	Elbow	100/80	126	756	6	0.3
Patient 2	knee	80/125	46	372	4	0.14
Patient 3	knee	80/100	111	440	4	0.17
Patient 4	Shoulder	120/100	132	528	4	3.43
Patient 5	Arm	120/75	162	650	4	0.26
Patient 6	hip	120/100	133	536	4	3.91
Patient 7	Knee	80/100	93	374	4	0.14
Patient 8	Hip	120/187	100	401	4	2.92
Patient 9	Spine	120/75	107	663	4	7.42
Patient 10	spine	100/100	75	603	4	6.75
Patient 11	Arm	80/75	88	355	4	0.142
Patient 12	Spine	120/150	243	973	4	10.8976
Patient 13	Knee	100/75	183	732	4	0.2928

CTDIvol = Volumic computed tomography dose index; DLP = Dose length product
Cov = Z-axis Coverage

Discussion:

The CT perfusion parameters of the nidi in the pre treatment studies were similar to what is described in the literature as typical of osteoid osteomas (10,20). An early and steep enhancement with a short delay between the arterial and nidus peak is characteristic of this tumor and is probably related to its high vascular nature (1). This enhancement pattern is clearly different fibrotic scarring and coagulative necrosis usually found after percutaneous ablation (10). Early enhancement at the nidus region after percutaneous ablation therapy is associated with osteoid osteoma recurrences. These finding might be related to the presence of residual or recurrent osteoid osteoma and can be used as a marker of nidus activity (7).

The presented results demonstrate a clear statistically significant difference in all semi-quantitative perfusion parameters of the osteoid osteomas related to the treatment outcome. Time-to-density curve types III and IV are suggestive of an active nidus and were only to be found in nidi without treatment or in patients with an osteoid

osteoma recurrence. Additionally, the time-to-peak and the arterial-nidus inter-peak delay of all pre-treatment and all recurrences were lower than 70 and 30 seconds respectively. In the studied population CT perfusion was 100% sensitive and specific for the detection of an osteoid osteoma recurrence. This performance is slightly better that what is reported for MR perfusion in the same clinical context (sensitivity and specificity of 92.3% and 95.2% for the diagnosis of recurrence) (7). These differences can be partially explained by a variation in number of post operative imaging controls between the two studies (13 versus 22). These results are supported by the literature since similar performances of CT and MR perfusion protocols have also been reported in neuro and cardiac imaging (21,22).

The diagnostic criteria used for the evaluation of the time-to-peak and the delay between artery and nidus peaks in CT perfusion were similar but not the same reported for MR perfusion. The time-to-peak threshold characteristic of an active osteoid osteoma nidus was longer with MR perfusion than with CT perfusion (120 versus 70 seconds). Moreover there was more variation in the delay between the arterial and nidus peaks in active nidi was smaller with CT perfusion than what has been reported for MR perfusion (0-25 seconds versus 0-46 seconds respectively) (7). The variation de in injection rate and of the injected volume between CT and MR perfusion protocols can probably explain to some extent this variation (23). Additionally when using a time resolved 3D MR sequence for perfusion the temporal resolution is dependent on the matrix and the slice number. In the CT protocol used in this study temporal and spatial resolution are independent which might help explain the smaller variation in the delay between the arterial and nidus peaks.

Quantitative perfusion parameters are potentially interesting for patient follow-up because they allow a direct comparison between perfusion results from the same patient or from different patients. Quantitative parameters may also facilitate the projection of the results to a larger population. Arterial flow represents the flow rate through the vasculature in the tissue and is related histopathologic features such as tumor vascularity and grade (24). There was significant reduction of the arterial flow (mean drop of 63%) in the nidus after treatment successful treatment with a in the arterial flow. The individual drop in the arterial flow after treatment was greater than 50% in 7 out of 8 patients with a successful treatment. There was a statistically significant change in the $V_p\%$ and K^{trans} after successful treatment with most of the patients presenting a drop in these parameters. Values for $V_p\%$, K^{trans} , $V_e\%$ and K_{ep} were similar between pre-treatment studies and recurrences. Additionally these $V_p\%$, K^{trans} , $V_e\%$ and K_{ep} values fall in the same range and vary in a similar fashion as those presented on MR perfusion of osteoid osteomas by Teixeira et al.

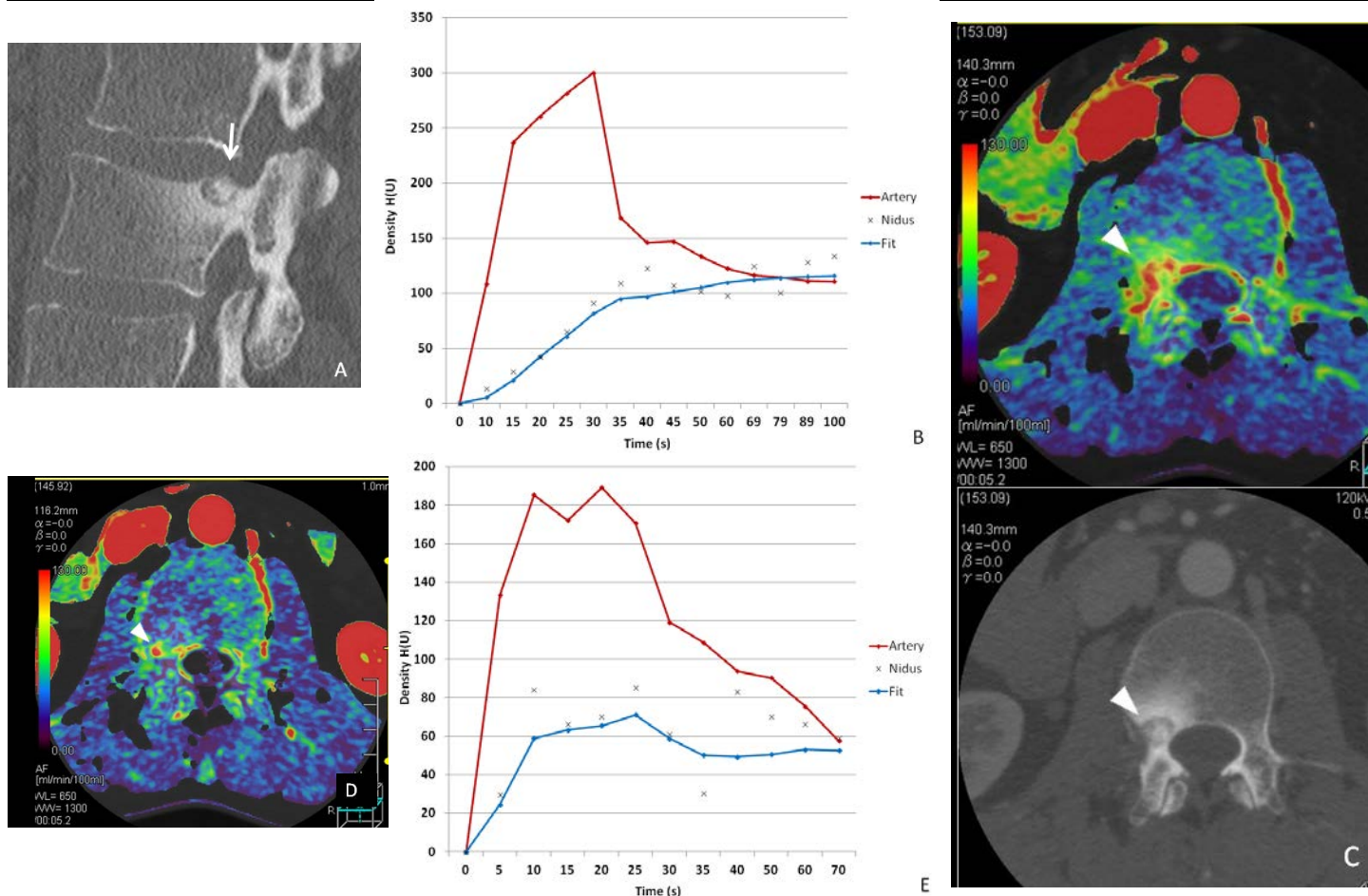


Fig. 3 – 33 year-old male with a biopsy proven osteoid osteoma who presented a recurrence of the symptoms 2 months after treatment (treatment failure). A) Sagittal CT image demonstrating a heavily calcified nidus at the right pedicle of L5 (white arrow). B) Pre-treatment CT perfusion time-to-density graph demonstrating a type IV enhancement curve of the nidus (blue curve) with an early enhancement with respect to the abdominal aorta (yellow curve). C) Arterial flow colored map in the axial plane demonstrating the high arterial flow in the periphery (non calcified portion) of the nidus (white arrowheads) and the corresponding CT image. D) Arterial flow colored map of the same patient 5 months after treatment in the axial plane demonstrating a persistent focus of high arterial flow in the nidus area (white arrowhead). E) Time-to-density curve graphic demonstrating the persistence of an early enhancement in the nidus (blue curve) with respect to the aorta (yellow curve).

Since osteoid osteomas are more frequent in children and young adults there is a great concern about the exposure of these patients to ionizing radiation (1,2). New advances in CT technology allow the acquisition of high quality images with only a fraction of the radiation dose delivered by conventional multidetector helical CT (12–14,25). CT has been used in the evaluation of pediatric patients with adapted protocol in many clinical situations (25). There was a small variation in the DLP with respect to the anatomic region studied (mean 567 +/- 185 mg.y.cm), however the anatomic region had a great impact on the effective dose. The effective dose was 95.2% lower in the extremities compared to the axial skeleton and pelvic and shoulder girdles (mean 2.92 versus 0.14 mSv). In the extremities the effective dose varied from 0.09 to 0.30 mSv. This variation is explained by the differences in the conversion coefficients between central and peripheral anatomic regions. Biswas et al reported effective doses of a single pass helical multidetector CT of 4.36 to 19.16 mSv for the spine; 2.06 mSv for the shoulder

and 3.09 mSv for the hip and 0.03 to 0.16 mSv in the extremities (14). These observations indicate that CT perfusion with large area detector systems has similar dose requirements then a conventional CT study and hence can be used in clinical practice. This technique is particularly interesting in the extremities where it can be performed with a sub-millisievert effective dose.

This study has several limitations. The number of patient was limited. Histologic confirmation was not possible for all the patients. Since minimally invasive percutaneous ablation has been adopted as the treatment of choice for osteoid osteomas the rate of histologic confirmation of these lesions has dropped considerably (4,10,26). Clinical and imaging signs of osteoid osteomas have been extensively described (1,2,10,27,28). That, added to the absence of alternative diagnosis in the bone biopsies performed per operatively provides sufficient evidence to support the diagnosis of osteoid osteoma in the patients without histologic confirmation. There was a small variation in the number of

venous phases in the CT perfusion protocol. These variations represented an attempt to optimize our protocol, keeping radiation exposure to the lowest level possible. The variation in the number of venous phases had little influence in the perfusion analysis since most perfusion parameters (curve morphology, delay between arterial and nidus peak, maximum slope, K^{trans} , K_{ep} , V_p and V_e) are evaluated in the arterial phase. The length of the acquisition protocol did not include the washout phase in lesions with delayed enhancement (curve type II). In these patients the k_{ep} and $V_e\%$ could not be calculated. Variations in the kVp may influence the density calculations in the CT perfusion, which in turn influence the quantitative enhancement analysis. There were kVp variations among the different anatomic regions studied. There were also small variations in kVp levels and between pre and post treatment studies in 6 patients. The lowest as possible kVp was used in order to reduce patient dose and to increase image contrast.

In conclusion, CT perfusion was 100% sensitive and specific for the identification of osteoid osteoma recurrences in the studied population. The identification of an enhancement curve type III or IV in the nidus with short time-to-peak and a short delay between the arterial and nidus peaks in the postoperative setting is highly indicative of an osteoid osteoma recurrence. The quantitative parameters studied, particularly arterial flow, $V_p\%$ and K^{trans} , correlated well with the treatment outcome. The perfusion parameters (quantitative and semi-quantitative) presented were similar to those reported with MR perfusion. Finally, CT perfusion can be performed with the same dose requirement as a conventional MDCT study and can be considered as an alternative to MR perfusion for the post treatment evaluation in some patients with osteoid osteoma.

Acknowledgments:

This work was supported by the French Society of Radiology (SFR- Société Française de Radiologie) through a research grant.

Bibliography:

- Kransdorf MJ, Stull MA, Gilkey FW, Moser RP Jr. Osteoid osteoma. *Radiographics*. July 1991;11(4):671–96.
- Lee EH, Shafi M, Hui JHP. Osteoid osteoma: a current review. *J Pediatr Orthop*. October 2006;26(5):695–700.
- Cioni R, Armillotta N, Bargellini I, Zampa V, Cappelli C, Vagli P, et al. CT-guided radiofrequency ablation of osteoid osteoma: long-term results. *Eur Radiol*. July 2004;14(7):1203–8.
- Cantwell CP, Obyrne J, Eustace S. Current trends in treatment of osteoid osteoma with an emphasis on radiofrequency ablation. *Eur Radiol*. April 2004;14(4):607–17.
- Gebauer B, Tunn P-U, Gaffke G, Melcher I, Felix R, Stroszczyński C. Osteoid osteoma: experience with laser- and radiofrequency-induced ablation. *Cardiovasc Intervent Radiol*. April 2006;29(2):210–5.
- Becce F, Theumann N, Rochette A, Larousserie F, Campagna R, Cherix S, et al. Osteoid osteoma and osteoid osteoma-mimicking lesions: biopsy findings, distinctive MDCT features and treatment by radiofrequency ablation. *Eur Radiol*. October 2010;20(10):2439–46.
- Teixeira PAG, Chanson A, Beaumont M, Lecocq S, Louis M, Marie B, et al. Dynamic MR imaging of osteoid osteomas: correlation of semiquantitative and quantitative perfusion parameters with patient symptoms and treatment outcome. *Eur Radiol*. May 22nd 2013;
- Omlor G, Merle C, Lehner B, Ewerbeck V, Rehnitz C, Weber M-A, et al. CT-guided percutaneous radiofrequency ablation in osteoid osteoma: re-assessments of results with optimized technique and possible pain patterns in mid-term follow-up. *Rofo*. April 2012;184(4):333–9.
- Lindner NJ, Ozaki T, Roedel R, Gosheger G, Winkelmann W, Wörtler K. Percutaneous radiofrequency ablation in osteoid osteoma. *J Bone Joint Surg Br*. April 2001;83(3):391–6.
- Vanderschueren GM, Taminiau AHM, Obermann WR, van den Berg-Huysmans AA, Bloem JL, van Erkel AR. The healing pattern of osteoid osteomas on computed tomography and magnetic resonance imaging after thermocoagulation. *Skeletal Radiol*. September 2007;36(9):813–21.
- IRM : les délais d'attente stagnent à 32 jours en France [Internet]. <http://sante.lefigaro.fr/actualite/2011/05/10/10863-irm-delaiss-dattente-stagnent-32-jours-france>
- Gervaise A, Osemont B, Lecocq S, Noel A, Micard E, Felblinger J, et al. CT image quality improvement using Adaptive Iterative Dose Reduction with wide-volume acquisition on 320-detector CT. *Eur Radiol*. February 2012;22(2):295–301.
- Rajiah P, Schoenhagen P, Mehta D, Ivanc T, Lieber M, Soufan K, et al. Low-dose, wide-detector array thoracic aortic CT angiography using an iterative reconstruction technique results in improved image quality with lower noise and fewer artifacts. *Journal of cardiovascular computed tomography* [Internet]. April 26th 2012 <http://www.ncbi.nlm.nih.gov/pubmed/22612906>
- Biswas D, Bible JE, Bohan M, Simpson AK, Whang PG, Grauer JN. Radiation exposure from musculoskeletal computerized tomographic scans. *J Bone Joint Surg Am*. August 2009;91(8):1882–9.
- Van Rijswijk CSP, Geirnaerd MJA, Hogendoorn PCW, Taminiau AHM, van Coevorden F, Zwinderman AH, et al. Soft-tissue tumors: value of static and dynamic gadopentetate dimeglumine-enhanced MR imaging in

- prediction of malignancy. *Radiology*. November 2004;233(2):493–502.
16. Brix G, Semmler W, Port R, Schad LR, Layer G, Lorenz WJ. Pharmacokinetic parameters in CNS Gd-DTPA enhanced MR imaging. *J Comput Assist Tomogr*. August 1991;15(4):621–8.
 17. Tofts PS. Modeling tracer kinetics in dynamic Gd-DTPA MR imaging. *J Magn Reson Imaging*. February 1997;7(1):91–101.
 18. Tofts PS, Brix G, Buckley DL, Evelhoch JL, Henderson E, Knopp MV, et al. Estimating kinetic parameters from dynamic contrast-enhanced T(1)-weighted MRI of a diffusible tracer: standardized quantities and symbols. *J Magn Reson Imaging*. September 1999;10(3):223–32.
 19. Juan C-J, Chen C-Y, Jen Y-M, Liu H-S, Liu Y-J, Hsueh C-J, et al. Perfusion characteristics of late radiation injury of parotid glands: quantitative evaluation with dynamic contrast-enhanced MRI. *Eur Radiol*. January 2009;19(1):94–102.
 20. Von Kalle T, Langendörfer M, Fernandez FF, Winkler P. Combined dynamic contrast-enhancement and serial 3D-subtraction analysis in magnetic resonance imaging of osteoid osteomas. *Eur Radiol*. October 2009;19(10):2508–17.
 21. Otton J, Morton G, Schuster A, Bigalke B, Marano R, Olivotti L, et al. A direct comparison of the sensitivity of CT and MR cardiac perfusion using a myocardial perfusion phantom. *J Cardiovasc Comput Tomogr*. April 2013;7(2):117–24.
 22. De Simone M, Muccio CF, Pagnotta SM, Esposito G, Cianfoni A. Comparison between CT and MR in perfusion imaging assessment of high-grade gliomas. *Radiol Med*. February 2013;118(1):140–51.
 23. Mathys C, Rybacki K, Wittsack H-J, Lanzman RS, Miese FR, Macht S, et al. A phantom approach to interscanner comparability of computed tomographic brain perfusion parameters. *J Comput Assist Tomogr*. December 2012;36(6):732–8.
 24. Kambadakone AR, Sahani DV. Body perfusion CT: technique, clinical applications, and advances. *Radiol Clin North Am*. January 2009;47(1):161–78.
 25. Fayad LM, Johnson P, Fishman EK. Multidetector CT of musculoskeletal disease in the pediatric patient: principles, techniques, and clinical applications. *Radiographics*. June 2005;25(3):603–18.
 26. Akhlaghpour S, Aziz Ahari A, Ahmadi SA, Arjmand Shabestari A, Gohari Moghaddam K, Alinaghizadeh MR. Histological evaluation of drill fragments obtained during osteoid osteoma radiofrequency ablation. *Skeletal Radiol*. May 2010;39(5):451–5.
 27. Chai JW, Hong SH, Choi J-Y, Koh YH, Lee JW, Choi J-A, et al. Radiologic diagnosis of osteoid osteoma: from simple to challenging findings. *Radiographics*. May 2010;30(3):737–49.
 28. Lee MH, Ahn JM, Chung HW, Lim HK, Suh JG, Kwag HJ, et al. Osteoid osteoma treated with percutaneous radiofrequency ablation: MR imaging follow-up. *Eur J Radiol*. November 2007;64(2):309–14.

Wide area detector CT perfusion: Can it differentiate Osteoid Osteomas from other lytic bone lesions?

Pedro A. Gondim Teixeira, Sophie Lecocq, Matthias Louis, Ariane Raymond, Sabine Aptel, François Sirveaux, Alain Blum

Submitted to the *Journal of Diagnostic and Interventional Imaging* on August 13th 2013.

Abstract

Objective: To compare the enhancement dynamics of osteoid osteomas with other benign and malignant lytic bone lesions using CT perfusion.

Methods: CT perfusion parameters of 15 patients with a final diagnosis of osteoid osteoma, 15 patients with lesions that mimic osteoid osteomas and 26 patients with other bone lytic lesions were compared.

Results: Enhancement curve morphology of the osteoid osteomas was significantly different from its mimickers. All osteoid osteomas had an early enhancement with a delay between nidus and arterial peak below 30 seconds. 80% of the mimickers demonstrated a slow and progressive enhancement. The perfusion parameters of the other lytic bone lesions were similar to those of the osteoid osteomas in 46.1% of the patients.

Conclusion: Early enhancement is suggestive but not pathognomonic of osteoid osteomas. Absent or delayed enhancement in similar lesions should evoke an alternative diagnosis. The same contrast enhancement dynamics of osteoid osteomas can be seen in other bone lesions, both malignant and benign.

Key words: Perfusion imaging, Multidetector Computed Tomography, Osteoid Osteoma, Bone neoplasms, differential diagnosis.

Introduction

Osteoid Osteomas are a relatively frequent benign bone tumor of children and young adults that typically causes chronic inflammatory type pain (1–3). The imaging diagnosis of osteoid osteomas is based on the identification of a small translucent nidus, with a central calcification and a marked reactive sclerosis surrounding it. These features can be identified on conventional radiographs but computed tomography (CT) remains the method of choice for the diagnosis (4).

The diagnosis of typical osteoid osteomas is usually straightforward. These lesions however, may lack its distinctive features, especially when they are intra-articular or located in the small carpal or tarsal bones (5). Imaging features of osteoid osteomas are less characteristic and may be misleading with magnetic resonance (MR) imaging (6,7). Additionally, other conditions such as sub acute osteomyelitis (brodie's abscess), stress fractures and other intra or peri-cortical bone neoplasms, may be difficult to differentiate from osteoid osteomas (1,5).

The evaluation of contrast enhancement dynamics has been shown to increase the accuracy of the non-invasive diagnosis of osteoid osteomas (8,9). Enhancement curves with an early enhancement and a distinct washout or with a plateau were described for osteoid osteomas (9). This enhancement pattern, however, has not yet been compared to that of potential osteoid osteomas mimickers or to that of other lytic bone lesions. Other lytic bone lesions with a similar enhancement pattern might hinder the diagnosis of osteoid osteomas and may be a potential source of diagnostic error.

CT is frequently used for the evaluation of lytic bone lesions. Low dose CT perfusion may have a role in the characterization and pre-operative planning of these patients. In some countries there is still a non negligible waiting time for an MR examination. In France the mean delay for an MR examination is 32 days, and it can be as high as 50 days depending on the region. Hence the use of CT perfusion could be interesting to expedite the diagnosis of a lytic bone lesion. The use of iterative reconstruction algorithms and large area detector CT systems to perform perfusion lead to a major reduction in radiation dose exposure which allows the use of this technique in selected patients (10–12). The purpose of this study is to compare the CT perfusion parameters (curve morphology, time-to-peak, and delay between arterial and tumor peaks) of osteoid osteomas to that of other lytic bone lesions.

P. Teixeira – Corresponding author, S. Lecocq, M. Louis, A. Raymond, S. Aptel, A. Blum
Service d'Imagerie Guilloz, Hôpital Central, CHU-Nancy, 29 Av. Mar Lattre de Tassigny, 54000 Nancy, France.
e-mail: ped_gt@hotmail.com

François Sirveaux
Service de Chirurgie Traumatologique et Orthopédique, Centre Chirurgical Emile Gallé, 54000 Nancy, France.

Material and Methods

Patients

54 patients who underwent CT perfusion at our institution from January 2010 to February 2012 were prospectively evaluated. This study, which includes MR and CT evaluations both, was approved by the local ethics committee and the AFSSAPS (French FDA equivalent). These patients had been referred for the evaluation of lytic bone lesions. All patients were over 18 years old and signed an informed consent for all the imaging studies performed. 15 of these patients had a final diagnosis of osteoid osteomas (osteoid osteoma group). 15 of these patients had bony lesions with conventional CT features suggestive of osteoid osteoma but the diagnosis of osteoid osteoma was ruled out by other imaging methods and/or clinical or histological findings (mimickers group). The other 26 patients had a histologically confirmed lytic bone lesion other than osteoid osteomas (other tumors group). MR imaging with sequences before and after injection of a gadolinium based contrast media was performed in all patients included.

The osteoid osteoma group was composed of 12 males and 3 females with an age range of 19 to 52 years. In all patients of the osteoid osteoma group were treated with percutaneous laser therapy or radiofrequency ablation. None of these patients have been previously treated. Bone biopsy was performed with 11 to 14G needles at the same time of treatment for all patients. All patients demonstrated a good response to the percutaneous treatment with a return to normal activities no residual diurnal or nocturnal pain two months after treatment. Histologic evaluation of the bone fragments yielded histological confirmation of osteoid osteoma in 7 patients. In the remaining 8 patients the histologic diagnosis of osteoid osteoma was not reached. The diagnostic confirmation in these cases was based on its imaging characteristics, clinical findings, response to therapy and absence of an alternative diagnosis at histologic analysis. The imaging signs considered as inclusion criteria and that were present in all patients in the osteoid osteoma group were: Hypodense lesion on CT (nidus) smaller than 2 cm; sclerotic bone reaction adjacent to the lesion; inflammatory type reactive changes on T2 weighted fat-saturated around the nidus and detectable nidus enhancement at MR. All patients were examined and interviewed by a radiologist (AB) with 21 years of clinical experience before and after percutaneous treatment. The clinical findings used as inclusion criteria and presented by all patients were: chronic non-mechanical pain for more than 6 months; pain worse at night; pain relieved by aspirin. All the patients without a histologic diagnosis were followed for at least 2 months after treatment. The bone biopsies of these patients yielded normal or sclerotic cortical tissue. The osteoid osteomas included were located at: Shoulder (2 patients), forearm, elbow, lumbar spine (3 patients), hip (2 patients), around the knee (4 patients) and foot and ankle region (2 patients).

The mimickers group was composed of 6 males and 9 females with an age range of 21 to 65 years. These patients had been referred for the investigation of bone tumors. The inclusion criteria for this group were: a small cortical/sub-cortical lytic bone lesion (13 cases) or an important bone/periosteal sclerosis without a well defined lytic lesion (2 cases) and a final diagnosis other than osteoid osteoma. Lesions larger than 2 cm in the long axis and without a cortical or sub-cortical location were excluded from this group.

In eight of the patients included in the mimickers group percutaneous bone biopsy yielded a diagnosis other than osteoid osteoma. In two patients bone biopsy revealed only normal bone tissue. One had a sclerotic bone reaction related to a systemic inflammatory disease confirmed by other imaging findings (bilateral sacroiliitis). Imaging follow up in this patient demonstrated a near complete regression of the lesion after medicamentous treatment. The second patient had an extra-articular lytic bone lesion of the distal femur with no bone marrow edema, no reactive sclerosis and no uptake in SPECT CT. These findings rule out the diagnosis of osteoid osteoma with reasonable confidence.

The other five patients included in the mimickers group had no histologic confirmation. One of these patients had an odd appearing bone stress reaction found to regress on an imaging control after the cessation of excessive physical activity. The other four patients had benign appearing lytic bone lesions with regular contours, no cortical rupture and no invasion of the adjacent soft tissues (no touch lesions). These patients were either asymptomatic (1 patient) or presented discomfort (3 patients) that was not clearly associated with the bone lesion. In these patients and the imaging aspect of these lesions did not warrant a bone biopsy. In one patient the lytic bone lesion disappeared spontaneously in the control study leaving a sclerotic bone reaction at its place. Patients without sufficient evidence to exclude the diagnosis of osteoid osteoma beyond reasonable doubt were excluded. The other tumors group was composed of 26 patients with lytic bone lesions of larger than 2 cm in any location with a final diagnosis other than osteoid osteoma confirmed either by percutaneous or surgical biopsy. This group was composed of 15 males and 11 females with an age range of 20 to 86 years.

Patients with metallic artifacts in the studied region, with a known malignancy diagnosed elsewhere and with known metastatic disease were excluded. Patients under 18 years old were not allowed to sign the informed consent and were also excluded.

Imaging protocol

All studies were performed in a CT scanner with a large detector system composed of 320-detector row (Aquilion ONE, Toshiba Medical Systems, Otawara, Japan). The patients with lesions located in the extremities were immobilized with an inflatable splint. Perfusion study was performed with an intermittent acquisition mode with no table feed. The protocol included 14-16 volumes (Tube rotation: 0.5 s, slice

thickness: 0.5 mm, matrix of 512 x 512). The first 10 volumes were acquired with a 5 second delay between them (arterial phase). The last 4-6 volumes were acquired with a 10 second delay between them (venous phase). Tube output parameters were adapted to the anatomic region. A dual injection pump (Stellant D, Medrad INC, Indianola, PA, USA) was used for contrast injection. Iomeron® 400 (Bracco Imaging, Evry, France), with a concentration of 400 mg/ml was injected in all patients. A total of 150 ml was injected in a single bolus through a peripheral venous access (18 G cannula) with an injection rate of 5 ml/s. Acquisition started 5 seconds after contrast injection. Total examination length was dependent on the number of volumes and varied from 85 to 105 seconds. The coverage in the z axis varied from 4 to 8 cm.

MR was performed with a GE Healthcare 1.5T Signa HDxt scanner using dedicated coils. MR studies were performed within less than a week delay from the CT perfusion study. Conventional sequences were acquired and included at least one T1 weighted sequence and T2 fat-saturated sequences in two different orthogonal planes. Gadolinium was injected in all patients. T2-weighted fat-saturated FSE images were used for the identification of bone marrow edema.

Image analysis and post processing

2 fellowship trained radiologists with 21 and 5 years of clinical experience in musculoskeletal radiology post processed all the images. CT perfusion images from the patients included were post processed using the AW console version 4.4 GE Healthcare in the same manner. The ROIs were placed inside the center of the lytic lesion and in a nearby artery in axial 0.5 mm images. In the osteoid osteoma and the mimickers group the slice that depicted the largest portion of the lytic lesion was selected for the whole evaluation. The ROIs were sized and positioned to occupy the largest area of the bone lysis. In the two patients with bone sclerosis and no visible lytic lesion the ROI was placed in least dense part of the sclerosis. In the other tumors group the ROIs were positioned in the region of maximal tumor enhancement. Time-to-density curves were constructed.

Curve morphology analysis was based on the classification proposed by Van Rijswijk et al. (13). Type I designates a flat curve, Type II a progressive enhancement with no enhancement peak, type III an enhancement peak followed by a plateau, type IV an enhancement peak followed by a washout and type V an enhancement peak followed by a progressive enhancement. The analysis of the perfusion parameters was performed in consensus. Semi-quantitative CT perfusion parameters (time-to-peak, delay between the arterial and lesion peaks) were calculated every time a peak of enhancement was identified (curves type III, IV and V). These parameters were not calculated for curves type I or II. Curves type I represent no detectable enhancement. With respect to curves type II the time-to-peak and the delay between the arterial and lesion peaks are entirely defined by the length of the acquisition, since the tumor probably

continues to enhance after the end of the acquisition. Enhancement was considered significant if an increase of more than 15 Hounsfield units (HU) was detected.

Table 1 – Perfusion characteristics of the lesions included in the Osteoid Osteoma group.

	Location	Curve	Time-to-peak (s)	Arterial-tumor peak delay (s)
Patient 1	knee	IV	44	5
Patient 2	Elbow	III	60	25
Patient 3	knee	IV	60	20
Patient 4	knee	IV	50	5
Patient 5	Shoulder	IV	50	15
Patient 6	fore arm	IV	45	5
Patient 7	foot	III	85	15
Patient 8	hip	IV	40	5
Patient 9	spine	IV	50	15
Patient 10	Knee	III	68	25
Patient 11	Hip	IV	38	11
Patient 12	Spine	IV	35	5
Patient 13	Shoulder	IV	43	7
Patient 14	Ankle	IV	43	5
Patient 15	Spine	IV	25	5

All conventional CT were evaluated in a PACS station (Impax V5, AGFA HealthCare, Ivry-sur-Seine, France). The Fisher exact test was used for the analysis of the statistic significance of the variation in curve types amongst the three different groups. The Students exact T test was used for the analysis of the statistic significance of quantitative data. A p value less than 0.05 was used as the threshold for statistic significance.

Results

All the nidi of the osteoid osteoma group showed a detectable enhancement on CT perfusion. Nidus size varied from 0.3 to 1.8 cm. All the lesions in this group presented an enhancement peak. In 12 lesions the enhancement curve was classified as type IV and in three as type III. In the osteoid osteoma group the time-to-peak varied from 35 to 85 seconds, with a mean of 49.0 (+/- 14.6) seconds. The lesion with an 85 second time-to-peak had an osteoid osteoma of the forefoot, explaining the longer delay with respect to the other lesions. The delay to the arterial peak varied from 5-25 seconds in this with a mean of 12.2 (+/- 7.5) seconds (table 1). In the mimickers group the lesion size varied from 0.3 to 1.9 cm, six of them had a central calcification. Five of the lesions in this group did not show a detectable enhancement on CT perfusion (curve type I). In the other 10 lesions the enhancement was detected on CT perfusion. The enhancement curve was classified as type II in seven cases, as type III in one case and as type IV in two cases (table 2). In the

Table 2 – Clinical and perfusion characteristics of the lesions included in the Mimickers group.

	symptoms	Location	Final diagnosis	Histology	curve type
Patient 1	local pain	greater trochanter	no touch lesion	no	I
Patient 2	post traumatic chronic pain	distal fibula	benign cortical hyperostosis	yes	I
Patient 3	inflammatory type pain	Proximal humerus	giant bone island	no	I
Patient 4	local pain	Tibia	Systemic inflammatory disease	normal bone	I
Patient 5	inflammatory type pain	Tibia	fibro-myxoid Chondroma	yes	II
Patient 6	Pain after exercise	greater trochanter	Chondroblastoma	yes	III
Patient 7	asymptomatic	Distal femur	giant cell tumor	yes	II
Patient 8	Local pain	Femur	no touch lesion	normal bone	II
Patient 9	inflammatory type pain	Pedicle L5	Systemic inflammatory disease	no	II
Patient 10	palpable mass no pain	Middle phalanx 4th finger	no touch lesion	no	IV
Patient 11	Pain after exercise	tibia	bone stress reaction	no	II
Patient 12	diffuse and chronic pain	ulna	Osteomyelitis	yes	IV
Patient 13	local pain	Proximal phalanx 3rd finger	encondroma	yes	II
Patient 14	asymptomatic	Distal phalanx hallux	encondroma	yes	I
Patient 15	local pain	Femur	Chondrosarcoma	yes	II

later three cases (curved types III and IV) the time-to-peak values were 60, 35 and 35 seconds with a mean of 43.3 (+/- 14.0) and the delays between the arterial and tumor peak were 5, 25 and 5 seconds with a mean of 11.6 (+/- 11.5) seconds. An osteomyelitis, a chondrosarcoma and a benign appearing asymptomatic lytic bone lesion with no histologic diagnosis were the final diagnosis in the cases with curves types III and IV. 80% of the lesions in this group presented curve types I or II. The differences in curve type between the osteoid osteoma group and the mimicker's group were statistically significant ($p < 0.0001$).

Among the lesions included in the other tumors group there were 10 chondrosarcomas, 3 giant cell tumors, 2 metastasis, one conventional osteosarcomas, one enchondroma, one paraosteal osteosarcoma, one aneurismal bone cyst, one

Ewing tumor, one adamantinoma, one clear cell chondrosarcoma, one eosinophilic granuloma, one unicameral bone cyst, one spindle cell sarcoma and one plasmacytoma. 18 out of 25 of these tumors were malignant. Lesion size varied from 3.8 to 24 cm (mean = 8.4 cm). There was no preferential curve morphology for malignant or benign lesions, and none of the perfusion parameters evaluate allowed this distinction in the population studied. In all the lesions included in this group conventional CT findings were sufficient to rule out the diagnosis of osteoid osteoma. A table with the histologic diagnosis and the perfusion parameters studied in this group is presented (table 3).

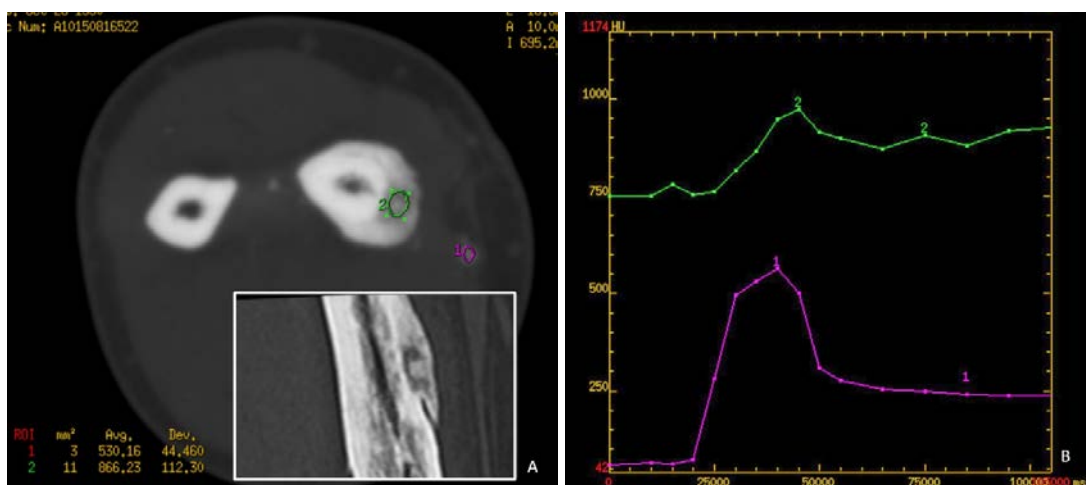


Fig. 1 - 26 year old male with a biopsy proven osteoid osteoma of the radius. A) Axial CT images demonstrating ROI placement in the nidus (green ellipsis) and in the nearby radial artery (purple ellipsis). Note the marked periosteal reaction around the lesion. The image in a white frame on the bottom left of A) demonstrates the global aspect of the lesion in a coronal oblique CT image. Note the central calcification and the reactive bone sclerosis. B) CT perfusion time-to-density curve (Hounsfield units x milliseconds) of the same patient demonstrating an early and steep enhancement of nidus (green curve) with respect to the artery (purple curve), followed by a washout (curve type IV).

Table 3 - Histology and perfusion characteristics of the tumors included in the other tumors group.

	Histology	Location	Curve type	TTP (s)	ATPD (s)
Patient 1	Chondrosarcoma	proximal femur	II	x	X
Patient 2	Chondrosarcoma	distal femur	II	x	X
Patient 3	Giant Cell Tumor	distal femur	II	x	X
Patient 4	Chondrosarcoma	proximal humerus	II	x	X
Patient 5	Chondrosarcoma	5th metatarsal	II	x	X
Patient 6	ABC	Distal fibula	III	44	9
Patient 7	Giant Cell Tumor	Distal femur	IV	45	10
Patient 8	Paraosteal Osteosarcoma	Iliac wing	II	x	X
Patient 9	Clear Cell Carcinoma	proximal humerus	IV	40	0
Patient 10	Chondrosarcoma	Distal femur	IV	70	30
Patient 11	Chondrosarcoma	Proximal femur	III	30	5
Patient 12	Chondrosarcoma	Acetabulum	II	x	X
Patient 13	Eosinophilic Granuloma	Scapula	II	x	X
Patient 14	Adamantinoma	Tibial diaphysis	II	x	X
Patient 15	Osteosarcoma	Iliac wing	I	x	X
Patient 16	Ewing's Sarcoma	Iliac wing	III	40	10
Patient 17	Chondrosarcoma	proximal humerus	I	x	X
Patient 18	Enchondroma	proximal humerus	II	70	35
Patient 19	Spindle Cell Sarc	Ischio pubic	IV	46	10
Patient 20	Chondrosarcoma	Femoral diaphysis	III	34	10
Patient 21	Simple Cyst	proximal humerus	I	x	X
Patient 22	Plasmocytoma	Ischium	IV	30	5
Patient 23	Metastasis	Ischio pubic	III	37	15
Patient 24	Metastasis	Iliac wing	III	37	5
Patient 25	Giant Cell Tumor	distal femur	III	36	10
Patient 26	Chondrosarcoma	Thumb	II	x	X

TTP = Time-to-peak

ATPD = Arterial-tumor peak delay

ABC = Aneurismal bone cyst

Three of the lesions in the other tumors group (11.5%) did not present a detectable enhancement (curve type I). Among the lesions that showed enhancement in 11 (42.3%) the curve was classified as type II and 12 (46.1%) were classified as types III or IV. In the later lesions (curve types III or IV) the time-to-peak varied from 30 to 70 seconds, with a mean of 40.7 (+/- 10.6) seconds. The delay to the arterial peak varied from 5-30 seconds in this with a mean of 9.9 (+/- 7.3) seconds. The perfusion pattern in this group was significantly different than that of the osteoid osteoma group ($p=0.0002$), however the difference between the time-to-peak and the delay to the arterial peak were not significant ($p=0.259$ and 0.84 respectively).

Among the lesions that presented a curves type III or IV there were three chondrosarcomas, two giant cell tumors, one aneurismal bone cysts, one clear cell sarcoma, one spindle cell sarcoma, one Ewing sarcoma, one plasmocytoma and two metastasis (adenocarcinoma and epidermoid carcinoma). When other imaging features were taken in account (lesion morphology and imaging characteristics on conventional CT or MR), the differentiation of these lesions from osteoid osteomas posed no difficulty.

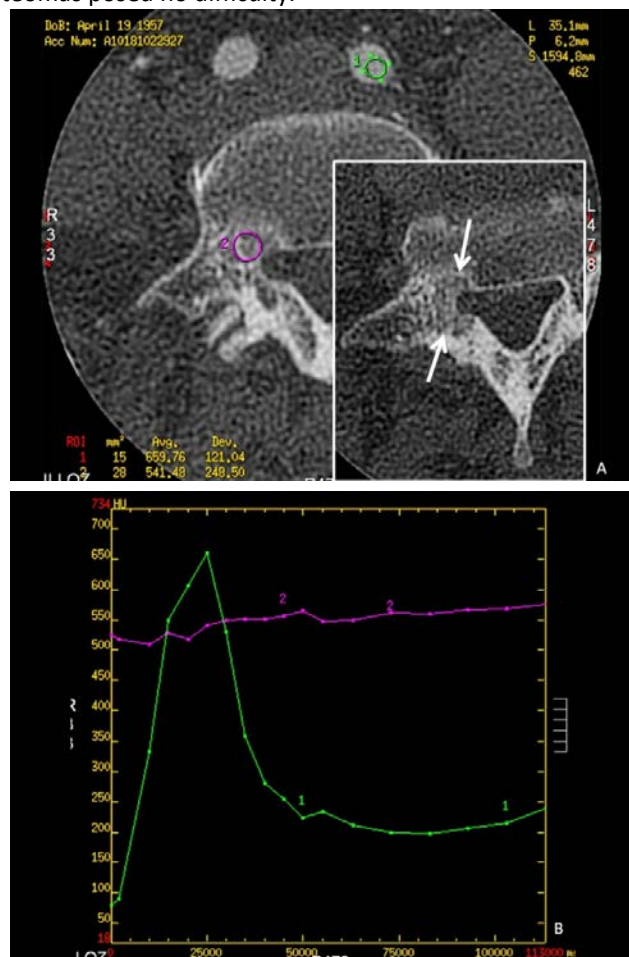


Fig. 2 – 54 year-old female with inflammatory type lumbar pain. A) Axial CT images demonstrating the ROI placement in a lytic bone lesion of the right pedicle of the 5th lumbar vertebra (purple circle) and in the right iliac artery (green circle). The picture in the white frame in A) shows the global aspect of the lytic lesion (white arrows) surrounded by reactive bone sclerosis. B) CT perfusion time-to-density curve (Hounsfield units x milliseconds) of the same patient demonstrating a delayed progressive enhancement of the lesion (purple curve) with respect to the artery (green curve). This lesion disappeared spontaneously in a control CT study performed 3 months later (images not shown).

Discussion

CT perfusion demonstrated a type III or IV in all osteoid osteomas studied. These lesions demonstrated an early enhancement with a peak enhancement shortly after the arterial peak (mean 11s). This finding is consistent with

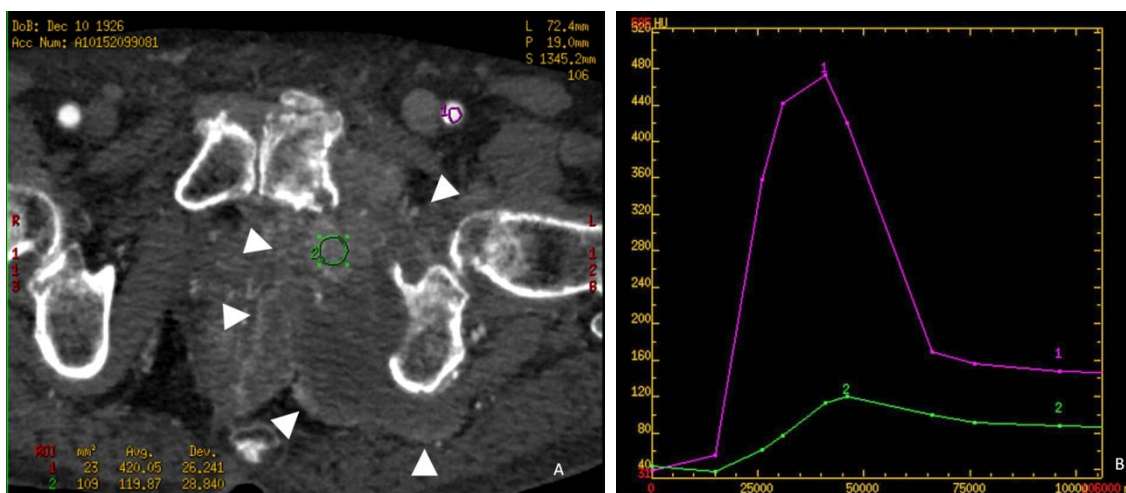


Fig. 3 – 84 year-old male with a biopsy proven spindle cell sarcoma of the left acetabulum and left ischio-pubic branch. A) Axial CT images demonstrating the ROI placement in a large lytic bone lesion with soft tissue invasion at the level left ischio-pubic branch (green circle) and in the left femoral artery (purple circle). The white arrowheads delineates the mass contours. B) CT perfusion time-to-density curve (Hounsfield units x milliseconds) of the same patient demonstrating an early and steep enhancement of lesion (green curve) with respect to the artery (purple curve), followed by a washout (curve type IV).

previous reports describing the enhancement dynamics of osteoid osteomas on MR perfusion and is probably related to highly vascular nature of the nidus (1,4,8,9,14,15) (Fig. 1). The pattern of enhancement in the osteoid osteomas group was significantly different than that of the mimickers and the other tumors groups. These results demonstrate that an early and steep enhancement (types III or IV) is indicative of osteoid osteomas but it is not pathognomonic of this lesion. A similar pattern was found in other lytic bone lesions studied. If curve type III or IV and a short delay between tumor and arterial peaks are considered as a diagnostic criteria for osteoid osteomas CT perfusion allowed to rule out the diagnosis of osteoid osteomas in 80% of the lesions included in the mimickers group (Fig. 2). Nevertheless this type of enhancement was found in a small percentage of the osteoid osteoma mimickers and in those cases the imaging findings were not sufficient to rule out the diagnosis of osteoid osteoma. Hence, the presented results demonstrate that for small lytic cortical or sub-cortical lesion the absence of enhancement or a delayed enhancement (curve type II) on CT perfusion makes the diagnosis of osteoid osteoma unlikely. The type of enhancement seen in osteoid osteoma group was significantly different than that of the other lytic lesions studied. In despite of this difference curves type III and IV were frequently found in the other lytic bone lesions studied. In 46.1% of the lesions included in the other tumors group an early enhancement (curves type III or IV) was found (Fig. 3). Additionally there were no significant differences in the time-to-peak and in the delay between the arterial and nidus peaks in these two groups. In these patients the differentiation from osteoid osteomas was not possible with CT perfusion alone. The diagnosis of osteoid osteomas in these patients was easily ruled out when conventional CT findings were taken in consideration, such as tumor size, surrounding sclerosis, periosteal reaction and etc.

Previous studies have suggested that an early enhancement is more frequent in malignant soft tissue lesions (13). Bone tumors are a very heterogeneous group of pathology with respect to histology and imaging features (16). There was no correlation between the enhancement pattern on CT perfusion and the histology in the population studied. An early and steep enhancement like the enhancement pattern found in the osteoid osteomas group was found in both benign and malignant lytic bone lesions.

This study has limitations worthy of notice. Histologic confirmation was not possible for all osteoid osteomas. Since minimally invasive percutaneous ablation has been adopted as the treatment of choice for osteoid osteomas the rate of histologic confirmation of these lesions has dropped considerably (17–19). Clinical and imaging signs of osteoid osteomas have been extensively described, and so has the clinical response to percutaneous ablation (1,2,5,19,20). That, added to the absence of alternative diagnosis in the bone biopsies performed at the time of treatment provides sufficient evidence to support the diagnosis of osteoid osteoma in the cases without histologic confirmation. Additionally the perfusion parameters found in those cases was similar to that of the other osteoid osteomas confirmed histologically and to what is described in the literature(8,9,21). In the mimickers group, some patients with benign appearing bone lesion did not have histologic confirmation. In these cases performing a bone biopsy (invasive procedure) was deemed unethical. There was a small variation in the number of venous phases in the CT perfusion protocol used. These variations represented an attempt to optimize our protocol, keeping radiation exposure to the lowest level possible. The variation in the number of venous phases had little influence in the perfusion analysis since the perfusion parameters evaluated (time-to-peak, delay between arterial and nidus peak and curve

morphology) related mostly to the enhancement on the arterial phase.

In summary, an early enhancement with a short delay between arterial and tumor peaks and curve morphology types III and IV are suggestive of osteoid osteomas. Absent or delayed enhancement (curve types I or II) in lesions with morphologic features of osteoid osteoma on conventional CT should evoke an alternative diagnosis. Although evocative of osteoid osteomas, CT perfusion alone is not sufficient for to make this diagnosis since the same contrast enhancement dynamics was found in various other lytic bone lesions, both malignant and benign. CT perfusion could represent an option to MR perfusion in selected patients, especially when the later is not readily available.

Acknowledgments

This work was supported by the French Society of Radiology (SFR- Société Française de Radiologie) through a research grant.

Bibliography

- Kransdorf MJ, Stull MA, Gilkey FW, Moser RP Jr. Osteoid osteoma. *Radiographics*. July 1991;11(4):671–96.
- Lee EH, Shafi M, Hui JHP. Osteoid osteoma: a current review. *J Pediatr Orthop*. outubro de 2006;26(5):695–700.
- Greco F, Tamburrelli F, Ciabattini G. Prostaglandins in osteoid osteoma. *Int Orthop*. 1991;15(1):35–7.
- Becce F, Theumann N, Rochette A, Larousserie F, Campagna R, Cherix S, et al. Osteoid osteoma and osteoid osteoma-mimicking lesions: biopsy findings, distinctive MDCT features and treatment by radiofrequency ablation. *Eur Radiol*. October 2010;20(10):2439–46.
- Chai JW, Hong SH, Choi J-Y, Koh YH, Lee JW, Choi J-A, et al. Radiologic diagnosis of osteoid osteoma: from simple to challenging findings. *Radiographics*. May 2010;30(3):737–49.
- Davies M, Cassar-Pullicino VN, Davies AM, McCall IW, Tyrrell PNM. The diagnostic accuracy of MR imaging in osteoid osteoma. *Skeletal Radiol*. October 2002;31(10):559–69.
- Hosalkar HS, Garg S, Moroz L, Pollack A, Dormans JP. The diagnostic accuracy of MRI versus CT imaging for osteoid osteoma in children. *Clin Orthop Relat Res*. April 2005;(433):171–7.
- Zampa V, Bargellini I, Ortori S, Faggioni L, Cioni R, Bartolozzi C. Osteoid osteoma in atypical locations: the added value of dynamic gadolinium-enhanced MR imaging. *Eur J Radiol*. September 2009;71(3):527–35.
- Von Kalle T, Langendörfer M, Fernandez FF, Winkler P. Combined dynamic contrast-enhancement and serial 3D-subtraction analysis in magnetic resonance imaging of osteoid osteomas. *Eur Radiol*. October 2009;19(10):2508–17.
- Gervaise A, Osemont B, Lecocq S, Noel A, Micard E, Felblinger J, et al. CT image quality improvement using Adaptive Iterative Dose Reduction with wide-volume acquisition on 320-detector CT. *Eur Radiol*. February 2012;22(2):295–301.
- Singh S, Kalra MK, Hsieh J, Licato PE, Do S, Pien HH, et al. Abdominal CT: comparison of adaptive statistical iterative and filtered back projection reconstruction techniques. *Radiology*. November 2010;257(2):373–83.
- Abadi S, Mehrez H, Ursani A, Parker M, Paul N. Direct quantification of breast dose during coronary CT angiography and evaluation of dose reduction strategies. *AJR Am J Roentgenol*. February 2011;196(2):W152–158.
- Van Rijswijk CSP, Geirnaerd MJA, Hogendoorn PCW, Taminiau AHM, van Coevorden F, Zwinderman AH, et al. Soft-tissue tumors: value of static and dynamic gadopentetate dimeglumine-enhanced MR imaging in prediction of malignancy. *Radiology*. November 2004;233(2):493–502.
- Liu PT, Chivers FS, Roberts CC, Schultz CJ, Beauchamp CP. Imaging of osteoid osteoma with dynamic gadolinium-enhanced MR imaging. *Radiology*. June 2003;227(3):691–700.
- Teixeira PAG, Chanson A, Beaumont M, Lecocq S, Louis M, Marie B, et al. Dynamic MR imaging of osteoid osteomas: correlation of semiquantitative and quantitative perfusion parameters with patient symptoms and treatment outcome. *Eur Radiol*. May 22nd 2013;
- Cotten A, Bera-Louville A. *Imagerie musculosquelettique*. Elsevier Masson; 2008.
- Cantwell CP, Obyrne J, Eustace S. Current trends in treatment of osteoid osteoma with an emphasis on radiofrequency ablation. *Eur Radiol*. April 2004;14(4):607–17.
- Akhlaghpour S, Aziz Ahari A, Ahmadi SA, Arjmand Shabestari A, Gohari Moghaddam K, Alinaghizadeh MR. Histological evaluation of drill fragments obtained during osteoid osteoma radiofrequency ablation. *Skeletal Radiol*. May 2010;39(5):451–5.
- Vanderschueren GM, Taminiau AHM, Obermann WR, van den Berg-Huysmans AA, Bloem JL, van Erkel AR. The healing pattern of osteoid osteomas on computed tomography and magnetic resonance imaging after thermocoagulation. *Skeletal Radiol*. September 2007;36(9):813–21.
- Lee MH, Ahn JM, Chung HW, Lim HK, Suh JG, Kwag HJ, et al. Osteoid osteoma treated with percutaneous radiofrequency ablation: MR imaging follow-up. *Eur J Radiol*. November 2007;64(2):309–14.
- Levine E, Neff JR. Dynamic computed tomography scanning of benign bone lesions: preliminary results. *Skeletal Radiol*. 1983;9(4):238–45.

Bone Marrow Edema Pattern Identification in Patients with Lytic Bone Lesions using Digital Subtraction Angiography-like Bone Subtraction on Large Area Detector CT.

Pedro A. Gondim Teixeira, Gabriela Hossu, Sophie Lecocq, Marco Razeto, Matthias Louis, Alain Blum

Accepted for publication in *Investigative Radiology* on September 13th 2013

Abstract

Objective: To evaluate the performance of CT with digital subtraction angiography (DSA) -like bone subtraction for the identification of BMEP in patients with lytic bone lesions.

Material and methods: 55 patients with a lytic bone lesion were included in this prospective study with ethics committee approval. All patients underwent MR imaging and low dose CT perfusion after signing an informed consent. Two CT volumes were used for bone subtraction, which was performed with two different algorithms (rigid and non-rigid). Enhancement at the non-lytic bone marrow was considered as a sign of BMEP. Two readers evaluated the images blindly. The presence of BMEP on bone subtracted CT images was evaluated subjectively and quantitatively. Image quality was assessed. MR imaging was used as the gold standard.

Results: Using a rigid registration method the sensitivity, specificity, PPV, NPV and accuracy of CT with DSA-like bone subtraction BMEP was 77%, 100.0%, 100.0%, 68%, 85%. The interobserver variability was good (Kappa 0.782). Image quality was better using a non-rigid registration. With this algorithm artifacts interfered with image interpretation in only 5% of cases. However, there was a noticeable drop in sensitivity and NPV when a non-rigid algorithm was used: 56% and 52% respectively. The interobserver variability was average with a non-rigid subtraction algorithm.

Conclusion: CT with DSA-like bone subtraction is sensitive and highly specific for the identification of BMEP associated with lytic bone lesions. Rigid registering should be preferred but non-rigid algorithms can be used as a second option when artifacts interfere with image interpretation.

Key words: Computed tomography; Bone marrow edema; Bone subtraction; bone tumors; image registration.

P. Teixeira – Corresponding author, S. Lecocq, M. Louis, A. Blum
Service d'Imagerie Guilloz, Hôpital Central, CHU-Nancy, 29 Av. Mar Lattre de Tassigny, 54000 Nancy, France.
e-mail: ped_gt@hotmail.com

P. Teixeira, G. Hossu. Université de Lorraine, IADI, UMR S 947, Tour Drouet
Rue du Morvan 54511 Vandoeuvre-lès-Nancy France.

M. Razeto. Toshiba Medical Visualization Systems Europe, Bonnington Bond
2 Anderson Place Edinburgh EH6 5NP, UK

Introduction

Some lytic bone lesions are associated with areas of bone marrow edema pattern (BMEP) on MR imaging. When present this feature is important for lesion characterization. Relatively few bone tumors (e.g. chondroblastoma, osteoid osteomas, osteoblastoma, eosinophilic granuloma, and malignant primary and secondary bone tumors) are associated with BMEP¹. Compared to malignant bone tumors, benign lesions tend to present larger surrounding areas of BMEP². In cases of malignant or aggressive bone tumors the extent of the peri-lesional BMEP zone is taken in consideration for the surgical planning, especially when a curative treatment is possible³. Additionally, the size of the edematous bone marrow reaction adjacent to a bone tumor may be used as a marker chemotherapeutic response⁴. Classically, BMEP zone can only be identified on MR imaging. It appears as an ill defined area of signal anomaly of the bone marrow, hypointense on T1 weighted images and hyperintense on T2 weighted sequences that enhances progressively after contrast injection^{5,6}.

CT remains the gold standard for the evaluation of tumoral calcification patterns, bone tumor margins and periosteal reaction which are important features for the characterization of bone neoplasms⁷⁻⁹. Contrast enhanced CT and MR imaging are part of the staging and pre-operative evaluation of bone tumors^{10,11}. Recent studies have demonstrated that BMEP can be identified using dual energy CT¹²⁻¹⁴. Digital subtraction angiography (DSA) -like bone subtraction allows calcification and bone removal (both cortical and trabecular) without any prejudice to the visualization contrast enhancement. This technique allows the identification of contrast enhancement on CT in a non-lytic bone background, and might be useful for the diagnosis of BMEP surrounding lytic bone lesions. DSA-like bone subtraction requires pre- and post- contrast volumetric acquisitions of the same anatomic area. Both volumes are then registered and subtracted by the use of dedicated software (fig. 1).

Multiple registering algorithms can be used to allow bone subtraction but there is no information in the literature as to which one is most useful for the evaluation of bone marrow enhancement. Additionally the performance of this technique

for the diagnosis of BMEP has not yet been assessed. The ability to identify BMEP on CT might increase the performance of this method in characterizing and staging bone tumors with minimal or no changes in the acquisition protocol. In this study we sought to evaluate the performance of DSA-like bone subtraction with two different registration methods (rigid and non-rigid) for the identification of BMEP in patients with lytic bone lesions using MR imaging as the gold standard.

Material and Methods

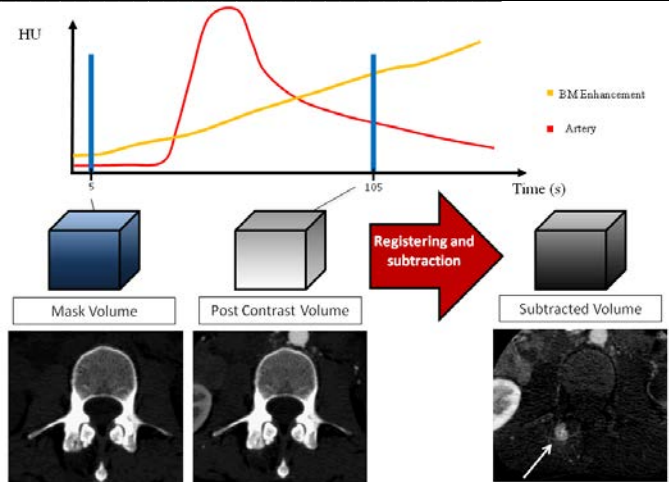
Patients

From October 2008 to March 2012 55 patients with a lytic bone lesion were included in a musculoskeletal tumor characterization protocol. This prospective study was approved by the local ethics committee. All patients were over 18 years old, signed an informed consent and underwent low dose CT perfusion and contrast enhanced MR imaging. Patients with previous surgery or with metallic implants or artifacts were excluded. One patient with a large bone tumor was excluded because there was no non-lytic bone marrow available in the study zone. Thus the final study population was composed of 54 patients.

Imaging protocol and post processing

The patients were imaged with a GE Healthcare 1.5T MR scanner Signa HDxt with dedicated coils and a standard acquisition protocol. A T1-weighted fast spin-echo (FSE) sequence and a T2-weighted fat-saturated FSE sequences in at least two orthogonal planes were available for every patient. The acquisition parameters varied with respect to the anatomic region.

CT perfusion studies were performed in a large detector system CT scanner with 320 detector rows (Aquilion ONE, Toshiba Medical Systems, Otawara, Japan). Perfusion study was performed with an intermittent acquisition mode with no table feed. The volume acquisition time was 0.5 seconds, with 0.5 mm slice thickness and a reconstruction matrix of 512 x 512. A dual injection pump (Stellant D, Medrad INC, Indianola, PA, USA) was used for contrast injection. Iomeron® 400 (Bracco Imaging, Evry, France), with a concentration of 400 mg/ml was injected in all patients. 2 ml/kg (Maximum of 150 ml) of iodinated contrast material was injected in a single bolus through a peripheral venous access (18 G cannula) with an injection rate of 5 ml/s. Five seconds after contrast injection a non-enhanced volume was acquired, then 14-17 volumes were acquired with a variable delay between them. The last volume of the perfusion protocol was acquired 85 to 105 seconds after contrast injection depending on the number of volumes on the venous phase. The first and the last volumes of the perfusion protocol were used for bone



bone subtraction on CT. In the time to density graphic the bone marrow (BM) enhancement is represented by the orange curve. The arterial enhancement curve is represented in red. The blue lines in the graphic represent a CT volumetric acquisition 5 seconds after injection (mask volume) and 105 after injection (post-contrast volume). The corresponding images are displayed. The large red arrow represents the post processing stage of this technique where registering and subtraction of the volumes acquired is performed. As a result a third volume is created (subtracted volume). In this example from 24 year-old male with a partially calcified focal bone lesion of right posterior arch of L5 the visualization of the lesion's enhancement is clearly facilitated by bone subtraction (arrow).

subtraction. The first volume (pre contrast) is used as a mask for bone subtraction. Then both volumes are registered and subtracted. As a result a third volume is created (subtracted volume) on which BMEP evaluation was performed.

DSA-like bone subtraction was performed using a Vitrea research workstation (v.6.2, Toshiba Medical Systems, Otawara, Japan) with the RWS application v. 8.0 beta 1688. Two types of image registering were performed for each patient: rigid and non-rigid. Mutual Information (MI) is used as a similarity metric for both algorithms. The rigid registration algorithm used a strongly constrained search space, with only limited translation and rotation allowed, and no scaling. Optimization was performed using Powell's algorithm. The non-rigid registration algorithm is based on Crum, Hill and Hawkes method to obtain non-rigid warp-fields using a gradient ascent scheme¹⁵.

Image analysis

2 fellowship trained radiologists with 6 years (reader 1) and 22 years (reader 2) of clinical experience in musculoskeletal radiology analyzed all the images. Bone morphology was classified in three types: Long tubular, short and flat bones. The bone subtracted images were analyzed in two reading sessions. The patient list was in alphabetic order. First subtracted images using a rigid registration algorithm were evaluated. A second readout session was performed to evaluate a non-rigid registration algorithm for bone subtraction two weeks later. The readers were blinded to the

MR results and to clinical patient data. Conventional CT images were evaluated together with subtracted images to assist in localizing the areas of enhancement. Bone subtracted images were evaluated with the same window settings (width: 400, level: 40). The readers were allowed to change the window level of the non-subtracted CT images only. Coronal and sagittal reformats were accessible to the readers. The MR images were analyzed after both CT readouts in consensus.

The presence of enhancement in the non-lytic bone marrow adjacent to a lytic bone lesion was considered as a sign of BMEP on bone subtracted CT images. First, the subtracted images were subjectively evaluated for the presence or absence of BMEP immediately adjacent to the lytic bone lesion. BMEP was considered to be present when the density of the bone marrow adjacent to the lytic bone lesion was higher than that of normal appearing bone marrow seen elsewhere in the same anatomic area. The confidence in the identification of BMEP was classified as follows: Grade 1: distinct sign of BMEP with pronounced enhancement of the bone marrow; Grade 2: Less pronounced bone marrow enhancement, probably related to BMEP; Grade 3: Equivocal bone marrow enhancement, most likely BMEP; Grade 4: No detectable BMEP. On MR BMEP was considered to be present when the signal of the bone marrow adjacent to the lytic bone lesion on T2 weighted fat-saturated images was higher than that of normal appearing bone marrow seen elsewhere in the same anatomic area. Only signal changes immediately adjacent to the lytic bone lesions were considered. The same grading system was used for the subjective analysis of BMEP on MR images.

After the completion of the subjective evaluation on bone subtracted CT images bone marrow enhancement was quantitatively evaluated. The bone marrow enhancement was quantified in Hounsfield units (HU). Two ROI were placed in all subtracted volumes (both rigid and non-rigid subtraction algorithms). One ROI was positioned adjacent to the lytic bone lesion at the zone of maximum enhancement. When no BMEP was visible the ROI was placed immediately adjacent to the lytic lesion's border. The other ROI was positioned at an area of normal appearing bone marrow the farthest away from the lytic bone lesion as possible within the same bone. If normally appearing bone marrow was not available far for the lytic lesion in the same bone, density measures were performed other bone present in the same anatomic area. Care was taken to prevent placing the ROI in areas with misregistration artifacts. The mean density in Hounsfield units (HU) of the ROI positioned was considered. The radius of BMEP using the lytic lesion border as reference was compared between MR imaging and CT with DSA-like bone subtraction (Fig. 2).

The image quality after bone subtraction was also taken in consideration. These artifacts were characterized by black and/or white bands or dots adjacent to interfaces with a large difference in density (e.g. cortico-medullary junction). The

influence of miss the registration artifacts on image analysis was evaluated as follows: Grade 1: no identifiable artifacts; Grade 2: Artifacts without any compromise to image interpretation; Grade 3: Artifacts that compromise image interpretation; Grade 4: Important artifact precluding image analysis. A quantitative quality evaluation was also performed by considering the standard deviation of the density measurements performed.

Statistics

Sensitivity, specificity, positive predictive value (PPV), negative predictive value (NPV) and accuracy of CT with DSA-like bone subtraction for the detection of BMEP were calculated using T2 weighted MR images as the gold standard. The reproducibility of this technique was evaluated by calculating the Kappa value.

Statistical analysis was performed by using R Development Core Team software version R 2.13.1 (2011). Significance levels for BME radius size were determined by using a non-parametric two sided paired Wilcoxon signed rank test. For this variable normal distribution assumption was not confirmed by the Shapiro Wilk test. The normal distribution assumption of all densities measurements was also tested by the Shapiro Wilk test. If the normal distribution was confirmed the two sided paired t-test used for p values and confidence intervals calculation, if not the two sided paired Wilcoxon signed rank test was used. A p value less than 0.05 was used as the threshold for statistic significance. When multiple variables were compared the Bonferoni method was used to establish the threshold of statistic significance.

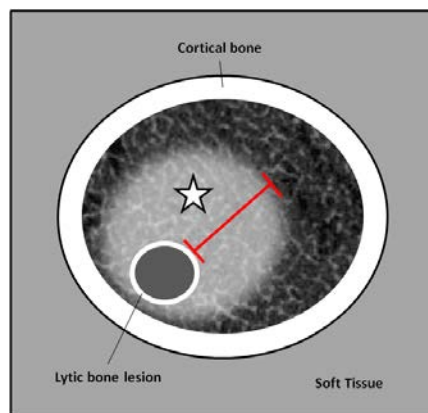


Fig. 2 – BMEP zone radius evaluation method. Scheme represents an axial CT image of a long tubular bone. A lytic bone lesion at the bone marrow is indicated. The BMEP zone is indicated by the white star. The distance from the lytic lesion's border and the outer limit of the BMEP zone was considered as measured.

Results

There were 38 male and 17 female patients in the studied population (M:F ratio = 1:0.4). The age varied from 18 to 77

years (mean 38.0 years). On MR images the justa lesional bone marrow was graded 1 or 4 in all but five patients. These patients were classified as 2 and 3 because there was a faint signal hyperintensity adjacent to the lytic bone lesion. These cases were considered as positive for BMEP. Based on this analysis two groups of patients were formed: with (36 patients) and without BMEP (19 patients). The mean age of the patients in these groups was 36.3 and 41.4 years respectively. 34 long tubular bones (20 with BMEP), 14 flat bones (11 with BMEP) and 7 (5 with BMEP) short bones were evaluated. Since the smaller coverage possible is used on CT to reduce dose exposure in two patients there was no normal appearing bone marrow within a reasonable distance from the lytic lesion. In these two cases quantitative analysis of the normal marrow was not possible.

If grades 1 to 3 were considered positive and grade 4 negative for BMEP the visual analysis of bone subtracted CT images using a rigid registration algorithm yielded a sensitivity, specificity, PPV, NPV and accuracy for the identification of BMEP of 69.4%, 100.0%, 100.0%, 57.8%, 80.0% for reader 1 and 86.1%, 100.0%, 100.0%, 79.1%, 90.0% for reader 2 respectively. Bone subtraction based on a non-rigid presented a lower performance for BMEP detection with a noticeable drop in specificity, and NPV for both readers: 47.2%, 89.4%, 89.4%, 52.7%, 61.6% for reader 1 and 66.6%, 73.6%, 82.7%, 53.8%, 69.0% for reader 2 respectively (Fig. 3). The interobserver variability was considered to be good when using the rigid registration algorithm (Kappa = 0.782) and average when using the non-rigid algorithm (kappa = 0.499). The diagnostic performance of DSA-like bone subtraction with both readers is summarized on table 1.

There was a significant difference in the density measurements with the two registering algorithms used. The density at the BMEP zones was significantly lower when using a non-rigid algorithm ($p = 0.0040$). The mean bone marrow

density adjacent to the lytic bone lesion was 51.1 ± 29.1 HU for the rigid registration and 37.9 ± 26.0 for the non-rigid registration. Inversely the density of the normal appearing bone marrow was higher when using a non-rigid algorithm ($p = 0.0020$). The mean density of the normal appearing bone marrow in the studied population was 12.3 ± 11.3 HU for the rigid registration and 17.5 ± 9.7 HU for the non-rigid registration. These differences in the density measurements with the two registrations algorithms used creates a higher contrast between the BMEP zones and the normal appearing bone marrow with the bone subtraction using rigid registration (Fig. 4). The mean CT number contrast between BMEP areas and the normal appearing bone marrow in the same patient for bone subtraction with rigid and non-rigid registration were 38.2 ± 28.8 HU and 19.4 ± 23.7 HU respectively. Quantitative analysis of bone subtracted CT images using a rigid registration algorithm using 18 HU as threshold yielded sensitivity, specificity, PPV, NPV and accuracy of 77.78%, 93.7%, 96.5%, 65.2% and 82.6% for the identification of BMEP. The same analysis this time using 10 HU as threshold with a non-rigid algorithm yielded the following sensitivity, specificity, PPV and NPV: 52.7%, 93.7%, 95.0%, 46.8% and 65.3%.

The BMEP zone radius was significant smaller on bone subtracted CT using both registration algorithms compared to T2 weighted fat-saturated MR images ($p < 0.0001$ for rigid and non-rigid registration). When the radius of BMEP zones calculated with rigid and non-rigid algorithms were compared the radius estimation tended to be smaller with the non-rigid registration. These differences were not statistically significant ($p = 0.0673$) (Fig. 5). The mean BMEP zone radius was 25.2 ± 16.1 mm on MR imaging, 12.0 ± 11.0 mm on CT with rigid bone subtraction and 8.1 ± 12.2 mm on CT with non-rigid bone subtraction.

Table 1- Diagnostic performance of CT with DSA-like bone subtraction with both registration methods evaluated.

Rigid Registration										
	TP	TN	FP	FN	Sensitivity	Specificity	PPV	NPV	ACC	Kappa
Reader 1	25	19	0	11	69.40%	100.00%	100.00%	57.80%	80.00%	0.77
Reader 2	31	19	0	5	86.10%	100.00%	100.00%	79.10%	90.00%	
Quantitative analysis	28	15	1	8	77.78%	93.70%	96.50%	65.20%	82.60%	
Non-Rigid registration										
	TP	TN	FP	FN	Sensitivity	Specificity	PPV	NPV	ACC	Kappa
Reader 1	17	17	2	19	47.20%	89.40%	89.40%	52.70%	61.80%	0.49
Reader 2	24	14	5	12	66.60%	73.60%	82.70%	53.80%	69.00%	
Quantitative analysis	19	15	1	17	52.70%	93.70%	95.00%	46.80%	65.30%	

TP = True positive, TN = true negative, FP = false positive, FN = false negative

PPV = Positive predictive value, NPV = negative predictive value, ACC = accuracy

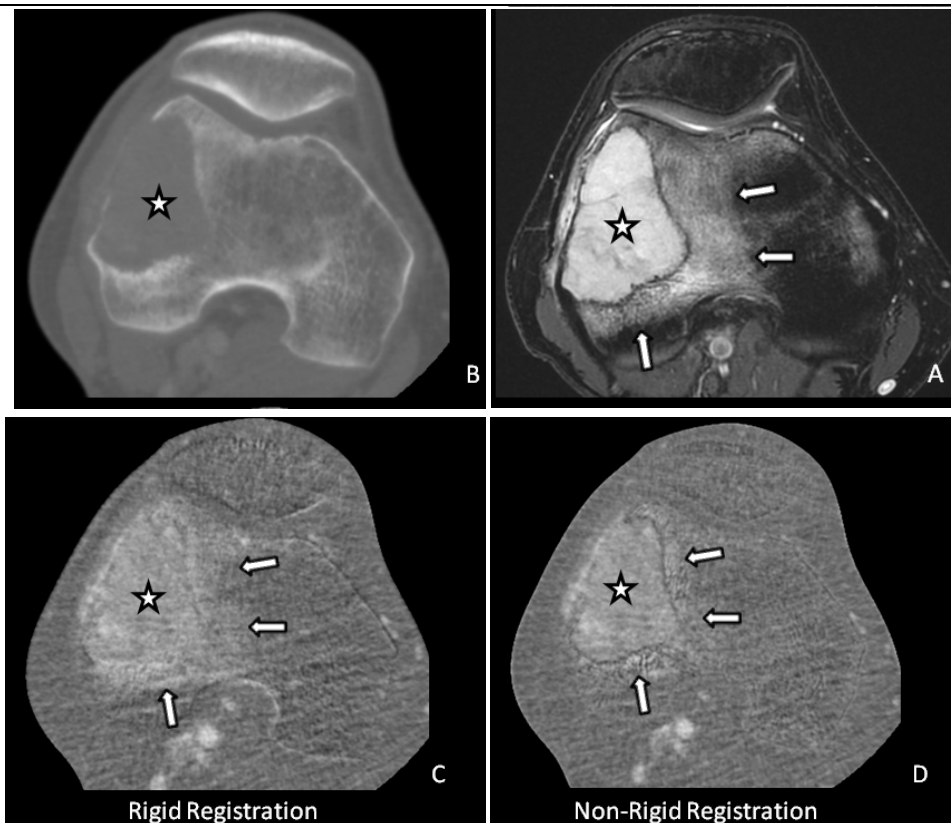


Fig. 3 - 30 year-old male with a histologically confirmed giant cell tumor of the distal femur. A) Axial T2 weighted fat-saturated MR image demonstrating a lytic bone lesion of the distal femur surrounded by an halo of BMEP (arrows). B) Axial conventional CT image of the same anatomic region with a bone window level. The lytic bone lesion is seen and there was no identifiable marrow enhancement, independent of the window level. C and D) CT with DSA-like bone subtraction with a rigid and non-rigid registration demonstrating a clear enhancement of the bone marrow adjacent to the lytic bone lesion indicative of the presence of BMEP (arrows). Note that the area of bone marrow enhancement has de same distribution as the BMEP seen on A). Intra lesion enhancement is also seen (star).

Misregistration artifacts were more frequent and important on bone subtraction with a rigid algorithm. Misregistration artifacts were identified by the two readers in 40 (72%) and 45 (81.4%) cases with rigid registration and in 11 (20%) and 24 (43.6%) cases with non-rigid registration (Fig. 6). With a rigid algorithm in 10 (18.1%) and 7 (12.7%) cases (for readers 1 and 2 respectively) these artifacts hindered image interpretation, whereas with a non-rigid algorithm this interference it was found only in 3 (5.4%) cases for both readers. Artifacts precluded bone marrow evaluation in two

patients for reader one using a rigid algorithm (these patients were considered to be negative for BMEP). The type of registration method also had a significant influence on the standard deviation (SDEV) of the density measurements in the studied population ($p = 0.0002$). The non-rigid registration yielded a smaller SDEV values. The mean SDEV at the bone marrow adjacent to the lytic bone lesion was 34.2 ± 15.3 HU and 29.3 ± 12.8 HU for rigid and non-rigid algorithms respectively.

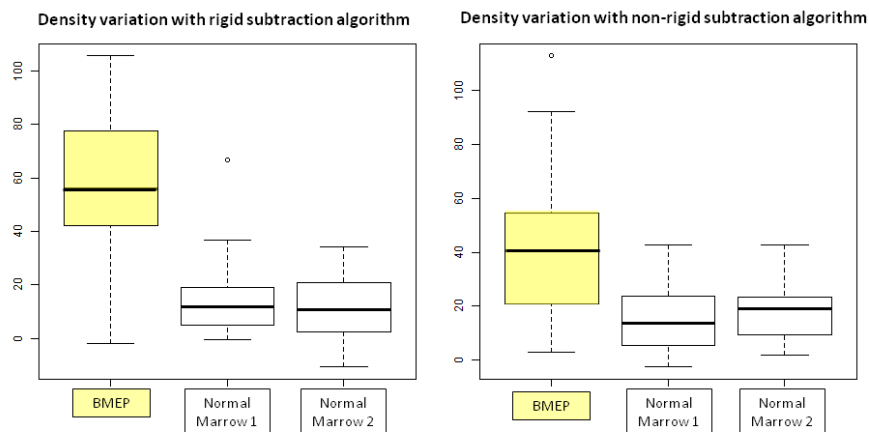


Fig. 4 - Boxplot graphic demonstration the density variation in Hounsfield units on CT with DSA-like bone subtraction of the BMEP areas and the normal appearing bone marrow adjacent to the lytic bone lesion (normal marrow 1) and away from the lesion (normal marrow 2) with rigid and non-rigid registration algorithms. Note the larger density contrast between BMEP areas and the normal marrow with rigid registration.

Table 2 summarizes the differences between bone subtraction with rigid and non-rigid registering algorithms.

The BMEP zone radius on MR imaging was smaller in false negatives than on true positive cases for both readers. The BMEP radii varied from 11.9-15.3 mm on false negative cases and 24.3- 27.3 mm for true positive cases with rigid registration. These figures were 16.5 - 16.6 mm and 30.4-26.2 mm with non-rigid registration. There were no identifiable differences in the patient age, BMEP location, image noise or artifact influence between true positive and false positive cases. The difference in density contrast between the BMEP zones and the normal bone marrow was inferior to 10 HU in 8 (72.7%) and 16 (84.2%) false negative cases for reader 1 using rigid and non-rigid registration respectively. For reader 2 the same was true in 3 (60%) and 6 (50%) cases for rigid and non-rigid registration. Additionally among the five cases which the BMEP was considered as grades 2 or 3 on MR images there were 4 false negatives with non-rigid registration for both readers. Using a rigid registration algorithm 4 of these cases for reader 1 and one for reader 2 were considered negative for BMEP (Fig. 7). In one case with no BMEP identifiable on MR there was a higher than 10 HU difference between the peri-lesional and the normal appearing bone marrow.

Discussion

Classic CT based bone subtraction techniques rely on the differences in density and morphology between the bone and the surrounding soft tissue¹⁶. Density based bone subtraction does not allow complete the visualization of intra-osseous enhancement. With this method the part of the intra-osseous contrast enhancement which shares a similar density with the surrounding bone trabeculae is subtracted from the image. Although bone marrow enhancement is measurable on conventional CT acquisitions, the high density background of non-lytic bone precludes visual identification of such enhancement on patients with a normal bone marrow mineralization. CT with DSA-like bone subtraction presented a high performance for the visual identification of BMEP adjacent to lytic bone lesions. The best performance was achieved when a rigid registering algorithm which had a sensitivity and specificity of 69-86% and 100% for BMEP identification. The inter-observer variability was good when rigid registering was used and average for when non-rigid registering was used. Quantitative analysis of the bone subtracted images using 18HU as a threshold presented similar results (77.7% and 93.7% of sensitivity and specificity). There are three reports in the literature on the use of dual energy CT with double source scanners for the diagnosis of BMEP¹²⁻¹⁴. The performance of dual energy virtual non-calcium for the evaluation of bone bruises after ankle trauma and for the identification of BMEP associated with vertebral compressive fractures has been evaluated in the literature^{13,14}. Compared to the performance of virtual non-calcium for the diagnosis of bone bruises at the ankle, DSA-like bone subtraction presented a discretely lower sensitivity (77.7% versus 90.0%) and a higher specificity and PPV (100% and 100% versus 80% and 25%). With respect to the detection of BMEP at the spine the overall performance between virtual non-calcium and DAS-like bone subtraction were also were practically the same¹³. The identification of BMEP associated with lytic bone lesions with a CT based technique has not yet been assessed. DSA-like bone subtraction requires two volumes (or phases) to be performed, one pre- and one post-contrast. Since a contrast injection is usually performed for the evaluation of some lytic bone lesions the use of DSA-like bone subtraction implies in minimal or no changes in the acquisition protocol^{10,11}. So far virtual non calcium technique has only been reported and evaluated using dual source CT scanners¹²⁻¹⁴. Dual energy with double source CT offers a wider spectral separation facilitation material decomposition¹⁷. In our experience virtual non-calcium images are difficult to acquire with other CT scanner designs such as wide area detector CT. In this context DSA-like bone subtraction can be considered as an alternative to virtual non-calcium dual-energy CT.

Image registration has been used in medical image analysis for over 20 years¹⁸. The goal of image registration is to establish a correspondence between two or more images of

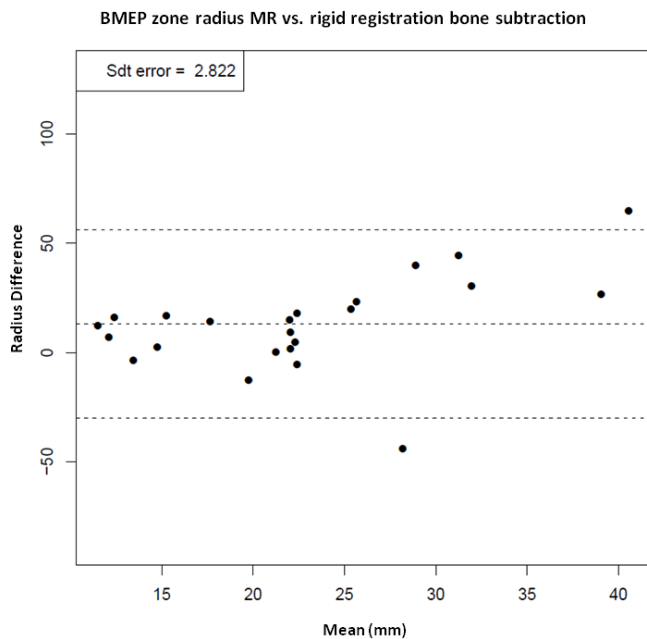


Fig. 5 – Bland Altman plot comparing the radius estimation between MR imaging and CT with DSA-like bone subtraction using a rigid algorithm. Note that the BMEP size is underestimated on CT with DSA-like bone subtraction and this effect tends to be more important when larger areas of BMEP are evaluated.

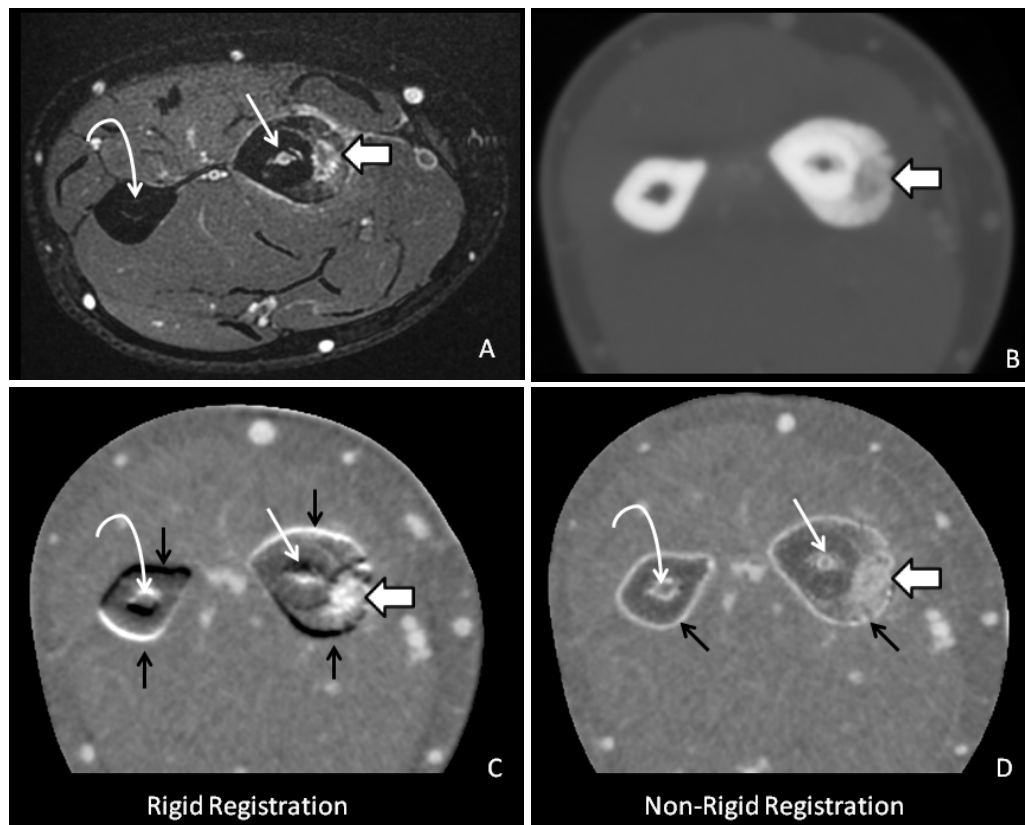


Fig. 6 - 20 year-old male with a radio-clinical diagnosis of an osteoid osteoma of the radius. MR, conventional CT, CT with DSA-like bone subtraction with rigid and non-rigid registration images are demonstrated in A, B, C and D respectively. The nidus is identified by the fat arrow in all images. A) BMEP is seen at the radius (straight arrow) but not at the ulna (curved arrow). C) Using a rigid registration bone subtraction prominent misregistration artifacts are identified as black and white bands adjacent to the boundaries of cortical bone (black arrows). These artifacts preclude a precise analysis of the bone marrow enhancement at the radius. D) With non-rigid registering misregistration artifacts are still and take the form of a white band adjacent to the bone cortex. Note that despite these artifacts a clear difference in enhancement is now identified at radial bone marrow.

the same anatomic region acquired in a different time¹⁹. Registration is the corner stone of DSA-bone subtraction and warrants an accurate bone removal with minimal influence on the enhancement analysis. There are basically two types of image registration: rigid, in which images are assumed to be objects that simply need to be rotated and translated with respect to one another to achieve correspondence; and non-rigid, in which the image has to be deformed to achieve correspondence due to through plane motion or biological change in tissue morphology²⁰. Non-rigid registration uses complex similarity and transformation models and requires longer post processing time²¹.

There were significant differences in the CT number measurements between rigid and non-rigid registering algorithms at both BMEP and normal appearing marrow areas. The contrast between BMEP zones and the adjacent bone marrow was lower using non-rigid subtraction. The mean density difference between normal marrow and BMEP zones was 19.3 HU lower with the non-rigid compared to the rigid registration. This reduction in image contrast explains

the lower sensitivity and inter-observer variability of bone subtraction with non-rigid registering for the identification of BMEP (69-86% versus 47-66% for rigid and non-rigid algorithms respectively). There are reports in the literature describing artefactual variations of perfusion parameters related to inconsistencies of non-rigid registration algorithms in separating motion artifacts from enhancement²². There are mainly two sources of error that may be caused by non-rigid registration algorithms: I) improper similarity measures may yield erroneous warp fields which may affect the texture of the image when large local contractions or expansions occur. In this case the intensity of the density alteration is related to the type of motion, the heterogeneity of the evaluated tissue (e.g. bone marrow) and the registering algorithm used²¹; II) an excessively narrow interpolation kernel may also have a smoothing effect. Both effects can lead to a global reduction of the density spectrum in the registered volume. The reduction in image contrast hinders the visual identification of BMEP using a non-rigid bone subtraction algorithm.

Table 2- Comparison between rigid and non-rigid registration algorithms for DSA-like bone subtraction

	Rigid	Non-Rigid
Performance for BMEP identification	High sensitivity and specificity	low sensitivity and high specificity
Interobserver variability	Good	Average
Estimation BMEP size	Underestimates the radius of the BMEP zone with respect to MR	Underestimates the radius of the BMEP zone with respect to MR
Artifacts	Frequent and may interfere with image interpretation in of about 15% of cases	Unusual. Interferes with image interpretation in 5% of cases

Robust motion correction is the main advantage of non-rigid registration algorithms²³. Misregistration artifacts appear most frequently as bands of black and white adjacent to the cortical bone borders (border-shift artifact) (Fig. 6). When a rigid subtraction algorithm was employed misregistration artifacts were more frequent (over 70% of cases) and interfered with image interpretation 12-18 % of cases. Additionally the standard deviation measures of the normal appearing bone marrow, used to estimate the background noise, was significantly lower with non-rigid registration ($p = 0.0002$). These results indicate that although rigid registering should be the first option for DSA-like bone subtraction non-rigid algorithms can be used as a second option when motion

artifacts or background noise are interfering with image interpretation.

The radius of the BMEP zone was significantly smaller using bone subtracted CT with respect to MR independent on the registering algorithm ($p < 0.0001$). Moreover the BMEP radius estimation tended to be lower when the non-rigid algorithm was used ($p = 0.0673$). These differences have two possible explanations. First, BMEP zones have hazy borders and its intensity tends to fade as the distance from the lesion epicenter increases. Since CT has a lower contrast resolution than MR the size of the BMEP tends to be underestimated. Second, on MR imaging BMEP is the expression of a mosaic of non specific histologic findings such as fibrosis, marrow necrosis, hemorrhage, trabecular reabsorption, and to a smaller extent edema²⁴. On the other hand CT assesses only enhancement variations between normal marrow and BMEP zones, which could lead to discrepancies on the radius measurements with these two methods.

The error analysis on the false negatives findings suggests that smaller BMEP zones are harder to identify on DSA-like bone subtraction CT. The mean size of BMEP radius on MR images in false negative cases was roughly half of that of the true positive cases. In the false negative cases the density difference between BMEP zones and normal bone marrow was also smaller. One possible explanation is that the variations in the red/yellow marrow ratio with patient age and anatomic location reduce the contrast between BMEP areas and the normal marrow²⁵. This hypothesis could not be verified with our results. A study with a larger patient population could help confirm these assumptions.

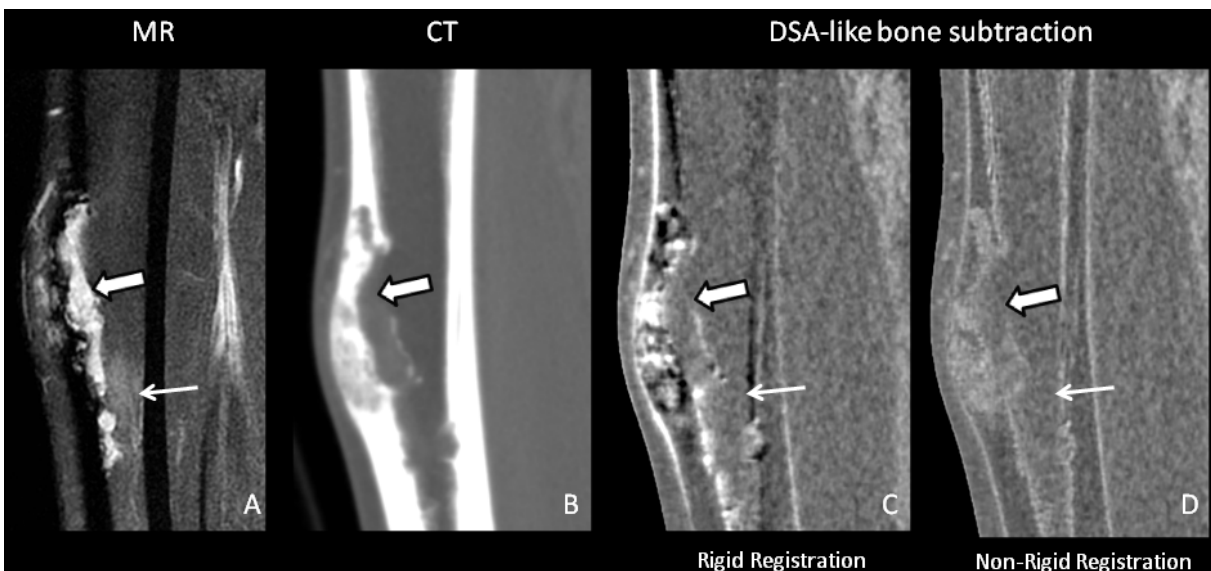


Fig. 7 - 21 year-old male with a slow growing cortical lesion of the tibia. Percutaneous bone biopsy was inconclusive. Imaging diagnosis was that of a osteofibrous dysplasia. A) Sagittal T2 weighted fat-saturated MR image of the tibia demonstrating a lytic bone lesion (fat arrow) and a small area of BMEP adjacent to the lower pole of the lesion (thin arrow). The corresponding image on CT is demonstrated on B), C) and D). Note that the foci of BMEP can be identified neither on conventional CT nor on CT with DSA-like bone subtraction independent of the subtraction algorithm used (thin arrows in B,C and D).

This work has important limitations. The readers were blinded to the MR findings and struggled to be impartial on subjective image analysis. However, the imaging aspect of the lytic bone lesion on conventional CT images, which were available at the time bone subtracted CT analysis, might have had an unintentional influence on the interpretation since some types of bone lesions are known to more frequently associated with BMPEP. The fact that the performance of the subjective and quantitative analysis was similar suggests that the influence of conventional CT imaging aspect on the results was minimal. Since histological confirmation of the areas of BMPEP was not available MR imaging was used as the gold standard. The influence of the different tissue components that are responsible expression of BMPEP on MR and on CT has been previously stated and are also a limitation for the direct comparison between CT and MR findings. Tube output parameters were adapted to the different anatomic areas studied, which might have influence the CT number of the iodinated contrast. This effect might have lead to location related variation in performance (lower sensitivity with high kVp values), which was not reflected in the results.

In conclusion the presented results indicate that CT with DSA-like bone subtraction can be used for the subjective and/or quantitative identification of BMPEP associated with lytic bone lesions with good sensitivity and high specificity. This technique may increase the diagnostic performance of CT for the characterization and for the pre-operative evaluation of patients with primary or secondary bone tumors. Despite the higher frequency of through plane motion artifacts rigid registration implies in a shorter post processing time and has better performance the identification of BMPEP. Rigid registering algorithms should be the first choice for DSA-like bone subtraction. Non-rigid registration offers an optimal motion correction at the expense of a lower specificity. It is an interesting option for selected studies in with persistent artifacts hindering image interpretation.

Acknowledgements

This work was supported by the French society of radiology (Société Française de Radiologie – SFR) through a research grant. We would like to thank Valerie Lamy for her great contribution on data transfer and post-processing.

Bibliography

- James SLJ, Panicek DM, Davies AM. Bone marrow oedema associated with benign and malignant bone tumours. *Eur J Radiol.* 2008;67(1):11–21. doi:10.1016/j.ejrad.2008.01.052.
- James SLJ, Hughes RJ, Ali KE et al. MRI of bone marrow oedema associated with focal bone lesions. *Clin Radiol.* 2006;61(12):1003–1009. doi:10.1016/j.crad.2006.07.007.
- Kawaguchi N, Matumoto S, Manabe J. New method of evaluating the surgical margin and safety margin for musculoskeletal sarcoma, analysed on the basis of 457 surgical cases. *J Cancer Res Clin Oncol.* 1995;121(9-10):555–563.
- Fletcher BD. Response of osteosarcoma and Ewing sarcoma to chemotherapy: imaging evaluation. *AJR Am J Roentgenol.* 1991;157(4):825–833. doi:10.2214/ajr.157.4.1892044.
- Wilson AJ, Murphy WA, Hardy DC et al. Transient osteoporosis: transient bone marrow edema? *Radiology.* 1988;167(3):757–760.
- Liu PT, Chivers FS, Roberts CC et al. Imaging of osteoid osteoma with dynamic gadolinium-enhanced MR imaging. *Radiology.* 2003;227(3):691–700. doi:10.1148/radiol.2273020111.
- Zimmer WD, Berquist TH, McLeod RA, et al. Bone tumors: magnetic resonance imaging versus computed tomography. *Radiology.* 1985;155(3):709–718.
- Teo HEL, Peh WCG. Primary bone tumors of adulthood. *Cancer Imaging Off Publ Int Cancer Imaging Soc.* 2004;4(2):74–83. doi:10.1102/1470-7330.2004.0004.
- Peh WC. The role of imaging in the staging of bone tumors. *Crit Rev Oncol Hematol.* 1999;31(2):147–167.
- Ma LD. Magnetic resonance imaging of musculoskeletal tumors: skeletal and soft tissue masses. *Curr Probl Diagn Radiol.* 1999;28(2):29–62.
- Ferrari S, Balladelli A, Palmerini E et al. Imaging in bone sarcomas. The chemotherapist's point of view. *Eur J Radiol.* 2011. doi:10.1016/j.ejrad.2011.11.028.
- Pache G, Krauss B, Strohm P, et al. Dual-energy CT virtual noncalcium technique: detecting posttraumatic bone marrow lesions--feasibility study. *Radiology.* 2010;256(2):617–624. doi:10.1148/radiol.10091230.
- Wang C-K, Tsai J-M, Chuang M-T et al. Bone Marrow Edema in Vertebral Compression Fractures: Detection with Dual-Energy CT. *Radiology.* 2013. doi:10.1148/radiol.13122577.
- Guggenberger R, Gnannt R, Hodler J, et al. Diagnostic performance of dual-energy CT for the detection of traumatic bone marrow lesions in the ankle: comparison with MR imaging. *Radiology.* 2012;264(1):164–173. doi:10.1148/radiol.12112217.
- Crum WR, Hill DLG, Hawkes DJ. Information theoretic similarity measures in non-rigid registration. *Inf Process Med Imaging Proc Conf.* 2003;18:378–387.
- Prêteux F, Laval-Jeantet AM, Roger B et al. New prospects in CT image processing via mathematical morphology. *Eur J Radiol.* 1985;5(4):313–317.
- Vrtiska TJ, Takahashi N, Fletcher JG et al. Genitourinary applications of dual-energy CT. *AJR Am J Roentgenol.* 2010;194(6):1434–1442. doi:10.2214/AJR.10.4404.
- Hill DL, Batchelor PG, Holden M et al. Medical image registration. *Phys Med Biol.* 2001;46(3):R1–45.
- Crum WR, Griffin LD, Hill DLG et al. Zen and the art of medical image registration: correspondence, homology, and quality. *Neuroimage.* 2003;20(3):1425–1437.
- Crum WR, Hartkens T, Hill DLG. Non-rigid image registration: theory and practice. *Br J Radiol.* 2004;77 Spec No 2:S140–153.
- Slomka PJ, Baum RP. Multimodality image registration with software: state-of-the-art. *Eur J Nucl Med Mol Imaging.* 2009;36 Suppl 1:S44–55. doi:10.1007/s00259-008-0941-8.

-
22. Melbourne A, Hipwell J, Modat M, et al. The effect of motion correction on pharmacokinetic parameter estimation in dynamic-contrast-enhanced MRI. *Phys Med Biol*. 2011;56(24):7693–7708. doi:10.1088/0031-9155/56/24/001.
 23. Lell MM, Ditt H, Panknin C, et al. Bone-subtraction CT angiography: evaluation of two different fully automated image-registration procedures for interscan motion compensation. *AJNR Am J Neuroradiol*. 2007;28(7):1362–1368. doi:10.3174/ajnr.A0558.
 24. Zanetti M, Bruder E, Romero J et al. Bone marrow edema pattern in osteoarthritic knees: correlation between MR imaging and histologic findings. *Radiology*. 2000;215(3):835–840.
 25. Griffith JF, Yeung DKW, Leung JCS et al. Prediction of bone loss in elderly female subjects by MR perfusion imaging and spectroscopy. *Eur Radiol*. 2011;21(6):1160–1169. doi:10.1007/s00330-010-2054-6.

Total hip prosthesis CT with single energy projection based metallic artifact reduction technique: Impact on the evaluation of specific peri-prosthetic soft tissue structures.

Pedro A. Gondim Teixeira, Jean-Baptiste Meyer, Cedric Baumann, Ariane Raymond, François Sirveaux, Henri Coudane, Alain Blum

Submitted to *European Radiology* on 12th September 2013.

Abstract

Objectives: to evaluate the impact of CT with single energy projection based MAR on the evaluation of specific peri-articular soft tissue structures.

Methods: The CT data from 47 consecutive patients a hip prosthesis (24 unilateral and 24 bilateral) was retrospectively reconstructed with two different methods (Iterative reconstruction [IR] only and IR and projection based MAR). The influence of metallic artifacts on the identification of various peri-articular structures was evaluated subjectively by two readers. The image quality was compared in patients with uni and bilateral prosthesis.

Results: the image quality for the evaluation of the peri-prosthetic soft tissue was significantly improved by the MAR algorithm ($p < 0.0001$). When the MAR algorithm was used the gluteus minimus and medius tendons, the obturator internus muscle, the prostate/uterus and the bladder could be evaluated with medium or high confidence. When the MAR algorithm was used there were no significant differences in the image quality between patient with uni- or bilateral prosthesis ($p > 0.2$). The use of projection MAR increased in 30% the detection of peri-articular masses.

Conclusion: With projection MAR CT can be used for the evaluation of peri-articular soft-tissue structures in patients with hip prosthesis.

Keywords: Computed tomography, hip arthroplasty, image quality, metal artifacts

P. Teixeira – Corresponding author, JB. Meyer, A. Raymond, A. Blum
Service D'imagerie Guilloz, Hôpital Central, CHU-Nancy, 29 Av. Mar Lattre de Tassigny, 54000 Nancy, France.
e-mail: ped_gt@hotmail.com

C. Baumann
Service d'épidémiologie et évaluation cliniques, CHU-Nancy, France.

F. Sirveaux
Service de Chirurgie Traumatologique et Orthopédique, Centre Chirurgical Emile Gallé, 54000 Nancy, France.

H. Coudane
Service de Chirurgie traumatologique et arthroscopique de l'appareil locomoteur (ATOL), CHU-Nancy, France.

Key points

- Projection MAR improve the evaluation of peri prosthetic soft tissue structures.
- Projection MAR increased the detection rate of peri-articular anomalies.
- A similar quality improvement was seen with uni or bilateral prosthesis.
- Gluteal tendons and internal obturator can be identified with good confidence.
- Even with MAR Sciatic nerve and ilio-psoas tendon evaluation remain difficult.

Abbreviations

MAR = metallic artifact reduction

IR = iterative reconstruction

CTDI_{vol} = volumic computed tomography dose index

DLP = dose length product

FBP = filtered back projection

FPJ = forward projection

Introduction

Total replacement surgery is frequently performed for the treatment of advanced degenerative joint disease of the hip [1]. Although complication rates are low the great number of prosthesis implanted renders radiologists prone to be confronted to post-surgical peri-prosthetic complications [2]. Soft tissue complications after hip prosthesis implants are less frequent than prosthetic loosening and displacement, but can cause significant patient disability. Multiple peri-articular soft-tissue structures can be implicated: gluteal tendons, psoas tendon and sciatic nerve [3–5].

Sonography is currently considered the imaging method of choice for the post-surgical evaluation of peri prosthetic soft tissues of the hip [1]. In the post operative setting, however, sonographic evaluation can be hindered by post surgical scarring, soft tissue calcifications and surgical material [6, 7]. Despite the use of adapted sequences and acquisition parameters metallic artifacts still deteriorates the quality of MR images and peri-prosthetic soft-tissue anomalies may be obscured. CT is frequently used as a supplementary imaging technique for the post operative evaluation of patients with hip

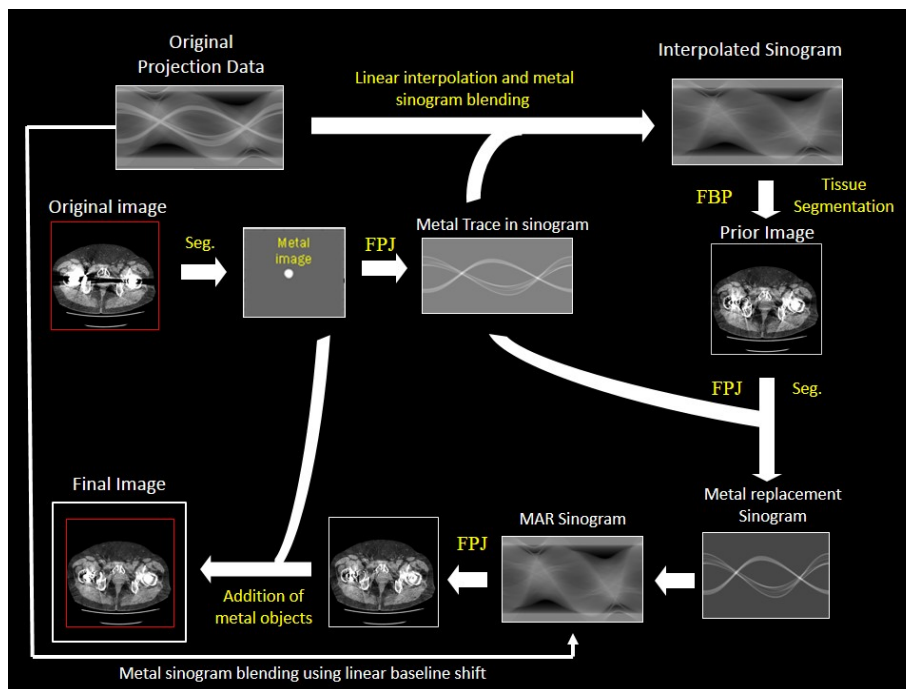


Fig. 1 – Diagram demonstrating the multiple steps of the MAR algorithm used. FPJ = Forward projection; FBP = filtered back projection; Seg. = segmentation of metallic artifacts in the image domain.

prosthesis [1, 2]. CT has been used with success for the evaluation bone and metal hardware complications of hip arthroplasty [8]. Additionally CT is the imaging method of choice for the evaluation of the bone stock in patients evaluated for prosthetic replacement [9]. If an evaluation of the peri-prosthetic soft tissue was feasible on CT this method could provide a complete diagnostic work-up for patients with hip arthroplasty.

Metallic implants cause photon starvation which leads to data inconsistencies, increase noise, beam hardening and scattering, significantly degrading the image quality of peri-prosthetic tissues on CT [10, 11]. The improvement of image of quality using projection raw data based algorithms for metallic artifact reduction (MAR) in patients with metallic implants is well documented in the literature [12–15]. Various authors have demonstrated the positive impact of projection based MAR techniques for the evaluation the pelvic organs in patients with total hip prosthesis. Despite this undisputed improvement in image quality by the use of projection based MAR various aspects related to the use of these techniques remain unknown. The diagnostic gain offered by these techniques for the evaluation of specific peri-articular soft tissue structures has not yet been completely evaluated in the literature. Additionally, the influence of the amount of metal on the performance of projection based MAR is another point that needs clarification.

In this article we sought to evaluate the impact of CT with single energy projection based MAR on the evaluation of specific peri-articular soft tissue structures in patients with hip prosthesis. Two groups of patients were evaluated: patients with a unilateral prosthesis and patients with a bilateral prosthesis. This information might be useful to ascertain the role of CT with projection based MAR in the diagnostic

workup and in the interpretation of CT images of patients with a hip prosthesis.

Material and Methods

Patients

From July 2012 to April 2013, CT was performed on the hips of 48 consecutive patients with a hip prosthesis referred to our institution. The raw data from these patients were retrospectively retrieved and reconstructed with a projection based MAR algorithm. This study was approved by the local ethics committee and all patients were over 18 years-old. An informed consent is not required by the ethics committee for retrospective studies based on post-processing of anonymized data. Patients had been referred for the evaluation of hip pain after total hip arthroplasty. Patients with hip arthrography were excluded. 24 of these patients had a unilateral prosthesis and 24 had a bilateral prosthesis. In 4 patients with a bilateral prosthesis arthrography was performed in one of the hips. In these patients only the contra-lateral hip was considered in the evaluation. A total of 68 hip prosthesis were evaluated.

Acquisition Protocol

All CT examinations were performed in a 320 detector-row CT scanner (Aquilion ONE, Toshiba Medical Systems, Otawara, Japan). A single volume with 16 cm of z-axis coverage was acquired in the sequential mode starting 3 cm proximal to the acetabular roof. The acquisition parameters were adapted to the patient's body mass index: tube rotation time 0.75-1.0 second, 120-135 kVp, 100-450 mAs, slice thickness 0.5 mm, FOV 32 cm, and matrix 512 x 512). In patients with bilateral

prosthesis the acquisition was performed to include both hips in the same volume.

Image analysis and post processing

Two volumes were reconstructed for each patient, one using an adaptive iterative reconstruction (IR) algorithm (AIDR 3D, Toshiba Medical Systems) and one using iterative reconstruction associated with a projection based MAR algorithm. After data acquisition the volume with iterative reconstruction only was automatically created by the scanner. Then the raw data was sent to an external research workstation to be reconstructed with the MAR algorithm.

The MAR algorithm is raw data based and uses various steps data segmentation, forward projection and interpolation (Fig. 1). First the raw data is forward projected to create a sinogram. In parallel the same data is reconstructed using standard filtered back projection (FBP) and the metal is segmented in the image domain. Metal segmented data is forward projected to create a metal-only sinogram. Then this metal only sinogram is subtracted from the original sinogram and linear interpolation is used to calculate the missing data. The interpolated sinogram is reconstructed with FBP and the resulting image volume is then segmented to further exclude residual metal artifacts. The resultant data is forward projected and again linear interpolation is performed to fill in the data gaps. Finally, from this last sinogram, an image volume is reconstructed with FBP and the metal data from the first segmentation is reintroduced in the image domain. This algo-

rithm has FDA approval and is to be commercialized as a product on the last trimester of 2013.

All images were analyzed independently by two musculoskeletal radiologists (P.T. and J.M) with 8 and 4 years of clinical experience blinded to clinical data. First, the IR only volumes were evaluated in a display console workstation v. 4.74 (Toshiba Medical Systems, Otawara, Japan). Then after a two weeks interval the MAR volumes were evaluated in the same manner. Images were analyzed in the axial plane with a 40/400 window width/level setting.

The influence of metallic artifacts on the evaluation of multiple soft-tissue peri-prosthetic structures was graded as follows: 0 = structure completely obscured; 1 = marked artifacts with questionable recognition; 2 = faint anatomic recognition; 3 = recognition with low confidence; 4 = recognition with medium confidence and 5 = recognition with high confidence. Eight soft tissue structures were evaluated: Gluteus minimus tendon, gluteus medius tendon, ilio-psoas tendon, sciatic nerve, obturator internus muscle, bladder, uterus/prostate. The axial slice that depicted most prominent metallic artifacts over these structures was chosen for the evaluation. A global evaluation score considering the added grades of each structure was calculated for each prosthesis. Minimal score was 0 and maximal score was 40. In patients with bilateral prosthesis, the image quality was evaluated independently on each side and was based only on the analysis of the specific anatomic structures described above (as opposed to global image aspect).

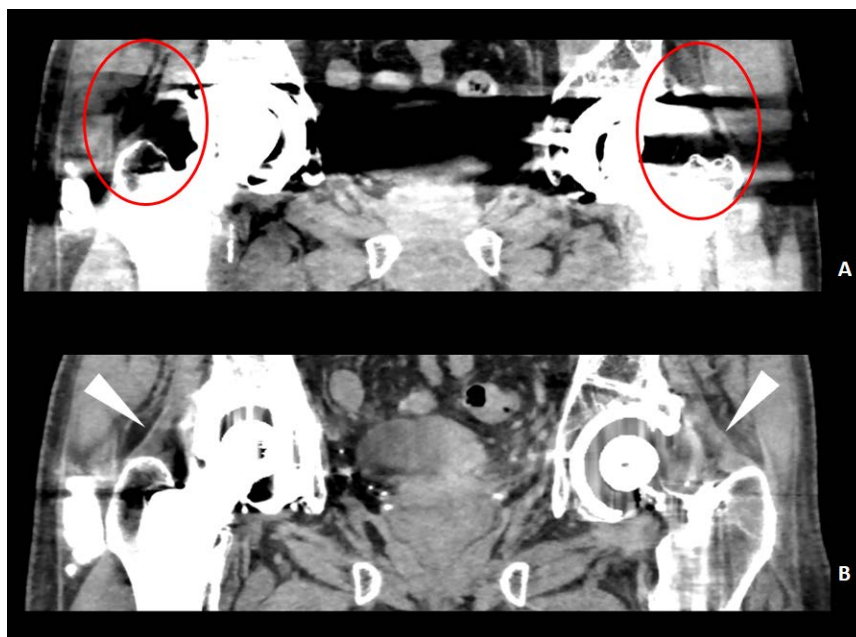


Fig. 2 – 54 year-old male with bilateral metal on polyethylene THP. A) Coronal CT image at the level of the gluteal minimus tendons with IR only reconstruction using a soft tissue window level. Note the prominent metallic artifact the obscure completely these tendons (red circles). B) Coronal CT image of the same anatomic region, with the same window settings using projection MAR. The image quality is significantly improved and the gluteal minimus tendons can now be identified with high confidence (with arrowheads). Note that compared to the opposite side the left tendon appears thickened.

The presence of articular capsule contour abnormalities and of peri-articular masses was also assessed by the readers. Capsular abnormalities were diagnosed when a definite anomaly altering the expected capsular contours. Peri-articular masses were characterized by the identification of a space occupying anomaly of soft-tissue density. The influence of the metallic artifacts on the evaluation of these abnormalities was classified in the same manner as previously described. In patients with bilateral prostheses, one hip was evaluated at a time in the same fashion as described above. The volume computed tomography dose index ($CTDI_{vol}$) and the global dose length product (DLP) were estimated based on a 32 cm phantom. Effective dose estimations were done with a constant (k-factor) in $mGy \cdot cm \cdot mSv^{-1}$ of 0.0073 for the hip [16].

Statistics

The paired two-tailed student T test was used for the comparison of the quality scores. The non-paired student T test was used to compare the quality scores between patients with uni- and bilateral prosthesis. A p value of less than 0.05 was considered as the threshold of statistic significance. Intra-class correlation coefficients were calculated to assess the inter-observer variability.

Results

There were 25 males and 23 females in the studied population (male-to-female ratio = 1:0.92). The population age varied from 26 to 90 years-old (mean = 66.7 +/- 14.9 years). The mean age in the unilateral and bilateral hip prosthesis groups were almost identical (66.6 +/- 14.8 and 66.8 +/- 15.3 years respectively). The body mass index (BMI) was also similar in these two groups (27.7 +/- 4.6 and 26.3 +/- 5.7 for uni- and bilateral groups respectively). There were 66 total hip prosthesis (THP) and 2 bipolar hemi-arthropathies. Among the THP evaluated there were 40 metal-on-polyethylene bearings, 12 ceramic-on-ceramic bearings, 6 ceramic-on-polyethylene bearings and 8 metal-on-metal bearings. Among the THP prosthesis evaluated 60 had and 6 did not have a metal back on the acetabular component. There were no resurfacing prosthesis in the studied population.

As expected, the image quality for the evaluation of the peri-prosthetic soft tissue was significantly improved by the MAR algorithm for both readers. The interobserver agreement was considered to be excellent with both reconstruction types (ICC = 0.91). The mean global score using IR only was 8.5 +/- 6.6 and 6.4 +/- 5.6 for readers one and two respectively. When MAR was used the mean global scores were significantly higher 28.0 +/- 4.4 and 26.8 +/- 4.5 for readers one and two respectively ($p < 0.0001$).

The influence of the metallic artifacts on image analysis was different depending on the anatomic structure evaluated. Table 1 demonstrates the structure specific scores for both readers. Considering the analysis of the image quality scores of

Table 1 – Mean quality scores per structure for both readers using IR and projection MAR

Anatomic structure	IR only		Projection MAR	
	Reader 1	Reader 2	Reader 1	Reader 2
Gluteus minimus	1.3 +/- 1.4	1.0 +/- 1.2	4.2 +/- 1.1	3.8 +/- 1.3
Gluteus medius	1.6 +/- 1.5	1.0 +/- 1.4	4.7 +/- 0.6	4.3 +/- 0.8
Sciatic nerve	1.6 +/- 1.8	1.3 +/- 1.5	3.6 +/- 1.5	3.6 +/- 1.6
Obturator internus	0.7 +/- 1.3	0.3 +/- 0.9	4.5 +/- 1.0	4.2 +/- 1.0
Ilio-psoas tendon	0.2 +/- 0.6	0.2 +/- 0.7	2.2 +/- 1.7	2.5 +/- 1.5
Prostate/uterus	2.0 +/- 2.2	1.7 +/- 1.9	4.8 +/- 0.5	4.4 +/- 0.7
Bladder	0.9 +/- 1.7	0.6 +/- 1.3	4.0 +/- 1.3	4.0 +/- 1.2
Global mean	1,22	0,92	4,02	3,86

both readers some observations can be made. When IR only was used at least part of the obturator internus muscle, the ilio-psoas tendon and the bladder were completely obscured by the metallic artifacts; the anatomic recognition of the gluteus minimus and medius tendons and the sciatic nerve was graded as questionable; a faint recognition was possible for the prostate/uterus. When the MAR algorithm was used the gluteus minimus and medius tendons, the obturator internus muscle, the prostate/uterus and the bladder could be evaluated with medium or high confidence (mean quality scores varied from 3.8 to 4.8) (Fig. 2, 3 and 4). In despite of the positive effect of the MAR algorithm on the image quality the evaluation ilio-psoas tendon and the sciatic nerve remained difficult (mean quality scores varied from 2.2 to 3.6) (Fig. 5 and 6). The recognition of the ilio-psoas tendon was considered faint and the sciatic nerve was recognized only with low confidence. Based on these results some practical recommendations could be proposed (table 2).

The use of MAR facilitated the identification of a larger number of peri-articular and capsular anomalies. On IR only images 14 and 13 of such anomalies were identified by readers one and two respectively. On MAR reconstructed images the number of anomalies identified increased to 20 for reader one and 19 for reader two with corresponded to a 30% and a 31.5% increase in the detection rate respectively. An increase in the diagnostic confidence of these anomalies was also noted when the MAR algorithm was used (Fig. 7). The mean grade of these lesions for reader one was 3.3 +/- 1.5 and 4.7 +/- 0.5 using IR only and MAR reconstruction respectively. For reader two these values were 3.4 +/- 1.1 and 4.7 +/- 0.4.

There was a significant drop in the quality of IR only images in patients with bilateral prosthesis when compared to patient with unilateral prosthesis ($p < 0.0001$ for both readers). The mean overall quality scores in patients with unilateral prosthesis were 14.5 +/- 6.1 and 11.4 +/- 5.3 for readers one and two. The mean overall quality scores in patients with bilateral prosthesis were 5.2 +/- 4.0 and 3.7 +/- 3.5 for readers one and two. With the use of the MAR algorithm, there were no significant

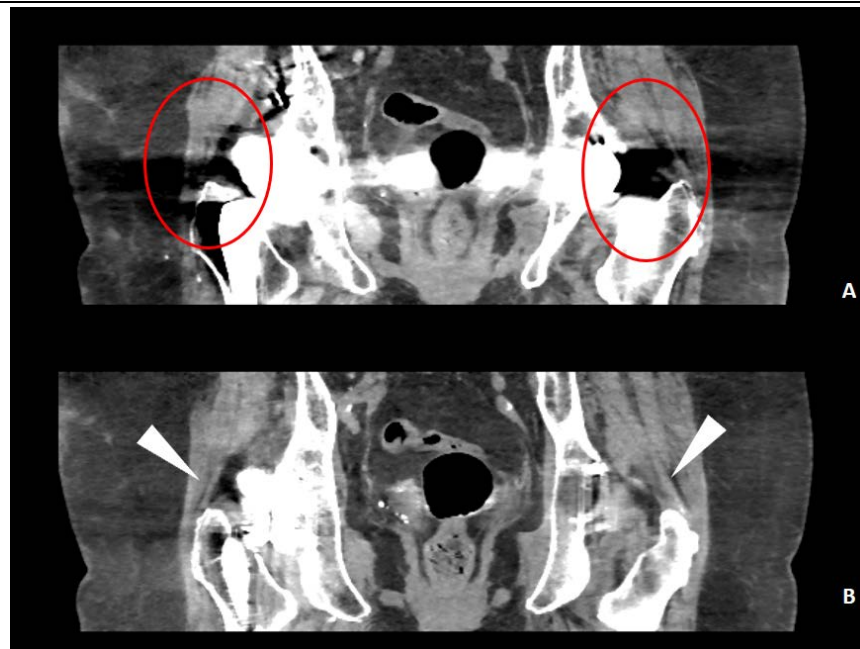


Fig. 3 – 77 year-old female with bilateral metal on polyethylene THP. A) Coronal CT image at the level of the gluteal medius tendons with IR only reconstruction using a soft tissue window level. Note the prominent metallic artifact the obscure completely these tendons (red circles). B) Coronal CT image of the same anatomic region, with the same window settings using projection MAR. The image quality is significantly improved and the gluteal medius tendons can now be identified with high confidence (with arrowheads). Note that there is an asymmetry of the myotendinous junction of these tendons. On the right the tendon appears longer, which can be related to partial tearing.

differences in the image quality between patient with uni- or bilateral prosthesis ($p > 0.2$ for both readers). With MAR reconstructed images the mean overall quality scores in patients with unilateral prosthesis were 28.8 ± 4.6 and 27.4 ± 4.9 for readers one and two. The mean overall quality scores in patients with bilateral prosthesis were 27.5 ± 4.3 and 26.4 ± 4.3 for readers one and two.

The mean CTDIvol, DLP and effective dose delivered to the patients evaluated were 32.5 ± 19.9 mGy, 520.0 ± 318.8 mGy*cm and 3.7 ± 2.3 mSv. The dose exposure was lower in patients with unilateral THP. Table 3 presents the mean values of CTDIvol, DLP and effective dose for patients with uni-bilateral THP.

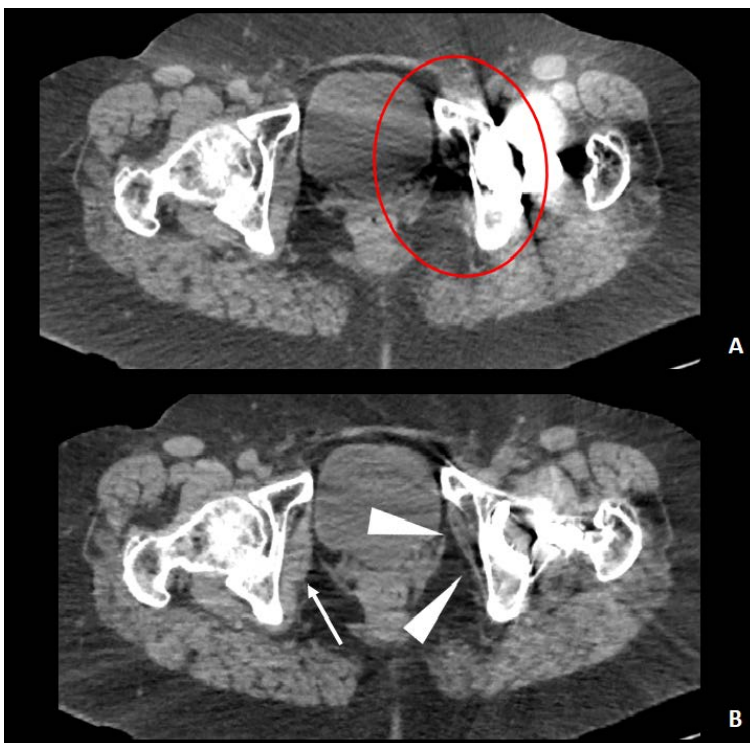


Fig. 4 – 70 year-old female with a left sided metal on polyethylene THP. A) Axial CT image reconstructed with IR only. Metal artifacts preclude the analysis of the ipsilateral internal obturator muscle (red circle). B) Axial CT image of the same anatomic region, with the same window settings using projection MAR in which the internal obturator muscle is identified with high confidence. In this case compared to the contralateral muscle (thin arrow) the left internal obturator muscle shows a loss in volume and a few areas of fatty atrophy.

Table 2 – Structure specific recommendations for each type of reconstruction used.

Anatomic structure	Recommendations	
	IR only	Single energy MAR
Gluteus minimus tendon	Evaluation severely hampered by metallic artifacts	Recognition with medium/high confidence, CT can be considered for evaluation
Gluteus medius tendon	Evaluation severely hampered by metallic artifacts	Recognition with medium/high confidence, CT can be considered for evaluation
Sciatic nerve	Evaluation severely hampered by metallic artifacts	Evaluation hampered by metallic artifacts but can be recognized in some patients
Obturator internus muscle	Completely obscured by metallic artifacts	Recognition with medium/high confidence, CT can be considered for evaluation
Ilio-psoas tendon	Completely obscured by metallic artifacts	Evaluation hampered by metallic artifacts but can be recognized in some patients
Prostate/uterus	Evaluation hampered by metallic artifacts but can be recognized in some patients	Recognition with medium/high confidence, CT can be considered for evaluation
Bladder	Completely obscured by metallic artifacts	Recognition with medium/high confidence, CT can be considered for evaluation

Discussion

The use of IR has been shown to improve the image quality in patients with metallic implants [17]. The presented results indicate that despite these improvements the evaluation of peri-prosthetic soft tissue structures using adaptive IR only remains greatly hampered by metallic artifacts. The anatomic structures evaluated (gluteal tendons, ilio-psoas tendon, obturator internus muscle, sciatic nerve, uterus/prostate and

bladder) were at best faintly recognized. The analysis of ilio-psoas tendon, anterior and in close proximity to the acetabular component and the obturator internus muscle medial to prosthetic femoral head using IR-only reconstructions was particularly hindered by metallic artifacts (mean scores 0.2 and 0.3-0.7 respectively). Thus, CT with adaptive IR cannot be recommended for the evaluation of peri-articular soft tissue complications of hip arthroplasty.

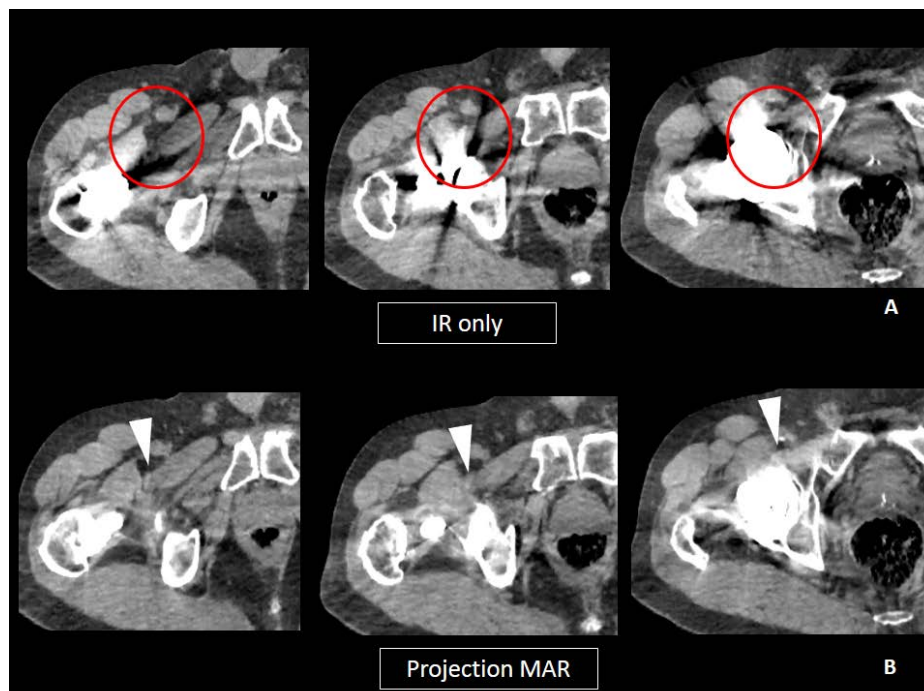


Fig. 5 – 52 year-old male with a right sided ceramic on polyethylene THP. Two series of Axial CT images from distal to proximal at the level of the proximal thigh with IR only (A) and with projection MAR (B). The red circles in A mark the expected position of the ilio-psoas tendon, which is completely obscured by the metallic artifacts. In B the distal portion of this tendon can be identified with high confidence (arrowheads in the first 2 images), however at the level of the acetabular cup this tendon is only faintly recognized (arrowhead in the third image).



Fig. 6 – 52 year-old male with a right sided ceramic on polyethylene THP. Axial CT images with projection MAR reconstruction. The residual metallic artifacts hinder the identification of sciatic nerve, which is only faintly recognized (red circle). The contralateral sciatic nerve is indicated by the white arrowhead.

The use of projection based MAR algorithm significantly improved the overall and the structure specific image quality ($p < 0.0001$). The use of MAR allowed the analysis of the gluteal tendons and the obturator internus muscle with medium to high confidence (mean quality scores varied from 3.8 to 4.7). Although significantly improved by projection based MAR with respect to adaptive IR de image quality for the analysis of the ilio-psoas tendon and the sciatic nerve remained mediocre. These findings are probably related with their anatomic disposition in close proximity with the metallic prosthetic components. The mean grade of these structures varied from 2.2 to 3.6. In light of these results CT with projection based MAR can be used for the evaluation of the peri-articular soft tissue structures in patients with THP particularly for the analysis of the gluteal tendons and the obturator internus muscle.

Whereas multiple articles demonstrate the benefits of using of projection based MAR, information on the clinical importance of these techniques is scarce [18–20]. There was a 30% increase in the detection rate of peri-articular masses with the use of projection based MAR. Not only both readers identified more lesions with MAR but the confidence in the analysis of these anomalies was also improved (quality scores 3.3-3.4 and 4.7 for IR only and MAR reconstructions respectively). These results indicate that the use of projection based MAR increases the performance of CT for the diagnosis of peri-prosthetic soft tissue anomalies in patients with THP.

Although prosthetic loosening is the first cause of hip pain after total hip arthroplasty, multiple soft-tissue complications may occur, leading to significant patient morbidity [1, 2]. Gluteal tendon ruptures and avulsions, impingement of the ilio-psoas tendon and the anterior portion of the acetabular component and post arthropathy sciatic neuropathy are potential complications of this treatment [3–5]. Additionally capsular contour abnormalities, peri-articular fluid collection and intra-pelvic extension of hip cystic masses displacing the obturator internus muscle can all be seen as a complication of hip arthroplasty. These anomalies can be secondary to various pathologic processes such as infection, capsular dehiscence,

impingement, metallosis, aseptic lymphocytic vasculitis-associated lesions (ALVAL) [21–24]. CT is frequently performed for the evaluation of hip prosthesis complications and the identification of soft tissue complications on CT may have an impact on patient management and imaging workup.

The impact of the number of prosthesis on Image quality had not yet been assessed in the literature. On IR-only images were considered there was a significant degradation of image quality with bilateral hip prosthesis. The global quality score for IR-only was 11-14 for unilateral prosthesis versus 3-5 for bilateral implants. However with MAR reconstructed images the quality was similar independent on the number of prosthesis (27-28 versus 26-27 for uni and bilateral prosthesis respectively) indicating that this technique is particularly useful in the setting of bilateral prosthesis.

In most studies projection based MAR techniques has been used in association with monochromatic dual-energy techniques. Using the same grading system and dual-energy monochromatic imaging associated projection based MAR Moshbach et al. reported a median score of 3 for the prostate and the bladder [12]. Still using the same scoring system Yu et al. also reported similar results using single energy projection based MAR (3.3 and 3.4 for the bladder and prostate respectively) [10]. The score for these structures using single energy projection based MAR was slightly better and varied from 4-4.8 in the population studied. There is no consensus in the literature about the optimal dual-energy protocol for MAR [25].

Table 3 – Dose exposure levels in the studied population

		CTDIvol (mGy)	DLP (mGy*cm)	effective dose (mSv)
Uni lat	mean	26,6	425,3	3,1
	sdev	19,1	306,9	2,2
Bilat	mean	38,4	614,8	4,4
	sdev	19,2	307,6	2,2
Global	mean	32,5	520	3,7
	sdev	19,9	318,7	2,3

Additionally various factors, such as patient size, prosthesis composition, dual energy acquisition method (e.g. dual source, sandwich detectors, rapid kV switching) may influence the effectiveness of dual-energy MAR [25, 26]. For a similar performance of MAR single-energy protocols are simpler and potentially applicable in all scanner models [14]. Finally, single dose MAR techniques can be potentially associated with low-dose acquisition. Further studies are necessary to explore the application of projection based MAR with a low-dose acquisition protocol.

Various limitations of this study should be acknowledged. Only the image quality improvement and not the diagnostic performance of the MAR technique were assessed in this study. We had no diagnostic confirmation of the capsular and peri-articular anomalies identified, however the high interobserver agreement helps support the validity of these findings. Various

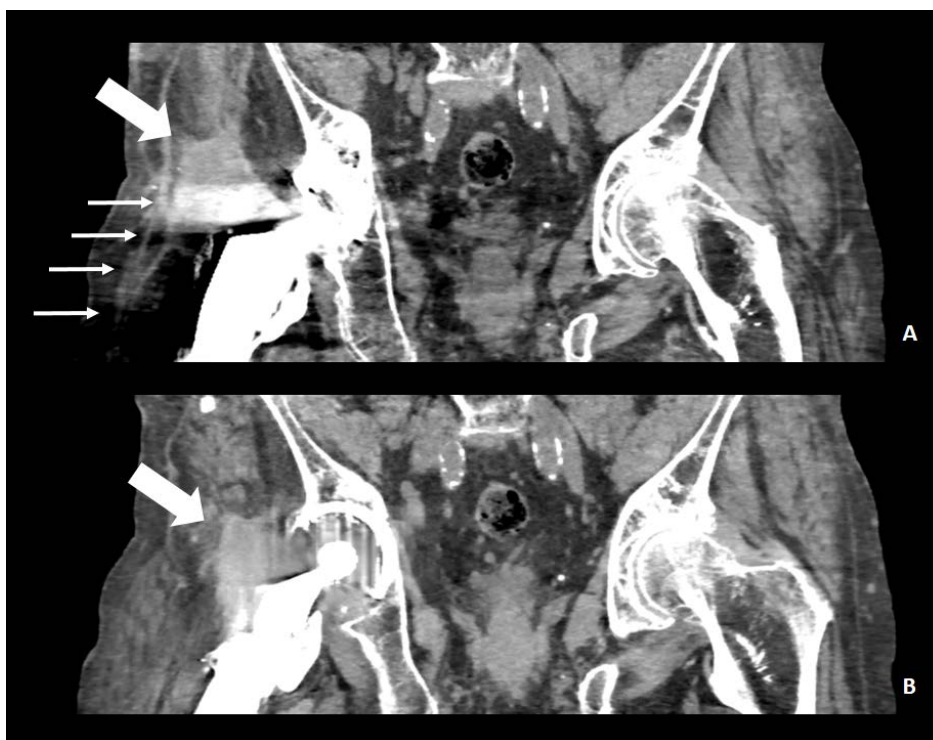


Fig. 7 – 74 year-old male with bilateral metal on polyethylene THP. A) Coronal CT image with IR only reconstruction using a soft tissue window level demonstrating a peri-articular soft tissue mass (fat arrow), which is partially obscured by metallic artifacts (thin arrows). B) Coronal CT image of the same anatomic region, with the same window settings using projection MAR. The image quality is significantly improved and the peri-articular soft tissue mass (fat arrow) can be identified with high confidence. On B) this mass seems to be continuous with articular cavity, feature that can have important diagnostic implications.

prosthesis types were present in the study population and the number of patients with each specific prosthesis type was limited. The influence of the prosthesis type on the image quality could not be assessed.

In conclusion, although CT images with IR only presented a poor quality for the evaluation of the peri-prosthetic soft tissue in patients with hip arthroplasty, the use of single energy projection based MAR lead to significantly improvement in quality even in patients with bilateral prosthesis. When the MAR technique was used the gluteal tendons and the obturator internus muscle could be evaluated with a medium to high confidence. Moreover, there was a 30% increase in the detection rate of capsular and peri-articular masses, suggesting that CT with projection based MAR can be useful in the post operative evaluation of patients with total hip arthroplasty. The performance of single and dual-energy projection based MAR techniques was comparable, making this MAR technique prone to application in a wide variety of scanner models.

Acknowledgments

This work was supported by the French Society of Radiology (SFR- Société Française de Radiologie) through a research grant. We thank Valerie Lamy and Laurent Raffray for their efforts in data transfer and post processing.

Bibliography

1. Miller TT (2012) Imaging of hip arthroplasty. *Eur J Radiol* 81:3802–3812. doi: 10.1016/j.ejrad.2011.03.103
2. Roth TD, Maertz NA, Parr JA, et al. (2012) CT of the hip prosthesis: appearance of components, fixation, and complications. *Radiogr Rev Publ Radiol Soc North Am Inc* 32:1089–1107. doi: 10.1148/rg.324115183
3. Bremer AK, Kalberer F, Pfirrmann CWA, Dora C (2011) Soft-tissue changes in hip abductor muscles and tendons after total hip replacement: comparison between the direct anterior and the transgluteal approaches. *J Bone Joint Surg Br* 93:886–889. doi: 10.1302/0301-620X.93B7.25058
4. Henderson RA, Lachiewicz PF (2012) Groin pain after replacement of the hip: aetiology, evaluation and treatment. *J Bone Joint Surg Br* 94:145–151. doi: 10.1302/0301-620X.94B2.27736
5. Park JH, Hozack B, Kim P, et al. (2013) Common peroneal nerve palsy following total hip arthroplasty: prognostic factors for recovery. *J Bone Joint Surg Am* 95:e551–555. doi: 10.2106/JBJS.L.00160
6. Douis H, Dunlop DJ, Pearson AM, et al. (2012) The role of ultrasound in the assessment of post-operative complications following hip arthroplasty. *Skeletal Radiol* 41:1035–1046. doi: 10.1007/s00256-012-1390-9

7. Long SS, Surrey D, Nazarian LN (2012) Common sonographic findings in the painful hip after hip arthroplasty. *J Ultrasound Med Off J Am Inst Ultrasound Med* 31:301–312.
8. Cahir JG, Toms AP, Marshall TJ, et al. (2007) CT and MRI of hip arthroplasty. *Clin Radiol* 62:1163–1171; discussion 1172–1173. doi: 10.1016/j.crad.2007.04.018
9. Choplin RH, Henley CN, Edds EM, et al. (2008) Total hip arthroplasty in patients with bone deficiency of the acetabulum. *Radiogr Rev Publ Radiol Soc North Am Inc* 28:771–786. doi: 10.1148/rg.283075085
10. Yu L, Li H, Mueller J, et al. (2009) Metal artifact reduction from reformatted projections for hip prostheses in multislice helical computed tomography: techniques and initial clinical results. *Invest Radiol* 44:691–696. doi: 10.1097/RLI.0b013e3181b0a2f9
11. Kataoka ML, Hochman MG, Rodriguez EK, et al. (2010) A review of factors that affect artifact from metallic hardware on multi-row detector computed tomography. *Curr Probl Diagn Radiol* 39:125–136. doi: 10.1067/j.cpradiol.2009.05.002
12. Morsbach F, Bickelhaupt S, Wanner GA, et al. (2013) Reduction of metal artifacts from hip prostheses on CT images of the pelvis: value of iterative reconstructions. *Radiology* 268:237–244. doi: 10.1148/radiol.13122089
13. Lee YH, Park KK, Song H-T, et al. (2012) Metal artefact reduction in gemstone spectral imaging dual-energy CT with and without metal artefact reduction software. *Eur Radiol* 22:1331–1340. doi: 10.1007/s00330-011-2370-5
14. Yu L, Leng S, McCollough CH (2012) Dual-energy CT-based monochromatic imaging. *AJR Am J Roentgenol* 199:S9–S15. doi: 10.2214/AJR.12.9121
15. Brook OR, Gourtsoyianni S, Brook A, et al. (2012) Spectral CT with metal artifacts reduction software for improvement of tumor visibility in the vicinity of gold fiducial markers. *Radiology* 263:696–705. doi: 10.1148/radiol.12111170
16. Biswas D, Bible JE, Bohan M, et al. (2009) Radiation exposure from musculoskeletal computerized tomographic scans. *J Bone Joint Surg Am* 91:1882–1889. doi: 10.2106/JBJS.H.01199
17. Gervaise A, Osemont B, Lecocq S, et al. (2012) CT image quality improvement using Adaptive Iterative Dose Reduction with wide-volume acquisition on 320-detector CT. *Eur Radiol* 22:295–301. doi: 10.1007/s00330-011-2271-7
18. Lee YH, Park KK, Song H-T, et al. (2012) Metal artefact reduction in gemstone spectral imaging dual-energy CT with and without metal artefact reduction software. *Eur Radiol* 22:1331–1340. doi: 10.1007/s00330-011-2370-5
19. Malan DF, Botha CP, Kraaij G, et al. (2012) Measuring femoral lesions despite CT metal artefacts: a cadaveric study. *Skeletal Radiol* 41:547–555. doi: 10.1007/s00256-011-1223-2
20. Verburg JM, Seco J (2012) CT metal artifact reduction method correcting for beam hardening and missing projections. *Phys Med Biol* 57:2803–2818. doi: 10.1088/0031-9155/57/9/2803
21. Bauer TW, Schils J (1999) The pathology of total joint arthroplasty. II. Mechanisms of implant failure. *Skeletal Radiol* 28:483–497.
22. Cooper HJ, Ranawat AS, Potter HG, et al. (2009) Magnetic resonance imaging in the diagnosis and management of hip pain after total hip arthroplasty. *J Arthroplasty* 24:661–667. doi: 10.1016/j.arth.2008.04.023
23. Pandit H, Glyn-Jones S, McLardy-Smith P, et al. (2008) Pseudotumours associated with metal-on-metal hip resurfacings. *J Bone Joint Surg Br* 90:847–851. doi: 10.1302/0301-620X.90B7.20213
24. Duggan PJ, Burke CJ, Saha S, et al. (2013) Current literature and imaging techniques of aseptic lymphocyte-dominated vasculitis-associated lesions (ALVAL). *Clin Radiol*. doi: 10.1016/j.crad.2013.04.017
25. Yu L, Christner JA, Leng S, et al. (2011) Virtual monochromatic imaging in dual-source dual-energy CT: radiation dose and image quality. *Med Phys* 38:6371–6379. doi: 10.1118/1.3658568
26. Vrtiska TJ, Takahashi N, Fletcher JG, et al. (2010) Genitourinary applications of dual-energy CT. *AJR Am J Roentgenol* 194:1434–1442. doi: 10.2214/AJR.10.4404

Discussion et conclusions

Les résultats présentés dans ce chapitre aident à définir la place de la TDM perfusionnelle dans l'évaluation des masses ostéo-articulaires. La réduction de la dose est particulièrement importante sur les protocoles perfusionnels qui comportent de multiples phases d'acquisition avec un grand potentiel d'irradiation. Plusieurs facteurs jouent sur l'irradiation délivrée au patient. Les scanners à large système de détection sont particulièrement économique en irradiation par rapport aux scanners multi détecteurs classiques. De plus, la reconstruction itérative qui permet une réduction de dose en améliorant le rapport signal sur bruit de l'image est une exigence pour les protocoles multiphasiques en TDM. Finalement, l'influence du comportement des radiologues et manipulateurs limitant la zone d'exploration, le nombre de phases et l'énergie du faisceau, a un impact important sur la dose finale.

La performance diagnostique du scanner de perfusion par rapport à l'IRM, est similaire dans la population étudiée. Les deux méthodes ont pu identifier les récives d'ostéomes ostéoïdes traités par ablation laser avec une sensibilité et une spécificité élevées (100% vs. 90% en scanner et en IRM respectivement). Les paramètres de perfusion quantitatifs eux aussi ont des valeurs absolues comparables et varient de façon similaire entre l'IRM et la TDM. Ces résultats suggèrent que le scanner de perfusion est une option pour le bilan de caractérisation des masses ostéo-articulaires. Compte tenu de son caractère irradiant, son application reste néanmoins en deuxième plan par rapport à l'IRM.

La soustraction osseuse type DSA s'est montrée sensible, spécifique et reproductible pour l'identification de la réaction œdémateuse de l'os en regard des lésions osseuses lytiques. Cette méthode permet un gain diagnostic significatif par rapport aux techniques scanographiques conventionnelles. Elle ne nécessite aucune modification particulière du protocole d'acquisition qui dans le contexte d'un bilan des tumeurs osseuses comporte systématiquement une injection endoveineuse de contraste iodé. La réaction oedémateuse de l'os péri-lésionnel, précédemment identifiable que sur l'IRM, est une particularité d'un nombre limité de lésions osseuses lytiques (e.g. chondroblastome, ostéome ostéoïde, ostéoblastome, tumeurs osseuses agressives) et est importante dans l'évaluation préopératoire des masses osseuses.

La soustraction osseuse type DSA est pourtant sensible aux artéfacts de mouvement. Dans le but de réduire ces artéfacts nous avons testé un algorithme de recalage élastique. Cette démarche a permis la quasi disparition des artéfacts de mouvement, mais au prix d'une perte de sensibilité pour l'identification du rehaussement intra-osseux. Basé sur ces résultats le recalage rigide conventionnel est recommandé en première intention et d'autres techniques, plus rudimentaires, pour réduire les mouvements des patients lors de l'acquisition doivent être employées.

Enfin, nous avons démontré que les algorithmes de réduction des artéfacts métalliques, basés sur l'analyse des projections ont un impact positif sur la qualité d'images des structures musculo-tendineuses de la hanche chez les patients porteurs de prothèses totales de hanche uni ou bilatérales. A partir de cette expérience, il est légitime de recommander ce type de post traitement d'image pour le suivi scanographique des patients traités chirurgicalement avec des techniques de sauvetage des membres.

CHAPITRE 3 – L'ECHOGRAPHIE

L'échographie est basée sur les propriétés des cristaux piézoélectriques qui convertissent les ondes sonores à haute fréquence en des différences de potentiel électrique (courant). Suite à l'émission d'une onde sonore, celle-ci sera reflétée par les différentes structures internes de la région d'étude et captée après un temps X par le transducteur (écho). Le temps écoulé entre l'émission et la réception des ondes sonores varie en fonction de la profondeur de la surface réfléchissante. La qualité de l'écho reçu est en rapport aux propriétés acoustiques du tissu exposé au faisceau sonore. Ces informations récoltées par la sonde permettent la reconstruction d'une image qui est représentative de la structure interne du corps humain.

Le développement des agents de contraste ultrasonores, associé à des méthodes innovantes de traitement du signal, a fortement amélioré la détection de la vascularisation intratumorale (Fig.8) (37). Les agents de contraste ultrasonores injectés dans la circulation sanguine en bolus ont, en effet, la particularité de réfléchir intensément les ondes ultrasonores et d'être exclusivement intravasculaires, ce qui en fait des outils de détection fine de la microvascularisation. La combinaison de l'imagerie harmonique avec des logiciels de traitements du signal, associée à des agents de contraste de deuxième génération (Sonovue[®], Bracco), injectés en bolus dans la circulation sanguine, a permis, à nouveau, d'améliorer la détection de la microvascularisation en augmentant le rapport signal sur bruit.

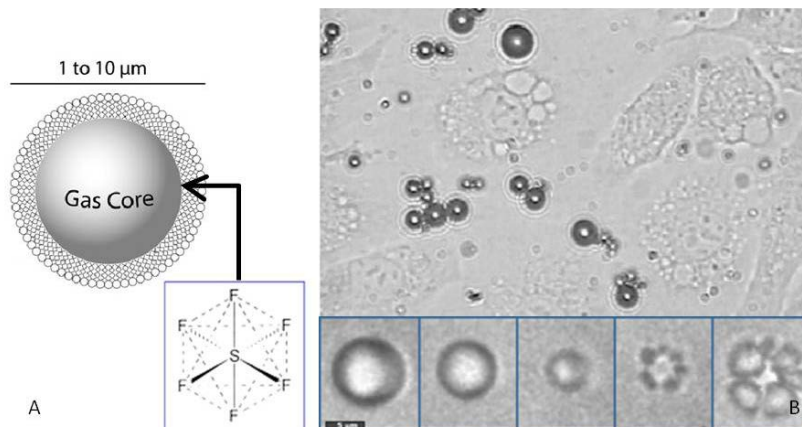


Fig. 8 : Structure et aspect des microbulles. A) Représentation schématique des microbulles. B) Photographie des microbulles du Sonovue et des cellules épithéliales bovines en culture (31).

Ces produits de contraste ont l'avantage de présenter une réponse non-linéaire lorsqu'on utilise un faible index mécanique (0,1 à 0,2). C'est cette propriété, qu'utilisent les nouveaux modes d'imagerie mis au point par les constructeurs, et qui permettent d'augmenter le signal provenant des microbulles circulant dans les vaisseaux par rapport au signal provenant des tis-

sus environnants. Le mode d'imagerie qui s'est imposé comme référence consiste en l'émission de deux impulsions ultrasonores consécutives de même amplitude et de phase opposée (Pulse Soustraction). Les deux signaux réfléchis en réponse à ces impulsions sont additionnés : la somme des signaux provenant des tissus est alors pratiquement nulle (addition de deux signaux de phase opposée), la somme des signaux provenant des microbulles, riches en composantes non linéaires, est très différente de zéro.

L'échographie de contraste a un rôle potentiel pas encore évalué pour la caractérisation des masses ostéo-articulaires des parties molles. Cette méthode est unique en plusieurs aspects : la dépendance de l'opérateur ; les propriétés pharmacocinétiques du produit de contraste ultrasonore ; une fenêtre d'exploration limitée ; une résolution temporelle et spatiale nettement supérieure à celle des autres méthodes. Les avantages et inconvénients de l'échographie par rapport aux autres méthodes perfusionnelles (TDM et IRM) dans l'exploration des tumeurs ostéo-articulaires ont été peu étudiés.



REVIEW / *Musculoskeletal imaging*

Tumours and pseudotumours of the soft tissue in adults: Perspectives and current role of sonography

A. Pierucci^a, P. Teixeira^{a,*}, V. Zimmermann^a,
F. Sirveaux^b, M. Rios^c, J.-L. Verhaegue^c, A. Blum^a

^a Guilloz Imaging Department (Prof. A. Blum), Central Hospital, Nancy University Hospital, avenue du Maréchal-de-Lattre-de-Tassigny, 54035 Nancy cedex, France

^b Trauma and orthopaedics clinic, 49, rue Hermitte, 54000 Nancy, France

^c Alexis Vautrin Centre, 6, avenue de Bourgogne, 54500 Vandœuvre-lès-Nancy, France

KEYWORDS

Tumours;
Pseudotumours;
Musculoskeletal
system;
Soft tissue;
Doppler sonography;
Elastography

Abstract Soft tissue tumours of the musculoskeletal system are reported relatively frequently. The quality of the information gained from different imaging modalities (Doppler sonography, multislice CT, MRI spectroscopy, and diffusion MRI) means that in a growing number of situations, we can envisage determining with great accuracy not only the usual information of tumour size and topography, but often the exact nature of the tissue, almost always identifying whether a lesion is aggressive or not. Of all these techniques, Doppler sonography has become the most widely used due to the striking improvements in its sensors, especially for superficial applications. Some other recent developments are: panoramic imaging, elastography (although its current contribution is still to be determined but it seems to offer promising potential), and, most importantly, specific contrast agents. These techniques have considerably refined the quality of the information obtained, and have particularly enhanced the degree of sensitivity with which lesion progression can be assessed. Ultrasonography is the very first investigation in our protocol. It is also very often used to close investigations, as it accurately guides core needle biopsy from these generally accessible lesions. The purpose of this article is to bring together updated information on the various collections of sonographic features seen in soft tissue tumours and pseudotumours and to emphasise the considerable contributions of these new technological developments, in particular contrast-enhanced sonography. The discussion will follow the World Health Organisation's anatomical pathology classifications of soft tissue tumours. We will close with a synthesis that summarises the main steps in our diagnostic process.

© 2012 Éditions françaises de radiologie. Published by Elsevier Masson SAS. All rights reserved.

* Corresponding author.

E-mail address: ped_gt@hotmail.com (P. Teixeira).

The spectacular improvements that have been made in superficial ultrasound imaging mean that sonography currently has an important role in the exploration of soft tissue tumours and pseudotumours. It should open the imaging investigations [1]. Apart from its contribution in terms of positive diagnosis, recent technical advances (specific contrast agent, elastography) have opened up interesting possibilities in terms of lesion characterisation.

Technique

We use an Aplio XG system, model SSA-790A, from the Toshiba Medical Systems Corporation (Zilverstraat 1. 2718 RP, Zootermeer, Netherlands). We always begin the examination using a high-frequency linear electronic transducer (8–15 Mhz). The multiple planes give us an overall view of the lesion and allow it to be measured in three spatial dimensions. When the mass is large, we take panoramic views that generally provide us with an exhaustive image of it that depicts all of its margins. For larger patients or in some anatomical areas (proximal thigh, buttocks), differently shaped transducers are required (curved surface) and a lower frequency (4–8 Mhz) is needed [2].

We also always use the different types of Doppler sonography (power, color and pulsed). Contrast-enhanced sonography forms an integral part of our protocol. We use an agent with a low mechanical index, consisting of an inert gas (sulphur hexafluoruride) stabilised by a fatty acid shell. We inject an ampoule of this as a bolus “pushed” by an infusion of normal saline solution at maximum output. It only diffuses into the vascular system. Contrast uptake, identified using VRI technology (vascular recognition imaging, which visualises both tissue, using normal frequency imaging, and vascularisation, using broadband Doppler imaging), is displayed as nodule-shaped areas that are either red or blue, depending on their orientation in relation to the transducer [3].

Elastography is still in its infancy in this field, but several studies have recently allowed us to anticipate that it will have real value for musculoskeletal imaging applications [4,5]. It should, in the near future, develop a more important role because of the valuable information it provides on the composition of lesion tissue (cellularity, extent of fibrosis) in comparison to adjacent healthy tissue.

For now, there is no proof that 3D imaging is of significant interest because of insufficient image quality. The improvements to transducers should relatively quickly allow it to play a role in these types of investigations because it offers the potential for a high quality frontal view. “Cross beam” techniques, or, in other words, orientations from the variable angles of the ultrasound beam, in our opinion do not notably improve the analysis in terms of either the content or margins of the lesion.

Sonographic analysis of lesions

Naturally, lesions will be assessed in view of the basic clinical features: speed of tumour growth, existence of pain, age and sex of the patient, and topography of the tumour. It is very useful to have standard radiographs available before

carrying out sonography. They can provide valuable diagnostic information [4]: radiolucent clarity of a fatty lesion, calcifications with fine outlines (phleboliths) in a haemangioma, linear or crescent-shaped calcifications in myositis ossificans, or even bone changes, which can be the consequence or origin of a tissue abnormality.

Sonography attempts to accurately gauge lesion size, and this process requires greater delicacy the larger the lesion. Equally, precisely situating the tumour’s topography can prove to be difficult when there is extended involvement in one compartment, or indeed to a greater extent, when multiple compartments are affected. There are numerous parameters to be taken into account when addressing the nature of a tumour or at least distinguishing an aggressive lesion from an inactive process [5]: is there a capsule, is it regular or otherwise, what is the echostructure, is it composed of tissue or fluid, and is it homogenous? It is crucial to look for zones of necrosis, calcifications, and fine or thick septations, and to assess whether the lesion is connected to a vascular, neural, or joint structure [6,7].

Doppler imaging demonstrates hypervascularisation that may be regular or anarchic (are there loops, areas of stenosis, occlusions, unbalanced or irregular vascular branches?) while pulsed wave Doppler may show localised accelerations in flow (stenoses) or a low resistive index (arteriovenous shunt) [8,9]. Does the administration of an ultrasound-enhancing contrast agent lead to enhancement? Is this early, prolonged, fleeting, or late? This contrast enhancement, in all its different manifestations, is usually a sign of an aggressive lesion, as was shown in a preliminary study on 80 cases [10], with, however, some particularities for specific tumor types (desmoid tumors). If the lesion no longer enhances further to treatment, this seems to be an argument for a favourable prognosis, at least in some types of tumours [3].

All of these parameters form an initial evaluation, which in a number of cases will lead to diagnosis: (lipoma, synovial cyst, ganglion cyst, vascular malformation, abscess, haematoma etc.) [6]. It often allows the distinction to be made between benign and malignant lesions in view of the collection of signs that are suspicious: large lesion size, usually with indistinct margins, anarchic vascularisation seen on power Doppler (Fig. 1) (occlusions, arterial stenosis, arteriovenous shunts), zones of necrosis (Fig. 2), a pattern of

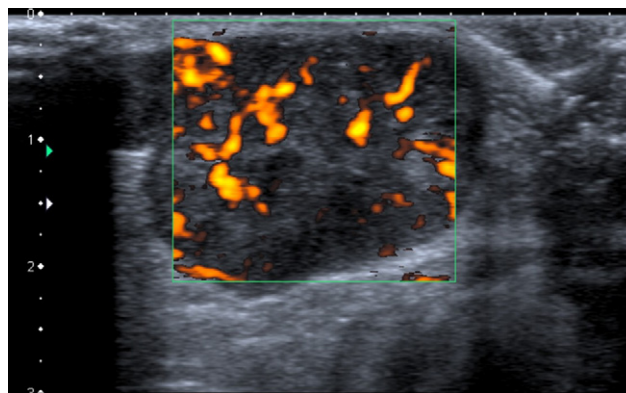


Figure 1. Power Doppler showing anarchic vascularisation (stenoses, anastomoses, “unbalanced” vascular branches) fitting a picture of an aggressive lesion.

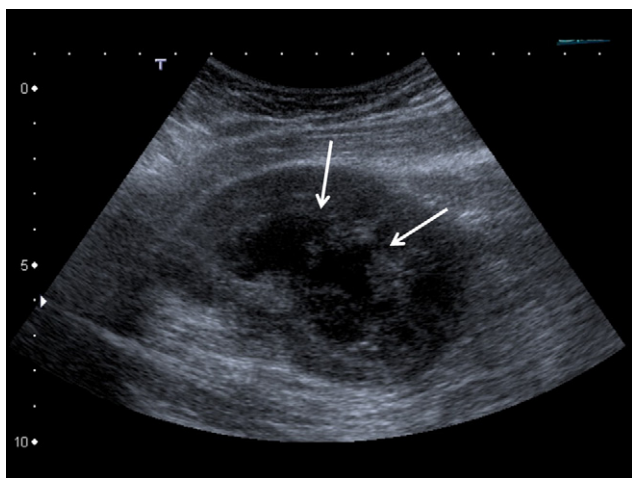


Figure 2. 75-year-old male. Investigation for a fast progressing soft tissue mass of the thigh. Sonography shows central zones of necrosis (white arrows) within a large solid mass, suggestive of an aggressive lesion.

spread across the aponeuroses, and early and significant contrast uptake (Fig. 3) are all features suggestive of an aggressive lesion [9]. This must, however, be contextualized: arteriovenous shunts are also seen in vascular malformations, and irregular tumour margins are sometimes seen in truly benign lesions, as is striking contrast uptake (some desmoid tumours).

This is why, except in some rare cases when sonography does lead to a confirmed diagnosis, complementary investigations are usually required. These include principally MRI, due to its accuracy in assessing topography and size, and its ability to determine lesion characteristics, and CT, which best identifies bone changes as well as calcifications in the soft tissue [11,12]. Nonetheless, there is a return to sonography to close diagnostic investigations by means of ultrasound-guided core needle biopsy of the zones within the tumour that have the potential to be the most informative (Fig. 4) [13].

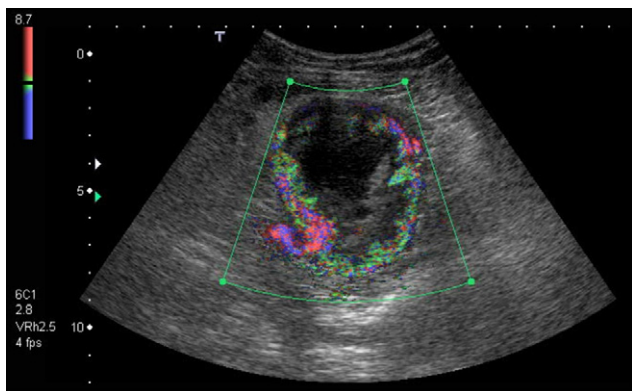


Figure 3. In the same patient, a quick (20 seconds) and considerable uptake of sonographic contrast agent. A strong argument in favour of an aggressive lesion (images 4 and 5 are drawn from a report of a dedifferentiated liposarcoma).



Figure 4. Ultrasound-guided needle biopsy of a soft tissue “tumefaction” of the arm. Needle clearly visible (white arrow).

Lesion classification based on anatomical pathology

For the purpose of clarity of the discussion, we must lean on a framework that is commonly accepted internationally. As a guiding principle we will use the World Health Organisation’s (WHO) anatomical pathology classification of soft tissue tumours [4]. It describes ten groups of soft tissue tumours:

- adipocytic tumours;
- fibroblastic/myofibroblastic tumours;
- fibro-histiocytic tumours;
- smooth muscle tumours;
- perivascular tumours;
- skeletal muscle tumours;
- vascular tumours;
- chondro-osseous tumours;
- neurogenic tumours;
- tumours of uncertain differentiation.

There are more than 80 possible histopathological diagnoses, but a small number of lesion types account for the vast majority of cases (at least 80 percent), and these include both benign and malignant lesions. (The relative proportion of malignant to benign lesions is one in one hundred).

We will firstly describe those pseudotumours with well-established sonographic signs: synovial cysts, ganglion cysts, haematoma, abscess, aneurysms and pseudoaneurysms, and epidermoid cysts. Even though these are not true instances of neoplasm, it is useful to have a good understanding of their sonographic appearance because they are common and need to be distinguished from true discrete masses.

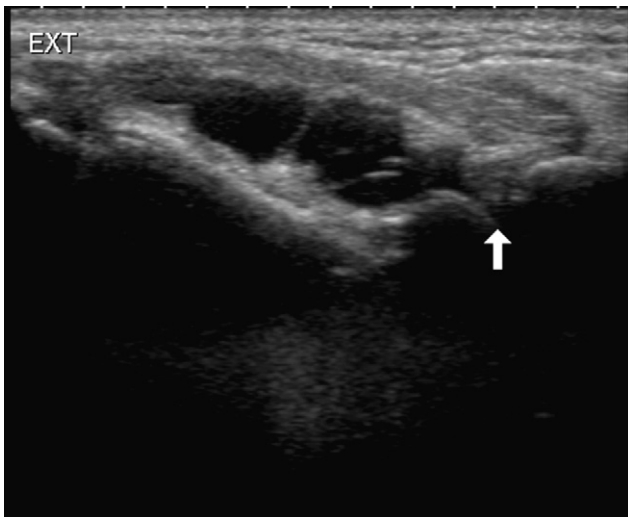


Figure 5. Tender tumefaction on the dorsal surface of the wrist in a 52-year-old woman. Sonography shows a cystic formation with septations that is “connected” to the joint (white arrow) suggesting a synovial cyst.

Commonly encountered pseudotumours

Synovial cyst

This is a “diverticulum” of the synovium that lines the joints, which is fluid-filled, can contain several echogenic zones, sometimes has septations, and varies in size from minimal to significant. It is crucial to demonstrate the essential feature of diagnosis: that there is continuity between the cyst and the joint (Fig. 5). This common lesion is readily found in two locations in our experience: the wrist, usually the dorsal surface, issuing from the interline separating the radial and ulnar epiphyses and the first row of the carpal bones; and the knee, developing within the semimembranosus bursa and medial head of the gastrocnemius muscle (Fig. 6) It can be large and cause disability (meaning ultrasound-guided drainage is indicated), or it can rupture (pseudothrombophlebitic picture) [13,14]. Any other joint can be affected, but this is less common. The

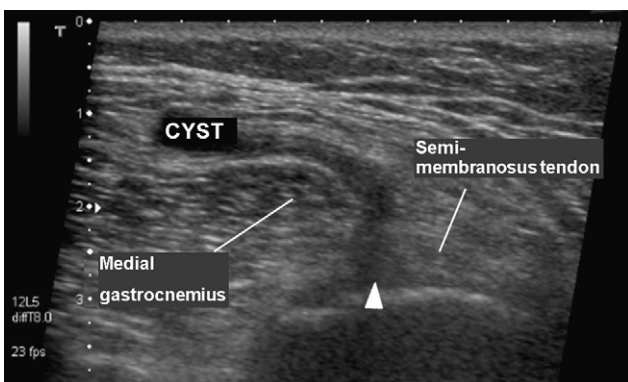


Figure 6. Popliteal cyst: topographical landmarks. Tumefaction of the popliteal fossa in a 56-year-old male. Axial view of the popliteal fossa highlights the cyst between the semimembranosus muscle and the medial head of the gastrocnemius muscle. Communication (arrowhead) with the joint.

signs on sonography would be the same as those described above.

Ganglion cysts

These are named for their morphology, and they are adherent to the joints (although communication has sometimes been lost), tendon sheaths, or bursae. These formations are made up of concentrated synovial and mucoid fluid [2,6,13]. They are lined with non-contiguous, flattened synovial cells and connective tissue. Sometimes large, their impact on the adjacent vessel and nerve structures can translate into clinical signs (disability, pain, paraesthesia etc.). There are some localisations that are classically seen: the dorsal surface of the wrist close to the scapholunate ligament; adjacent the spinoglenoid notch (Fig. 7a) on the posterior surface of the shoulder complicating a labral fissure and sometimes involving the suprascapular nerve; on the hip, as a result of the same process; and on the knee, due to a meniscal lesion. They can also develop in contact with a nerve or an artery (Fig. 7b) [15].

Haematoma

These often appear in a suggestive context (direct or indirect trauma in athletes) or in elderly people being treated with vitamin K antagonists. They have an echostructure that changes over time: although relatively echogenic at first, the contents gradually become almost entirely liquid (Fig. 8), usually starting at the periphery and progressing towards the centre, and in the final stages the centre alone is slightly echogenic. They are avascular. They can persist, becoming calcified at the periphery, or continuing to bleed (chronic haematoma). Any haematoma of the soft tissue that does not fit into this classic pattern, and in which the circumstances causing it are not clear, must be considered with suspicion and be subject to close monitoring. Haematoma can accompany or “mask” a true neoplastic lesion. MRI and sometimes a biopsy [2,6] will be necessary.

Abscess

These can be seen in a context of general infection or secondary to local “traumas” (injections in drug users), and are facilitated by a state of immunodeficiency. The content is usually fluid, often with a few areas producing low amplitude internal echoes, and they are sometimes scattered with clearly visible septa. They are enclosed in a thick capsule (Fig. 9) and are avascular. Sonography is useful to guide punctures for bacteriology sampling and drainage [2,6].

Vascular pseudotumours

These may be true aneurysms (often in the popliteal fossa) that are generally fusiform, with the edges of the arteries losing their parallel structure, and they can sometimes be part of a syndrome in which multiple aneurysms are formed. Otherwise they may be pseudoaneurysms secondary to local trauma (bone fractures, injections in drug users, instrumental manoeuvres in interventional radiology) and color Doppler imaging has made distinguishing them straightforward. It demonstrates, except in rare cases of

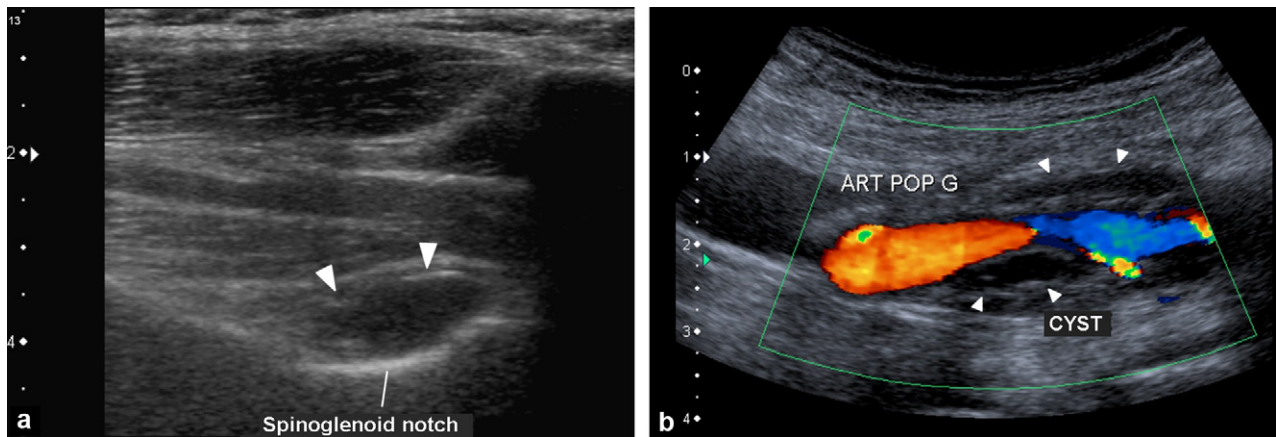


Figure 7. a: posterior axial view of the shoulder just below the scapular spine in a patient with chronic pain: presence of an ovoid formation of the spinoglenoid notch (arrowheads): ganglion cyst secondary to a labral fissure demonstrated on a CT scan of the joints; b: longitudinal view of the popliteal fossa in a 59-year-old male who had undergone an operation several years previously for a "cyst" in the region: cystic formation with septations (arrowheads) "enveloping" the popliteal artery: ganglion cyst.

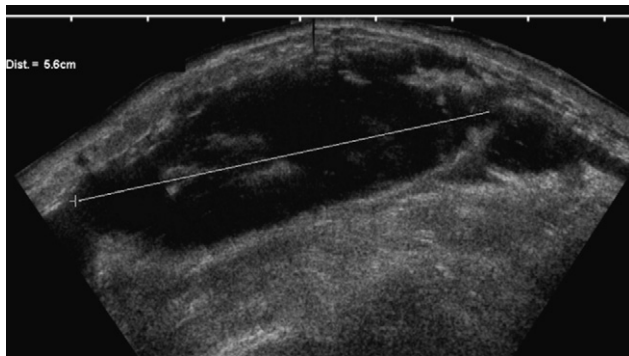


Figure 8. Longitudinal view of the thigh in an elderly patient treated with vitamin K antagonists, who had had a fall a few days previously: large fluid-filled formation corresponding to a haematoma undergoing "liquefaction".

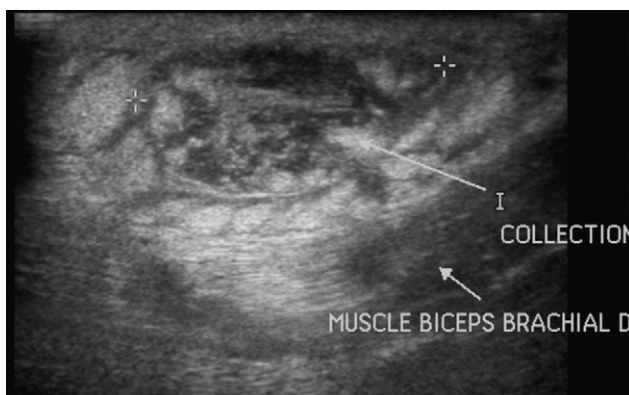


Figure 9. Fluid collection with echogenic, non-homogenous contents and a thick shell (long white arrow) which has a highly inflammatory appearance, secondary to an injection in the soft tissue of the arm in a drug-using patient: abscess of the soft tissue.

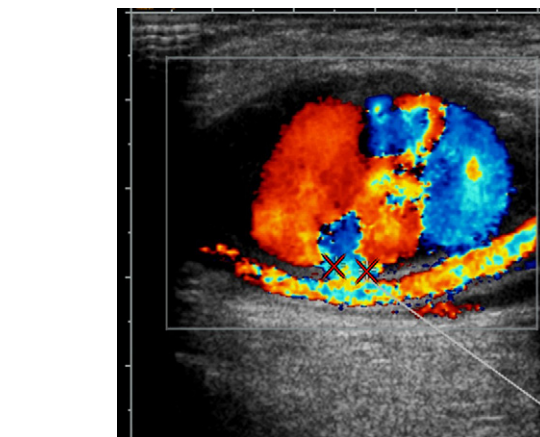


Figure 10. Color Doppler sonography showing a pseudoaneurysm of the femoral artery complicating an interventional radiology procedure. The communication between the artery and fluid collection (red crosses) is clearly visible and the flow within has a whirlpool-like appearance (flow colored red and blue).

almost complete thrombosis, linear blood flow within true aneurysms, and swirling blood flow within pseudoaneurysms, in which another finding is communication between the "mass" and the arterial lumen (Fig. 10) [2,13].

Epidermoid cysts

These are found at very superficial sites and are oval with a soft tissue echostructure. They are slightly echogenic, homogenous overall, having just a few internal linear hyper-echoic areas (corresponding to keratin), and their margins are well-defined except at each extremity, where acoustic shadowing is frequently seen. No vascularisation is found and the thickness of the subcutaneous layer of fat is normally reduced in respect of the mass (Fig. 11) [6].

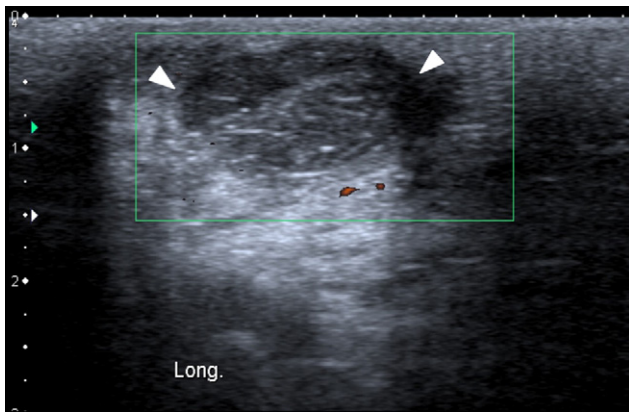


Figure 11. Sonography of the upper part of the back: Superficial, solid, ovoid formation that is non-homogenous, avascular on Doppler imaging, and contains linear echogenic zones. This is an epidermoid cyst.

Adipocytic tumours

Lipoma

Lipoma is the most common benign soft tissue tumour, and it is usually situated in the subcutaneous tissue. It produces a fusiform image with its long axis parallel to the skin line, has a soft tissue echostructure, is homogenous, being hyperechoic overall, and it has a micronodular appearance due to very fine septations with the lesion [2,5,6,14]. It has ill-defined margins (Fig. 12). Power Doppler demonstrates an absence of vascularisation. There is no enhancement after contrast injection. Other deep forms may be encountered, and these may be intra (Fig. 13) or intermuscular [16]. They usually have the same sonographic features, but “atypical” features are sometimes seen: large size, permeative margins, or heterogeneous echostructure, consisting of nodules with variable appearances or thick septations [17]. All these unusual features in a fatty lesion call for caution, and MRI

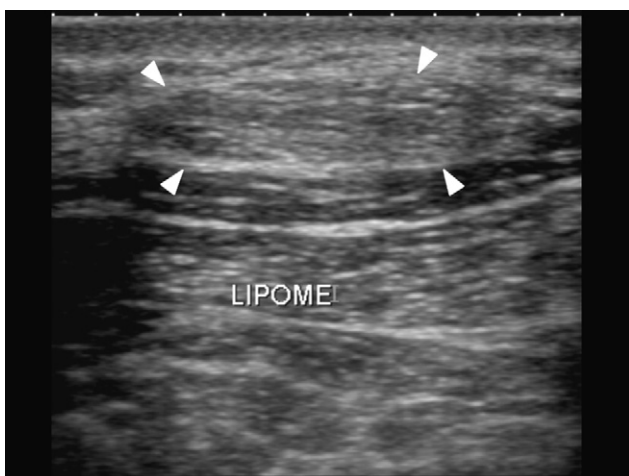


Figure 12. Sonography of the neck in an 80-year-old patient who had for a number of years been aware of a painless tumefaction that was stable in size on the posteroinferior part of the neck: hyperechoic mass sited in the subcutaneous tissue with narrow margins that is avascular (arrowheads): superficial lipoma.

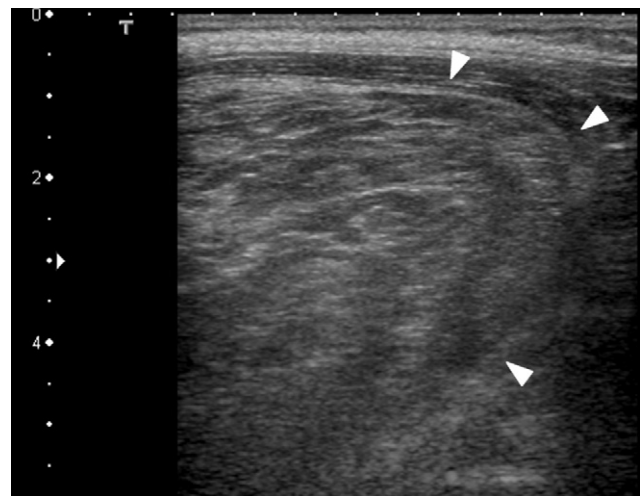


Figure 13. Longitudinal view of the thigh in a 52-year-old woman who had reported a painless swelling in this area that had progressed over several years: intramuscular lipoma (arrowheads) in the anterior compartment of the thigh.

and biopsy should be carried out in order to exclude a well-differentiated liposarcoma (containing at least 75% adipose tissue), as this is the main differential diagnosis.

Malignant adipocytic tumours are often large in size, sometimes painful, and are mainly seen in men in the proximal lower limbs. The wide variety of histologic types (myxoid, round cell, pleomorphic, undifferentiated) explain why there are so many possible presentations on sonography, which have in common an aggressive appearance, with occasional calcifications. Naturally this means that further investigations and biopsy are indicated (Fig. 14a and b).

A specific case: neural fibrolipoma

This usually affects the median nerve. There is a tumefaction of the wrist that is tender on pressure, which on axial plane sonography appears as an oval formation that is centred on the nerve with multiple small hypoechoic nodules (Fig. 15). On longitudinal views it appears as multiple intercommunicating fascicles [2,5,14,18]. It has a heterogeneous appearance because it is composed of a juxtaposition of hyperechoic fatty tissue and hypoechoic nerve tissue. It is avascular on Doppler imaging, and the use of a contrast agent has no effect. MRI features overlap with the sonographic findings.

Fibroplastic/myofibroplastic tumours

Nodular fasciitis

This a benign and reactive proliferation of myofibroblasts that is usually seen in young adults at the extremities of the upper limbs, with the neck and lower limbs being the next most common sites [19]. More rarely it can develop in muscle and it is then known as proliferative myositis. On sonography it appears as a solid oval formation with low or iso echogenic that is well-defined with regular or

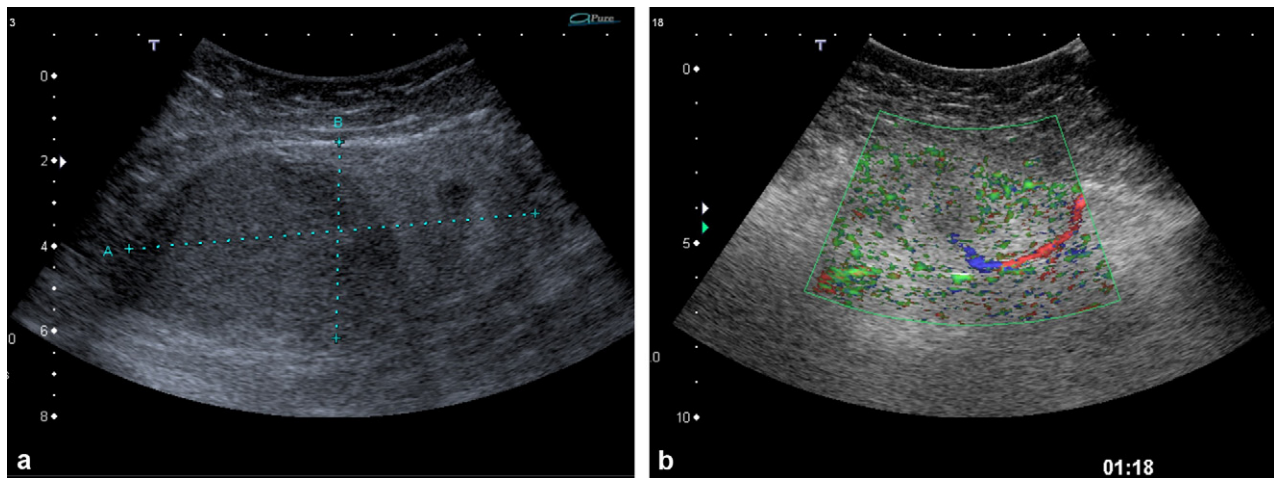


Figure 14. a: longitudinal view of the internal aspect of the thigh in a 75-year-old female who reported a tumefaction that had developed relatively recently (one year) and was growing in size: a voluminous, solid mass on the internal aspect of the thigh that is non-homogenous and consists of large hyperechoic areas (fatty tissue); b: contrast-enhanced sonography view showing contrast uptake, a strong argument in favour of an aggressive lesion. Anatomical pathology diagnosis: dedifferentiated liposarcoma.

slightly lobulated margins, and is avascular both with and without contrast material administration. Its main characteristic is that it maintains a connection with a connective tissue sheath, fascia, or aponeurosis.

Fibroma of tendon sheath

This affects adults between the ages of twenty and fifty. It manifests as a lesion similar to a giant cell tumour, and these two could be considered together as one entity. The only differences between them are variations in their respective distributions of cellular and stromal collagen content, with fibroma being low in cells and rich in connective tissue, and the opposite being true for giant cell tumours. Between these two ends of the spectrum, all possible distributions may be found. Their clinical and sonographic features are identical (see giant cell tumours) [19].

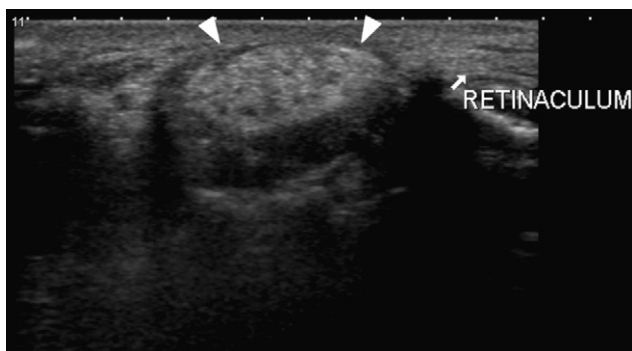


Figure 15. Axial sonographic view of the anterior aspect of the wrist in a young 25-year-old woman who reported a tender tumefaction that had developed several years previously. Multilobulated formation that is non-homogenous, with both hypoechoic and hyperechoic areas, centred on the medial nerve (arrowheads): neural fibrolipoma.

Elastofibroma

An elastofibroma is a reaction to a repeated mechanical irritation (pseudotumour) rather than a true neoplasm. It is usually situated in the connective tissue between the posterior chest wall and the inferior scapular angle, deeper than the rhomboid muscles and latissimus dorsi muscle in relatively elderly patients (mean age: 70). Other localisations are possible: the peri-trochanteric area of the hip, or in the elbow adjacent to the olecranon. It is sometimes bilateral. Clinically, there is pain and induration. On histology, it is made up of an accumulation of collagen and abnormal elastic fibres that is interspersed with a contingent of cells, adipose tissue, fibroblasts, and myoblasts. The image seen on sonography is one of a well-defined, ovoid formation with its long axis parallel to the wall. It is made up of tissue, and it is heterogeneous, having striations alternating with linear or curved bands that are hyper and hypoechoic (Fig. 16). It shows no enhancement after contrast injection [20,21].

Superficial fibromatosis

These originate in the palmar or plantar fascias or aponeuroses. They are made up of fusiform myofibroblastic cells, intercellular collagen deposits within a myxoid matrix and "constricted" vessels [19,22].

Palmar fibromatosis (Dupuytren's contracture) [22]

This affects the palmar aponeurosis on the anterior surface of the hand. It causes an indurated subcutaneous thickening with finger contractures. It mainly affects men over the age of thirty, with a clear predominance in the sixth decade. It is often bilateral, and appears on sonography as hypoechoic avascular thickening of the aponeurosis, most commonly affecting the fourth finger, followed by the fifth, third, and finally the second finger, without flexor tendon involvement (Fig. 17). Postoperative recurrence is common.

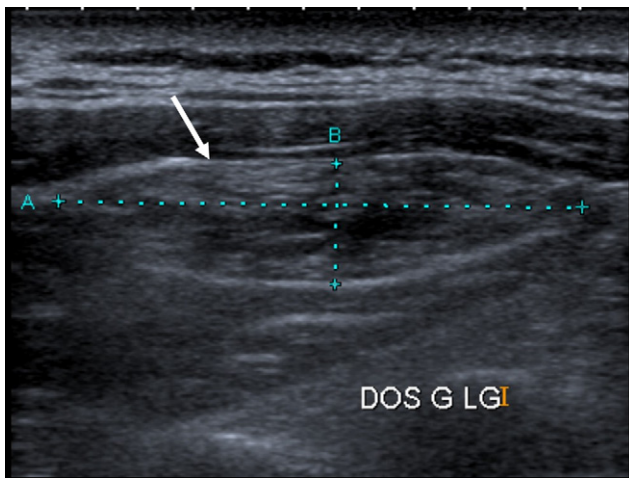


Figure 16. Transverse view of the back, at the lower internal pole of the scapula, in a 73-year-old male who reported a tender and firm tumefaction dating back several years: solid, ovoid, well-defined, deep mass that is avascular and non-homogenous, consisting of alternating hyperechoic and hypoechoic bands (white arrow): elastofibroma confirmed on biopsy.

Plantar fibromatosis (Ledderhose’s disease) [22]

This leads to single or multiple confluent nodules along the central or medial component of the plantar aponeurosis. It is sometimes bilateral. Concomitant presentation of the palmar form is possible. It affects both sexes equally, generally between the third and fifth decade. On sonography, one or several confluent nodules are visualised that are oval, solid, hypoechoic, avascular, circumscribed margins, connected into the superficial part of the plantar aponeurosis. They can spread into deep tissue, muscle, or superficial subcutaneous tissue, but this is rare. They do not enhance after contrast agent injection (Fig. 18). If symptomatic, they are

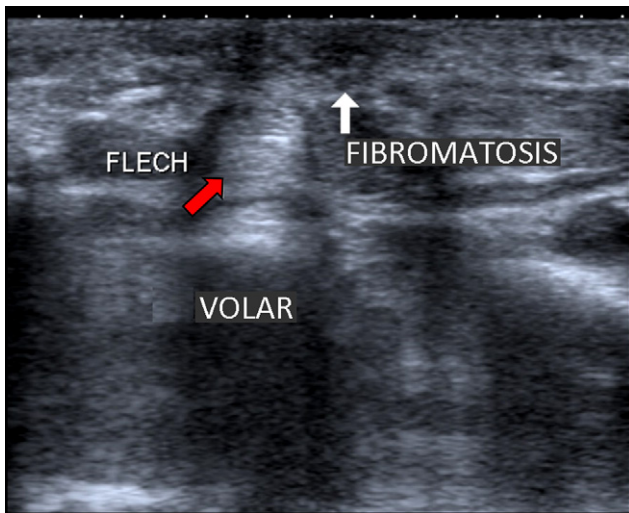


Figure 17. A 58-year-old male who reported a nodular “induration” on the volar aspect of the hand at the base of the fourth and fifth fingers with retraction and flexion of these fingers. The axial sonography view demonstrated thickening of the palmar aponeurosis (white arrow) above the flexor tendons (red arrow): palmar fibromatosis (Dupuytren’s contracture).

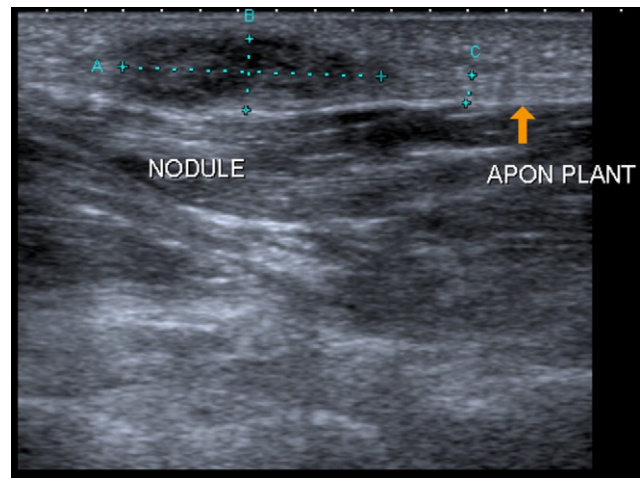


Figure 18. A 53-year-old woman who suffered from a painful nodule on the medial plantar surface of the foot. Sonography shows a nodule (between the dotted lines) attached to the plantar aponeurosis (orange arrow): plantar fibromatosis or Ledderhose’s disease.

thought to ideally require surgical removal although some advise the use of local steroid injections. Radiotherapy has sometimes been used postoperatively but functional sequelae are possible.

Deep fibromatoses

Desmoid tumours

These originate in the connective tissue of muscle, fascias, or aponeuroses, and they mainly affect young adults. There are three possible types: intra-abdominal, abdominal wall, or extra-abdominal. These types all have the same sonographic features: they are often quite large by the time they are investigated, with irregular finely spiculated margins, with thin peripheral extensions (Fig. 19). Their echostructure is solid, heterogeneous, and is made up of alternate linear zones or strips, that are hyper and hypoechoic, and of variable relative proportions. This seems to

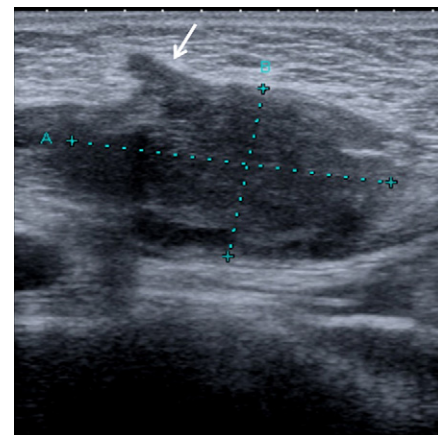


Figure 19. Desmoid tumour of the abdominal wall (rectus abdominis muscle) in a young 26-year-old woman. Sonogram in the axial plane demonstrates a wedge-shaped spiculated extension radiating between the intermuscular fascia (white arrow): very useful diagnostic sign.

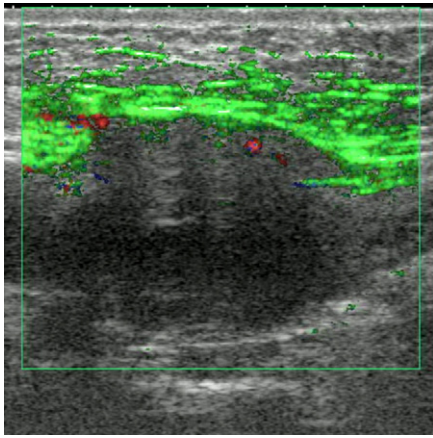


Figure 20. After administration of a contrast agent, minimal enhancement of the anterior part of the mass: a finding usually reported in inactive desmoid tumours. This particular lesion is situated in the rectus abdominus muscle of the abdominal wall (Same case as in Fig. 22).

correlate to the composition of the tissue, which is made up of cells (echogenic), fibres, and collagen (hypoechoic). On Doppler studies, vascularisation made up of a number of diffuse components is nearly always present. Findings vary on contrast-enhanced sonography. Although they can be considered to always enhance, this enhancement may be minimal (Fig. 20) or it can on the contrary be very intense (Fig. 21). This difference is doubtless related to the progression of the tumour. (We have observed that significant contrast uptake is seen in tumours that are often clinically tender and that are growing in size in spite of treatment). Certainly, these findings are similar to those of the highly aggressive lesions, a group to which desmoid tumours do not belong (they do have a tendency to relapse locally but they do not cause metastases). Both clinical (predisposition) and sonographic factors (spiculated margins, fine peripheral extensions, echostructure made up of alternate zones of

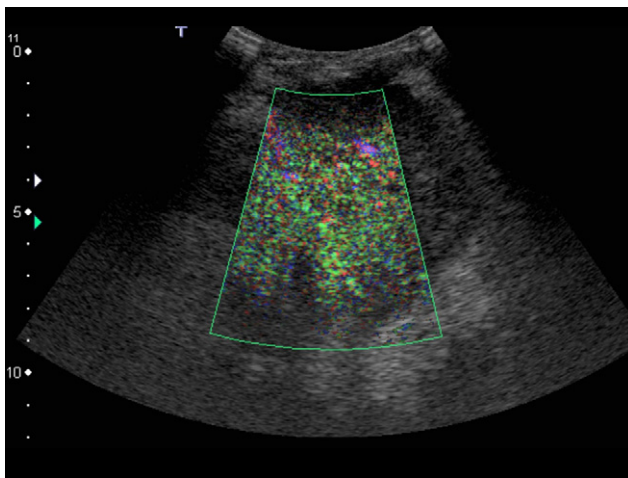


Figure 21. Quick and considerable contrast uptake in a desmoid tumour of the shoulder that had been causing the patient significant pain for around one month. The patient also reported a sensation of increased volume. This is a finding reported in “flare-ups” of desmoid tumours.

high and low echogenicity) can all be arguments in favour of a relatively reassuring diagnosis. Nonetheless, this does not mean that MRI and biopsy are not required for diagnostic confirmation [19,22,23].

Intra-abdominal fibromatoses

These are not tumours of the musculoskeletal system in the strictest sense. They are usually isolated, but can sometimes (in 15% of cases) be associated with familial adenomatous polyposis (Gardner’s syndrome). In these patients, localisation to the muscles or aponeuroses can also be seen [24].

Abdominal fibromatosis

This lesion presents a distinctive set of findings. It affects women and is very often connected to childbearing, occurring during or very soon after a pregnancy (within a year after the birth). It is known to be hormone-dependent since oestrogens seem to promote the proliferation of fibroblasts. The internal oblique and rectus abdominus muscles are the ones most commonly affected [25].

Extra-abdominal fibromatoses

These lesions originate close to the fascias of the shoulder muscles, chest wall, back, thighs, and in the knee area [24]. They produce the same sonography findings as are usually seen in desmoid tumours. They may be single or multiple (in over 15% of cases), and the younger the patient is, the more like they are to relapse [23].

Fibrosarcomas

A fibrosarcoma is a malignant proliferation of fibroblasts that are predominantly sited on the trunk and the extremities. They have the non-specific sonographic appearance of a highly aggressive lesion [6,14]. These lesions enhance after contrast injection. Histology and, to a lesser extent, MRI are used to distinguish them from other malignant lesions and even from some desmoid tumours, which can produce similar findings on sonography.

Fibrohistiocytic tumours and pseudotumours

Giant cell tumours of tendon sheath

This is a nodular form of pigmented villonodular synovitis [14]. It is firmly fixed to the underlying tendon sheath (Fig. 22). Usually found on the hand (it is one of the most common soft tissue lesions in this site), the wrist, or the volar aspect of the fingers close to an interphalangeal joint, it is seen in adults between their third and fifth decade, with a slight predominance in females. It is less commonly found in the knee or ankle. It is fusiform, well-defined, more echogenic than muscle, homogenous, and shows no cystic areas or calcification. It is not interdependent from the tendon fibres and when the fingers are moved, this can be nicely demonstrated during a dynamic examination. Sonography is the ideal modality for this purpose [2,4,13,26]. Doppler sonography can in rare cases show slight vascularisation. These lesions are non-enhancing.

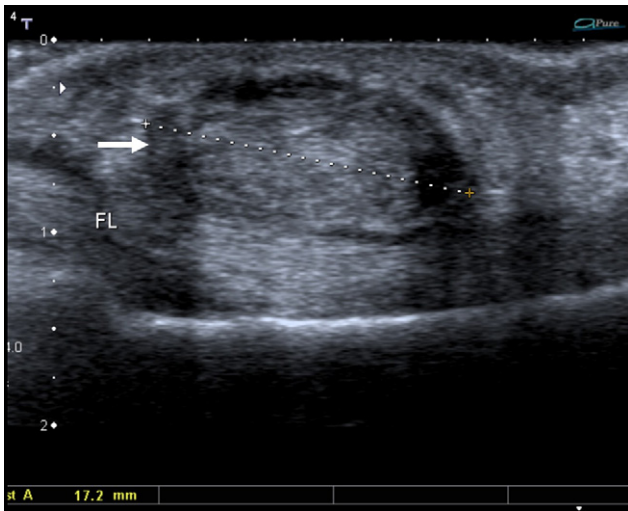


Figure 22. A 50-year-old male. Painless and non-progressive tumefaction of the anterior aspect of a finger. Sonography showed a solid, ovoid, well-defined, avascular formation (white arrow) ‘sitting’ on the tendon sheath of the superficial flexor of the finger (FL): giant cell tumour of the tendon sheath.

Benign fibrous histiocytoma

This is a hypoechoic, heterogeneous lesion with slight vascularisation. It is impossible to distinguish from a low-grade malignant lesion. MRI and biopsy are essential [27].

Malignant fibrous histiocytoma

This lesion used to be considered to be the most common malignant tumour in adults until the WHO recategorised it as a high-grade pleomorphic sarcoma (with the sub-groups: fibrous tissue and histiocyte predominant, giant cell predominant and inflammatory predominant) [4]. It has the sonographic features of an aggressive tumour, which means a biopsy is required as soon as possible.

A specific case of a benign pseudotumour: Xanthoma

A xanthoma is a localised proliferation of lipid-laden histiocytes that develops in patients with hypercholesterolaemia. They are usually known of, can be single or multiple, and are found in the cutaneous or subcutaneous layers, synovium, tendons, and in very rare cases, the bone [5,14]. It is usually caused by a reactive process rather than being a true neoplasm. On sonography, the classic findings are a tendon that appears ‘black and white’ and nodular on axial views, with a fibrillar pattern on the long axis [2]. Unusual features can be found (Fig. 23): solid formation, hypoechoic with lobulated margins, located on a tendon and sometimes causing bone remodeling, and avascular, both before and after administration of a contrast agent. In these atypical forms, laboratory tests for background information and, where necessary, a biopsy will shed light on these findings.

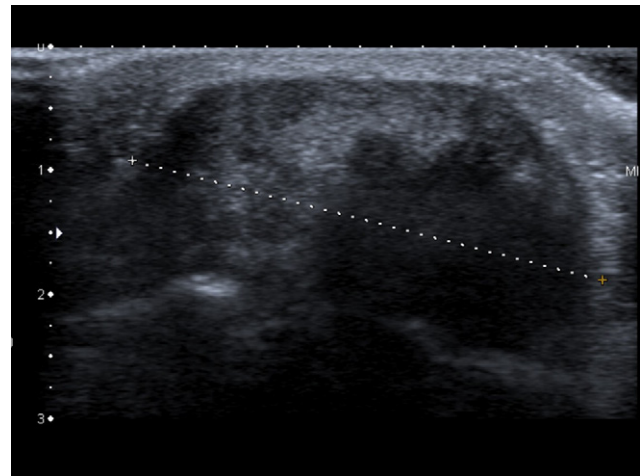


Figure 23. Sonography: axial view of the tibial insertion of the patellar tendon. Large, solid formation that is hypoechoic, painless, non-progressive, not vascularised either on Doppler imaging or after contrast agent administration, that ‘blends’ with the patellar tendon, in a 50-year-old female with hypercholesterolaemia. Biopsy confirmed a xanthoma.

Tumours and pseudotumours of the peripheral nerves

Schwannoma

These develop in the neck (vagus nerve, sympathetic nervous system) and the limbs (nerves of the flexor muscles) originating from the cells of the nerve sheath (meaning they have an eccentric growth with respect to the central nerve axis). Adults between the ages of twenty and fifty are affected, with equal distribution in both sexes [28,29].

Neurofibroma

Neurofibromas arise from constituents within the nerve (so they are centred on the nerve). They are usually single and affect young men and women in equal numbers, between the ages of twenty and thirty. In some rare cases (around 10%), they are associated with neurofibromatosis type 1.

Sonographic features are almost identical: fusiform, solid, moderately echogenic, sometimes with small, well-defined cystic areas, and an inconsistent finding is posterior enhancement. The essential point for diagnosis is a connection between the lesion and a nerve, which should ideally be demonstrated in real time (Fig. 24). Whether the lesion is eccentric to the nerve (schwannoma) or not (neurofibroma) seems to us to be a merely theoretical distinction in practical sonography. They are both generally avascular on Doppler imaging, and there is no contrast enhancement (in a few cases, it is possible to find minimal vascularisation on Doppler imaging, just as contrast enhancement can also be seen in rare cases) [29].

Morton neuroma

This term is misleading because this is in fact fibrosis of an intermetatarsal plantar nerve. It is mechanical in origin,

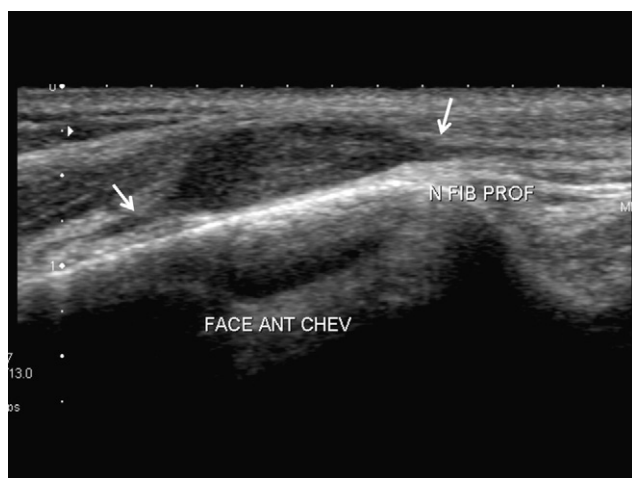


Figure 24. Longitudinal view of the anterior surface of the ankle in a 20-year-old woman who reported a tender nodule in this area, which was especially noticeable on mobilisation. Sonography did indeed demonstrate this small fusiform mass, which was solid, slightly echogenic, and without hypervascularisation shown either on Doppler imaging or after contrast agent administration (images not shown). The essential sign is present, in that it reattaches to the nerve at both extremities (white arrows): most likely a schwannoma.

being secondary to repeated micro trauma. There is a clear predominance in females. It causes pain on weight-bearing that is relieved by rest. It usually cannot be felt on palpation. Single, multiple, and bilateral forms are all found. It is investigated using the dorsal approach (with the help of Mulder's sign, which consists of firmly compressing the plantar surface of the forefoot while exerting a lateral pressure on the metatarsal heads) or the plantar approach, (the opposite finger is used to compress the dorsal side of the intermetatarsal space opposite to the probe). It is nearly always sited in the second or third intermetatarsal space. It is a bulbous and roughly oval formation that is hypoechoic, with indistinct margins, seen on longitudinal views to be positioned between the two nerves that are involved [30]. There is no vascularisation seen either before or after contrast agent administration (Fig. 25). It can be associated with intermetatarsal-phalangeal bursitis and this must not be allowed to mask a Morton neuroma [31].

Post-traumatic scar neuromas secondary to resection of the nerve must be mentioned, and these can be considered together with forms seen after amputation.

Malignant tumours of the peripheral nerve sheaths

These tumours are often, but not always (25–70% of cases), associated with neurofibromatosis, and they usually affect the major nerve networks (sciatic nerve, brachial plexus, or sacral plexus) [14]. They affect men and women in equal measure, except for those connected to neurofibromatosis type 1 (NF 1) in which there is a clear predominance in males. Usually developing between ages twenty and fifty, it is often seen earlier in these patients. These lesions are mainly deteriorating neurofibromas and a transformation

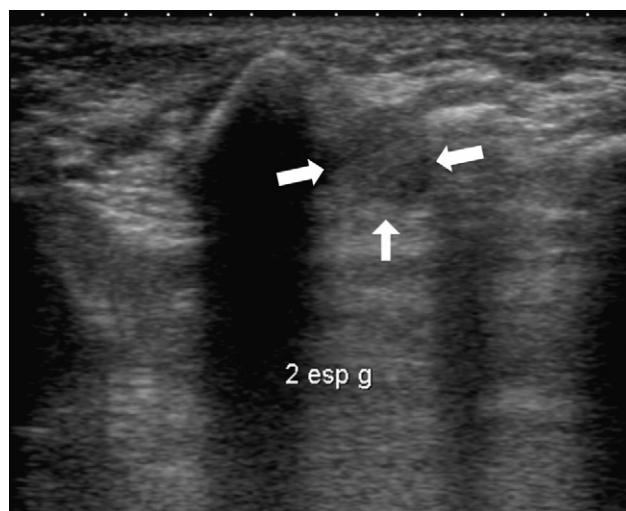


Figure 25. A 58-year-old female, complaining of diffuse forefoot pain on weight-bearing for more than one year, and difficulty putting on her shoes. Axial sonogram views of the area, taken both from the dorsal and plantar approaches, show a small, solid, hypoechoic formation (white arrow) of the second intermetatarsal space, that was linked to a plantar digital nerve, with no vascularisation either on Doppler imaging or with contrast-enhancement (images not shown).

into schwannoma is rare. They are often a source of pain along the nerve path (sciatica), and on sonography they appear as a large mass (with a diameter of several centimetres) that is solid, well-defined, heterogeneous, with several areas of necrosis, that is also continuous with the nerve structure it originates from [18]. Doppler imaging usually shows vascularisation within the lesion (except when there is significant necrosis) and, most importantly, use of a contrast agent demonstrates a warning sign as it shows intense and early enhancement, meaning that a biopsy is indicated (Fig. 26).

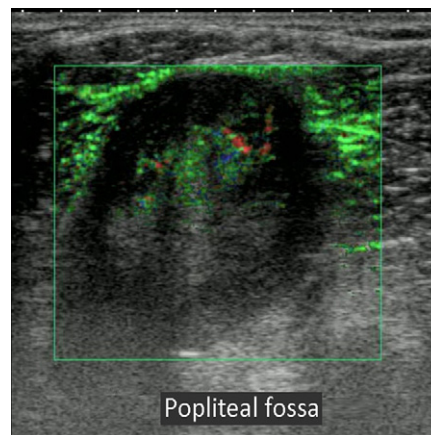


Figure 26. Large, painful and fast progressing tumour of the popliteal fossa, connected to the tibial nerve in a 20-year-old male with neurofibromatosis type 1. The transverse sonogram view of this region showed a discrete tumour with contrast uptake (aggressive lesion). This is a schwannosarcoma.

Extraskelatal osseous and cartilaginous tumours

Benign tumours or pseudotumours

Myositis ossificans circumscripta

This is a benign heterotopic ossification of the soft tissue that is sometimes due to trauma. It is made up of fibroblasts and myofibroblasts, which explains why it is currently classified under fibroblastic/myofibroblastic tumours (we preferred to consider it in this category because this seems to us to correspond to the reality of its sonographic features) [4]. Osteoblasts and chondrocytes subsequently appear and ultimately, mature bone. The clinical picture sometimes consists of pain and local inflammation, or the lesion may be inactive, and discovered accidentally. Although in the early stages misdiagnosis may be made on sonography (it is thought that, if carried out an early stage, sonography sometimes shows a small hypoechoic zone within the muscle that is surrounded by vessels, findings that could also be seen in an early, aggressive extraskelatal tumour), when it is carried out later, it is by contrast able to show, with good sensitivity, crescent-shaped peripheral calcifications that generate a shadow cone and prevent exhaustive investigation of the lesion (Fig. 27a) [6]. It may be situated in the subcutaneous tissue (panniculitis ossificans) or in the fascias (fasciitis ossificans) and of course, in the skeletal muscle, which is the reason for the name it bears myositis ossificans. When local inflammation is present, this explains the hypervascularisation seen on color Doppler sonography, as well as the rapid and intense contrast uptake (Fig. 27b). When it becomes asymptomatic there is only moderate vascularisation at the point of contact with the calcifications. A CT scan is the best modality for examining the lesion in its entirety.

There are other lesions that arise from periosteum such as Nora's tumour (bizarre parosteal osteochondromatous proliferation), which can be uncovered on sonography, but accurate diagnosis of these does rely on other techniques [32].

Chondroma and osteochondroma of the soft tissue

These are small cartilaginous nodules that sometimes also ossified and they are predominantly found in the hands and feet. They are more usually investigated with standard radiography and CT [5,14]. If there is exostosis, sonography may prove to be useful to measure the thickness of the cartilaginous layer, as this can give an idea of its aggressiveness [2].

Malignant tumours

Extraskelatal chondrosarcomas and osteosarcomas: these are rare and CT and MRI are the most suitable investigations [5,14].

Vascular and lymphatic system tumours

This category includes haemangiomas and lymphangiomas, whether benign or intermediately malignant, haemangi endotheliomas and haemangiopericytomas, and the malignant processes angiosarcoma and Kaposi's sarcoma. We also discuss a specific lesion in this section: the glomus tumour.

Benign tumours

Haemangiomas [14,33,34]

Haemangiomas are the most common hamartomas of the soft tissue. They make up 7% of benign tumours. They are usually identified before the age of three and are the lesion most often found in infants and children. They can also be seen in adolescents and adults. They predominantly affect females. Their location can be superficial or deep, and in the latter case they are nearly always intramuscular. On histology, they are made up of a wide range of tissue types. Anatomical pathology classes them according to the dominant vessel type: capillary, cavernous, arteriovenous, or venous. A capillary haemangioma is superficial, situated in the skin and subcutaneous tissue, and is reported in infants

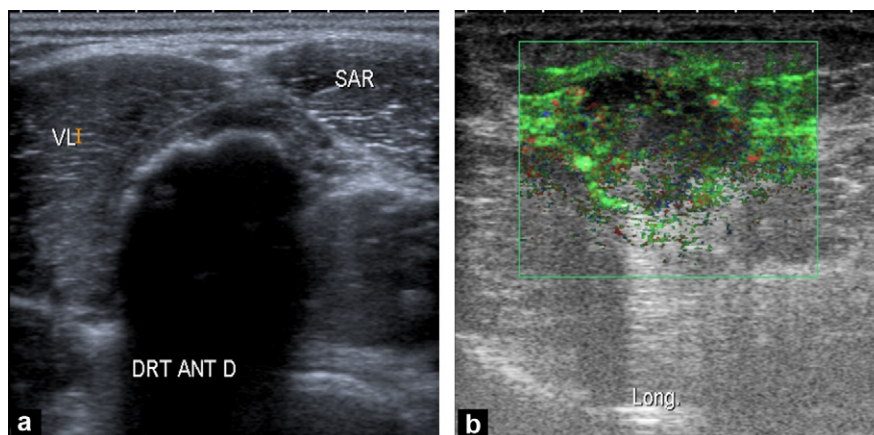


Figure 27. a: transverse sonogram view of the proximal thigh in a 40-year-old male who reported pain. Crescent-shaped intramuscular calcification producing a shadow cone and preventing overall visualisation of the lesion: myositis ossificans; b: early and considerable contrast uptake in a young woman presenting a picture of soft tissue inflammation of the internal aspect of the thigh: flare-up of myositis ossificans related to progression demonstrated by anatomical pathology explorations.

and young children. It involutes before the age of seven and there is no need for imaging.

A cavernous haemangioma is intramuscular, made up of dilated blood-filled spaces that are lined by a flattened endothelium. They are mainly seen in young children and adults. They do not involute. This type of haemangioma is the one most often explored using imaging. Sonography shows a formation bordered by an echogenic, thin, and slightly irregular boundary (fatty in nature) containing a complex echostructure, that is non-homogenous, being made up of hyperechoic (lipids) or isoechoic areas (smooth muscle, fibrosis, hemosiderin) amongst which are scattered zones of fluid and vasculature, which are demonstrated well by all types of Doppler imaging. Spectral tracings of systolic-diastolic flow that are indicative of arteriovenous shunts are a classic finding. Phleboliths and dystrophic calcifications of an organised thrombus may also be identified (Fig. 28a and b). These lesions are sometimes very large and spread into the adjacent soft tissue, or even the bone. They are contrast-enhancing, though this is seen relatively late (around 1 minute 30 s) (Fig. 28c).

An arteriovenous haemangioma reproduces the model of the foetal capillary network. They are sited in the soft tissue in young children. Characterised by increased blood output, they can sometimes cause malformations (enlargement of the extremities, venous distension etc.).

A venous haemangioma is made up of vessels with thick muscular walls. They are usually deep (retroperitoneum, mesentery), meaning they are almost never reported in the musculoskeletal system.

Lymphangiomas [14,35]

Lymphangiomas are made up of "excluded" lymphoid tissue that does not communicate with the lymphatic system and they are lined by lymphatic endothelium. They are classified according to the size of the vessel: capillary, cavernous, and, the most common type, cystic hygroma. The latter are usually present from birth and are always diagnosed before the age of two. They are usually found in the axilla, sub-mandibular region, and posterior neck (from where they can spread to the mediastinum).

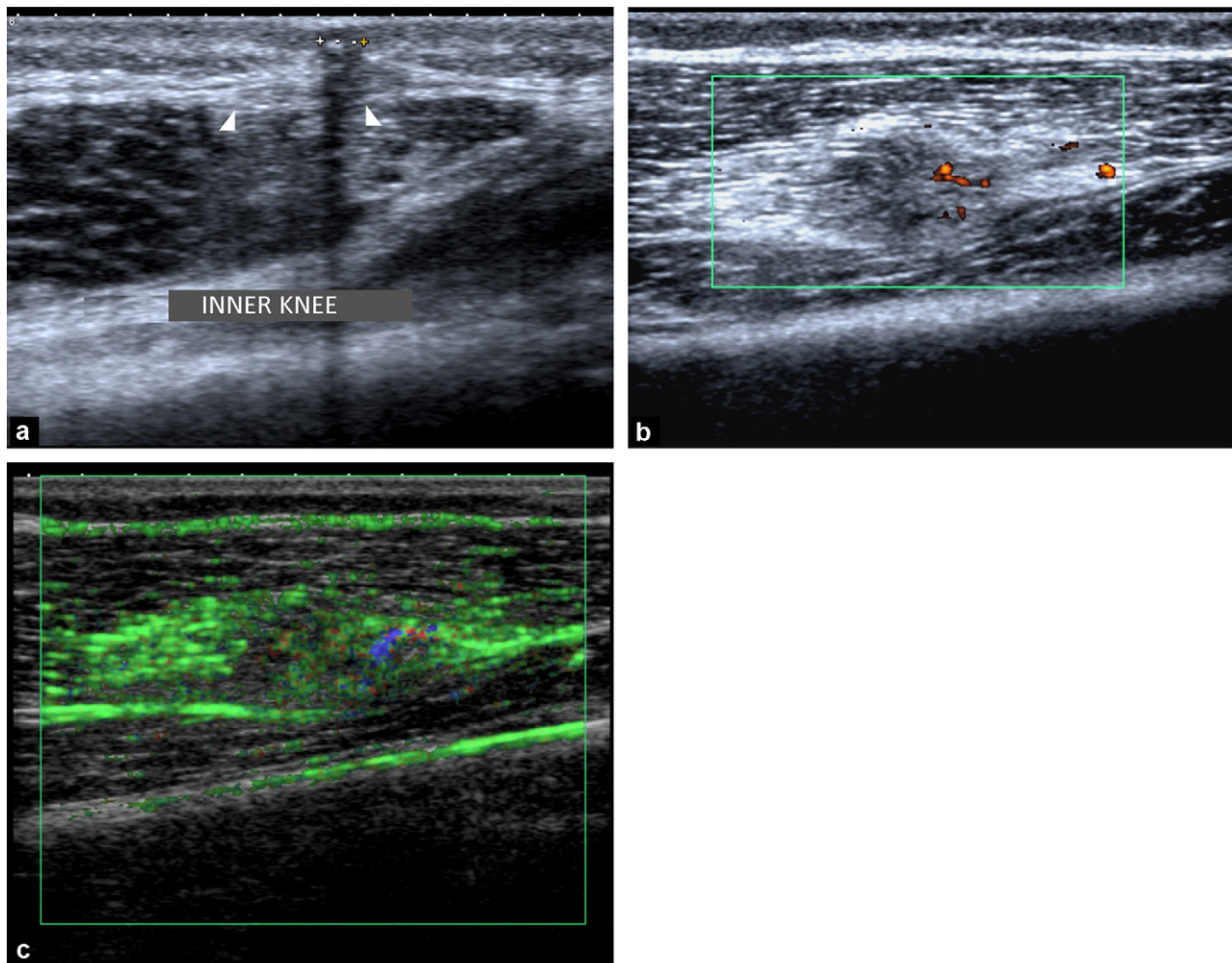


Figure 28. a: young 14-year-old male who reported asymmetrically sized thighs and pain on mobilisation. Sonography showed a deep, intramuscular formation that was immediately sub-aponeurotic (arrowheads) with a phlebolith (measurement shown by small crosses): intramuscular haemangioma. Hypervascularisation shown on color Doppler (b) and late contrast uptake (around 1 min 30 s) (c) after injection.

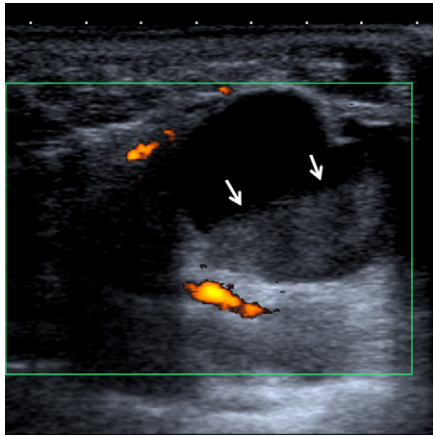


Figure 29. Haemolymphangioma of the sub-mandibular triangle, already known of, in a 14-year-old girl who was examined due to acute and painful swelling. Visualisation of the lesion showed an air-fluid level (white arrows) and echogenic sediment: very likely to be intralesional bleeding.

Sonography demonstrates a cystic mass with multiple septations, the septa being of variable thickness. A few solid components or septations may be seen. Complications can develop: infections, causing the contents to appear more echogenic, bleeding, in which an air-fluid level may appear, or even in rare cases, rupture (Fig. 29).

Intermediate malignancy tumours

A haemangiopericytoma is a proliferation of endothelial vascular cells that varies in terms of site and topography (deep or superficial) [2,14]. A haemangiopericytoma is made up of pericytes, contractile cells that surround the capillaries and post-capillary venules, and it affects middle-aged adults with no predominance in either sex, developing mainly on the extremities of the lower limbs and the retroperitoneum [14]. Features on sonography are non-specific.

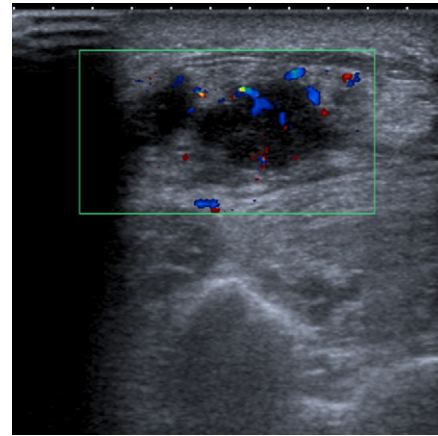


Figure 30. Fast progressing mass of the posteroinferior part of the leg in an 80-year-old male. Sonography showed a lesion with irregular margins, areas of necrosis, and anarchic hypervascularisation: this lesion presented significant uptake of sonographic contrast material (image not shown): aggressive lesion: biopsy confirmed leiomyosarcoma.

Malignant tumours

Angiosarcomas, whether superficial or deep, affect older patients and are twice as common in men. Chronic lymphoedema is a predisposing factor [14,35].

Kaposi’s sarcoma is a malignant cutaneous vascular proliferation associated with a viral infection. There are four different clinical contexts: chronic, lymphadenopathic, in transplant patients, and in patients with AIDS, for whom the prognosis is poorer.

On sonography, it is impossible to determine whether any of this group of tumours is of intermediate or certain malignancy because there are no specific signs. MRI has greater possibilities. Biopsy is essential [14].

Glomus tumours

This is a benign neoplasm that arises from a neuromyoarterial glomus body. It is usually found on the dorsal surface of

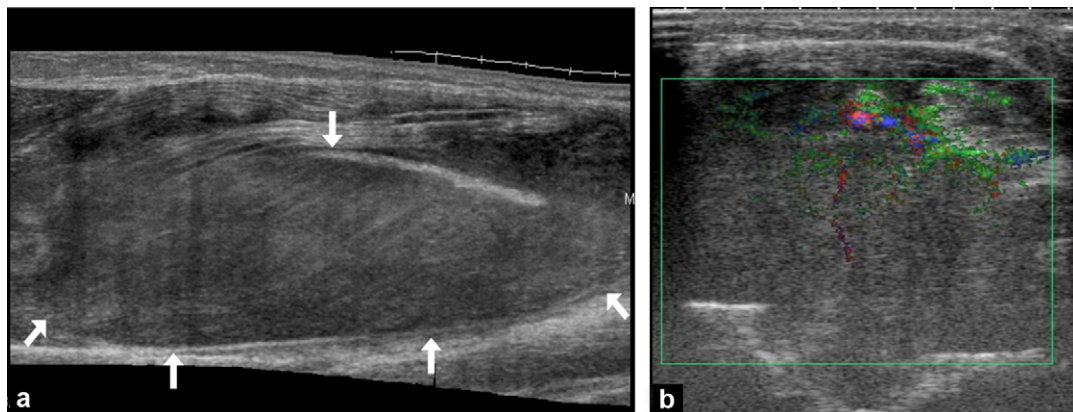


Figure 31. Painful, fast growing mass of the anterior surface of the arm in a 14-year-old male: a: sonography demonstrated a discrete, solid mass with a feathered appearance occupying the anterior brachial compartment; b: after administration of contrast agent, the tumour quickly showed enhancement: aggressive lesion of the anterior compartment of the arm in an adolescent: rhabdomyosarcoma confirmed on biopsy.

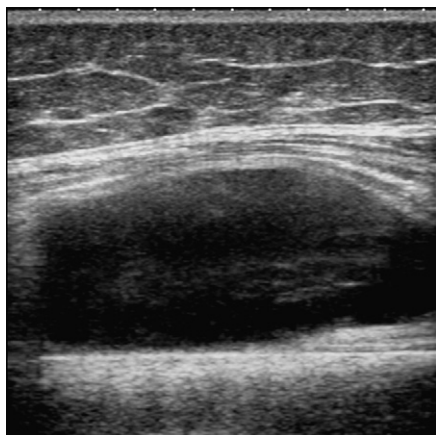


Figure 32. Sonography in a 65-year-old female presenting a large tumefaction on the external surface of the right thigh: ovoid, intramuscular formation with an almost-fluid echostructure and no contrast-enhancement seen. Histology confirmed a myxoma.

the fingers, under the nails. Other possible locations are the wrist, forearm, and foot. There is a clear predominance in females. Clinically, there is a small bluish or reddish nodule that presents paroxysmal pain or pain on pressure and they are often sensitive to cold. It is difficult to make a diagnosis using sonography when the tumour is small as the nail can act as a barrier to ultrasound waves. When sonography does find this tumour, it is in the form of a small sub-ungual hypoechoic mass that shows hypervascularisation on Doppler imaging [5,14].

Tumours and pseudotumours of the muscles

Smooth muscle

Benign tumours: leiomyoma, usually small, superficial, cutaneous or subcutaneous, not investigated by imaging.

Malignant tumours: leiomyosarcomas, which have no specific characteristics and the only feature to look for, especially if it is a venous lesion, is a point of contact between the tumour and vascular wall that the process could have originated from [2,14]. The usual features are once again those seen in aggressive lesions (Fig. 30) [2].

Striated muscle

Benign tumours: rhabdomyoma is very rare and affects middle-aged adults with a clear male predominance [2,5,14]. It is usually sited in the head or neck and has no particular features on sonography.

Malignant tumours: rhabdomyosarcoma, which is the most common soft tissue tumour in children [2,5,14]. Its features on sonography are those seen in all aggressive tumours (Fig. 31a and b). MRI and ultimately biopsy are essential.

We include under this section muscular abnormalities that are in fact anatomical variants: supernumerary muscles that take on the clinical appearance of a tumefaction, the true cause of which will generally be quickly identified on sonography [36].

Tumours of uncertain differentiation

Myxoma

This is a benign mesenchymal tumour seen in adults that is rich in stroma, avascular, myxoid, and has a minimal cellular component. It is predominantly sited in the muscles of the thighs, shoulders, buttocks, and arms [37].

On sonography, it appears as a well-defined ovoid mass within the muscle that is highly hypoechoic, almost fluid, not vascularised on Doppler imaging (Fig. 32), and is non-enhancing. There is an association with polyostotic fibrous dysplasia, a presentation that constitutes Mazabraud's syndrome.

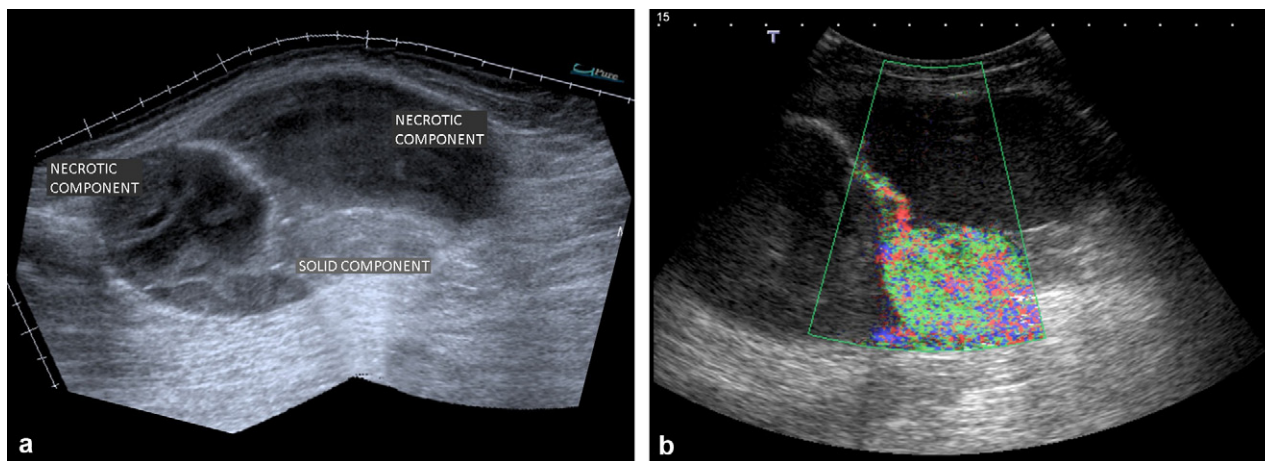


Figure 33. Fast progressing “mass” of the internal surface of the thigh in a 55-year-old female. Sonography shows a large, non-homogenous formation that is made up of both solid and fluid zones, separated by thick septations (a). After contrast agent administration, there is fast and significant contrast uptake in the solid section and the septations (b). Synovial sarcoma identified on histology investigations.

Disclosure of interest

The authors declare that they have no conflicts of interest concerning this article.

References

- [1] Blum A, Louis M, Lecocq S, Detreille R, Roch D, Batch T, et al. Comment j'explore une tumeur de parties molles. In: Formation médicale continue. Paris, France: Société française de radiologie; 2008, pp. 657–66.
- [2] Brasseur J, Tardieu M. Échographie du système locomoteur. Elsevier Masson; 2006.
- [3] Lassau N, Brule A, Chami L, Benatsou B, Péronneau P, Roche A. Evaluation of early response to antiangiogenic treatment with dynamic contrast enhanced ultrasound. *J Radiol* 2008;89(5 Pt 1):549–55.
- [4] Wu JS, Hochman MG. Soft-tissue tumors and tumor-like lesions: a systematic imaging approach. *Radiology* 2009;253(2):297–316.
- [5] Schepper AMAD, Parizel PM, Vanhoenacker FM. Imaging of soft tissue tumors. Springer; 2006.
- [6] Widmann G, Riedl A, Schoepf D, Glodny B, Peer S, Gruber H. State-of-the-art HR-US imaging findings of the most frequent musculoskeletal soft-tissue tumors. *Skelet Radiol* 2009;38(7):637–49.
- [7] Vanel D, Bidault F, Bonvalot S, Le Pechoux C, Terrier P, Le Cesne A. Imagerie des sarcomes des tissus mous. *Oncologie* 2007;9(2):97–101.
- [8] Beaman FD, Kransdorf MJ, Andrews TR, Murphey MD, Arcara LK, Keeling JH. Superficial soft-tissue masses: analysis, diagnosis, and differential considerations. *Radiographics* 2007;27(2):509–23.
- [9] Bodner G, Schocke MFH, Rachbauer F, Seppi K, Peer S, Fierlinger A, et al. Differentiation of malignant and benign musculoskeletal tumors: combined color and power Doppler US and spectral wave analysis. *Radiology* 2002;223(2):410–6.
- [10] Lux G, Pierucci F, Detreille R, Roch D, Moisei A, Batch T, et al. Comparaison de l'échographie de contraste avec l'IRM dynamique dans l'exploration des masses des tissus mous. *J Radiol* 2008;89:1456.
- [11] van Rijswijk CSP, Geirnaerdt MJA, Hogendoorn PCW, Taminiou AHM, van Coevorden F, Zwinderman AH, et al. Soft-tissue tumors: value of static and dynamic gadopentetate dimeglumine-enhanced MR imaging in prediction of malignancy. *Radiology* 2004;233(2):493–502.
- [12] Kransdorf MJ, Murphey MD. Radiologic evaluation of soft-tissue masses: a current perspective. *AJR Am J Roentgenol* 2000;175(3):575–87.
- [13] Bianchi S, Martinoli C, Derchi LE, Baert AL, Rizzato G, Abdelwahad IF, et al. Ultrasound of the musculoskeletal system. Springer; 2007.
- [14] Kransdorf MJ, Murphey MD. Imaging of soft tissue tumors. Lippincott Williams & Wilkins; 2006.
- [15] Burk DL, Dalinka MK, Kanal E, Schiebler ML, Cohen EK, Prok RJ, et al. Meniscal and ganglion cysts of the knee: MR evaluation. *AJR Am J Roentgenol* 1988;150(2):331–6.
- [16] Kransdorf MJ, Moser RP, Meis JM, Meyer CA. Fat-containing soft-tissue masses of the extremities. *Radiographics* 1991;11(1):81–106.
- [17] Murphey MD, Carroll JF, Flemming DJ, Pope TL, Gannon FH, Kransdorf MJ. From the archives of the AFIP: benign musculoskeletal lipomatous lesions. *Radiographics* 2004;24(5):1433–66.
- [18] Murphey MD, Smith WS, Smith SE, Kransdorf MJ, Temple HT. From the archives of the AFIP: Imaging of musculoskeletal neurogenic tumors: radiologic-pathologic correlation. *Radiographics* 1999;19(5):1253–80.
- [19] Dinauer PA, Brixey CJ, Moncur JT, Fanburg-Smith JC, Murphey MD. Pathologic and MR imaging features of benign fibrous soft-tissue tumors in adults. *Radiographics* 2007;27(1):173–87.
- [20] Brandser EA, Goree JC, El-Khoury GY. Elastofibroma dorsi: prevalence in an elderly patient population as revealed by CT. *AJR Am J Roentgenol* 1998;171(4):977–80.
- [21] Naylor MF, Nascimento AG, Sherrick AD, McLeod RA. Elastofibroma dorsi: radiologic findings in 12 patients. *AJR Am J Roentgenol* 1996;167(3):683–7.
- [22] Murphey MD, Ruble CM, Tyszko SM, Zbojniec AM, Potter BK, Miettinen M. From the archives of the AFIP: musculoskeletal fibromatoses: radiologic-pathologic correlation. *Radiographics* 2009;29(7):2143–73.
- [23] McDonald ES, Yi ES, Wenger DE. Best cases from the AFIP: extraabdominal desmoid-type fibromatosis. *Radiographics* 2008;28(3):901–6.
- [24] Casillas J, Sais GJ, Greve JL, Iparraguirre MC, Morillo G. Imaging of intra- and extraabdominal desmoid tumors. *Radiographics* 1991;11(6):959–68.
- [25] Teo HEL, Peh WCG, Shek TWH. Case 84: desmoid tumor of the abdominal wall. *Radiology* 2005;236(1):81–4.
- [26] Karasick D, Karasick S. Giant cell tumor of tendon sheath: spectrum of radiologic findings. *Skelet Radiol* 1992;21(4):219–24.
- [27] Hannachi Sassi S, Trabelsi M, Abid L, Mrad K, Abbess I, Dhoub R, et al. Deep benign fibrous histiocytoma: a case report. *Rev Chir Orthop Reparatrice Appar Mot* 2006;92(8):809–12.
- [28] Beaman FD, Kransdorf MJ, Menke DM. Schwannoma: radiologic-pathologic correlation. *Radiographics* 2004;24(5):1477–81.
- [29] Stuart RM, Koh ESC, Breidahl WH. Sonography of peripheral nerve pathology. *AJR Am J Roentgenol* 2004;182(1):123–9.
- [30] Quinn TJ, Jacobson JA, Craig JG, van Holsbeeck MT. Sonography of Morton's neuromas. *AJR Am J Roentgenol* 2000;174(6):1723–8.
- [31] Bencardino J, Rosenberg ZS, Beltran J, Liu X, Marty-Delfaut E. Morton's neuroma: is it always symptomatic? *AJR Am J Roentgenol* 2000;175(3):649–53.
- [32] Moisei A, Gauchotte G, Sanou R, Dautel G, Vignaud J, Blum A. What is your diagnosis? *J Radiol* 2009;90(12):1874.
- [33] Olsen KI, Stacy GS, Montag A. Soft-tissue cavernous hemangioma. *Radiographics* 2004;24(3):849–54.
- [34] Ly JQ, Sanders TG, SanDiego JW. Hemangioma of the triceps muscle. *AJR Am J Roentgenol* 2003;181(2):544.
- [35] Murphey MD, Fairbairn KJ, Parman LM, Baxter KG, Parsa MB, Smith WS. From the archives of the AFIP: Musculoskeletal angiomatous lesions: radiologic-pathologic correlation. *Radiographics* 1995;15(4):893–917.
- [36] Sookur PA, Naraghi AM, Bleakney RR, Jalan R, Chan O, White LM. Accessory muscles: anatomy, symptoms, and radiologic evaluation. *Radiographics* 2008;28(2):481–99.
- [37] Murphey MD, McRae GA, Fanburg-Smith JC, Temple HT, Levine AM, Aboulafia AJ. Imaging of soft-tissue myxoma with emphasis on CT and MR and comparison of radiologic and pathologic findings. *Radiology* 2002;225(1):215–24.
- [38] Murphey MD, Gibson MS, Jennings BT, Crespo-Rodríguez AM, Fanburg-Smith J, Gajewski DA. From the archives of the AFIP: imaging of synovial sarcoma with radiologic-pathologic correlation. *Radiographics* 2006;26(5):1543–65.



ORIGINAL ARTICLE / echography

Contrast-enhanced ultrasonography of peripheral soft-tissue tumors: Feasibility study and preliminary results

F. Gay^{a,*}, F. Pierucci^a, V. Zimmerman^a,
S. Lecocq-Teixeira^a, P. Teixeira^a, C. Baumann^b,
A. Blum^{a,c}

^a Guilloz Imaging Department, Nancy University Hospital—Central Hospital, 54000 Nancy, France

^b Department of Epidemiologic and Clinical Evaluation, Marin Hospital, Nancy University Hospital, 54000 Nancy, France

^c UMR 7561 CNRS—UHP/Nancy 1, 54000 Nancy, France

KEYWORDS

Microbubble-enhanced US;
Soft tissue tumor;
Desmoid tumor;
Sarcoma;
Neoangiogenesis

Abstract

Objectives. — To determine the diagnostic value of contrast-enhanced ultrasonography, to differentiate benign and malignant soft-tissue tumors and to assess the feasibility and interest of modelling enhancement curves.

Patients and methods. — This retrospective study includes 118 patients with soft-tissue tumors, examined with ultrasound after injection of SonoVue[®], a contrast product. The raw data were treated with CHI-Q acquisition software to model the enhancement curves. We analyzed tumor uptake of the contrast product visually and studied the enhancement curves, characterized by five parameters: peak intensity, time to peak, mean transit time, initial slope, and area under the curve.

Results. — There were 81 benign and 37 malignant tumors. For a diagnosis of benign tumor, the absence of contrast uptake had a sensitivity of 60%, a specificity of 68%, a positive predictive value of 50% and a negative predictive of 83%. Study of the 70 curves obtained (48 benign and 22 malignant tumors) showed that the parameters of area under the curve ($\text{Chi}^2 = 8.6$ and $P < 0.005$), slope ($\text{Chi}^2 = 8.12$ and $P = 0.004$), and peak intensity ($\text{Chi}^2 = 7.55$, $P = 0.005$) differed significantly between the two populations.

Conclusion. — Absence of contrast uptake suggests a benign lesion. The study of enhancement curves showed significant differences between the different tumor populations.

© 2011 Éditions françaises de radiologie. Published by Elsevier Masson SAS. All rights reserved.

* Corresponding author.

E-mail address: frederique.gay1@gmail.com (F. Gay).

The characterization of soft-tissue tumors is based essentially on morphologic study by MRI [1,2]. Except for some lesions with a specific appearance, such as artery-to-vein malformations (AVM), lipomas, and elastofibromas, histologic verification is often necessary. The new techniques for studying neovascularization, cellularity, and biochemical characterization improve both tissue characterization and analysis of response to treatment [3–7].

Contrast-enhanced ultrasonography (CEUS) is one of these techniques. Some recent studies have shown that CEUS can be used to assess neoangiogenesis of tumors in the liver [8–10], lungs, thyroid, ovaries, and prostate [11–14] and to determine their response to treatment very quickly [15]. A group at the Gustave Roussy Institute (IGR) has also shown that the use of a perfusion model improves the analysis of contrast uptake and the specificity of the data [16,17]. Few studies, however, have examined the characterization of peripheral soft-tissue tumors as benign or malignant [18].

The aim of our study was to determine the diagnostic value of CEUS of peripheral soft-tissue tumors and the use of software to model enhancement curves for analyzing contrast uptake.

Patients and methods

Population

This open, single-center retrospective study includes 160 patients seen between January 2008 and June 2010 who were referred for ultrasonography (and MRI) to characterize a soft-tissue tumor suspected either of malignancy or of further development after it was considered cured or stabilized (desmoid tumor). Patients with a tumor originating in bone and extending into soft tissue were not included.

Patients were excluded when raw data during ultrasound acquisition were incomplete ($n = 11$), quality acquisition was

poor (patient moved, or region of interest, [ROI], could not be determined) ($n = 26$), or the final diagnosis was uncertain ($n = 5$). Forty-two patients were excluded, mainly at the beginning, when we first started working with this method.

In all, imaging was successfully completed for 118 patients (47 men, 71 women, mean age: 57.4 years, range: 18–92 years).

The final diagnosis was based either on histologic criteria ($n = 78$) or on a characteristic appearance with clinical and imaging follow-up longer than 6 months ($n = 40$).

Three subgroups of patients were identified: the first (group 1) comprised those with benign tumors ($n = 81$), group 2 the malignant primary soft-tissue neoplasms ($n = 23$), and the third, all of the malignant neoplasms studied, including group 2 and all metastases and lymphomas ($n = 37$) (Table 1).

Technique

The examinations were performed by three persons qualified in osteoarticular ultrasound and trained in the acquisition techniques for CEUS, with an Aplio XG ultrasound device (Toshiba Medical, France) and two probes, one superficial PLT-805AT (frequency 8 MHz, ranging from 5 to 12 MHz) and the other a convex abdominal PVT-375BT (frequency 3.5 MHz, ranging from 1 to 6 MHz) for the larger lesions. The raw linear data were acquired with CHI-Q acquisition software, at frequencies of 10 MHz, 41 frames per second in soft-tissue mode, and 2.8 MHz, 39 frames per second in abdominal mode. These data were analyzed on an UltraExtend® workstation (Toshiba Medical, France), with enhancement curve modeling software developed by the IGR (patent PCT/IB2006/003742 described in article [19]).

The ultrasonography was initially performed in B mode to identify the focal lesion. Lesions were measured, localized, their characteristics described (edges, echogenicity, and shape), and then their vascularization studied with

Table 1 Histology of tumors (number of patients).

Benign tumor ($n = 81$)	PDC		Malignant tumor ($n = 37$)	PDC			
	Yes	No		Yes	No		
Lipoma	16	1	<i>Soft tissue sarcoma (n = 19)</i> Undifferentiated, pleiomorphic, with fusiform cells Liposarcoma Leiomyosarcoma Synovial sarcoma Dermatofibrosarcoma <i>PNST</i> <i>Poorly differentiated malignant tumor</i> <i>Sarcomatoid carcinoma and infiltrating prickle cells</i> <i>Lymphoma</i> <i>Metastases</i>	11	8	3	
AVM-hemangioma	14	5		9	5	3	2
Schwannoma, neurofibroma	10	6		4	1	1	0
Desmoid tumor	8	5		3	1	1	0
Pseudotumors and diverse	9	2		7	1	0	1
GCT	7	3		4	1	0	1
Isolated fibrous T	4	4		0			
Myositis ossificans	3	0		3	1	1	0
Myxoma	3	0		3	1	0	1
Plantar fibromatosis nodule (Ledderhose disease)	2	0		2	2	2	0
Elastofibroma	2	0		2			
Mucoid cyst	1	0		1			
Epidermoid cyst	1	0		1	3	2	1
Xanthoma	1	0		1	11	8	3

GCT: giant cell tumor; PNST: peripheral nerve sheath tumor; T: tumor.

Doppler color flow. This examination made it possible to determine the level of the plane where the tumor appeared most tissular.

The CEUS was then performed at the level determined in B mode, with a bolus injection of 4.8 mL SonoVue® (Bracco Imaging, France) injected into a vein in the elbow crease. The tubing was then rinsed with isotonic saline solution. The acquisition was performed at a low mechanical index in real time, which enabled a quantitative approach.

The sequence of recording the raw data of the contrast uptake process lasted at least 3 minutes or until the uptake disappeared completely. The region with the greatest vascularization density was targeted as the ROI.

Assessment criteria

The contrast uptake was analyzed visually, during acquisition, in a binary mode: contrast uptake/no contrast uptake. After application of the curve modelling software, the patients were classified into four groups: contrast uptake visible and curve obtained; no contrast uptake and no curve; contrast uptake visible but no curve modelled; no contrast uptake but curve present.

In the group with a curve, the modelling software furnished five parameters that were analyzed statistically: peak intensity, time to peak, initial slope, mean transit time, and area under the curve.

The intensity of the signal cannot be assessed by visual analysis of the curves, as the scale adapts to the results. Fig. 1, which depicts the superposition of these curves, shows real disparities in tumor vascularization.

Statistical analysis

For the visual assessment of contrast uptake, we calculated the specificity, sensitivity, positive predictive value (PPV) and negative predictive values (NPV) of the absence of contrast uptake in a diagnosis that the tumor is benign. The enhancement curve parameters were analyzed with the Kruskal–Wallis non-parametric test for quantitative variables, to compare the different groups of patients.

Results

Of 118 tumors, 81 were benign, 23 primary malignant neoplasms, 11 metastases, and three lymphomas. The mean size of the lesions in their longest dimension was 69 mm (4–220 mm) in the benign group, 72 mm (16–320 mm) in the malignant group, and 67 mm in group 3 (7–320 mm).

Overall, in all four groups, 45 patients had visible contrast uptake and a curve, 42 neither visible contrast uptake nor a curve, and six visible contrast uptake but no curve (Table 1). No curves were obtained from any patients for whom contrast uptake was not visible.

After the SonoVue® injection, contrast uptake could be seen in 26/81 benign tumors (32.1%) (Fig. 2), 16/23 primary malignant neoplasms (69.5%) (Fig. 3), and ten of 14 patients with lymphoma or a metastasis (71.4%).

When we took all the lesions into account, the absence of contrast uptake had a sensitivity of 70%, a specificity of

Table 2 Statistical analysis of curve parameters.

	Benign			Malignant			Malignant-metastasis-lymphoma		
	Mean	Standard deviation	Median	Mean	Standard deviation	Median	Mean	Standard deviation	Median
Slope (10E-5 AU/s)	12.36	33.28	1.2	160.9	260.94	28.1	109.6	217.68	6.7
Peak intensity (10E-5 AU)	93.84	263.1	8	955.3	1529.52	132.4	645.9	1276.76	45.9
Time to peak(s)	15.62	15.25	9.6	10.54	11.24	7.25	10.93	9.59	8.15
Mean transit time (s)	30.32	33.36	19.4	19.14	13.16	16.35	22.03	13.42	19.75
Area under the curve (10E-5 AU.s)	4465	14917.5	277.1	15580	19678.53	2545	11530	16874.68	1211

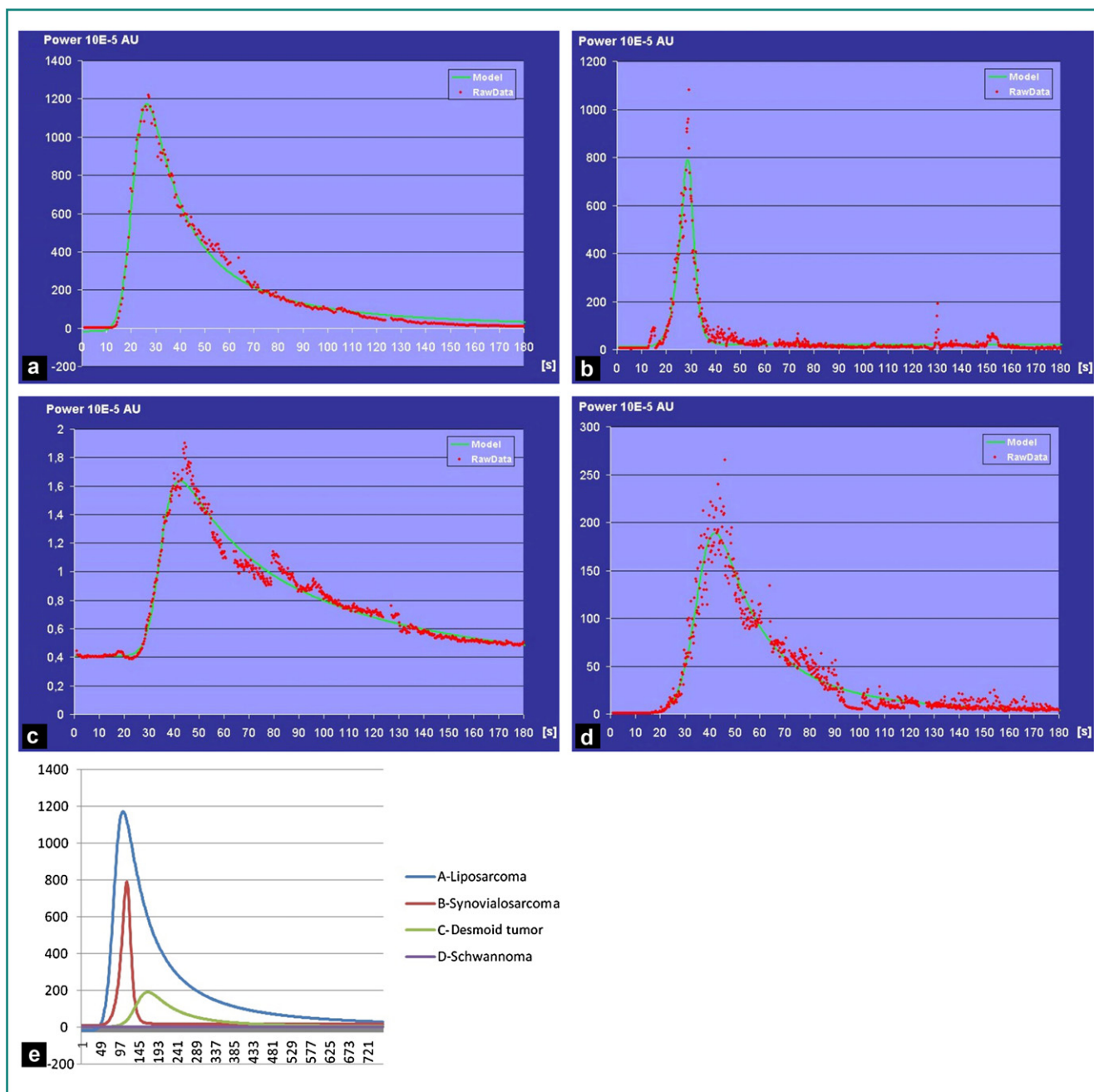


Figure 1. Comparative curves at the same scale of four tumors with different contrast uptake. a: Dedifferentiated liposarcoma; b: Synovial sarcoma; c: Schwannoma; d: Desmoid tumor; e: Summary graph of curves.

68%, a PPV of 50%, and a NPV of 83% for a diagnosis that the lesion was benign.

The parametric study was performed from 69 curves obtained with the modelling software (60% of cases), that is, 47/81 in group 1 and 22/37 in group 3 (including 14 in group 2). Table 2 summarizes these results and Table 3 presents their statistical analysis.

The area under the curve was the most discriminating measure, with a $\text{Chi}^2 = 8.61$ and $P < 0.005$ for discriminating

benign from malignant tumors among all the lesions studied and $\text{Chi}^2 = 7.71$ ($P = 0.005$) when metastases and lymphomas were excluded.

Two other indicators emerged as significant: slope ($\text{Chi}^2 = 8.12$, $P = 0.004$) and peak intensity ($\text{Chi}^2 = 7$; 55, $P = 0.005$). On the other hand, study of time to peak and mean transit time showed no exploitable variability (Fig. 4). Nor was it possible to define a cut-off point for distinguishing benign from malignant tumors because the

Table 3 Kruskal-Wallis Chi².

	Benign/malignant		Benign/malignant + metastases + lymphoma	
	Kruskal-Wallis Chi ²	P value	Kruskal-Wallis Chi ²	P value
Slope	7.5561	0.005981	8.121	0.004375
Peak intensity	7.4845	0.006223	7.5581	0.005974
Time to peak	0.5697	0.4504	0.2788	0.5975
Mean transit time	1.059	0.3034	0.1078	0.7426
Area under the curve	7.7196	0.005463	8.6185	0.003328

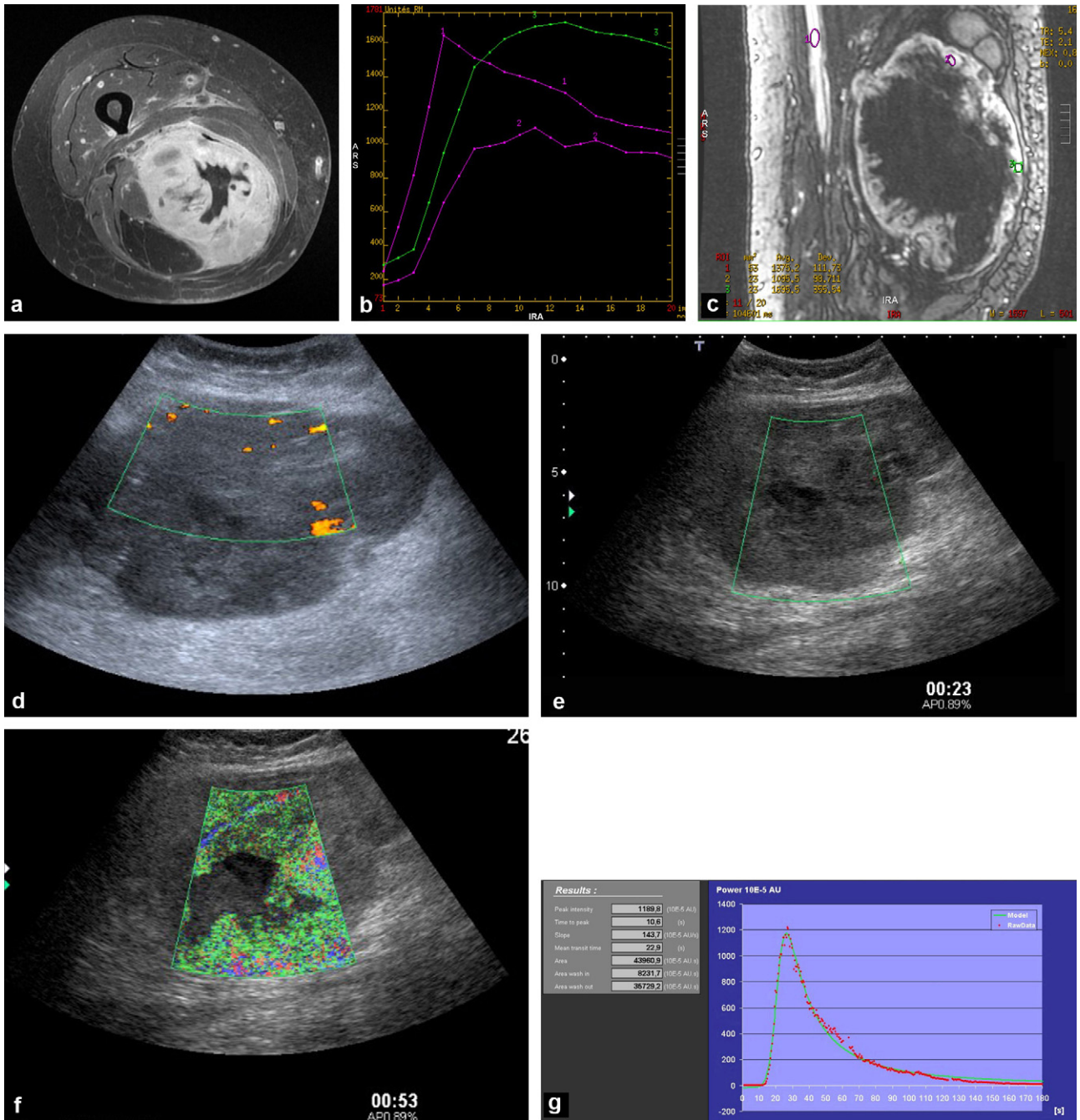


Figure 2. Patient with a dedifferentiated liposarcoma of the thigh. a, b, c: MRI and perfusion; d: Ultrasonography; e, f: Contrast-enhanced ultrasonography at 22 and 53 s; g: Raw data in red, model of the curve in green, table of parameter calculation.

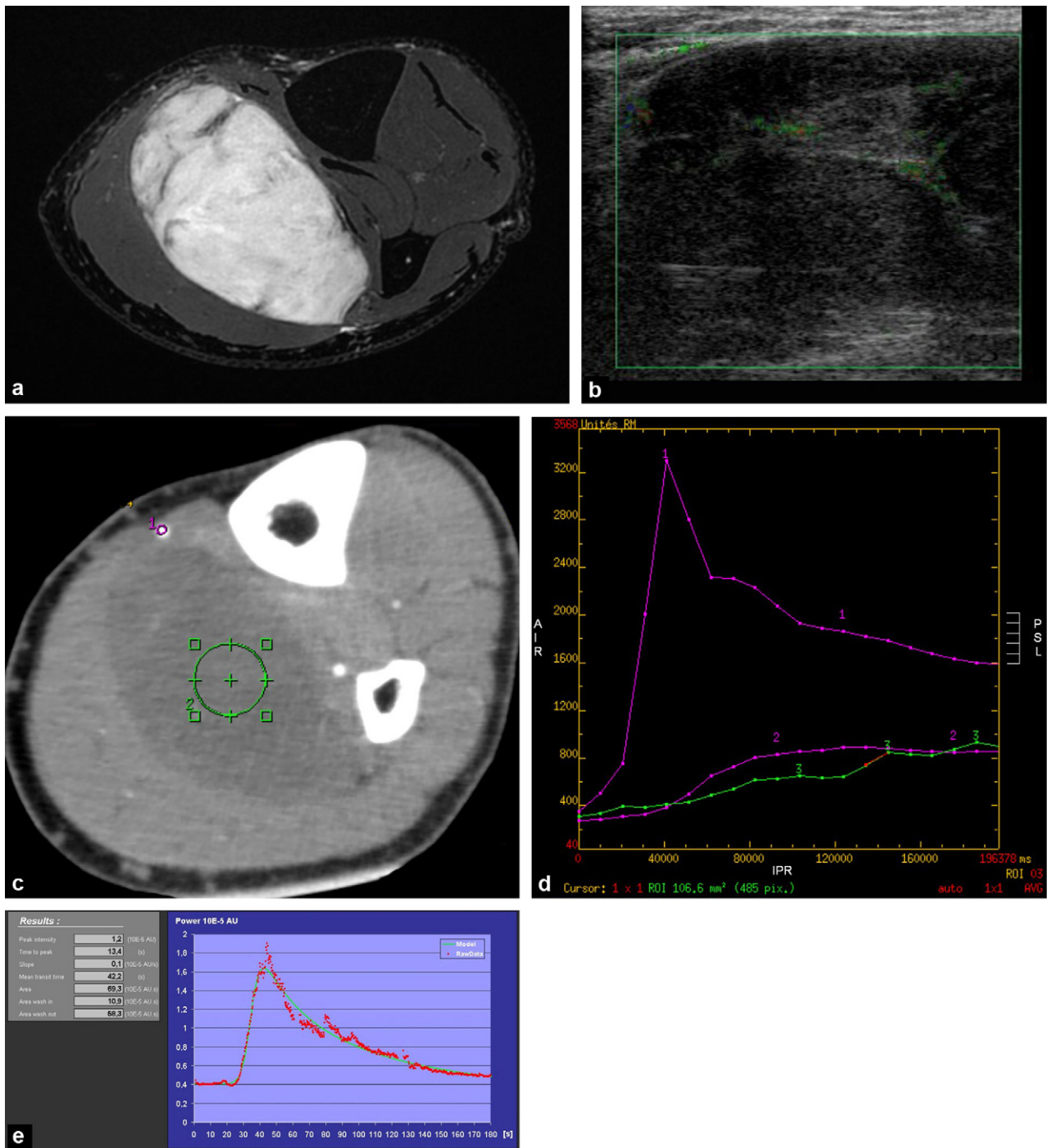


Figure 3. Leg schwannoma. a: MRI; b: Contrast-enhanced ultrasonography at 1 min 13; c, d: Perfusion CT; e: Parameter calculation table, model of the curve.

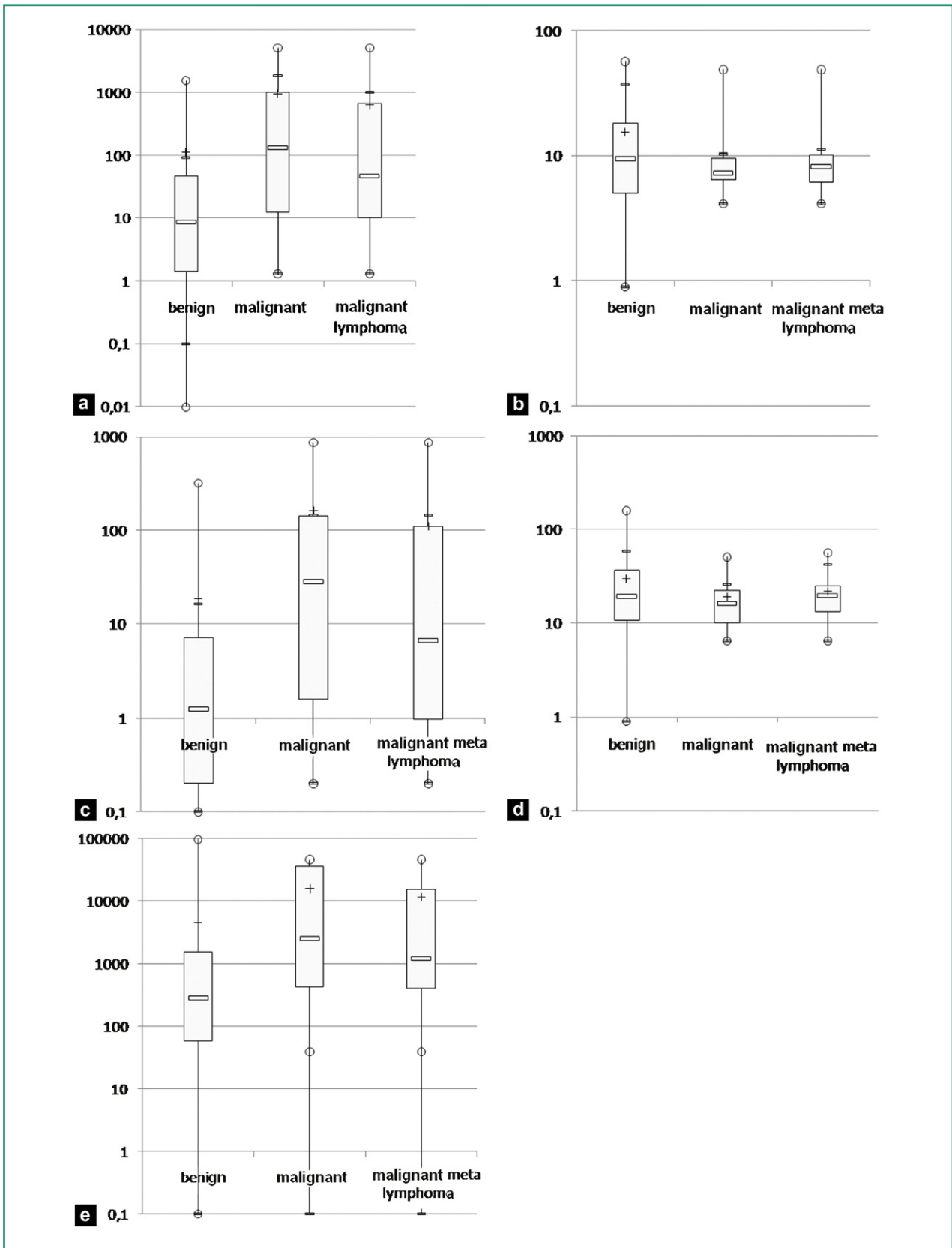


Figure 4. Box plot. Upper and lower edges of the box: first and third quartile. a: Peak intensity; b: Time to peak; c: Slope; d: Mean time transit; e: Area under the curve. Logarithmic scale used in the vertical axis: : median; long horizontal line within the rectangular box. +: medium. o: minimum and maximum.

cut-off values varied too much in relation to the number of subjects.

Discussion

Characterization of the tumor remains a major issue in the management of soft-tissue tumors. Some lesions with an appearance on imaging characteristic of benign tumors (lipoma, AVM, elastofibroma, or mucoid cyst) may not justify a biopsy. Inversely, any tumor that is either malignant or uncertain requires histologic verification. Nonetheless, despite the progress in techniques of biopsy, guidance, and cytologic and histologic analyses, some biopsies remain negative and create the risk of erroneous diagnoses and complications. Moreover, it is not unusual to observe that some biopsies follow an extra compartmental route that modifies the prognosis and management of malignant neoplasms. For these reasons, numerous authors underline that these procedures should be performed only in specialized centers where the type and route of biopsy are decided by a multidisciplinary decision treatment committee [20–22].

It is nonetheless true that the improvement of the tools for characterizing benign lesions or for differentiating benign and malignant tumors should make it possible to avoid some biopsies and facilitate management. Neoangiogenesis is an independent and quantifiable criterion of malignancy [23,24], widely used in MRI and still more promisingly in CT [25–27]. Nonetheless, perfusion studies lack specificity. In CT, as in MRI, contrast products diffuse through the tumor's vascular sector and then its interstitial tissue. In malignant neoplasms, microvascularization, stimulated by angiogenic factors, is formed by abnormal microvessels that are fragile and extremely permeable, generating in a characteristic fashion a contrast uptake that is rapid, intense, and heterogeneous with small, irregular, anarchic vessels. These abnormalities may be missing or not detectable with current techniques [3,28–30].

CEUS is different from Doppler ultrasound because it detects the microcirculation better. It is different from MRI or CT for several reasons:

- enhancement in CEUS reflects the vascular portion of neo-vascularization, without passing through the interstitial sector, unlike contrast products in CT and MRI, where a portion of the tumor enhancement is due to the presence of contrast product in the interstitial area. With CT and MRI, the speed and amplitude of the enhancement associated with exchanges between the plasma and the interstitial tissue depend respectively on capillary permeability and on the dilution volume in the interstitial tissue;
- although the spatial analysis in the plane is well correlated with the MRI [31], its temporal resolution is much better than those of CT and especially MRI. Ultrasonography obtains 12 to 24 images/s and records the raw linear data at four images per second. In comparison, perfusion CT can obtain a measurement every 0.3 to 5 s, and MRI generally furnishes images at a still greater interval. The initial phase, which reflects perfusion and blood volume, is very brief, on the order of 10 to 20 s and thus theoretically requires a temporal resolution on the order of one

image per second. The mathematical models that adapt to poorer temporal resolution have numerous limitations [2];

- finally, like CT but unlike MRI, in CEUS the intensity of the signal is proportional to the concentration of the contrast product.

For all of these reasons, the results obtained with CEUS differ from those obtained with MRI or CT. Our study shows that modelling the contrast uptake is possible in 60% of cases: the area under the enhancement curve is probably a good reflection of neoangiogenesis although it does not appear sufficiently discriminant. In the absence of the curve, binary analysis (contrast uptake or none) remains possible. The absence of contrast uptake is a good negative predictive factor for malignancy but its specificity is insufficient. From a practical point of view, visual analysis of the contrast uptake represents the first stage. That is, the absence of contrast uptake has a strong NPV for malignancy and makes any attempt at modelling futile.

Several studies have shown the interest of this technique in other fields of application. In the multicenter study reported by H Trillaud, CEUS was more effective than either CT or MRI in characterizing focal hepatic lesions [32]. It enables an earlier determination of the efficacy of antiangiogenic treatment than does either CT or MRI because hemodynamic modifications occur several days before the tumor actually shrinks [17,19]. Finally, the multicenter study reported by F Tranquard demonstrates the excellent acceptability and economic benefits of CEUS compared to either CT or MRI in the diagnosis of nodular hepatic lesions [33].

This technique has several limitations. As for any relatively new method, it comes with a specific learning curve, as shown by the exclusion of our earliest patients. It requires an appropriate ultrasound device with software for curve modelling. This equipment is becoming more widely used, and numerous devices today have built-in quantification software, although the use of an external workstation facilitates data treatment. It is necessary to choose carefully the plane passing through the zone most representative of the tumor, which probably makes CEUS a second-line technique, possibly after CT or MRI. A double injection is also conceivable, with a first acquisition of the entire tumor to identify the most vascularized area.

This study involves several biases. There is a selection bias since it is a retrospective study and numerous benign lesions did not benefit from this technique. Accordingly, the proportion of malignant neoplasms to benign tumors is higher than in most series but nonetheless lower than that seen in some oncology centers [34–36]. The ratio thus remains acceptable. The second bias involves the visual and therefore subjective choice of the ROI. Unlike the studies of treatment follow-up, where the ROI must include the entire tumor [19,37], it is preferable in characterizing lesions to avoid areas of necrosis or of myxoid degeneration. Nonetheless, positioning the ROI can be difficult when only the capsule or extreme periphery is vascularized. Finally, it is probable that the curves obtained for the tumors that did not take up the contrast product reflect the noise of tissue backscatter rather than any real neoangiogenesis. We have chosen to conserve these curves as long as the data appeared

consistent because noise is inherent in the technique and therefore present in all the curves.

Finally, the results probably depend on the equipment and technology used, but these are currently the only ones available on the market.

Conclusion

CEUS is a technique easily applicable to soft-tissue tumors. It is potentially interesting for characterizing them. This interest is strengthened by the use of software for modelling the kinetics of the contrast uptake. A prospective study comparing the relative utility of MRI and ultrasonography for this subject and assessing the correlation of the results as a function of the tumor volume is currently underway in our department.

Disclosure of interest

The authors declare that they have no conflicts of interest concerning this article.

Acknowledgments

Pierre-André Vuissoz, CIC IT Nancy.

References

- [1] Gustafson P, Akerman M, Alvegård TA, Coindre JM, Fletcher CD, Rydholm A, et al. Prognostic information in soft tissue sarcoma using tumour size, vascular invasion and microscopic tumour necrosis-the SIN-system. *Eur J Cancer* 2003;39:1568–76.
- [2] De Bazelaire C, Farges C, Albiter M, Chapellier-Canaud M, Pluvinage A, Saksouk A, et al. Imagerie de l'angiogénèse tumorale: principes et applications en CT et IRM. In: SFR., editor. *Formation Médicale Continue*. 2009. p. 757–68.
- [3] Huwart L, Michoux N, Van Beers BE. Imagerie par résonance magnétique de l'angiogénèse tumorale. *J Radiol* 2007;88:331–8.
- [4] Mayerhoefer ME, Breitenhofer M, Amann G, Dominkus M. Are signal intensity and homogeneity useful parameters for distinguishing between benign and malignant soft tissue masses on MR images? Objective evaluation by means of texture analysis. *Magn Reson Imaging* 2008;26:1316–22.
- [5] Wilson SR, Burns PN. Microbubble-enhanced US in body imaging: what role? *Radiology* 2010;257:24–39.
- [6] Schnapauff D, Zeile M, Niederhagen MB, Fleige B, Tunn PU, Hamm B, et al. Diffusion-weighted echo-planar magnetic resonance imaging for the assessment of tumor cellularity in patients with soft-tissue sarcomas. *J Magn Reson Imaging* 2009;29:1355–9.
- [7] Nagata S, Nishimura H, Uchida M, Sakoda J, Tonan T, Hiraoka K, et al. Diffusion-weighted imaging of soft tissue tumors: usefulness of the apparent diffusion coefficient for differential diagnosis. *Radiat Med* 2008;26:287–95.
- [8] Seitz K, Strobel D, Bernatik T, Blank W, Friedrich-Rust M, Herbay A, et al. Contrast-enhanced ultrasound (CEUS) for the characterization of focal liver lesions - prospective comparison in clinical practice: CEUS vs. CT (DEGUM multicenter trial). Parts of this manuscript were presented at the Ultrasound Dreiländertreffen 2008, Davos. *Ultraschall Med* 2009;30:383–9.
- [9] Beaton C, Cochlin D, Kumar N. Contrast enhanced ultrasound should be the initial radiological investigation to characterise focal liver lesions. *Eur J Surg Oncol* 2010;36:43–6.
- [10] Jang HJ, Yu H, Kim TK. Contrast-enhanced ultrasound in the detection and characterization of liver tumors. *Cancer Imaging* 2009;9:96–103.
- [11] Catalano O, Sandomenico F, Matarazzo I, Siani A. Contrast-enhanced sonography of the spleen. *AJR Am J Roentgenol* 2005;184:1150–6.
- [12] Eckersley RJ, Sedelaar JP, Blomley MJ, Wijkstra H, deSouza NM, Cosgrove DO, et al. Quantitative microbubble enhanced transectal ultrasound as a tool for monitoring hormonal treatment of prostate carcinoma. *Prostate* 2002;51:256–67.
- [13] D'Arcy TJ, Jayaram V, Lynch M, Soutter WP, Cosgrove DO, Harvey CJ, et al. Ovarian cancer detected non-invasively by contrast-enhanced power Doppler ultrasound. *BJOG* 2004;111:619–22.
- [14] Halpern EJ. Contrast-enhanced ultrasound imaging of prostate cancer. *Rev Urol* 2006;8:529–37.
- [15] Cosgrove D, Harvey C. Clinical uses of microbubbles in diagnosis and treatment. *Med Biol Eng Comput* 2009;47:813–26.
- [16] Cosgrove D, Lassau N. Évaluation de l'angiogénèse tumorale à l'aide de l'échographie de contraste. *J Radiol* 2009;90:156–64.
- [17] Lassau N, Chebil M, Chami L, Bidault S, Girard E, Roche A. Dynamic contrast-enhanced ultrasonography (DCE-US): a new tool for the early evaluation of antiangiogenic treatment. *Target Oncol* 2010;5(1):53–8 [Epub 2010 Apr 9].
- [18] Cyteval C, Baron M, Hoa D, Thouvenin Y. Innovations techniques en échographie ostéo-articulaire. *JFR* 2010.
- [19] Lassau N, Brule A, Chami L, Benatsou B, Peronneau P, Roche A. Évaluation précoce des traitements anti-angiogéniques par échographie dynamique de contraste. *J Radiol* 2008;89:549–55.
- [20] Rougraff BT, Aboulafia A, Biermann JS, Healey J. Biopsy of soft tissue masses: evidence-based medicine for the musculoskeletal tumor society. *Clin Orthop Relat Res* 2009;467:2783–91.
- [21] Kasraeian S, Allison DC, Ahlmann ER, Fedenko AN, Menendez LR. A comparison of fine-needle aspiration, core biopsy, and surgical biopsy in the diagnosis of extremity soft tissue masses. *Clin Orthop Relat Res* 2010.
- [22] Ng VY, Thomas K, Crist M, Wakely Jr PE, Mayerson J. Fine needle aspiration for clinical triage of extremity soft tissue masses. *Clin Orthop Relat Res* 2010;468:1120–8.
- [23] Cuenod CA, Fournier L, Balvay D, Guinebretiere JM. Tumor angiogenesis: pathophysiology and implications for contrast-enhanced MRI and CT assessment. *Abdom Imaging* 2006;31:188–93.
- [24] Turkbey B, Kobayashi H, Ogawa M, Bernardo M, Choyke PL. Imaging of tumor angiogenesis: functional or targeted? *AJR Am J Roentgenol* 2009;193:304–13.
- [25] Provenzale JM. Imaging of angiogenesis: clinical techniques and novel imaging methods. *AJR Am J Roentgenol* 2007;188:11–23.
- [26] von Herbay A, Westendorff J, Gregor M. Contrast-enhanced ultrasound with SonoVue: differentiation between benign and malignant focal liver lesions in 317 patients. *J Clin Ultrasound* 2010;38:1–9.
- [27] Charnley N, Donaldson S, Price P. Imaging angiogenesis. *Methods Mol Biol* 2009;467:25–51.
- [28] Goh V, Padhani AR. Imaging tumor angiogenesis: functional assessment using MDCT or MRI? *Abdom Imaging* 2006;31:194–9.
- [29] Tuncbilek N, Karakas HM, Okten OO. Dynamic contrast enhanced MRI in the differential diagnosis of soft tissue tumors. *Eur J Radiol* 2005;53:500–5.
- [30] Daldrup H, Shames DM, Wendland M, Okuhata Y, Link TM, Rose-nau W, et al. Correlation of dynamic contrast-enhanced MR imaging with histologic tumor grade: comparison of macro-molecular and small-molecular contrast media. *AJR Am J Roentgenol* 1998;171:941–9.

- [31] Yankeelov TE, Niermann KJ, Huamani J, Kim DW, Quarles CC, Fleischer AC, et al. Correlation between estimates of tumor perfusion from microbubble contrast-enhanced sonography and dynamic contrast-enhanced magnetic resonance imaging. *J Ultrasound Med* 2006;25:487–97.
- [32] Trillaud H, Bruel JM, Valette PJ, Vilgrain V, Schmutz G, Oyen R, et al. Characterization of focal liver lesions with SonoVue-enhanced sonography: international multicenter-study in comparison to CT and MRI. *World J Gastroenterol* 2009;15:3748–56.
- [33] Tranquart F, Correas JM, Ladam Marcus V, Manzoni P, Vilgrain V, Aubé C, et al. Échographie de contraste temps réel dans la prise en charge diagnostique des lésions nodulaires hépatiques: évaluation des performances diagnostiques et de l'impact économique sur une étude multicentrique française. *J Radiol* 2009;90:109–22.
- [34] Blum A, Lecocq S, Louis M, Detreille R, Roch D, Proust C, et al. Comment j'explore une tumeur des parties molles. In: JFR., editor. *Formation Médicale Continue*. 2008. p. 657–66.
- [35] Kransdorf MJ. Malignant soft-tissue tumors in a large referral population: distribution of diagnoses by age, sex, and location. *AJR Am J Roentgenol* 1995;164:129–34.
- [36] Kransdorf MJ. Benign soft-tissue tumors in a large referral population: distribution of specific diagnoses by age, sex, and location. *AJR Am J Roentgenol* 1995;164:395–402.
- [37] Ignee A, Jedrejczyk M, Schuessler G, Jakubowski W, Dietrich CF. Quantitative contrast enhanced ultrasound of the liver for time intensity curves-reliability and potential sources of errors. *Eur J Radiol* 2010;73:153–8.

Discussion et conclusions

Les travaux réalisés avec l'échographie contrastée ont démontré que cette méthode fournit des informations importantes pour la caractérisation tumorale. Après la modélisation des courbes, plusieurs paramètres de perfusion, extraits des données échographiques ont pu être étudiés.

Trois paramètres perfusionnels étaient significativement différents entre les lésions bénignes et malignes : l'aire sur la courbe, la pente et l'intensité du pic de rehaussement. Le temps de transit moyen et le temps de pic étaient similaires entre les tumeurs étudiées, ce qui est probablement expliqué par la pharmacocinétique intra-vasculaire stricte du produit de contraste ultrasonore. Les paramètres perfusionnels en échographie contrastée semblent être bien corrélés à la densité capillaire des tumeurs. Les différences marquées des valeurs de l'aire sur la courbe entre des lésions bénignes et malignes en sont témoins. La distribution variée des valeurs des paramètres perfusionnels étudiés n'a pas permis d'établir de critères diagnostics valables, ce qui est probablement en rapport avec l'hétérogénéité histologique des lésions étudiées. Une évaluation de l'échographie contrastée ciblée sur un sous-groupe de tumeurs pourrait être plus concluante.

A partir de la corrélation entre l'analyse subjective du rehaussement à l'échographie contrastée, le type histologique des lésions et l'aspect échographique en mode B, le rôle de la technique dans la caractérisation tumorale a pu être vérifié. La valeur prédictive négative élevée (80%) de l'échographie contrastée pour les lésions malignes doit être soulignée. Une courbe d'apprentissage relativement longue et une fenêtre d'évaluation restreinte à une zone limitée de la tumeur constituent des difficultés importantes à l'utilisation de cette méthode. Bien que utile dans la caractérisation tumorale, l'échographie contrastée reste mieux adaptée à une évaluation initiale et l'IRM et/ou la TDM restent incontournables au bilan d'imagerie d'une masse des parties molles.

CONCLUSION

Cette thèse aide à confirmer le rôle des techniques d'imagerie fonctionnelle dans l'évaluation des tumeurs ostéo-articulaires. Ces outils permettent d'avoir plus de critères pour juger l'agressivité d'une masse tumorale, augmentant ainsi la sensibilité du bilan d'imagerie. Malgré cet apport diagnostique bénéfique l'imagerie fonctionnelle doit avoir une utilisation complémentaire et non substitutive par rapport aux critères classiques d'évaluation morphologique. Ces derniers restent le pilier central de l'évaluation en radiologie oncologique. L'impact diagnostique positif des méthodes fonctionnelles est certain, mais pas encore mesuré.

Les données perfusionnelles acquises par trois méthodes différentes ont pu être étudiées. Le post traitement de ces données a généré des paramètres visuels, semi-quantitatifs et quantitatifs, permettant une confrontation entre les performances de ces méthodes. L'IRM, sensible et non-irradiante garde son poste de méthode préférentielle. Cette méthode s'est montrée très performante pour l'identification d'un nidus d'ostéome ostéoïde viable chez les patients traités par ablation laser. La TDM s'est montrée une option attractive pour l'évaluation des extrémités où des protocoles multiphasiques peuvent être utilisés avec une très basse dose effective. L'association entre la perfusion en TDM et la soustraction osseuse par masque permet une nette amélioration de l'analyse des lésions osseuses en TDM. Finalement, l'échographie de contraste, du fait de sa disponibilité et de son coût (37,86 euros contre 100,51 euros pour le scanner et 192,34 euros pour l'IRM), a un rôle dans l'évaluation initiale des tumeurs des parties molles. L'étude de la perfusion en échographie est probablement la meilleure façon d'évaluer la densité capillaire d'une tumeur.

Les techniques qui sensibilisent l'analyse des valeurs d'ADC sur les séquences de diffusion en IRM sont fondamentales. L'évaluation centrée sur la zone d'ADC minimale et l'appréciation de l'intensité de signal de la masse étudiée sur les séquences T2 ont permis une amélioration de la performance de cette technique par rapport aux études précédentes. Cependant, l'interprétation des valeurs d'ADC des lésions osseuses et hypo-intenses en T2 est plus difficile, nécessitant encore des études ciblées pour établir des critères diagnostiques spécifiques à ces sous-groupes.

Beaucoup de travail sera encore nécessaire avant que la spectroscopie de protons quantitative en IRM puisse être couramment appliquée en pratique clinique. Néanmoins, ces résultats ont permis d'avancer sur la compréhension de l'influence de la composition et la structure du tissu évalué sur les spectres acquis et servira comme base pour de futures recherches. L'expérience avec la spectroscopie des tissus calcifiés sert comme une alerte à l'interprétation des mesures

d'amplitude et de concentration sur des spectres provenant de lésions calcifiées, qui sont fortement influencées par la présence des cristaux de calcium.

Le développement et l'amélioration des outils pour la caractérisation des tumeurs du système ostéo-articulaire constituent un vaste champ de recherche. L'impact potentiel de ces outils sur le pronostic des patients porteurs d'une néoplasie ostéo-articulaire justifie l'effort scientifique sur cette thématique. Cette thèse présente des résultats positifs qui contribuent au développement de l'imagerie fonctionnelle, mais la route qui mène à une caractérisation tumorale non-invasive fiable en imagerie ostéo-articulaire est encore longue.

Références bibliographiques :

1. Wu JS, Hochman MG. Soft-Tissue Tumors and Tumor-like Lesions: A Systematic Imaging Approach. *Radiology*. 11 Janvier 2009;253(2):297–316.
2. Van Rijswijk CSP, Geirnaerd MJA, Hogendoorn PCW, Taminiau AHM, van Coevorden F, Zwinderman AH, et al. Soft-tissue tumors: value of static and dynamic gadopentetate dimeglumine-enhanced MR imaging in prediction of malignancy. *Radiology*. November 2004;233(2):493–502.
3. Springfield D. Surgery for MSK tumors: 1971-2011. *Skeletal Radiol*. Septembre de 2011;40(9):1233–7.
4. Alter CL, Pelcovitz D, Axelrod A, Goldenberg B, Harris H, Meyers B, et al. Identification of PTSD in cancer survivors. *Psychosomatics*. Avril 1996;37(2):137–43.
5. Wiener L, Battles H, Bernstein D, Long L, Derdak J, Mackall CL, et al. Persistent psychological distress in long-term survivors of pediatric sarcoma: the experience at a single institution. *Psychooncology*. Octobre 2006;15(10):898–910.
6. Mary P, Thévenin-Lemoine C. [New surgical procedures in musculoskeletal sarcomas of the child]. *Bull Cancer (Paris)*. Mai 2011;98(5):515–26.
7. Errani C, Longhi A, Rossi G, Rimondi E, Biazzo A, Toscano A, et al. Palliative therapy for osteosarcoma. *Expert Rev Anticancer Ther*. Février 2011;11(2):217–27.
8. Fletcher CDM, Unni KK, Mertens F. *Pathology & Genetics: Tumours of Soft Tissue and Bone*. IARC; 2002.
9. Jemal A, Siegel R, Ward E, Murray T, Xu J, Thun MJ. Cancer statistics, 2007. *CA Cancer J Clin*. Février 2007;57(1):43–66.
10. Howlader N, Noone AM, Krapcho M, Garshell J, Neyman N, Altekruse SF, et al. *SEER Cancer Statistics Review, 1975-2010*. National Cancer Institute. Bethesda, MD;
11. Walker EA, Fenton ME, Salesky JS, Murphey MD. Magnetic resonance imaging of benign soft tissue neoplasms in adults. *Radiol Clin North Am*. Novembre 2011;49(6):1197–1217, vi.
12. Ducimetière F, Lurkin A, Ranchère-Vince D, Decouvelaere A-V, Isaac S, Claret-Tournier C, et al. [Incidence rate, epidemiology of sarcoma and molecular biology. Preliminary results from EMS study in the Rhône-Alpes region]. *Bull Cancer (Paris)*. Juin 2010;97(6):629–41.
13. Anract P. *Cancers osseux*. John Libbey Eurotext; 2007.

14. Ruggieri P, Mavrogenis AF, Mercuri M. Quality of life following limb-salvage surgery for bone sarcomas. *Expert Rev Pharmacoecon Outcomes Res.* Février 2011;11(1):59–73.
15. Allison DC, Carney SC, Ahlmann ER, Hendifar A, Chawla S, Fedenko A, et al. A meta-analysis of osteosarcoma outcomes in the modern medical era. *Sarcoma.* 2012;2012:704872.
16. Gielen JLMA, De Schepper AM, Vanhoenacker F, Parizel PM, Wang XL, Sciot R, et al. Accuracy of MRI in characterization of soft tissue tumors and tumor-like lesions. A prospective study in 548 patients. *Eur Radiol.* Décembre 2004;14(12):2320–30.
17. Mankin HJ, Mankin CJ, Simon MA. The hazards of the biopsy, revisited. Members of the Musculoskeletal Tumor Society. *J Bone Joint Surg Am.* Mai 1996;78(5):656–63.
18. Fayad LM, Jacobs MA, Wang X, Carrino JA, Bluemke DA. Musculoskeletal tumors: how to use anatomic, functional, and metabolic MR techniques. *Radiology.* Novembre 2012;265(2):340–56.
19. Fayad LM, Salibi N, Wang X, Machado AJ, Jacobs MA, Bluemke DA, et al. Quantification of muscle choline concentrations by proton MR spectroscopy at 3 T: technical feasibility. *AJR Am J Roentgenol.* Janvier 2010;194(1):W73–79.
20. Herneth AM, Friedrich K, Weidekamm C, Schibany N, Krestan C, Czerny C, et al. Diffusion weighted imaging of bone marrow pathologies. *Eur J Radiol.* Juillet 2005;55(1):74–83.
21. Bowden DJ, Barrett T. Angiogenesis imaging in neoplasia. *J Clin Imaging Sci.* 2011;1:38.
22. Vries HE de, Kuiper J, Boer AG de, Berkel TJCv, Breimer DD. The Blood-Brain Barrier in Neuroinflammatory Diseases. *Pharmacol Rev.* 6 Janvier 1997;49(2):143–56.
23. Tofts PS, Brix G, Buckley DL, Evelhoch JL, Henderson E, Knopp MV, et al. Estimating kinetic parameters from dynamic contrast-enhanced T(1)-weighted MRI of a diffusable tracer: standardized quantities and symbols. *J Magn Reson Imaging JMRI.* Septembre 1999;10(3):223–32.
24. Bloch F. The Principle of Nuclear Induction. *Science.* 16 Octobre 1953;118(3068):425–30.
25. Purcell EM, Torrey HC, Pound RV. Resonance absorption by nuclear magnetic moments in solid. 69^o ed *Physical Review* 69; 1946;37–8.
26. Larsen VA, Simonsen HJ, Law I, Larsson HBW, Hansen AE. Evaluation of dynamic contrast-enhanced T1-weighted perfusion MRI in the differentiation of tumor recurrence from radiation necrosis. *Neuroradiology.* Février 2013;55(3):361–9.
27. Sugahara T, Korogi Y, Tomiguchi S, Shigematsu Y, Ikushima I, Kira T, et al. Posttherapeutic intraaxial brain tumor: the value of perfusion-sensitive contrast-enhanced MR imaging for

- differentiating tumor recurrence from nonneoplastic contrast-enhancing tissue. *AJNR Am J Neuroradiol*. Mai 2000;21(5):901–9.
28. Khoo MMY, Tyler PA, Saifuddin A, Padhani AR. Diffusion-weighted imaging (DWI) in musculoskeletal MRI: a critical review. *Skeletal Radiol*. Juin 2011;40(6):665–81.
 29. Fayad LM, Bluemke DA, McCarthy EF, Weber KL, Barker PB, Jacobs MA. Musculoskeletal tumors: use of proton MR spectroscopic imaging for characterization. *J Magn Reson Imaging JMRI*. Janvier 2006;23(1):23–8.
 30. Fayad LM, Barker PB, Jacobs MA, Eng J, Weber KL, Kulesza P, et al. Characterization of musculoskeletal lesions on 3-T proton MR spectroscopy. *AJR Am J Roentgenol*. Juillet de 2007;188(6):1513–20.
 31. Wang C-K, Li C-W, Hsieh T-J, Chien S-H, Liu G-C, Tsai K-B. Characterization of bone and soft-tissue tumors with in vivo ¹H MR spectroscopy: initial results. *Radiology*. Août 2004;232(2):599–605.
 32. Smith-Bindman R, Miglioretti DL, Larson EB. Rising Use Of Diagnostic Medical Imaging In A Large Integrated Health System. *Health Aff (Millwood)*. 11 Janvier 2008;27(6):1491–502.
 33. Kambadakone AR, Sahani DV. Body perfusion CT: technique, clinical applications, and advances. *Radiol Clin North Am*. Janvier 2009;47(1):161–78.
 34. Yu L, Li H, Mueller J, Kofler JM, Liu X, Primak AN, et al. Metal artifact reduction from reformatted projections for hip prostheses in multislice helical computed tomography: techniques and initial clinical results. *Invest Radiol*. Novembre 2009;44(11):691–6.
 35. Kataoka ML, Hochman MG, Rodriguez EK, Lin P-JP, Kubo S, Raptopoulos VD. A review of factors that affect artifact from metallic hardware on multi-row detector computed tomography. *Curr Probl Diagn Radiol*. Août 2010;39(4):125–36.
 36. Morsbach F, Bickelhaupt S, Wanner GA, Krauss A, Schmidt B, Alkadhi H. Reduction of metal artifacts from hip prostheses on CT images of the pelvis: value of iterative reconstructions. *Radiology*. Juillet 2013;268(1):237–44.
 37. Deelman LE, Declèves A-E, Rychak JJ, Sharma K. Targeted renal therapies through microbubbles and ultrasound. *Adv Drug Deliv Rev*. 30 Novembre 2010;62(14):1369–77.

Annexe 1 – Classification des tumeurs des parties molles de l’OMS simplifié.

ADIPOCYTIC TUMOURS		
Benign	Intermediate	Malignant
Lipoma, Lipomatosis, Lipomatosis of nerve, Lipoblastoma / Lipoblastomatosis, Angiolipoma, Myolipoma, Chondroid lipoma, Extrarenal angiomyolipoma, Extra-adrenal myelolipoma, Spindle cell, Pleomorphic lipoma, Hibernoma	Atypical lipomatous tumour/Well differentiated liposarcoma	Dedifferentiated liposarcoma, Myxoid liposarcoma, Round cell liposarcoma, Pleomorphic liposarcoma, Mixed-type liposarcoma, Liposarcoma, not otherwise specified
FIBROBLASTIC / MYOFIBROBLASTIC TUMOURS		
Benign	Intermediate	Malignant
Nodular fasciitis, Proliferative fasciitis. Proliferative myositis, Myositis ossificans, fibro-osseous pseudotumour of digits, Ischaemic fasciitis, Elastofibroma, Fibrous hamartoma of infancy, Myofibroma / Myofibromatosis, Fibromatosis colli, Juvenile hyaline fibromatosis, Inclusion body fibromatosis, Fibroma of tendon sheath, Desmoplastic fibroblastoma, Mammary-type myofibroblastoma, Calcifying aponeurotic fibroma, Angiomyofibroblastoma, Cellular angiofibroma, Nuchal-type fibroma, Gardner fibroma, Calcifying fibrous tumour, Giant cell angiofibroma	Superficial fibromatoses, Desmoid-type fibromatoses, Lipofibromatosis, Solitary fibrous tumour, haemangiopericytoma, Inflammatory myofibroblastic tumour, Myxoinflammatory, fibroblastic sarcoma, Infantile fibrosarcoma	Adult fibrosarcoma, Myxofibrosarcoma, Low grade fibromyxoid sarcoma, hyalinizing spindle cell tumour, Sclerosing epithelioid fibrosarcoma
SO-CALLED FIBROHISTIOCYTIC TUMOURS		
Benign	Intermediate	Malignant
Giant cell tumour of tendon sheath, Diffuse-type giant cell tumour, Deep benign fibrous histiocytoma	Plexiform fibrohistiocytic tumour, Giant cell tumour of soft tissues	Pleomorphic ‘MFH’, Giant cell ‘MFH’, Inflammatory ‘MFH’
SMOOTH MUSCLE TUMOURS		
Benign	Intermediate	Malignant
Angioleiomyoma, Deep leiomyoma, Genital leiomyoma,	-	Leiomyosarcoma
PERICYTIC (PERIVASCULAR) TUMOURS		
Benign	Intermediate	Malignant
Glomus tumour, Myopericytoma	-	Malignant glomus tumour
SKELETAL MUSCLE TUMOURS		
Benign	Intermediate	Malignant
Rhabdomyoma	-	Embryonal rhabdomyosarcoma, Alveolar rhabdomyosarcoma, Pleomorphic rhabdomyosarcoma
VASCULAR TUMOURS		
Benign	Intermediate	Malignant
Haemangiomas of subcut/deep soft tissue, Epithelioid haemangioma, Angiomatosis, Lymphangioma	Kaposiform haemangioendothelioma, Papillary intralymphatic angioendothelioma, Composite haemangioendothelioma	Epithelioid haemangioendothelioma, Angiosarcoma of soft tissue
CHONDRO-OSSEOUS TUMOURS		
Benign	Intermediate	Malignant
Soft tissue chondroma		Mesenchymal chondrosarcoma, Extraskeletal osteosarcoma,
TUMOURS OF UNCERTAIN DIFFERENTIATION		
Benign	Intermediate	Malignant
Intramuscular myxoma, Juxta-articular myxoma, Deep (‘aggressive’) angiomyxoma, Pleomorphic hyalinizing, angiectatic tumour, Ectopic hamartomatous thymoma	Angiomatoid fibrous histiocytoma, Ossifying fibromyxoid tumour, Mixed tumour, Myoepithelioma, Parachordoma	Synovial sarcoma, Epithelioid sarcoma, Alveolar soft part sarcoma, Clear cell sarcoma of soft tissue, Extraskeletal myxoid chondrosarcoma, PNET / Extraskeletal Ewing tumour, pPNET, extraskeletal Ewing tumour, Desmoplastic small round cell tumour, Extra-renal rhabdoid tumour, Malignant mesenchymoma, Neoplasms with perivascular epithelioid cell differentiation (PEComa), Intimal sarcoma

Annexe 2 – Classification des tumeurs osseuses de l’OMS simplifié.

CARTILAGE TUMOURS	
Benign	Malignant
Osteochondroma, Chondroma, Enchondroma, Periosteal chondroma, Multiple chondromatosis, Chondroblastoma, Chondromyxoid fibroma,	Chondrosarcoma (Central, primary,secondary, Peripheral, Dedifferentiated, Mesenchymal), Clear cell
OSTEOGENIC TUMOURS	
Benign	Malignant
Osteoid osteoma, Osteoblastoma	Osteosarcoma (Conventional, chondroblastic, fibroblastic, osteoblastic, Telangiectatic, Small cell, Low grade central, Secondary, Parosteal, Periosteal, High grade superficial)
FIBROGENIC TUMOURS	
Benign	Malignant
Desmoplastic fibroma	Fibrosarcoma
FIBROHISTIOCYTIC TUMOURS	
Benign	Malignant
Benign fibrous histiocytoma	Malignant fibrous histiocytoma
EWING SARCOMA/PRIMITIVE NEUROECTODERMAL TUMOUR	
-	Malignant - Ewing sarcoma
HAEMATOPOIETIC TUMOURS	
Benign	Malignant
Plasma cell myeloma	Malignant lymphoma
GIANT CELL TUMOUR	
Benign	Malignant
Giant cell tumour	Malignancy in giant cell tumour
NOTOCHORDAL TUMOURS	
Benign - Chordoma	-
VASCULAR TUMOURS	
Benign	Malignant
Haemangioma	Angiosarcoma
SMOOTH MUSCLE TUMOURS	
Benign	Malignant
Leiomyoma	Leiomyosarcoma
LIPOGENIC TUMOURS	
Benign	Malignant
Lipoma	Liposarcoma
NEURAL TUMOURS	
Benign - Neurilemmoma	-
MISCELLANEOUS TUMOURS	
-	Malignant - Adamantinoma, Metastatic malignancy
MISCELLANEOUS LESIONS	
Benign - Aneurysmal bone cyst, Simple cyst, Fibrous dysplasia, Osteofibrous dysplasia, Langerhans cell histiocytosis, Erdheim-Chester disease, Chest wall hamartoma	-
JOINT LESIONS	
Benign - Synovial chondromatosis	-

RESUME

L'imagerie médicale joue un rôle majeur dans l'identification, la caractérisation et le bilan d'extension des lésions tumorales du système ostéo-articulaire. La grande majorité de ces néoplasies est bénigne et il est important de savoir les reconnaître et les distinguer des lésions malignes. Ces dernières ont un pronostic beaucoup plus sombre et sont l'objet d'une prise en charge nettement plus agressive. L'IRM est actuellement la technique de choix pour l'évaluation des tumeurs ostéo-articulaires. Malgré une très haute sensibilité pour la détection des tumeurs osseuses et des parties molles, un grand nombre de lésions identifiées ne sont pas caractérisables. Récemment des nouvelles techniques d'imagerie fonctionnelle sont apparues permettant une évaluation tumorale au niveau biochimique et cellulaire. Ces techniques, initialement conçues pour l'évaluation des tumeurs cérébrales comme la perfusion, la diffusion et la spectroscopie ont commencé à être utilisées pour l'évaluation des néoplasies ostéo-articulaires avec des résultats préliminaires prometteurs. Parallèlement, avec le développement en scanner de systèmes de détection à large surface et l'échographie de contraste, l'étude de la perfusion tumorale basée sur ces méthodes est plus accessible en pratique courante. L'imagerie fonctionnelle reste, néanmoins peu accessible en dehors de la recherche. Des difficultés techniques inhérentes à l'application clinique de ces nouvelles méthodes et l'hétérogénéité histologique des tumeurs ostéo-articulaires constituent encore un obstacle important. Dans ce travail la performance diagnostique de plusieurs méthodes d'imagerie fonctionnelle en pratique courante a été évaluée. En outre, des améliorations permettant une augmentation de la qualité d'image et une réduction des artéfacts des méthodes fonctionnelles ont été testées. Secondairement, les performances diagnostiques de différentes méthodes de perfusion tumorale (échographie, tomодensitométrie et imagerie par résonance magnétique) ont été comparées.

Mots clefs : tumeurs, système ostéo-articulaire, imagerie, IRM, tomодensitométrie, échographie.

ABSTRACT

Medical imaging plays a major role in the identification, characterization and staging of tumor lesions of the musculoskeletal system. The vast majority of these neoplasms are benign and it is important to recognize and distinguish them from malignant lesions. Malignant lesions carry a worse prognosis and are usually treated aggressively. MRI is currently the method of choice for evaluating musculoskeletal tumors. Despite a high sensitivity for the detection of bone and soft tissue tumors, a large number of identified lesions remain indeterminate in origin after imaging work-up. In recent years, new functional imaging techniques, which allow tumor evaluation in a biochemical and cellular level, have emerged. These techniques such as perfusion, diffusion weighted imaging and MR spectroscopy, originally designed for the evaluation of brain tumors, began to be used for the evaluation of musculoskeletal neoplasms with promising preliminary results. Meanwhile, with the development of wide area-detector CT systems and contrast enhanced ultrasound (CEUS) new ways of assessing tumor perfusion became available in clinical practice. Functional imaging nevertheless remains largely inaccessible outside research oriented imaging centers. The clinical application of these new methods is hindered by various factors, which include the great histological heterogeneity of musculoskeletal tumors and patient related technical difficulties. In this project, the diagnostic performance of several functional imaging methods in clinical practice was assessed. Additionally tools for image quality improvement and artifact reduction were tested. Finally, the diagnostic performance of different perfusion methods (ultrasound, computed tomography and magnetic resonance imaging) was compared.

Key words: tumors, musculoskeletal system, imaging, MRI, computed tomography, ultrasound.